OPTICAL DEPHASING AND ENERGY TRANSFER IN ORDERED AND DISORDERED SOLIDS: STUDIES BY LASER SPECTROSCOPY AND OPTICAL-MICROWAVE DOUBLE RESONANCE

Thesis by

Duane D. Smith

In Partial Fulfillment of the Requirements

for the Degree of

Doctor of Philosophy

California Institute of Technology

Pasadena, California

1981

(Submitted March 2, 1981)

ACKNOWLEDGEMENTS AND RETROSPECTIVE

My years at Caltech have been valuable. What I have learned here should serve me well. My own modest hope is that this thesis is only the beginning of my scientific contribution. Those people, who in one way or another, were involved in my graduate studies and to whom I owe a debt, best know who they are. However, it is customary to list them here. First my parents, for the financial and moral support necessary to start a career. Of course Debbie, who taught me more than she suspects and made what would have been a pauper's existence comfortable. Ahmed, for outstanding support and insight into fundamental and contemporary solid state problems. My sincere gratitude goes to three colleagues and collaborators who were visiting scientists: Richard Powell (chapter II), Jean Lemaistre (chapter III) and Max Glasbeek (chapter IV). Very, very importantly, the group, which for 4 years was my principal source of scientific and social interaction. Since the group was half Applied Physics, half Chemical Physics, I feel my education was immeasurably better than if we had each been in our separate buildings. The small (if it exists) interdepartmental barrier at Caltech is a marvelous asset whose worth should not be underestimated.

I wish to thank the Caltech shops for their superlative craftsmanship. The cryogenic design of Anton Stark and Bill Scheulke in the instrument shop deserves special mention. Toni is a master of upwards compatibility and simple elegance, which to my way of thinking, can only be learned or appreciated by example. It is certain that such talented individuals are essential to any serious experimentalist. Thanks also go to Fran Bennet and her colleagues for being so extremely

efficient in handling purchase orders and other administrative headaches. They are crucial to the Caltech infra-structure.

It is worth mentioning that this thesis was written on the Caltech word processing VAX computer (Digital Equipment Corporation) and printed on a Nippon Electric Corporation 5520 spinwriter with a math thimble. The thesis files were created and preprocessed by the Interactive Systems Corporation INed screen editor. Then, abstracts, headers, paragraphs, pages, references, etc. were processed (formatted) by the Bell labs NROFF memorandum and scientific macro packages. Finally, with a program I had written in the Bell UNIX editor , ed, the thesis was postprocessed to generate the equations and special character set on the spinwriter. Prolix as it may sound, it was rapid and error free. As the American Physical Society has officially adopted NROFF/TROFF as its official formatting language (Physics Today June 1980, pg. 71) it should prove to be a rapid means of preparing, submitting and distributing scientific papers over telecommunications networks.

Finally, I wish to express my gratitude to IBM, Kodak, and the National Science Foundation for fellowships and financial support. Also, Caltech for the Herbert Newby McCoy award.

TABLE OF CONTENTS

LIST OF ILLUSTRATIONS

CHAPTER I. PAGE

CHAPTER IV.

CHAPTER V.

PROPOSAL I.

PROPOSAL II.

LIST OF TABLES

THESIS ABSTRACT

Electronic energy transfer and optical dephasing of ordered and disordered molecular crystals is studied theoretically and experimentally. Data on impurity band transport are presented which are consistent with the Anderson transition. The effect of dimensionality on trap-trap energy transfer thresholds is experimentally measured and modeled.

Experiments focus on 1,4-dibromonaphthalene whose lowest triplet exciton is quasi-one-dimensional. Steady state and transient line narrowing laser spectroscopy provide the first unequivocal measurement of the inelastic scattering rate amongst the band states. The inelastic scattering rate (intraband exchange rate) is slow and of the order of 10 μsec at 20 K. Further, the elastic scattering rate is ~10 psec at 20 K and is describable as Raman scattering by ~ a 42 cm^{-1} phonon. It is significant that there is a six order of magnitude separation of time scales for the elastic and inelastic scattering, demonstrating that pure dephasing dominates the intraband exchange. From the broadening and the lack of a relative shift of the two sublattice $\underset{\sim}{k}\sim 0$ absorptions, it is concluded that the interband exchange rate is negligible compared to the pure dephasing. It is found that disordering H_6 DBN with up to 16% D_6 DBN, the inelastic scattering rate is unaltered, being 10 μsec at 20 K! Pumping the $\underset{\sim}{k}\sim 0$ state of the upper sublattice, relaxation is exclusively to the $\underset{\sim}{k}\sim 0$ state of the lower sublattice, implicating single phonon resonant relaxation.

For heavily trap-disordered DBN (up to 24% H_6/D_6) it is found that

(1) excitation migration is step-wise incoherent, (2) energy transfer to deep traps is best fit with a $t^{-1/2}$ energy transfer rate, (3) there are no mobility edges in the trap inhomogeneous profile and (4) an upper limit for the trap homogeneous linewidth at 1.3 K is 9 Ghz.

Using lifetimes and temperature-dependent lineshapes, optical dephasing of F and F_2^{2+} center triplet states in CaO is is consistent with Raman scattering by effective oscillators of 89 and 151 cm^{-1}, respectively.

Vibrational dephasing of the CO stretch for benzophenone matrix-isolated in 4,4'-dibromodiphenyl ether at 2.1 K was investigated with a novel application of <u>emission</u> spectroscopy. It was found that the total dephasing rate of the CO stretch was linear in the CO quantum number, consistent with recent theoretical predictions for carbonyl moieties.

CHAPTER I.

CONCENTRATION DEPENDENT TRANSPORT THRESHOLDS IN ISOTOPICALLY DISORDERED PHENAZINE AND 1,4-DIBROMONAPHTHALENE: THE ANDERSON TRANSITION AND DIMENSIONALITY*

---

*D. D. Smith, D. P. Millar and A. H. Zewail, J. Chem. Phys. 72 (1980) 1187.

ABSTRACT

Presented are measurements on the localization of triplet Frenkel excitons in isotopically doped phenazine and 1,4 dibromonaphthalene (2-D and 1-D effective transfer topology, respectively). Dependence of the steady state impurity aggregate (monomer, dimer, etc.) emission intensity on dopant concentration, temperature and dimensionality is experimentally measured and theoretically modeled. Effects of phonons and excited state lifetimes are explicitly included in a numerical simulation of the data by average lattice rate equations. The rate equations explain the major features of the data quite well. For use in the rate equations, Monte Carlo calculations have been performed to determine impurity cluster spatial and probability distributions in 1-D and 2-D anisotropic lattices. A discussion of the relevance of the results towards the Anderson Transition and percolation theory ensues.

I. INTRODUCTION

In the past few decades, interest in molecular solids has largely been confined to identifying the energetic structure of Frenkel exciton (singlet and triplet state) bands [1]. More recently, dynamics of exciton transport in pure crystals (i.e., there is no impurity introduced but intrinsic impurities and defects are present) were studied to elucidate the effect of strong and weak exciton-phonon couplings on the mode of transport--coherent or incoherent [2]. Disorder of the crystals alters the energetic structure

as well as the dynamics. The former has been treated by several groups for isotopically mixed crystals in the heavy-doping limit and the latter has just begun to be of interest to theorists and experimentalists.

In recent work, Kopelman et al. [3], Colson et al. [4a], and Smith et al. [5] have shown experimentally that disordered naphthalene, benzene and phenazine exhibit a ''critical'' dopant concentration for energy transfer amongst the impurities. Kopelman et al.'s system consisted of naphthalene-H_8, (host), naphthalene-H_8 (trap), and beta-methylnaphthalene which acted as a low-energy trap (called a supertrap, s, in their publication). Exciting with a filtered xenon lamp at about 1.8 K, they observed an abrupt change in the phosphorescence intensity ratio $I_s/(I_s + I_a)$, as a function of the trap concentration, I_a being the naphthalene-H_8 energy acceptor. These studies have led Kopelman and his co-workers to conclude that percolation theory can be used to explain the results. They have made use of dynamic, static, and site percolation concepts and have used percolation to obtain exciton coherence lengths.

Colson and his group [4a] have studied benzene isotopic mixed crystals both in the singlet and triplet states. Their low-energy trap was a chemically distinct specie, pyrazine. Energy transfer thresholds were found at 2.8% for the triplet state and about 40% for the singlet state. The thresholds were discussed in terms of percolation, pointing out that the excitation lifetime is a key factor in determining the difference in trap concentration for

singlet and triplet percolation thresholds. The shorter singlet lifetime limits the energy transfer range despite the longer range coupling compared to the short range exchange coupling in the triplet state.

Smith et al. [5], using isotopically doped phenazine have taken a different approach. The two component system of phenazine-H_8 in phenazine-D_8 at any concentration has H_8 monomers and dimers isolated by D_8 host. For concentrations less than 5%, the number of trimers is negligible and the dimer alone serves as a trap for monomer excitation. The ratio of dimer to monomer phosphorescence intensity as a function of H_8 concentration showed a threshold at ~5% only at low temperatures (1.13 - 1.4 K). This was interpreted as a transport threshold in the context of Klafter-Jortner model [6] which applies the well-known theory of P. W. Anderson [7] to energy transfer in organic crystals. We did not test the applicability of classical percolation theory in our original paper (henceforth referred to as I) because of our belief, as that of Klafter and Jortner, that quantum mechanical tunneling prevails in these systems. As pointed out by Mott, [8] percolation may not be profitably applied to electron transport in microscopically homogeneous crystals.

In this chapter quantitative steady-state studies on phenazine and 1,4-dibromonaphthalene (DBN) are presented. In the following chapter time-resolved experiments on ordered and disordered DBN are presented and discussed. The effects of concentration, temperature, and dimensionality are theoretically modeled and experimentally tested. We perform a numerical simulation of the

experimental data using average rate equations and from the expressions derived herein present physical interpretations of the data. We discuss the relevance of the results to Anderson and percolation models. This paper addresses itself to the very specific problem of energy localization in these organic crystals and it should be recognized that statements in the text may only apply to such crystals.

II. EXPERIMENTAL

A simplified schematic of the optical and magnetic resonance spectrometer used in these experiments is shown in Fig. 1. The spectrometer was used for optically detected magnetic resonance (ODMR), phosphorescence microwave double resonance (PMDR), microwave-optical hole burning, optical emission, and optical absorption experiments. In what follows we divide the experimental procedure and apparatus into four categories--samples, cryogenics, optical detection and data processing, and microwave electronics.

A. Samples

Raw perprotophenazine, (9,10-diazaanthracene, $C_{12}H_8N_2$) was obtained from the Aldrich Chemical Company and purified by extensive zone refining under oxygen-free conditions. Perdeuterophenazine ($C_{12}D_8N_2$) was obtained from Merck, Sharp and Dohme of Canada, Ltd. and subsequently zone refined. Mass spectroscopic analysis showed the deuterophenazine to be better than 98% isotopically pure. Mixed single crystals of proto in

Figure 1. Block diagram of the low temperature optical and magnetic resonance spectrometer used in the experiments.

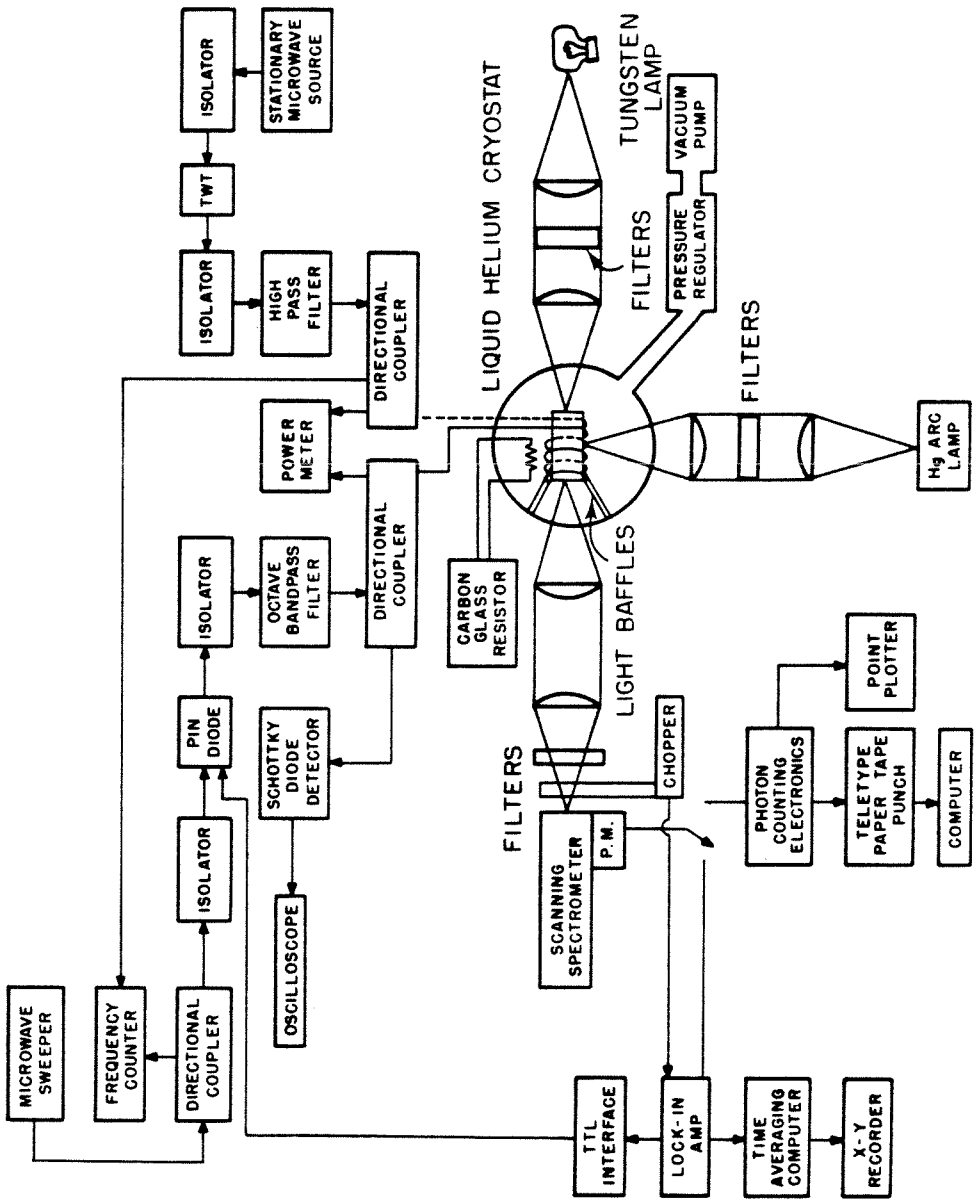
MICROWAVE SWEEPER
FREQUENCY COUNTER
DIRECTIONAL COUPLER
ISOLATOR
PIN DIODE
ISOLATOR
OCTAVE BANDPASS FILTER
DIRECTIONAL COUPLER
SCHOTTKY DIODE DETECTOR
OSCILLOSCOPE
POWER METER
DIRECTIONAL COUPLER
ISOLATOR
HIGH PASS FILTER
TWT
ISOLATOR
STATIONARY MICROWAVE SOURCE
CARBON GLASS RESISTOR
LIQUID HELIUM CRYOSTAT
LIGHT BAFFLES
FILTERS
TUNGSTEN LAMP
FILTERS
VACUUM PUMP
PRESSURE REGULATOR
FILTERS
Hg ARC LAMP
CHOPPER
SCANNING SPECTROMETER
P.M.
TTL INTERFACE
LOCK-IN AMP
TIME AVERAGING COMPUTER
X-Y RECORDER
PHOTON COUNTING ELECTRONICS
POINT PLOTTER
TELETYPE PAPER TAPE PUNCH
COMPUTER

deuterophenazine were grown in small and large temperature gradient Bridgman furnaces (1/2 K/15 cm and 5 K/cm, respectively) under oxygen free conditions. After growth the mixed crystals were analyzed on a mass spectrometer, yielding the mole fractions of deuterated, partially deuterated, and protonated phenazine present in each sample. For reproducibility, several mass spectra of each crystal were run and the statistically averaged results are presented in Table I. Care was taken to use a low ionizing voltage (~10 eV) and low source pressure ($\sim 2 \times 10^{-7}$ Torr) yielding a typical ion current of 6×10^{-8} Amp to minimize isotopic exchange and fragmentation effects (in particular, those dissociations yielding parent ions minus one hydrogen or deuterium). Even with these low ionization voltages we have found some differences in the analysis.

Raw perproto 1,4-dibromonaphthalene (DBN), $C_{10}H_6Br_2$, was obtained from Eastman Chemical Company, raw perdeuterated 1,4-dibromonaphthalene, $C_{10}D_6Br_2$, from Merck, Sharp, and Dohme of Canada, Ltd. Proto and deutero DBN were purified by extensive zone melting. Isotopically mixed crystals were grown, again by standard Bridgman techniques. The isotopic composition of the mixed crystals, as determined by the mass spectrometric analysis of Merck, Sharp, and Dohme, is shown in Table II. Throughout the paper, we will refer to the crystals by the percentage of the perproto specie present.

The samples were cooled slowly from room temperature to 77 K in a helium atmosphere over ~ 6 h. No fracturing of crystals was visible at that point. The crystals were then cooled to 4.2 K by the transfer of liquid helium into the cryostat, still no fracturing observable.

TABLE I. Mole percentage isotopic composition of mixed phenazine crystals

CRYSTAL	$C_{12}H_8N_2$	D_6	D_7	$C_{12}D_8N_2$
1*	0.6 ± 0.1	2.0 ± 0.2	17.3 ± 0.2	80.0 ± 0.2
2	2.0 ± 0.1	4.0 ± 0.3	17.1 ± 0.7	76.9 ± 1.0
3	3.0 ± 0.2	3.5 ± 0.2	16.7 ± 0.4	76.8 ± 0.4
4	4.44 ± 0.02	3.4 ± 0.2	17.2 ± 0.1	76.0 ± 2.0
5	5.65 ± 0.06	1.8 ± 0.1	16.7 ± 0.2	76.0 ± 0.2

*Only one mass spectrum was available, so statistically averaged results are not possible. Errors estimated (very generously) from peak heights.

TABLE II. Mole percentage isotopic composition of mixed DBN crystals

CRYSTAL	$C_{10}H_6Br_2$	D_4H_2	D_5H_1	$C_{10}D_6Br_2$
1	$\leq$ 0.3	0.6 ± 0.2	10.2	88.9
2	2.9	0.3 ± 0.3	10.5	86.3
3	4.8	0.3 ± 0.3	9.7	85.2
4	8.2	0.2 ± 0.2	8.7	82.9
5	11.9	0.2 ± 0.3	8.6	79.3
6	14.5	1.1 ± 0.5	11.5	72.9
7	21.8	< 1	7.7	70.5
8	24.1	< 1	7.1	68.5

Care was taken so as not to allow the crystals to warm up between subsequent liquid helium transfers, as rapid thermal cycling over large temperature ranges may affect the strain broadening of the crystals, which in turn might affect the transport dynamics under study. In addition, while making temperature dependent measurements, care was taken to allow the crystals a minimum of 7 minutes to come to thermal equilibration with the helium bath (while irradiating with the light source). We have observed, while doing temperature-dependent measurements on phenazine-H_8 in superfluid helium, that equilibration times much less than 5 minutes give irreproducible emission intensities for temperature changes of ~0.8 K. Equilibration times should in principle be longer for the low temperature measurements as the Kapitza contact resistance [9] goes roughly as T^{-3} (and increases with the number of asperities on the sample surface). We did not make detailed measurements of equilibration times, yet we wish to bring attention to this potential source of error. Further, for temperatures close to but below the lambda point, we have observed local boiling of the superfluid on the surface of the light baffles, which implies sample heating may also occur (keep in mind that for T greater than 1 K, He II will not support temperature gradients).

Our measurements were tested for equilibration by finishing the temperature run (say, ending at high temperature) then redoing the initial measurement (low temperature) using a temperature sensor near the crystal. When equilibration was complete, excellent agreement was found. For the magnetic resonance

experiments and most optical experiments the samples were mounted in as strain-free a manner as was possible by placing the crystals within a helix and supporting the crystals from beneath with tape. (The weight of the crystal on itself and the hydrostatic pressure of the helium bath which changes during the experiment may contribute to the crystal strain.) For the experiment in which the trap depth and temperature dependent emission intensity were measured, the samples were gently taped into a sample compartment (which was attached to light baffles) using black photographic tape. In these experiments all crystals were mounted on the same holder which has large open windows to insure helium circulation around the crystals.

B. Cryogenics

The sample holder was immersed in a 10 liter Janis immersion dewar. The temperature of the helium bath was regulated to $\pm$ 5 mK between 4.2 and 1.12 K. For temperatures above 1.6 K, regulation was achieved with a Lakeshore Cryotronics model 329 vacuum regulator. For all but one experiment, helium reservoir temperatures were measured with a calibrated carbon glass resistor to $\pm$ 5 mK. The immersion thermometer was placed as close as was practical to the samples ($\leq$30 mm). For one experiment (the temperature dependence of the emission intensity for the 2% H_8/D_8 phenazine) the crystal temperature was measured by vapor pressure thermometry, which reproduced the earlier results for the dimer to monomer ratio measured by the carbon glass resistor to within 4%.

C. Optical detection and data processing

Light from the samples was dispersed with a 0.5 m Ebert mount scanning spectrometer with a 2400 groove/mm grating and detected with an EMI 9659QB photomultiplier tube enclosed in a cooled housing. For the optical absorption and emission experiments the slits were held constant at 20 μ x 10 mm yielding a spectral resolution of approximately 0.32 Å at 6470 Å. To reduce the scattered light within the spectrometer, sharp-cut filters passing only long wavelengths were placed directly in front of the entrance slit. All emission and absorption spectra are unpolarized and uncorrected for instrument response. Appropriate solution filters were used to absorb unwanted visible and IR radiation from the 1 kW tungsten lamp or an Oriel 200 W Hg arc lamp.

Phenazine optical spectra were obtained by chopping the luminescence. The chopped luminescence was phase sensitively detected at 100 or 975 Hz and the signal fed to a Varian C-1024 time averaging computer. The spectrum was averaged, if necessary, and plotted on a X-Y or strip chart recorder. The phenazine spectrum was calibrated by placing an Fe-Ne hollow cathode lamp (20 mA current) directly in front of the spectrometer entrance slit. Without interrupting the scan, the calibration lamp was then removed from optical path and the absorption or emission line was recorded. The scan still uninterrupted, the calibration lamp was reinserted in the optical path and the second calibration line was recorded.

Absorption and emission experiments used to determine the trap depth were done on the same crystal at the same temperature without

moving the sample in order to insure against artifacts.

DBN emission spectra were obtained with a Nuclear Data series 2200 photon counting system. A hard copy of the digitized spectrum was recorded on HP 7590C point plotter. Using a nonlinear regression computer program, the emission spectra were fit as the sum of Gaussian line shapes. The phenazine emission spectra were digitized by hand and the line shapes were fit in a manner similar to that above. Details of the line shape analysis and results are in Sec. III.

D. Microwave electronics

Samples for the low temperature magnetic resonance experiments were held with a German silver helix wound to dimensions slightly smaller than the lowest order transverse mode. The helix was connected only to the silver plated center conductor of a chrome-plated semirigid coaxial cable, the last two windings being shorted. For the microwave-optical hole burning experiment, concentric helices separated by a 1 mm thick wall quartz cylinder were used. We did not control the inductive coupling of the helices. In fact, it is not clear that one could control the mutual coupling if one wanted to. The best approach would be to use horn antennas external to the dewar for the two different frequencies. However, one then needs to use a glass dewar since diffraction and pseudo-cavity effects at the metal dewar windows and sample chambers are expected to be severe, especially at the frequencies used (500 Mhz - 5 Ghz). The microwaves were square-wave amplitude-modulated to a depth of $\geq$ 40 dB with Narda 411DJ201 PIN diodes. The square wave for the

modulation was derived from the sine wave reference of the lock-in amplifier via a homemade comparator circuit used as a Schmitt trigger. The frequency swept, leveled (± 1 dB) microwaves were supplied by an HP 8620C oscillator which was amplified by a Hughes model 1277H (specially selected) 60 Watt traveling wave tube amplifier, appropriately filtered and isolated. Isolators were used on both sides of the PIN diode to protect the sweeper's YIG oscillator and prevent unwanted reflections. The modulated output of the diodes was passed through an octave bandpass filter. Microwave power incident on the helix was measured by use of a HP 430B power meter connected to a directional coupler situated directly on top of the experimental dewar.

III. RESULTS

A. Phenazine and DBN crystalline structure and intermolecular interactions

Phenazine crystals grown from the melt are of the monoclinic α form [10] with space group $P2_1/a$, two molecules per unit cell. At room temperature, the unit cell has the dimensions $|a| = 13.22 \pm 0.01$, $|b| = 5.061 \pm 0.005$, $|c| = 7.088 \pm 0.007$ Å, $\beta = 109°13' \pm 15'$. The most salient feature of the crystal structure is chains of plane parallel packed phenazine molecules at 45° with respect to the short axis, $\underset{\sim}{b}$. Neighboring chains in the $\underset{\sim}{ab}$ plane have their long molecular axes perpendicular to one another (shown clearly in Fig. 2). As we shall discuss later, intermolecular interactions are highly anisotropic for the $^3\pi\pi^*$ band, with $\underset{\sim}{b}$ axis coupling dominating at 6.5 cm^{-1},

Figure 2. Projection of the contents of the phenazine unit cell onto a plane perpendicular to the $\underset{\sim}{c}$ axis [10].

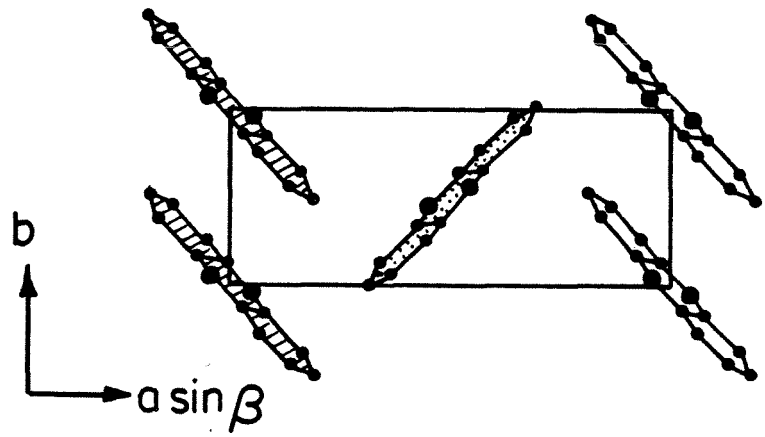
b
a sin β

[11] ab plane interchange equivalent-pair interaction energy of 0.5 cm^{-1}, [12] and coupling along the c axis being immeasurably small by conventional optical techniques. (The 6 cm^{-1} value was obtained after correcting for guest-host interactions.) Thus, one obtains essentially a two-dimensional topology in the ab plane that resembles that of naphthalene.

DBN crystallizes [13] in a $P2_1/a$ (C_{2h}^5) space group, 8 molecules per unit cell. Crystallographic axes a = 27.45 ± 0.08, b = 16.12 ± 0.04, c = 4.09 ± 0.01 Å, β = 91°51′ ± 10′.

The spectra of DBN neat [14] and isotopically mixed [15] exhibit the characteristics of a linear chain with nearest-neighbor interaction of -6.2 cm^{-1} [15].

B. Vibronic emission spectrum of isotopically mixed phenazine

The unpolarized vibronic emission spectrum of the isotopically mixed single crystal 2% proto in deutero phenazine is shown in Fig. 3. The relative intensities, wavelengths, reciprocal wavelengths (corrected to vacuum) and energy splittings in cm^{-1} are recorded in Table III. The sample was optically excited by a 200 W mercury arc lamp filtered to a passband from 3050 to 4700 Å. Spectral resolution of approximately 20,000 was used.

We record the (0,0) origin of the proto monomer to be at 15,453 ± 3 cm^{-1}, whereas the neat phenazine crystal absorption has Davydov components at 15,448 and 15,452 cm^{-1} [12]. With trap states as shallow

Figure 3. Vibronic emission spectrum of 2% H_8 in D_8 phenazine at 1.6 K. From 6820 to 7200 Å. The sensitivity has been increased by a factor of 10. The inset shows the side-band spectra at higher sensitivity to reveal the structure. Correction for phototube response would enhance the low energy lines relative to the vibrational origin. The scan is only of moderate sensitivity, making it difficult to see the 4.4 cm^{-1} splitting that occurs on a large number of the vibrational lines (however, see Table III and Fig. 4).

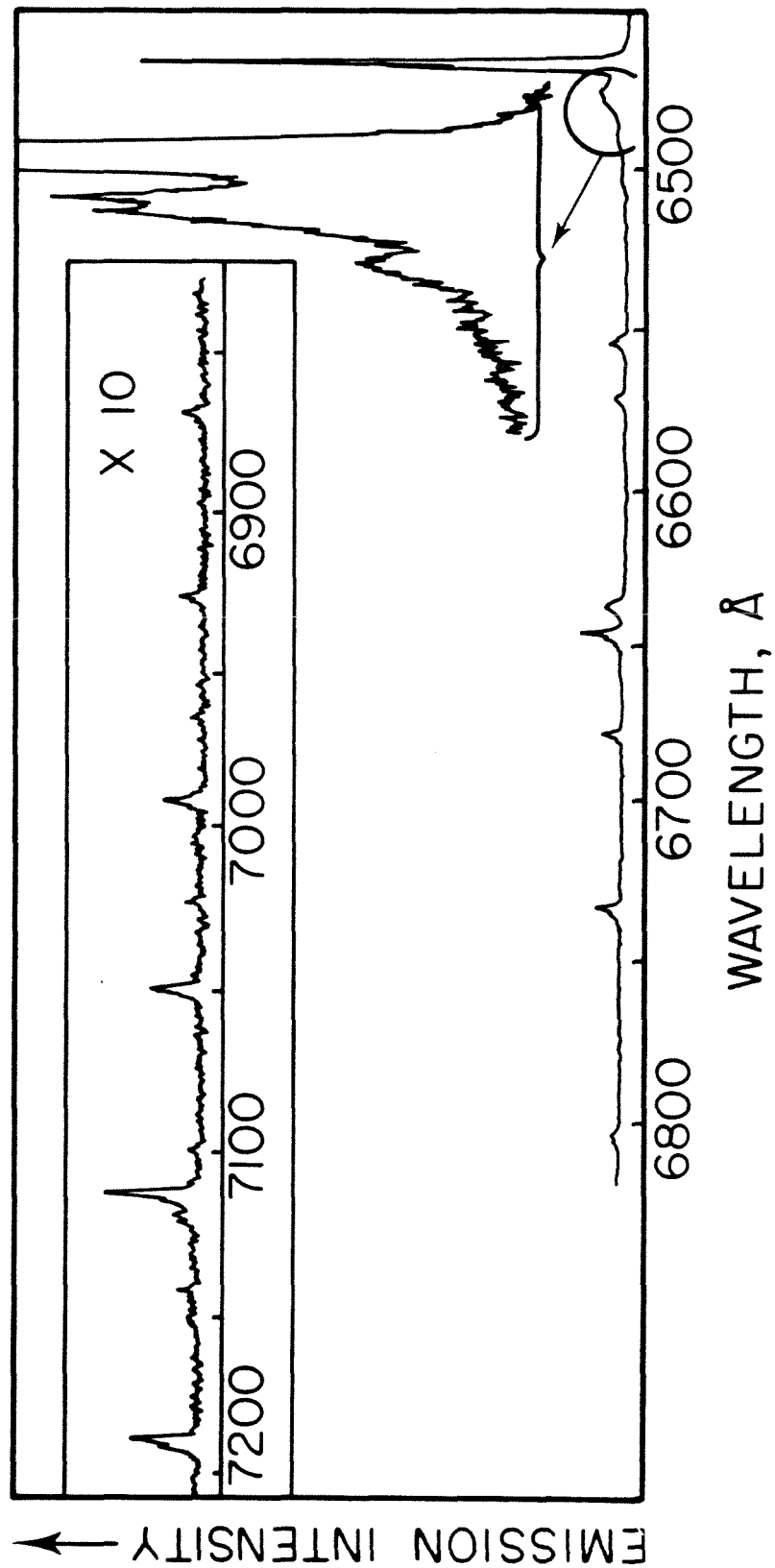
EMISSION INTENSITY
WAVELENGTH, Å
6500
6600
6700
6800
X 10
6900
7000
7100
7200

TABLE III. Analysis for the phosphorescence ($^3B_{2u} \rightarrow {}^1A_{1g}$) of 2% proto in deutero phenazine at 1.6°K

WAVELENGTH* (Å)	E/hc (cm^{-1}) (vacuum) ± 3 cm^{-1}	Relative† Intensities	$\delta\tilde{\nu}(cm^{-1})$	Possible assignment and activity††
6468.58	15455.1	vs	M_{00}	monomer origin
6470.24	15451.1	vs	D_{00}	dimer origin
6477.61	15433.5	s	M_{00}-21.6	NA,NR } (16)
6480.27	15427.2	s	M_{00}-27.9	NA,NR } (16)
6491.09	15401.5	w	M_{00}-53.6	NA,NR } (16)
6554.51	15252.5	w	M_{00}-202.6	0,NA
6556.50	15247.8	m	D_{00}-203.3	0,NA
6573.98	15207.3	w	M_{00}-247.8	0,NA
6638.56	15059.3	w	M_{00}-395.8	NR,NA
6645.72	15043.1	s	M_{00}-412.0	417 (R)
6647.55	15039.0	m	D_{00}-412.1	417 (R)
6681.67	14962.2	m	M_{00}-492.9	474 (IR)
6683.5	14958.1	w	D_{00}-493.0	474 (IR)
6734.77	14844.2	s	M_{00}-610.9	612 (R)
6736.43	14840.6	w	D_{00}-610.5	612 (R)
6805.01	14691.0	w	M_{00}-764.1	751 (IR)
6807.34	14686.0	w	D_{00}-765.1	751 (IR)
6871.09	14549.7	vw	M_{00}-905.4	902 (IR)
6927.85	14430.5	vw	M_{00}-1024.6	1011 (R)
6991.44	14299.3	w	M_{00}-1155.8	1156 R(IR)
6993.60	14294.8	vw	D_{00}-1156.3	1156 R(IR)
7050.86	14178.8	w	M_{00}-1276.3	1279 (R)
7114.28	14052.4	w	M_{00}-1402.7	1404 (R)
7116.27	14048.4	w	D_{00}-1402.7	1404 (R)
7120.77	14039.6	vw	M_{00}-1415.5	NR,NA
7122.93	14035.3	vw	D_{00}-1415.8	NR,NA
7143.74	13994.4	vw	M_{00}-1460.7	1475 (R)
7190.51	13903.4	w	M_{00}-1551.7	1554 (R)
7192.84	13898.7	w	M_{00}-1552.4	1554 (R)

TABLE III (continued)

*The numbers quoted in this table are no more accurate than ± 3 cm^{-1} and therefore the decimals do not reflect high accuracy (see also Table IV).

† >10 very strong, 7-10 strong, 4-7 medium, 1-4 weak, < 1 very weak.

†† See references 17 and 18. NA = not assigned, NR = not reported, 0 = observed.

as in the isotopically mixed phenazine crystal, significant host-band mixing will be present and, as a consequence, the energies of trap and host states are influenced and the dimer and monomer may borrow different amounts of oscillator strength from the host band.

When the signal-to-noise ratio permitted, an average splitting of 4.2 cm^{-1} (standard deviation 0.3 cm^{-1}) was observed in most emission lines. The structure at 21, 27, and 54 cm^{-1} to lower energy from the (0,0) origin has not been positively assigned [16].

The vibronic line intensities decrease as one goes to lower energy, yielding a Franck-Condon envelope in rough agreement with other work [17]. The observed average monomer-dimer splitting of 4.2 cm^{-1} for all lines agrees well with the splitting of 4.4 $cm^{-1} \pm 0.5$ cm^{-1} from the work of Zewail [11,19] and the high resolution computer fit data described later in this work. In the emission spectrum to the vibrational levels of the ground electronic state, one would expect to see the 4.2 cm^{-1} splitting on all lines only if the ground state vibrational splittings were small and the line broadenings were negligible. If the vibrational splittings were considerable compared to the excited state splittings, the 4.2 cm^{-1} splitting might be altered and for the case of dimer emission, new selection rules for optical emission would likely be involved. One can conclude then, for most vibronic lines of the phenazine emission that ground state splitting is relatively small.

The ratio of the dimer to monomer emission intensity (D/M), within experimental error, appears to be the same for all relevant vibronic lines [20]. For example, for the (0,412) transition, the D/M intensity ratio is 0.45 ± 0.03 compared to 0.50 ± 0.02 for the (0,0) orgin, with splittings of 4.0 and 4.1 cm^{-1} (within our resolution), respectively. The (0,412) transition and (0,0) transition at 1.6 K are shown in Fig. 4. At this temperature and from the impurity emission spectrum of the 2% crystal, we also obtain an optical Debye-Waller factor [21] of 0.2 to 0.25, as measured by use of a polar planimeter averaged for several different spectra. An insert, showing the detailed structure of the phonon sideband is depicted in Fig. 3.

Spectroscopic trap depths were measured for the 0.5% and 6.6% H_8 in D_8 phenazine crystals at 1.36 K. Measurement of absorption spectra for the two crystals yielded the Davydov splitting of the host band. Measurement of the emission spectrum of the 0.5% and 6.6% crystals yielded the trap depths of the monomer and dimer, respectively. The measurements indicate; (1) a trap depth in the 0.5% crystal of 23 ± 2 cm^{-1} from the middle of the host deutero $\underset{\sim}{k} = 0$ bands to the ''isolated'' proto impurity; (2) a possible weak dependence of the trap depth on dopant concentration, since there is a 1.6 cm^{-1} red shift between the dimer in the 6.6% crystal from where one might expect it from the 0.5% measurements. However, this shift is due in part to the emission of trimer aggregates building a shoulder upon the true dimer emission, and is within our experimental error; and (3) a Davydov splitting of 4 cm^{-1} for the deutero host which contains

Figure 4. Monomer and dimer emission lines for the 412 cm^{-1} molecular vibrational mode and the vibrational origin of the 2% phenazine crystal at 1.6 K. Relative intensities of the vibrational lines may be seen in Fig. 3. The gently sloping baseline that increases to lower energy is present in 412 cm^{-1} vibronic line and the (0,0) origin.

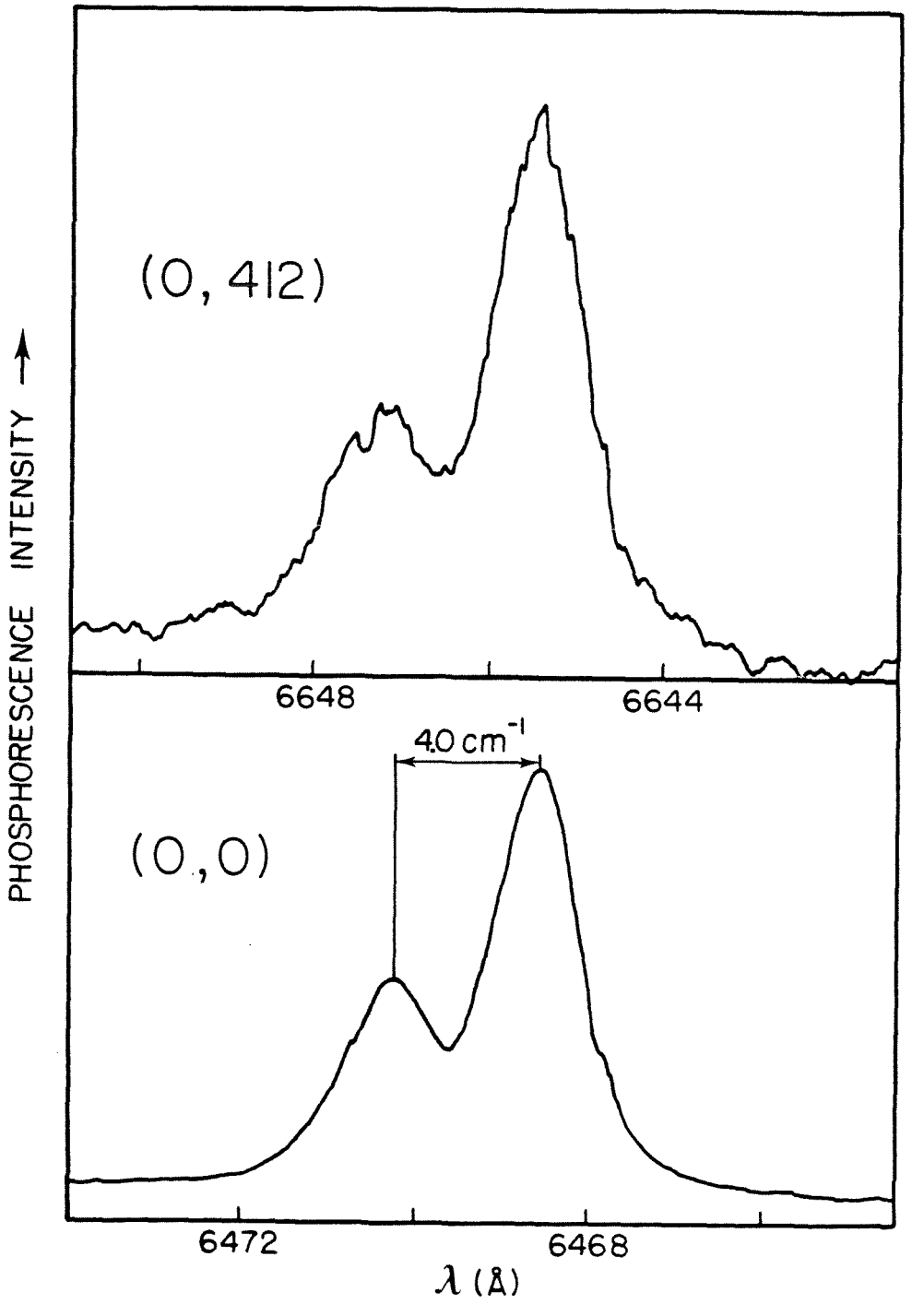
(0, 412)
6648
6644
4.0 cm⁻¹
(0,0)
6472
6468
λ (Å)
PHOSPHORESCENCE INTENSITY

impurity band states in good agreement with earlier work [12]. These results, together with other measurements, are compiled in Table IV. The calibrated absorption and emission spectra for the 6.6% crystal are shown in Fig. 5 with an insert to show the Davydov doublet more clearly.

For DBN, the optical spectroscopic properties have been well characterized [14,15] and when applicable our measurements agree well with previous work dealing with monomer–dimer–trimer splittings.

C. Effect of guest concentration on emission spectra

The observation of abrupt changes in intercluster energy transfer rates for phenazine and DBN was accomplished by comparing the populations of different impurity clusters (monomers and dimers) as a function of dopant concentration and sample temperature. In this section we present the experimentally measured trap emission intensities (energy resolved) as a function of impurity concentration.

Figure 6 shows the dimer to monomer emission intensity ratio as a function of concentration for phenazine, presenting new data in addition to those shown in earlier work by us [5]. The dimer and monomer emission intensities in Fig. 6 are the integrated peak areas as fit by a computer generated line shape function (see Fig. 7). Due to splittings that are small in comparison to the broadening, it is reasonable to fit the emission line shape only to monomer, dimer, and to some extent, trimer. Emission from translationally inequivalent dimers, translationally equivalent monomers separated by one host

TABLE IV. Emission (E) and absorption (A) spectra of pure and doped phenazine crystals

CRYSTAL % h_8	T(k)	$\lambda(cm^{-1})^{\dagger}$	ASSIGNMENT	INVESTIGATORS
6.6	1.36	15477.8 15474.1	Davydov doublet (A)	This work
		15447.6	dimer & trimer (E)	This work
0.5	1.36	15477.9 15474.3	Davydov doublet (A)	This work
		15453.2	monomer trap (E)	This work
pure D	4.2	15467 15471	Davydov doublet (A)	Clarke and Hochstrasser*
pure H	4.2	15448 15452	Davydov doublet (A)	Clarke and Hochstrasser*

*See reference (12).

†The values we report are <u>in vacuo</u> and are regarded to be accurate to ± 3 cm^{-1}. The values of Clarke and Hochstrasser are possibly in air (private communication) and for the deutero Davydov states differ from our measurements by 4.6 Å. Note that the trap depth of the 6.6% (Fig. 5) can be corrected for the dimer and trimer emission to yield a monomer trap depth of 22 cm^{-1}, which is in excellent agreement with the 0.5% result (23 cm^{-1}).

Figure 5. Superimposed absorption and emission spectra of a 6.6% phenazine at 1.36 K calibrated by standard neon lines at 15364.9 and 15512.3 cm^{-1}. The Davydov doublet is shown at higher resolution in the inset in the figure. The emission in the spectrum is dominated by the dimer and trimer, since at 1.36 K the deeper traps acquire the majority of the population. The 28 cm^{-1} measured from the middle of the Davydov doublet to the peak of the trap emission is not the true trap depth of any cluster. Computer fit of the emission yields 22 cm^{-1} as the energy difference between the middle of the two $\underset{\sim}{k} = 0$ states and the monomer, which is within experimental error of the 0.5% results. Note that the Davydov doublet in the 6.6% crystal is still clearly resolved (indicating the band states are not totally disrupted). The 6.6% crystal was 5 mm thick.

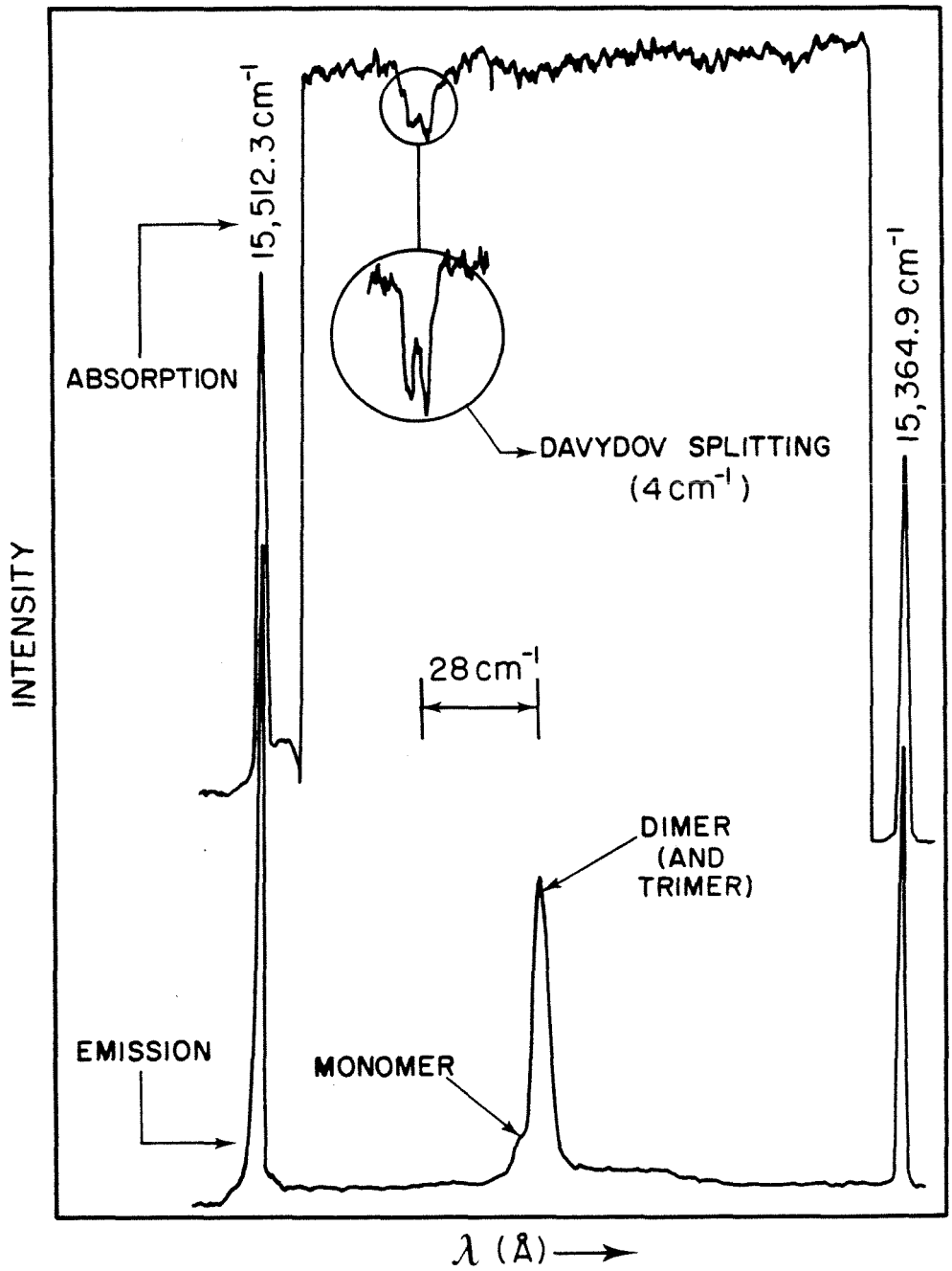
15,512.3 cm⁻¹
ABSORPTION
DAVYDOV SPLITTING
(4 cm⁻¹)
15,364.9 cm⁻¹
28 cm⁻¹
INTENSITY
DIMER
(AND
TRIMER)
EMISSION
MONOMER
λ (Å)

Figure 6. The computer fit (integrated peak area) dimer/monomer phosphorescence intensity ratio as a function of proto trap concentration for 1.92 and 1.34 K. The data for 2.99 K are from peak heights, as the signal/noise was insufficient to permit reliable computer analysis. For the computer fits, the error bars are those determined by the nonlinear regression and represent 80% confidence limits of a 5 degree of freedom double-tailed student ''t'' statistic (see e.g. [61]). The new data agree within error with the data published previously [5]. The crystal concentrations are those of a statistically averaged mass spectral analysis (see Table I). The data for 1.92 and 2.99 K yield very nearly straight lines and were fit by linear least squares to yield $D/M = 0.02 + 0.36C$ ($\sigma = 0.06$) and $D/M = 0.09 + 0.12C$ ($\sigma = 0.07$), respectively.

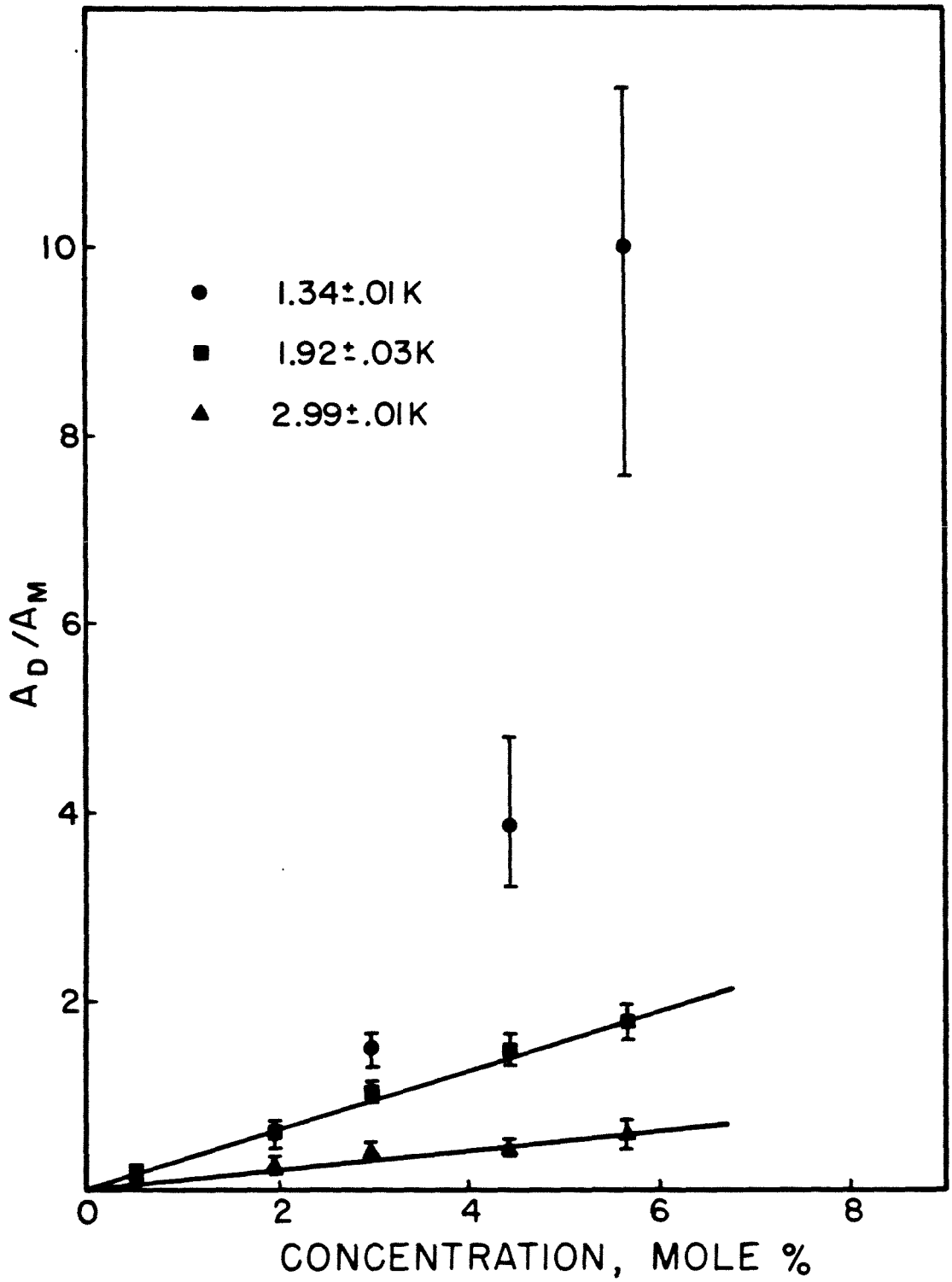
1.34±.01K
1.92±.03K
2.99±.01K
A_D/A_M
10
8
6
4
2
0
2
4
6
8
CONCENTRATION, MOLE %

molecule (double monomer), and other more complex impurity clusters can be compensated for a posteriori, but their precise position and linewidths cannot be extracted with certainty from the measurements herein alone.

The trap emission envelope was fit as the sum of a straight baseline and Gaussian line shapes for the monomer, dimer, and trimer (if present). In principle, each cluster emission envelope should have a phonon sideband of its own. Thus, the monomer sideband will contribute more to the baseline offset of the dimer than the monomer emission. We make the approximation that the sum of the sidebands results in a linear sloping baseline for all trap emission. No noticeable change in slope over the temperature range from 1.3 to 3 K was observed. However, there was a slight increase in baseline slope with increasing dopant concentration.

Using the computer fits, the monomer–dimer splitting was experimentally determined in the 2% H_s in D_s phenazine crystal at 1.33 K to be 4.4 cm^{-1}. The 2% crystal was chosen for the determination of the resonance splitting so that in the computer fit of the data, trimer emission would be negligible and use of two Gaussians whose FWHM, amplitude, and center were parameters would produce a fit which is most nearly correct. Further, the low temperature spectrum was chosen since the S/N ratio increases as the sample temperature decreases (see Sec. D on the effects of temperature). The 4.4 cm^{-1} splitting was then used as a fixed parameter in the remainder of the computer generated fits. The linewidths from the 2% crystal analysis were not useful in fitting other

crystal spectra, likely due to the difference in strain broadening from sample to sample (see Table V) or due to intrinsic correlation effects that are a function of concentration. However, no obvious trend for the linewidths as a function of concentration was found. For the 5.65% crystal the dimer–trimer splitting was a fixed parameter (from knowledge of the monomer–dimer splitting) and trimer amplitude and FWHM were variable. Examples of computer fits are shown in Figs. 7 and 8 for phenazine and DBN, respectively.

In I, we used peak heights for calculating D/M. Here, we used the integrated areas with and without the trimer and find the D/M ratio is still within our error. The small but noticeable broadening and shift of the dimer line to lower energy for the 5.65% crystal as the temperature is reduced is due to trimer population increasing as the temperature is lowered, which is shown clearly in the computer fits of Fig. 7. If one attempts to fit the 1.33 K data for the 5.65% crystal with just two Gaussians (monomer and dimer) one finds splittings inconsistent with the 4.4 cm^{-1} value for the 2% crystal and an unphysically large FWHM for the dimer peak.

Similarly, the computer fit of DBN emission spectra provided us with the dimer–to–monomer ratio as a function of temperature and concentration. The monomer and dimer are well resolved for the DBN case but the carbon 12 monomer is closely flanked by the carbon 13 monomer and the (presumably) double monomer [15] (DHDHD...) such that they form shoulders. Using carbon 13–carbon 12 monomer splitting (1.9 cm^{-1}) from previous high resolution work [15] as a fixed

TABLE V. Computer fit inhomogeneous linewidths of cluster emission in mixed phenazine crystals

Protoisotopic Conc.,mole%	T (K)	FWHM$^{*}_{monomer}$ (cm^{-1})†	FWHM$^{**}_{dimer}$ (cm^{-1})†	FWHM$_{trimer}$ (cm^{-1})†
0.6	1.92	2.6 ± .1	3.6 ± .8	
2.0		3.4 ± .1	3.8 ± .2	
3.0		3.3	3.7	
4.44		3.1 ± .2	3.1 ± .1	
5.65		3.6 ± .3	3.4 ± .1	4.0 ± .8
0.6	1.34	2.8 ± .1	3.5 ± .8	
2.0		4.0 ± .1	4.0 ± .2	
3.0		3.7 ± .3	3.8 ± .2	
4.44		2.7 ± .3	3.1 ± .1	
5.65		3.4 ± .6	3.7 ± .1	3.2 ± .2

*average FWHM$_{monomer}$ = 3.26 cm^{-1}; σ = 0.46 (14% standard error)

**average FWHM$_{dimer}$ = 3.57 cm^{-1}; σ = 0.31 (9% standard error).

†All error bars are from 80% confidence interval of student "t" statistics (63).

Figure 7. Examples of computer optimized line shape fits (smooth lines) of the data (dots) for the vibrational origin of 2% and 5.65% phenazine. Only the relative energies of the fitted peaks are shown as absolute values are listed in Table III. The histogram bars superimposed on the emission spectra are the relative statistical probabilities for each cluster (see section on cluster statistics). The fit for the sloping base line is not shown to avoid confusion in the figure. However, one can see the slope is greater for the 5.65% crystal than the 2% crystal.

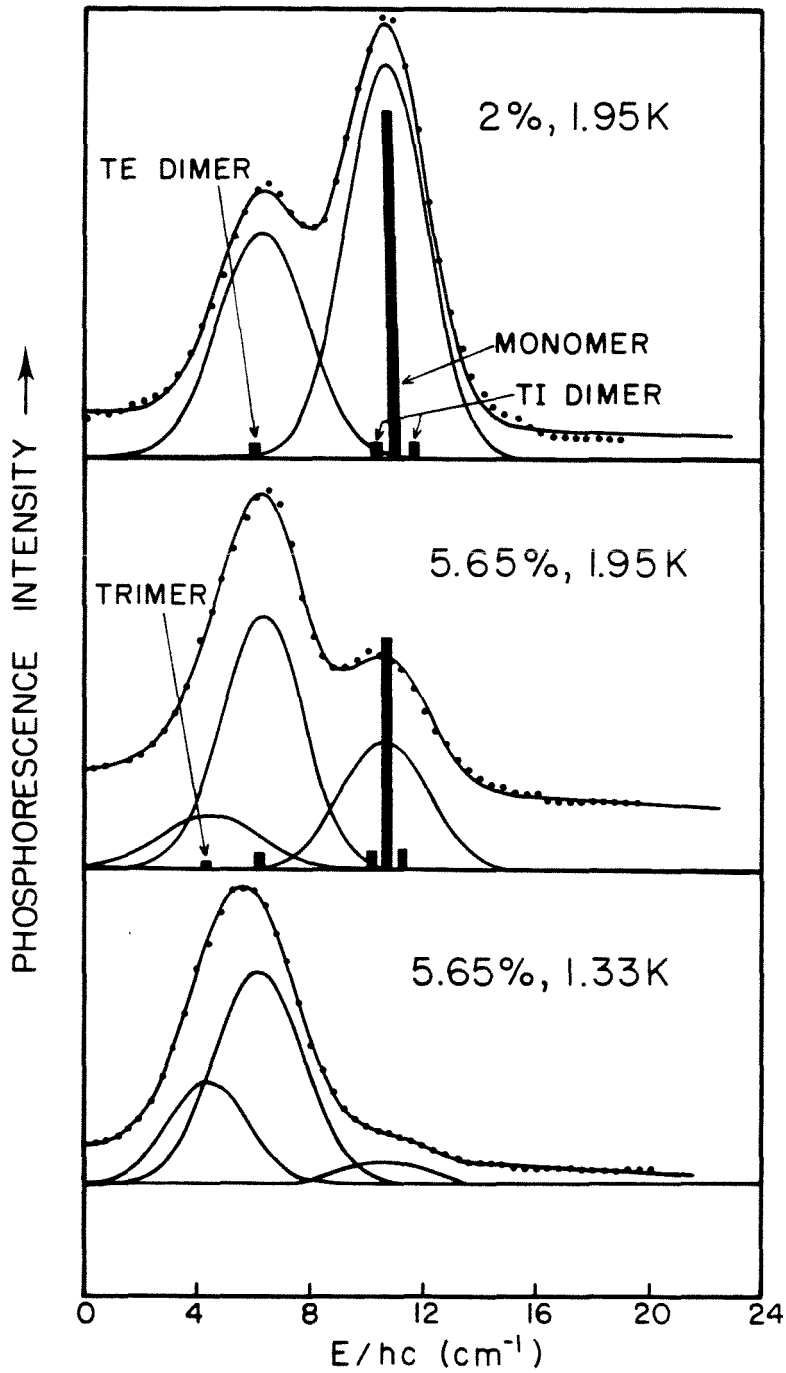
2%, 1.95K
TE DIMER
MONOMER
TI DIMER
5.65%, 1.95K
TRIMER
5.65%, 1.33K
PHOSPHORESCENCE INTENSITY
0
4
8
12
16
20
24
E/hc (cm⁻¹)

Figure 8. Computer fit (smooth line) of data (dots) for 11.9% DBN at 4.19 K. Legend: ^{13}C = carbon 13 monomer, M = monomer, DM = double monomer, D = dimer, Tr = trimer, Tet = tetramer. Histogram bars indicate relative cluster probability from the exact results of Sec. IV A. The monomer–dimer splitting was variable in the computer fit from which the dimer–trimer and trimer–tetramer splittings were fixed. The double dimer was not included in the fit due to the vanishing statistical probability of occurrence. All peaks' FWHM and height were variable in the fits. In all cases, the $^{13}C/^{12}C$ monomer emission intensity ratio was that expected by isotopic abundance, i.e., 11% (within the error bars).

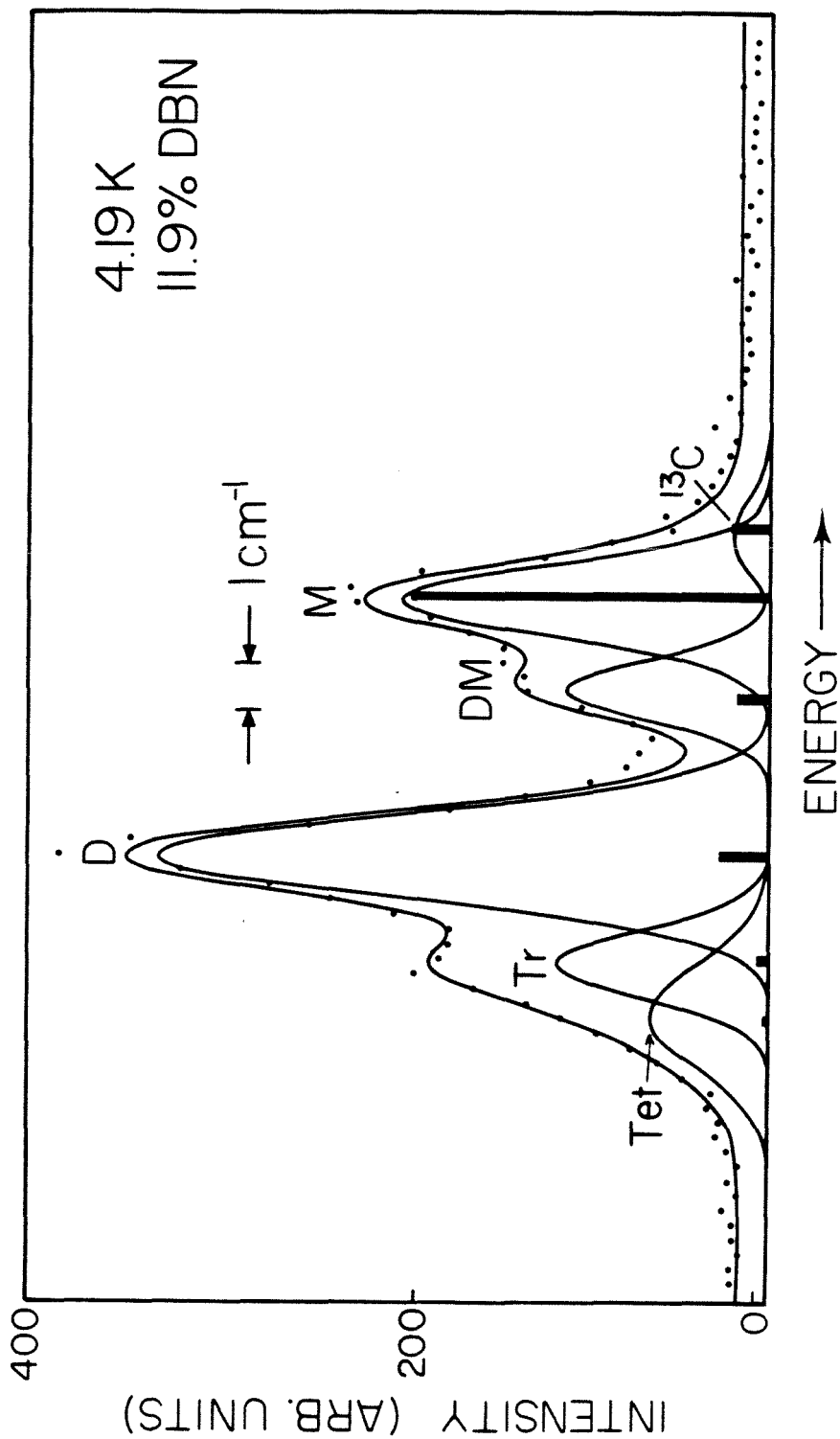
4.19 K
11.9% DBN
1 cm⁻¹
D
M
DM
Tr
Tet
¹³C
400
200
0
INTENSITY (ARB. UNITS)
ENERGY

parameter and letting the dimer–monomer splitting and monomer–double monomer splitting be adjustable parameters produced good fits. Furthermore, knowing the monomer–dimer splitting accurately, we predicted, for a linear chain, the position of the trimer and tetramer; thus trimer and tetramer positions became fixed parameters. In all cases, peak amplitudes and FWHM were adjustable parameters (see Fig. 8). For comparison of the results of DBN, the quasi-one-dimensional system, with that of phenazine, the quasi-two-dimensional system, we depict the concentration dependence of dimer-to-monomer ratio for DBN in Fig. 9. Again, for DBN as in phenazine, one notices the disappearance of the abrupt change in D/M as the temperature increases. However, this ''abrupt'' change in D/M occurs at a critical concentration much different in DBN compared to phenazine, a point that we shall discuss in the coming sections.

The error bars for the DBN data are determined by a nonlinear regression routine and are large for high concentrations due to the overlap of dimer, trimer, tetramer emission. Where only one data point is shown for lightly doped crystals, data for all three temperatures coincide well within the error bars. Thus, only one data point is shown to avoid confusion. Comparison of the spectra for DBN at higher concentration at two temperatures can be found in the insert of Fig. 9.

D. Temperature effects

We have measured the temperature dependence of: (1) the dimer/monomer intensity ratio as a function of dopant

Figure 9. The computer fit areas for the dimer/monomer emission intensity ratio for DBN as a function of temperature and concentration. Observe the ''sluggishness'' of the threshold behavior in this quasi-1-D system as compared with phenazine (Fig. 6). This is due in part to the fact that the superexchange coupling scales exponentially as C^{-1} for 1-D and $C^{-1/2}$ for 2-D (see Sec. VI A). The uncertainty in D/M for the 21.8 and 24.1% crystals results from the congestion of cluster emission lines and reflect approximately 70% confidence limits. However, from the inset for the 24.1% case, it is clear that D/M changes considerably. In low temperature fits, peak positions from the high temperature fit were used to locate the dimer, trimer and tetramer. For low concentrations, when only one point is shown, the D/M ratios for all three temperatures coincide well within the error bar. In the insert, the 24.1%, 4.2 K spectrum shows the ''quasi-Boltzmann'' behavior (see Fig. 11) of the D/M ratio: $2(0.24)\exp(5.5/4.2 \times 0.69)$. For the trimer and tetramer the errors on the intensities from the computer fit are quite large due to the absence of (apparent) splitting. At lower temperature we do not expect this quasithermal behavior to hold. The result of the 14.5% sample of Ref. 15 fits smoothly with our curves.

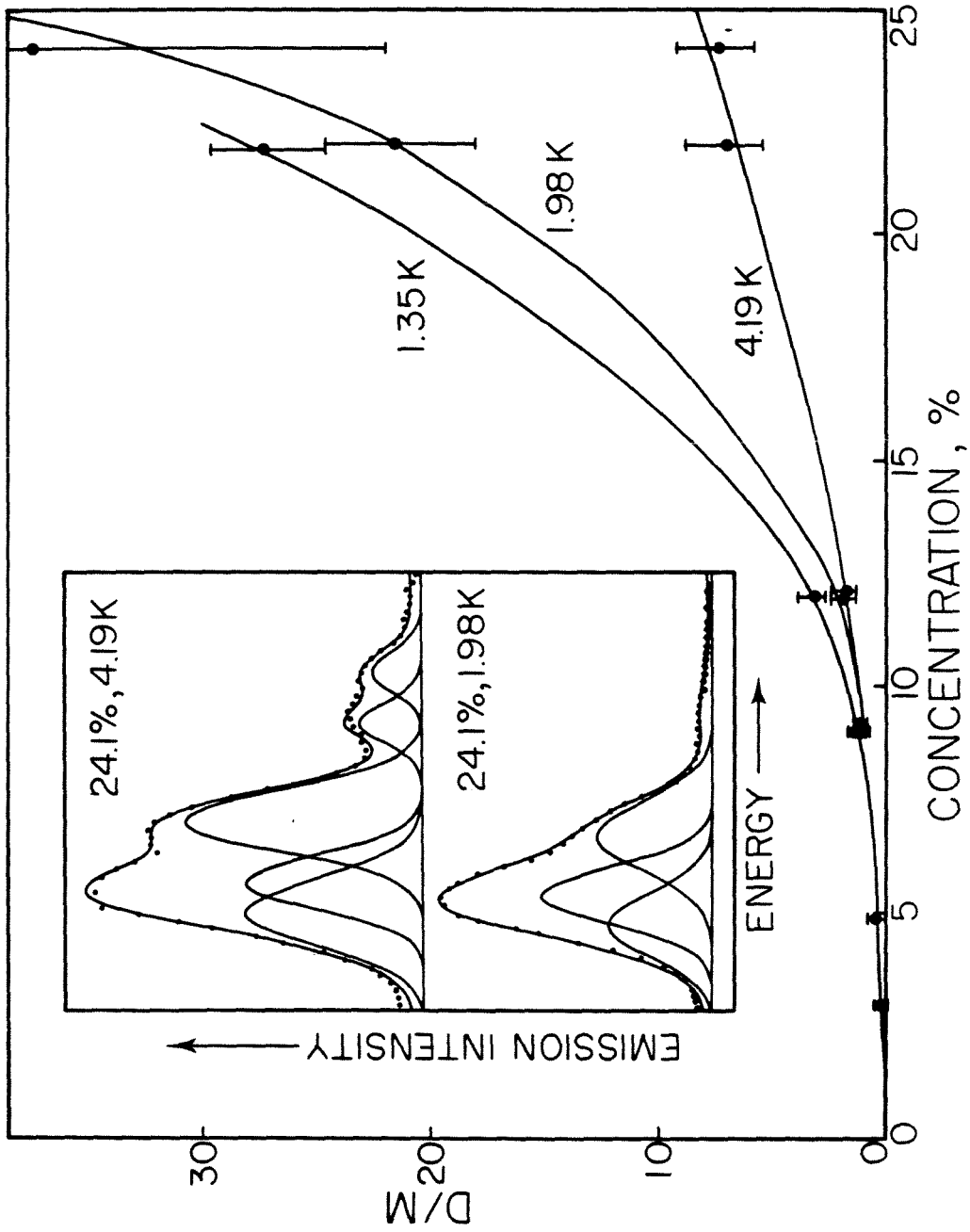
D/M
0
10
20
30
0
5
10
15
20
25
CONCENTRATION, %
1.35K
1.98K
4.19K
EMISSION INTENSITY
ENERGY
24.1%, 4.19K
24.1%, 1.98K

concentration in phenazine, as shown in Fig. 10 (a portion of the data in Fig. 10 is also present in Fig. 6); (2) dimer/monomer intensity ratio for DBN at various dopant concentrations (Fig. 11); and finally (3) the emission intensity of monomer and dimer trap states for phenazine (Figs. 12 to 15). Again in all these experiments, the temperature was carefully regulated and measured near the crystal. When S/N permitted, emission intensities and error bars were obtained from computer-analyzed experimental data. In Fig. 10, the 0.5% crystal has two sets of data points. Curve F was taken using the regrown crystal of curve E. The major difference between the samples is presumably the crystal strain; curve F is likely to be the less strained of the two, due to the method of preparation and number of thermal cyclings it had undergone.

We mention that for the 0.5% phenazine crystal, temperature dependence of the emission intensity was measured in two independent experiments to demonstrate the reproducibility and to ascertain the largest possible error in the measurement of signals with relatively much less intensity (in this case, the dimer). Further, one set of measurements was taken by going up in temperature and the other by going down in temperature. As expected, the experiment demonstrated no temperature dependent hysteresis effects. We note that in this work we did not attempt to make measurements above or near the lambda point of helium in the immersion dewar. This is because, from previous experience, we could not reproduce data at these temperatures, perhaps due to emission scattered

Figure 10. Plot of log(D/M) vs. T^{-1} for (A) 5.65%, (B) 4.4%, (C) 3%, (D) 2%, (E), and (F) 0.5% H_s in D_s phenazine. The D/M ratios are from peak heights. The new data in this plot for the 2% crystal clearly show the ''knee'' at $T^{-1} = 0.5\ K^{-1}$. In the previous work, signal-to-noise did not permit unequivocal identification of the knee. An asymptotic high temperature activation energy of $\sim 4\ cm^{-1}$ is observed for high concentration crystals. When more than one set of symbols appears for a given curve, data were recorded in two entirely different experiments.

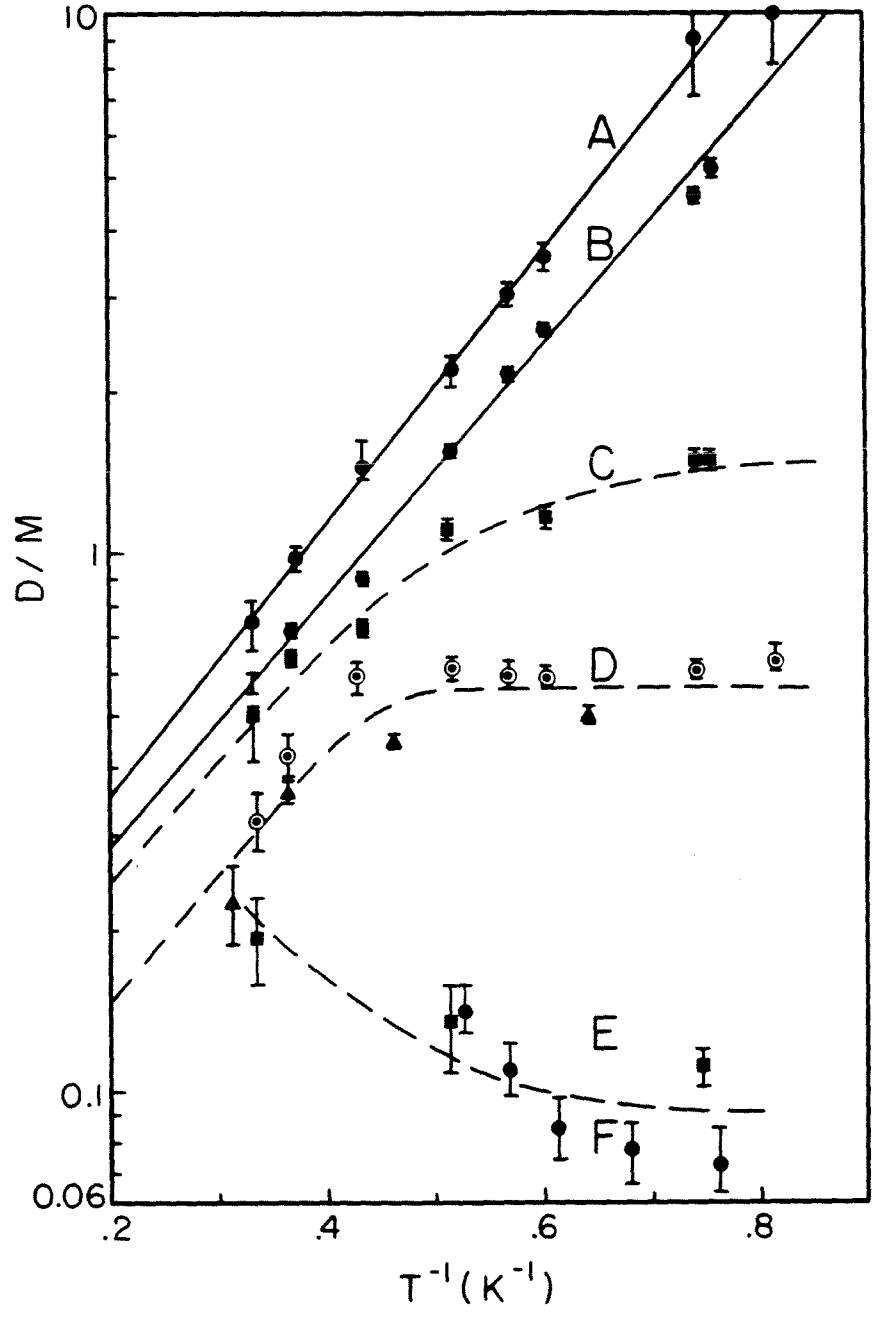
10
1
0.1
0.06
D/M
.2
.4
.6
.8
T⁻¹(K⁻¹)
A
B
C
D
E
F

Figure 11. log(D/M) vs T^{-1} for the following DBN crystals: (A) 21.8% H_6 in D_6, (B) 14.5%, (C) 11.9%, (D) 8.2%, (E) 4.8%, and (F) 2.9%. The dimer was not observed in the 0.1% crystal. The ratios are from computer fits of the experimental data except for the 14.5% crystal which is from peak heights. Curve B was taken from Ref. 15.

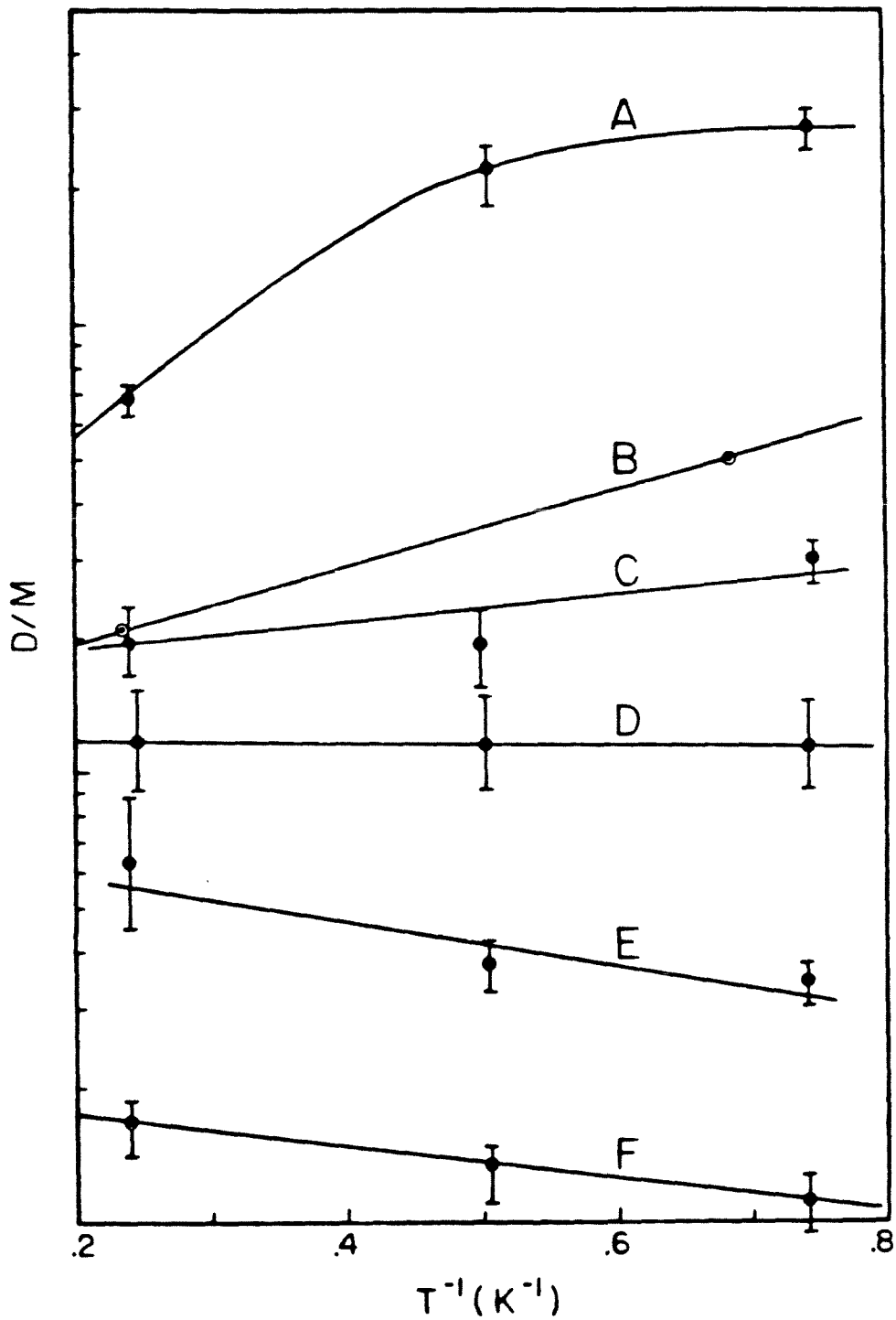
A
B
C
D
E
F
D/M
.2
.4
.6
.8
T⁻¹(K⁻¹)

Figure 12. Normalized emission intensities (peak heights) of the phenazine dimer (or dimer + trimer in the 6.6% crystal) as a function of temperature. The data (and the error bars for each crystal) are multiplied by a constant to make their intensities commensurate at 1.3 K. The data for the 0.5% crystal show a net increase in dimer population with temperature where the 6.6% crystal has the opposite behavior. These trends indicate indirect and direct communication channels, respectively (see text). The 2% crystal would then represent the ambivalent direct and indirect channels. When more than one symbol is shown for a given curve, each symbol represents a different experiment.

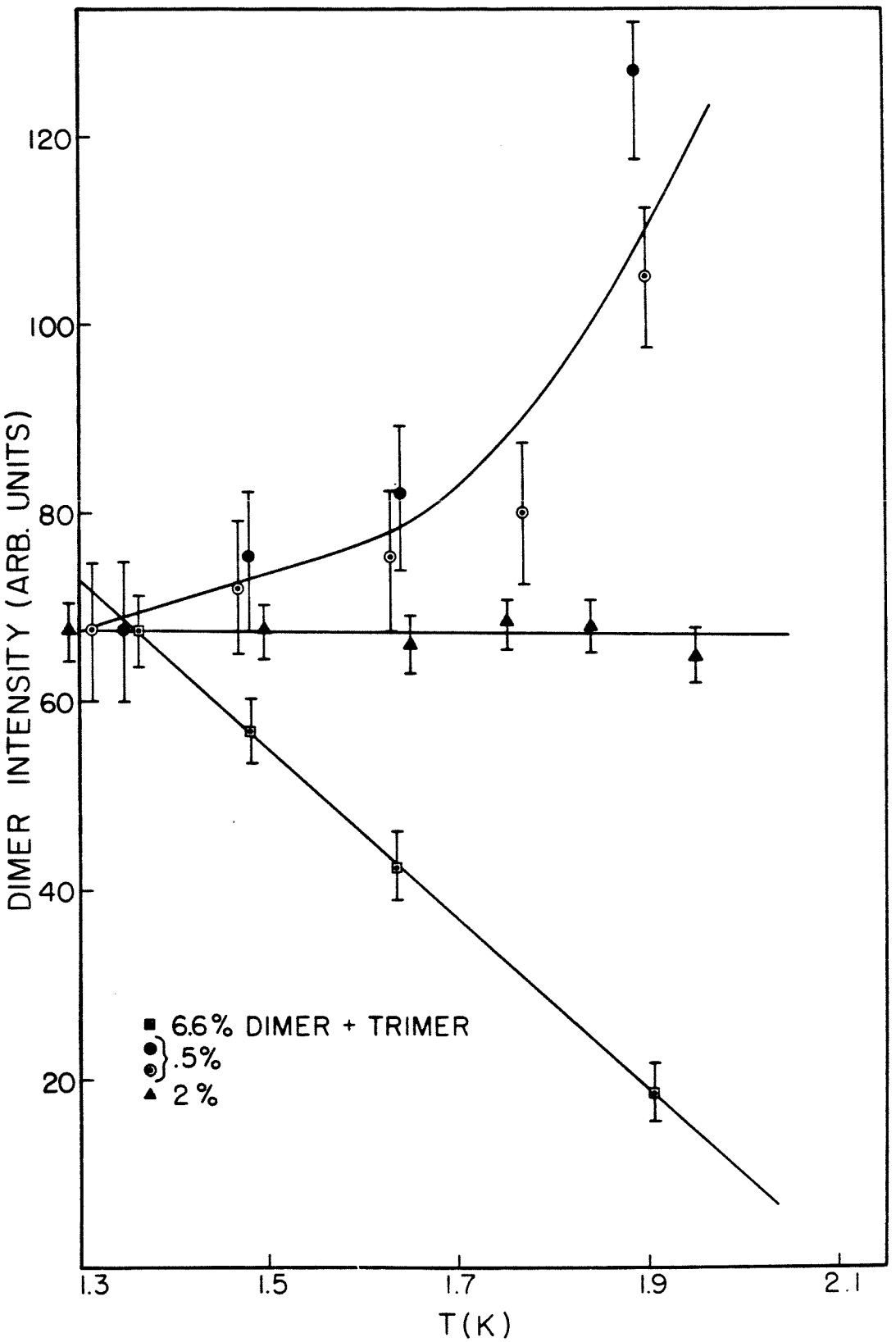
DIMER INTENSITY (ARB. UNITS)
120
100
80
60
40
20
1.3
1.5
1.7
1.9
2.1
T(K)
6.6% DIMER + TRIMER
.5%
2 %

Figure 13. Phenazine monomer emission intensity as a function of concentration and temperature normalized in the same manner as the data in Fig. 12. In all cases, the intensity decreases (or slightly changes) as temperature increases and is most pronounced in the ''pure'' D_s crystal. The pure D_s crystal shows the loss of population with roughly an 18 cm^{-1} activation energy (see Fig. 14). The remaining crystals all show a similar general trend for loss with no well defined activation energy.

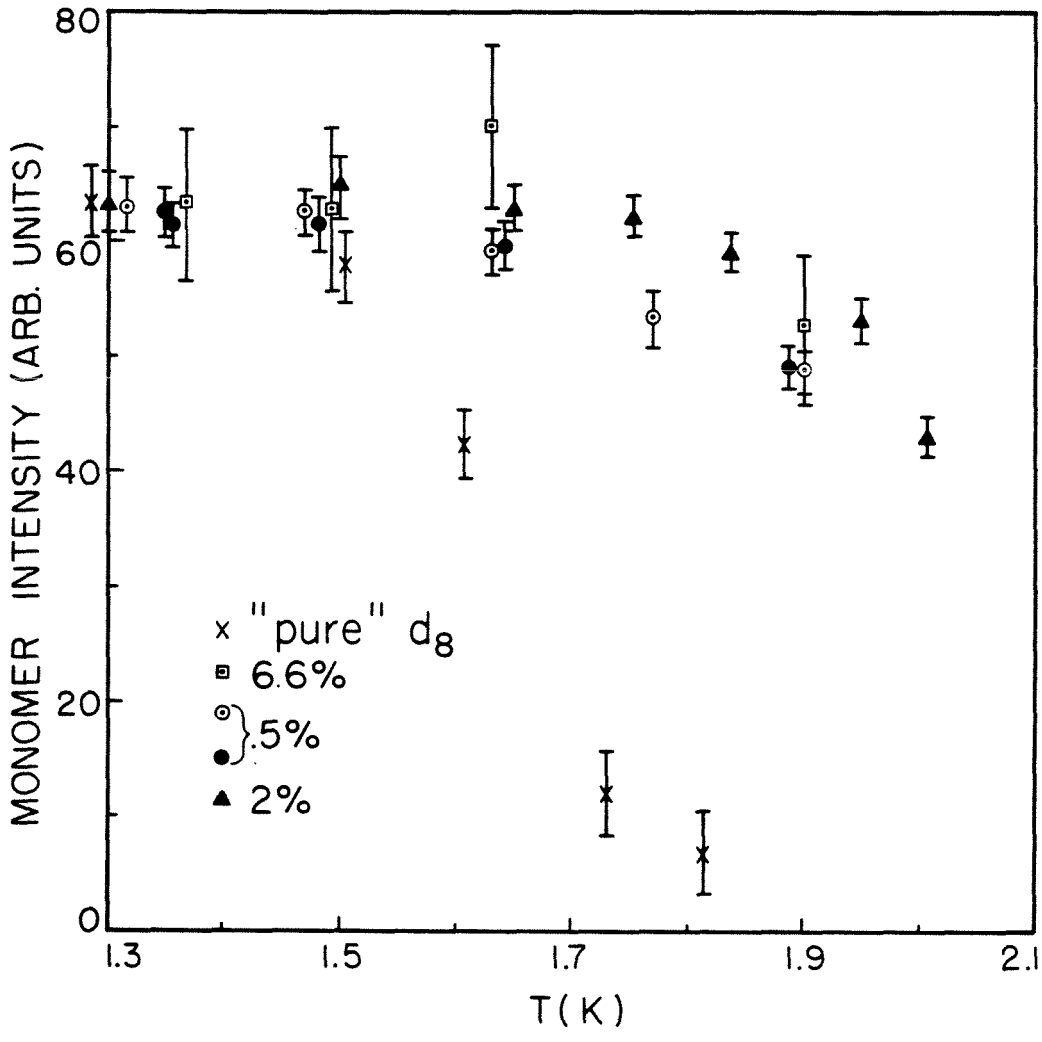
80
60
40
20
0
MONOMER INTENSITY (ARB. UNITS)
1.3
1.5
1.7
1.9
2.1
T(K)
x "pure" d_8
6.6%
.5%
2%

Figure 14. Arrhenius-type plot for pure D_s phenazine showing an 18 ± 1 cm^{-1} activation energy (using the 5 data points at highest temperature). Thus we have clear illustration of detrapping most likely to host states. The activation energy differs slightly from the trap depth, most probably due to the presence of states below the host band (see [58]).

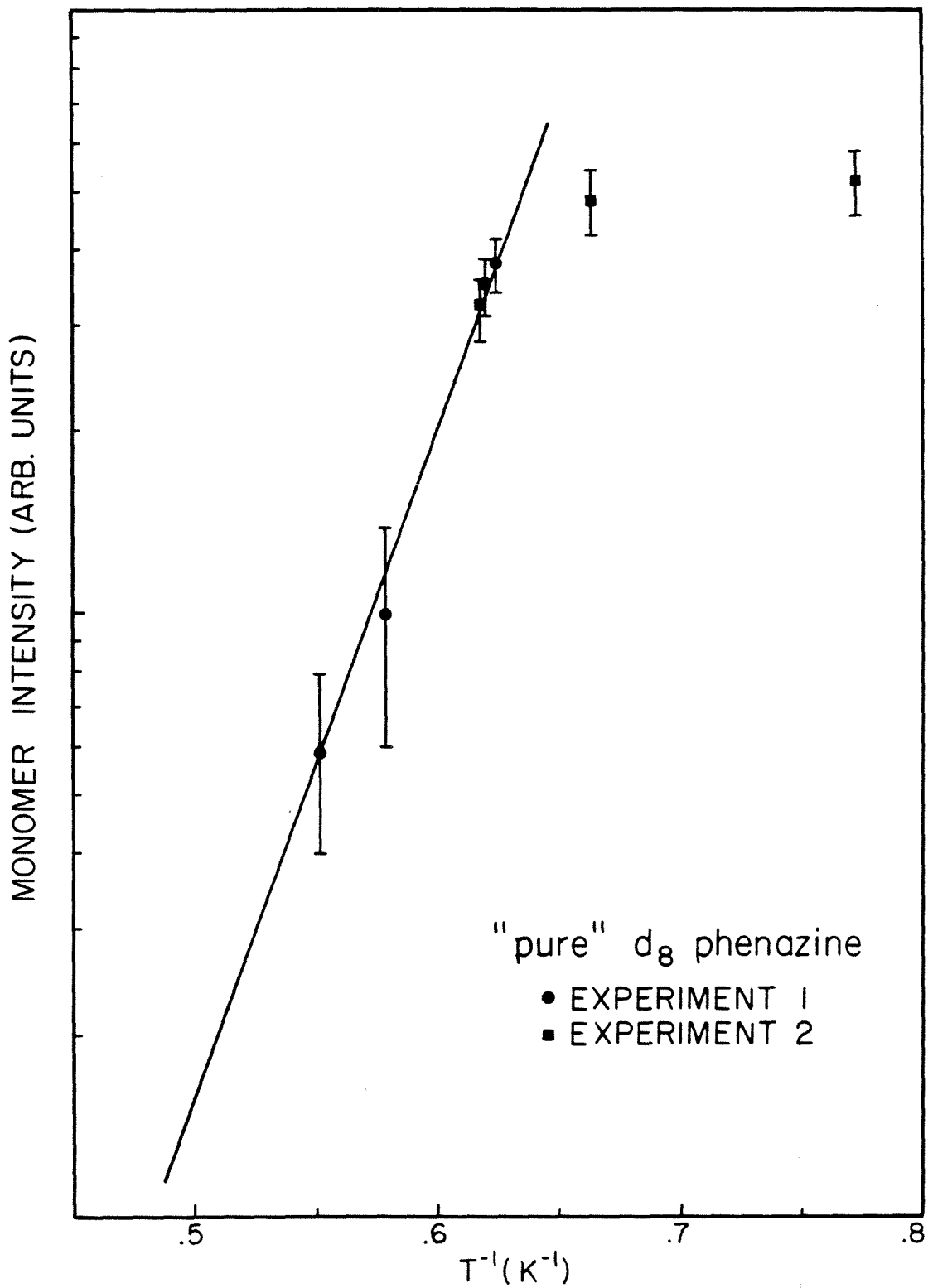
MONOMER INTENSITY (ARB. UNITS)
"pure" d_8 phenazine
• EXPERIMENT 1
▪ EXPERIMENT 2
.5
.6
.7
.8
$T^{-1}(K^{-1})$

Figure 15. Activation energy plots of specific cluster (phenazine) emission intensity for the following: (A) dimer, 5.65%, (B) monomer, 5.65%, (C) monomer, 2%, (D) dimer, 2%, (E) monomer, 0.5%, and (F) dimer, 0.5%.

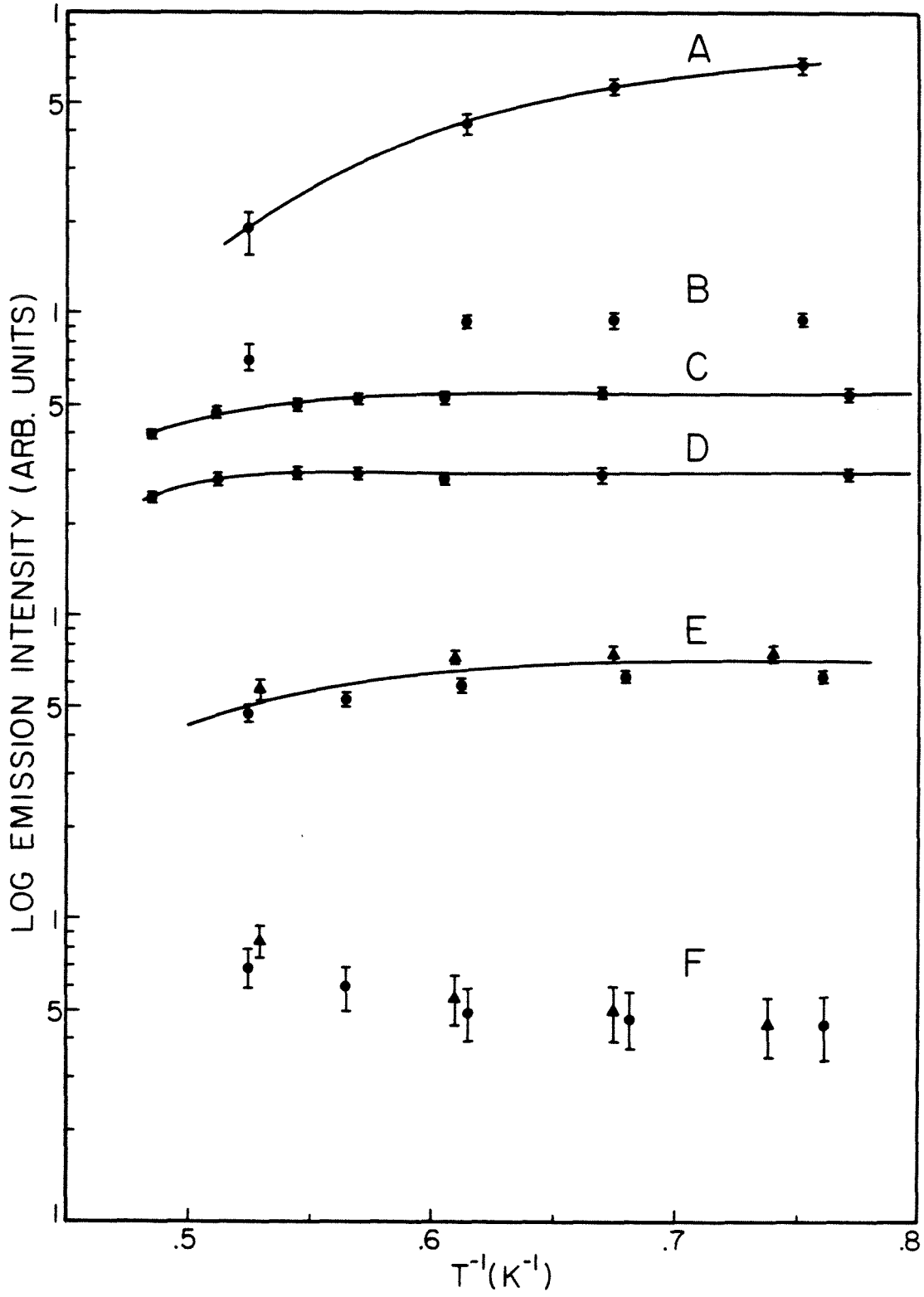
A
B
C
D
E
F
LOG EMISSION INTENSITY (ARB. UNITS)
.5
.6
.7
.8
T⁻¹(K⁻¹)

by boiling helium or thermal effects that take place in these (molecular) solids.

For comparison to the normalized emission intensity vs. T plots, we have prepared log of emission intensity vs T^{-1} plots for a ''pure'' D_8, 0.5%, 2%, and 6.6% crystals. The pure D_8 crystal which contained a vanishingly small amount of proto monomer was chosen in order to have a lattice with monomers as dilute as was possible. The 6.6% crystal was chosen as a sample beyond the critical transition. The 6.6% and pure D_8 crystal were not mass spectrally analyzed, but this was not necessary for the purposes of the emission intensity experiment. The large error bars for the 0.5% and 6.6% crystals are due to the dimer or monomer peak being very small.

E. ODMR, PMDR, and hole burning

The ODMR of the monomer and dimer shows a central peak flanked by satellites due to hyperfine splittings. The transitions in zero field for the monomer (D + E = 2562.3 MHz and 2E = 640.8 MHz) are different from those of the dimer [11]. The results are consistent with early work on phenazine in a diphenyl host, [22] and also with recent work [23].

Knowing the frequencies for the monomer and the dimer in the isotopic mixed crystals, we detected the emission of the dimer (or monomer) alone by scanning the total emission in wavelength while the modulated microwave pump was fixed at the frequency of the dimer (or monomer). This high-resolution PMDR method was useful in determining the optical inhomogeneous broadening of the dimer [5].

An example of inhomogeneous broadening in the ODMR spectrum is shown in Fig. 16. To obtain these spectra we have used 60 mW (continuous) microwave power as the swept frequency, chopped at 110 Hz, and the stationary field of 125 mW was applied to the outer helix (unchopped) at the frequency indicated in Fig. 16. Better S/N was obtained at lower guest concentrations.

Figure 16. Hole burning in the ODMR spectrum for 2% H_s in D_s phenazine. Spectrum A was taken using 60 mW (cw) microwave power, 1.6 K. Spectrum B: all conditions identical to A, except that a stationary microwave field is applied (125 mW at 2.5635 GHz; arrow marks stationary frequency in diagram). The microwaves were square wave modulated at 110 Hz to a depth of 40 dB. Spectral diffusion may be occurring which would alter the depth and width of the microwave absorption hole. Better S/N are obtained when wide-slit detection is used.

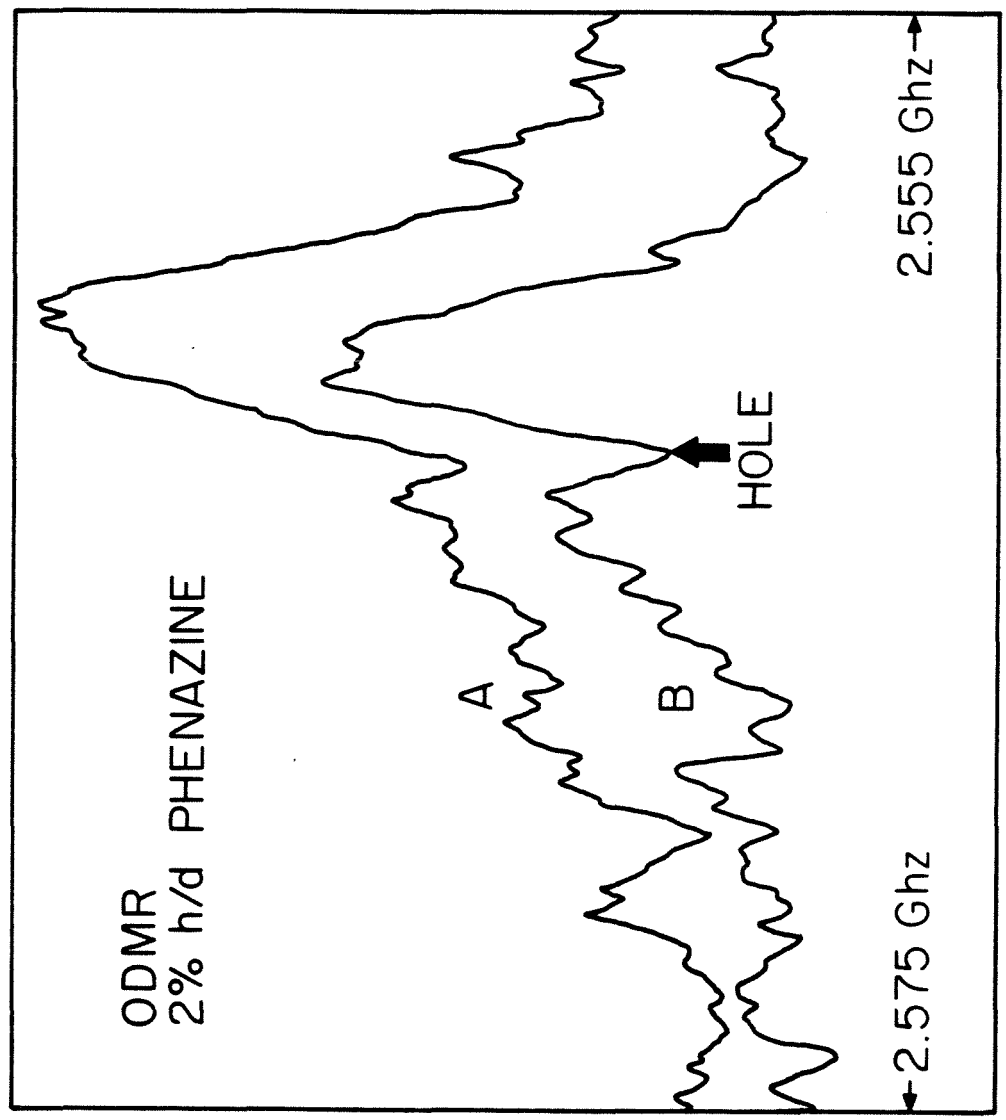
ODMR
2% h/d PHENAZINE
A
B
HOLE
2.555 Ghz
2.575 Ghz
FREQUENCY (Ghz)

IV. THEORETICAL CONSIDERATIONS

A. Cluster statistics

Given a linear array of N sites randomly occupied by G guests and H hosts, the number q_n, of guest clusters containing n contiguous guests, where n = 0, 1, 2... is

(IV.1) $$q_n = N(1 - C)^2 C^n$$

$$= N(1 - G/N)^2 (G/N)^n.$$

Similarly, one can predict in a chain N long, the total number of j contiguous n-mers to be

(IV.2) $$d_{jn} = (N - G - q_n)(1 - q_n/N - G)(q_n/N - G)^j .$$

For j = 2, n = 1 one has the so-called ''double monomer'' whose configuration is shown in Fig. 17. These results were derived by the use of Lagrange multipliers and a derivation is in Appendix I.

A linear chain of 10,000 sites was used to model the infinite 1-D lattice. An appropriate number of computer-generated random numbers between 1 and 10,000 were used to populate the lattice with the desired number of impurities. (The computer program must be able to choose another random number in the event that a particular random number is generated more than once. Otherwise, in the process of generating, say, 1,000 random numbers, less than 1,000 sites may be populated by impurities and this incomplete population

Figure 17. Guest clusters in 1-D. Each box represents a site in a one dimensional chain which must be occupied by either a guest (G) or a host (H). (a) The single host specie or null cluster for n = 0 (see text for explanation of symbol) which fills sites between guest clusters. (b) the guest monomer, n=1. (c) The guest dimer, n=2. (d) the ''double monomer''.

(a) |H|

(b) |G|H|

(c) |G|G|H|

(d) |G|H|G|H|

will vary in an unpredictable manner from run to run.) An algorithm to count the isolated and multiple contiguous impurity clusters was written and the Monte Carlo results are shown in Fig. 18 for DBN type lattices (one dimensional). The program for the 1-D cluster counting is listed in Appendix II.

To obtain information about cluster distributions [24-28] in 2-D, we have performed 2-D Monte Carlo calculations on a rectangular 65 x 300 lattice. Opposite sides of the 65 x 300 sheet were connected to form a torus in order to: (a) preserve periodic boundary conditions, and (b) eliminate edge effects in counting finite-sized samples. Clusters were counted and dissimilar cluster separations were computed. The prime goal of the 2-D simulation was to mimic the anisotropic phenazine lattice and produce the distribution of impurity clusters as a function of impurity concentration. The results are depicted in Fig. 19. One should note that Hoshen and Kopelman [28b] have written an assembly language algorithm that cleverly counts the number of n-mers in a random 2-D or 3-D array. However, their algorithm is for isotropic 2 and 3-D lattices and it is difficult to compare their results with our Monte Carlo.

Over the concentration range from 1% to 25%, the number of monomers precisely fits the functional form of $NC(1 - C)^6$, where N is the total number of sites. For the dimer, the Monte Carlo results fit $(3.1 \pm 0.1)NC^2(1 - C)^8$. Theoretically, [27] one expects the monomer coefficient [in front of the $NC(1 - C)^6$] to be 1 since there is only one distinct way to build a monomer on a given site. Similarly, for a dimer the expected coefficient is 3 by symmetry for (2-D) phenazine type systems. This is in good agreement with the Monte Carlo results. Further, for all

Figure 18. Theoretical (smooth curves) and computer Monte Carlo values (crosses) for the number of various types of clusters in a 10,000 site linear chain. (A) monomer, (B) dimer, (C) trimer, (D) double monomer. The squares are computer results for the number of directly adjacent monomer and dimer clusters (i.e., GHGGH or GGHGH, not like GHHHGGH). To our knowledge, there is no analytic solution for the number of neighboring monomer and dimer clusters and the results would be difficult to obtain by use of Lagrange multipliers (as in Appendix I). For all other clusters we have only shown experimental results for 25%, 50%, and 75%. We have exhaustively compared theory and experiment from 1% to 20% and find agreement to better than 1%. Error bars are the size of the crosses or smaller.

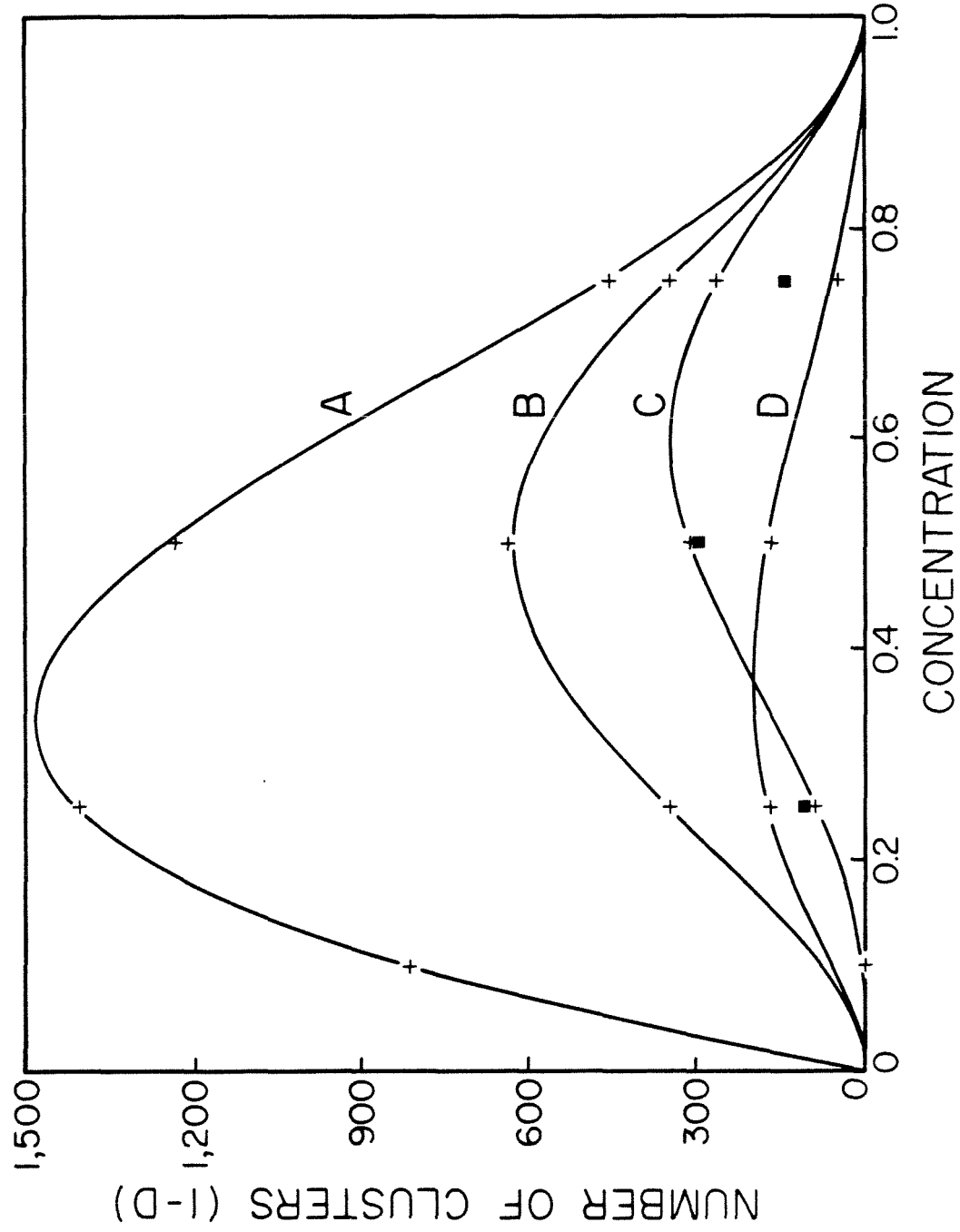
NUMBER OF CLUSTERS (1-D)
1,500
1,200
900
600
300
0
0
0.2
0.4
0.6
0.8
1.0
CONCENTRATION
A
B
C
D

Figure 19. Two-Dimensional Monte Carlo computer simulation for cluster numbers on a 19,500 site lattice. (A) monomer, (B) all dimers (includes TI and TE dimers), (C) total number of trimers (many of which are spatially distinguishable), (D) tetramers. Error bars are the standard deviation of the mean resulting from setting the $\underset{\sim}{b}$ axis parallel to different edges of the computer simulation. Numbers in parentheses are the statistical dimer/monomer ratios from theory. The solid line for curve A is a plot of $C(1-C)^6$; the line for curve B is a plot of $3C^2(1-C)^8$. Although no theoretical expression is available for the larger clusters, workers in the field often use a low density expansion for the perimeter polynomials [62].

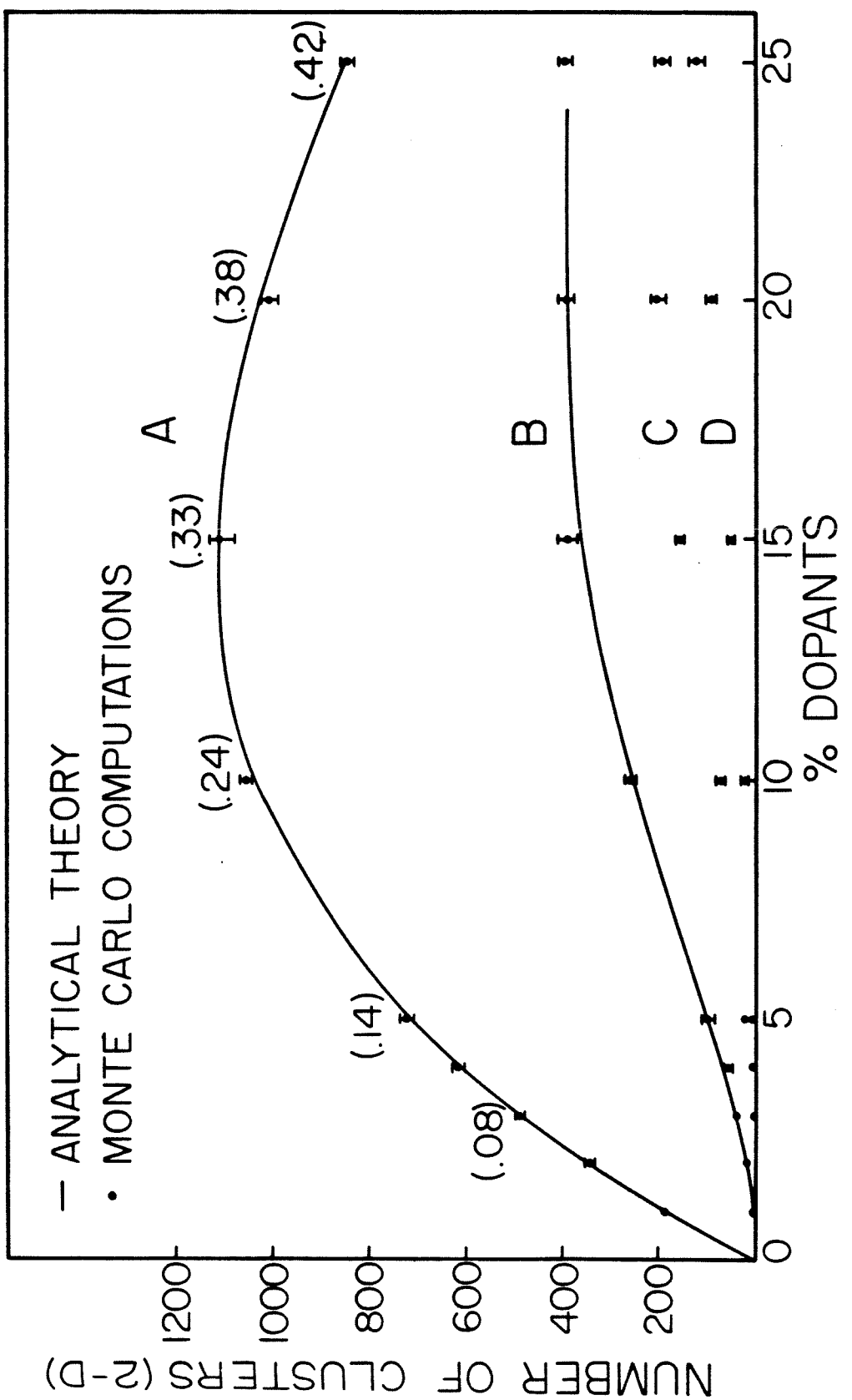
— ANALYTICAL THEORY
• MONTE CARLO COMPUTATIONS
A
B
C
D
(.08)
(.14)
(.24)
(.33)
(.38)
(.42)
NUMBER OF CLUSTERS (2-D)
200
400
600
800
1000
1200
0
5
10
15
20
25
% DOPANTS

concentrations investigated, we counted twice as many translationally inequivalent dimers as translationally equivalent dimers. This is reasonable and can be understood by recalling that there are four available TI sites and two TE sites around each lattice point on which one may build a dimer. Note that the Monte Carlo calculations (a) give the TI/TE ratio, (b) assures us that there is no spatial correlation between clusters up to the 5% concentration range that we are dealing with, and (c) provide the cluster separations.

Our Monte Carlo experimental results differ from those of another recent work [28] done on naphthalene, in that we found substantially fewer dimers (our dimer to monomer ratio was smaller by a factor of 1.5 to 2). Note that for a given concentration, their total number of cluster molecules does not add up to the number of occupied sites (even when considering the larger cluster counts which are not displayed). In this work, for each 2-D simulation, the number of clusters was counted and then from the number of clusters of each type, the total impurity count was determined and checked with the expected number of impurities (to be sure that all impurities were accounted for). For a 5% concentration 10,075 site simulation, we have measured the average impurity-impurity separation to be slightly greater than 2.1 lattice constants (using an average lattice constant) with a standard deviation of 1 lattice constant. In other words, the number of intervening host molecules is 1.1. The standard deviation is due in part to the dimers and trimers present which have impurity separations of 1 lattice constant and should not be construed to strictly represent the average fluctuation in distance between clusters. We also find for the 5%

simulation that the average monomer–nearest dimer separation is slightly greater than 2.6 lattice constants with a standard deviation of 1.

B. The origin of the energy transfer threshold: Percolation vs. the Anderson transition (AT)

The explanation of the energy transfer ''threshold'' in disordered molecular crystals is shared by two groups of thought. On one hand Kopelman et al. [3] believe in the use of percolation theory to explain the phenomenon. They introduced different kinds of percolation methods (called static, dynamic and sometimes quasistatic percolations). Colson et al., [4a] in clear papers, have discussed the validity of such concept to the solids studied in their laboratory and applied the approach to the benzene data.

Klafter and Jortner, [6] on the other hand, have applied Anderson theory of localization [7,8,29–32] and concluded using the Mott argument [8] that percolation [33,34] theory will not be applicable to the case of molecular crystals. We, in our first note, [5] applied Klafter–Jortner (KJ) theory and found good agreement for the phenazine system.

In the Anderson transition approach the threshold concentration is given by [Eq. (5) of Ref. 6]:

$$\text{(IV.3)} \qquad \bar{C} = 0.25[\ln(2z\alpha\beta/w)/\ln(\Delta/\beta) + 1]^3 ,$$

where $\alpha \sim 2.7$ and z (coordination number) ~ 4. w is the inhomogeneous linewidth of the impurity ''band'', Δ = the trap depth and β the

nearest neighbor resonance interaction. For phenazine and DBN these parameters are known. One should note that choosing a coordination number for an anistropic lattice is an ill-defined procedure. We have taken the approach of using a weighted average. The weighting factors are determined by the coupling matrix element in a given direction relative to the strongest couplings, giving essentially 4 for the phenazine system.

An important point about the AT is that it is a theory for the zero-Kelvin limit. As the above equation depicts, there is no temperature dependence for $\bar{C}$. Also, the impurity-impurity coupling may be nonuniform. This fact was realized by KJ and they introduced off-diagonal disorder to account in part for this problem. We, in our note, [5] bypassed the phonon problem by introducing a kinetic model for trapping and detrapping among the monomers and dimers at high temperatures. (A connecton between this model and the model discussed here will be made in the coming section.) But, we did not know how to connect the very low temperature (AT) limit with the high temperature kinetic model.

It seems that by use of the percolation approach or the AT approach one is able to predict a threshold for the transfer of energy. The question we are therefore faced with is: which of the two approaches is adequate for molecular crystals? Conceivably, both schools of thought are the right track, since, after all, elements of Anderson's original work involved percolation theory. In the limit of infinte trap depth for an infinite-life particle (excitation), classical percolation theory is exact. In practice neither the trap depth nor lifetime is infinite.

Mott [8] has argued against the use of percolation theory in microscopically homogeneous systems. If the ensemble does not show ''local'' inhomogeneities or near-macroscopic clustering, then macroscopically the transfer of electrons by quantum mechanical tunneling effects prevail. As a result, Mott and others have argued that the inhomogeneous broadening of the solid relative to the bandwidth will be an important factor in determining the formation of extended or localized states (in other words, the Anderson Model).

The other advocates say that even though inhomogeneous broadening may be important, there are two problems in applying the AT to organic crystals: the finite lifetime of the trap state and the small bandwidth expected in molecular crystals in triplet states. KJ have shown that the former point can explain the change in the threshold for the transfer, depending on whether $k_t\tau \gg 1$ or $\ll 1$, where k_t is the trapping rate constant and τ is the lifetime. In other words, there is no conflict between the finite lifetime and the concept of using AT. As for the second point, KJ have calculated a bandwidth on the order of 10^{-2} cm^{-1}. Kopelman et al. [35] argued that this number should be 2×10^{-8} cm^{-1}. As we shall see later, our calculation agrees with that of KJ. A check on these calculations is made by comparing the analytical result with computer calculations done for diagonal disorder and off-diagonal disorder [36,6]. The results agree to within an order of magnitude with the configurationally averaged results of KJ and of ours, but differ by five orders of magnitude from the 2×10^{-8} cm^{-1} naphthalene result. Finally, it is clear that these organic mixed crystals are inhomogeneously broadened. We are not arguing that the presence of

inhomogeneous broadening alone means that we should use AT and not percolation, but we are saying that its presence together with the reasonably large impurity bandwidth supports, but does not prove, the application of AT to the phenazine system, as we shall discuss later.

V. DISCUSSION OF THE PHENAZINE AND DBN RESULTS

A. Calculation of the impurity bandwidth

To calculate β from the observed M-D splitting we [11] diagonalized a large cluster matrix [37-39] to correct for the quasi-resonance interactions between guest and host molecules.

In order to calculate the average spatial separation between impurities and thus the average impurity-impurity interaction energy (''bandwidth''), we shall use the first moment of a probability distribution function developed by Hertz [40,41]. The application of this distribution to our situation is not exact, since it smooths the anisotropic topology and produces an isotropic impurity superlattice. Clearly, it is possible to calculate the effects of higher moments of the distribution of the impurity bandwidth, but we find the average adequate in view of other approximations made.

We model the near impurity-impurity neighbor distribution as being isotropic, continuous, and unimodal, assuming substitutional impurities to be spatially uncorrelated. By extension of Hertz's results [40], the distribution function representing the number of impurities between r and r + dr in one dimension is

(V.1) $$P(r) = e^{-\bar{\rho}r}\bar{\rho}\, dr,$$

where r is the distance and $\bar{\rho}$ is the average impurity number density per unit length which is equal to the fractional number of impurities divided by the lattice constant, d. Thus, the average separation, $\langle r \rangle$, becomes

(V.2) $$\langle r \rangle = \int_0^\infty r\bar{\rho}e^{-\bar{\rho}r}dr = \gamma(2)/\bar{\rho} = (\bar{\rho})^{-1},$$

where $\gamma(2)$ is the gamma (factorial) function of 2. Clearly the mean number of host sites between impurities (n), is equal to $[(\langle r \rangle/d) - 1]$. Similarly, for 2-D we have $\langle r \rangle = 0.5(\rho)^{-1/2}$, where ρ is now the impurity number density per unit area. One should notice that the average distance is inversely proportional to root of the impurity density; at higher densities, $\langle r \rangle$ is shorter. Furthermore, the distribution for the 2-D case is not symmetrical about its mean. The standard deviation about the mean can be calculated in terms of the first and second moments: $\sigma = 0.26(\rho)^{-1/2}$

We now make bandwidth calculations specific to the phenazine system. In order to use the statistical forumulas one needs an average lattice constant for phenazine, and we shall use the geometrical average, d, of $\underset{\sim}{a}$ and $\underset{\sim}{b}$ (such that the cell area is conserved) which is $(|a||b|)^{1/2} = 8.2$ Å. We compute $\langle r \rangle$ for C = 0.05, d = 8.2: $\langle r \rangle = 0.5(\rho)^{-1/2} = 0.5(C/d^2)^{-1/2} = 18.3$ Å. Immediately, $\langle n \rangle = 1.23$, which is likely an underestimate of $\langle n \rangle$ due to neglect of clustering effects in the continuum distribution. This is in good agreement with our Monte Carlo

result of $\langle n \rangle$ slightly greater than 1.1. The distribution of cluster separations for the 2-D Monte Carlo is depicted in Fig. 20.

Now that we can calculate average distances, the interaction energy between impurities, and hence the bandwidth (B), can be calculated. At zero Kelvin there is no thermal promotion into the host band and the transfer may proceed by superexchange '' tunneling'' through the host barriers which are located at + Δ from the impurity monomer. (More accurately, a mixing of guest and host states is responsible for the guest-guest coupling.) This tunneling mechanism formulated first by Nieman and Robinson [42] has recently been used for treating exciton percolation [3,4], exciton coherence [43], and trap-to-trap energy transfer [4,42,44]. The idea behind this coupling scheme is simple, but accurate calculation is singularly difficult for anisotropic 2-D and 3-D systems where the two traps have different energies, or a distribution of energies.

For a linear chain of n intervening host (H) sites separating two monomer traps (M1) and (M2), J = (B/2z) takes a simple form [42,4]:

$$(V.3) \qquad J_n = (F_{M1}\beta_o)(F_H\beta_o)^{n-1}(F_{M2}\beta_o)\Delta^{-n} \; ;$$

$$F\beta_o << \Delta \; ,$$

where F_M and F_H are, respectively, the Franck-Condon factors for the monomer and the host. β_o is the nearest neighbor (pure electronic interaction) matrix element and is assumed to be the same for M-H, H-H, and H-M

Figure 20. A bin-sort plot of nearest particle separations in the anisotropic 2-D phenazine lattice. All particles whose nearest neighbor is between one and two lattice constants away are summed to give the first point, all particles whose nearest neighbor is between two and three lattice constants away are summed to give the second point, and so on. Despite clustering effects, the distribution is not too different from that of predicted by the continuum model.

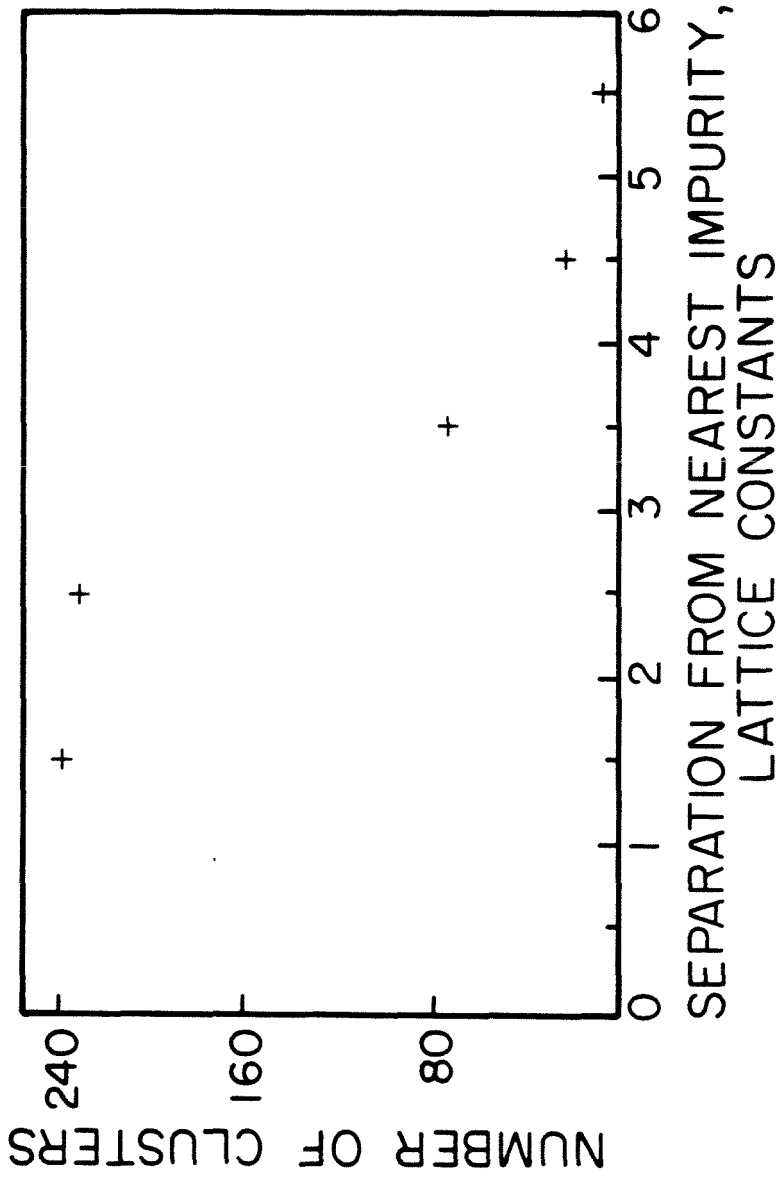
NUMBER OF CLUSTERS
240
160
80
0
1
2
3
4
5
6
SEPARATION FROM NEAREST IMPURITY,
LATTICE CONSTANTS

coupling. For completeness, one notes there is evidence [4b] that the electronic coupling is not isotope-independent in naphthalene. However, from the experimental data herein and from previous work, it is clear that to first order the Davydov splitting is isotope invariant in DBN. Colson et al. [4a] have presented formulas for cases where the two traps are much different in energy. In this case β_0 of the host to the lowest energy trap is generally different from β_0 of H-H, since the lowest energy (or super) trap is chemically different from the host molecules. Because of the large energy gap between the trap and the super-trap, additional Franck-Condon factors were added to account for the mismatch in energy. However, later on in their calculation they have assumed that terms in front of $(F\beta_0/\Delta)^n$ simply give a constant of one [see expression (III.8) in their paper].

We treat the energy transfer between the two impurities (in our case the monomer and dimer) which are separated by only 4 cm^{-1} as a ''resonant'' process among the monomers, accompanied by absorption (or emission) of phonons of the lattice. (As we shall see later, the results are satisfactory and explain many of the experimental features of the temperature-dependent studies.) The average value of J is therefore:

$$\text{(V.4)} \qquad \langle J\rangle \sim \langle \beta^{n+1}{}_{\Delta}{}^{-n}\rangle \sim \beta^{\langle n\rangle+1}{}_{\Delta}{}^{-\langle n\rangle}$$

$$= \beta e^{-\alpha\langle n\rangle} \; ; \; \alpha = \ln(\Delta/\beta) \; .$$

This averaging is certainly not exact but its accuracy for different ranges of n can be tested as we did elsewhere [65].

The value of β in the above expression is difficult to ascertain for anisotropic lattices. However, we shall perform two calculations to show the dependence of J on β. In the first calculation we simply use the 6 cm^{-1} value for β. In this case J = 1.2 cm^{-1}. The second calculation is for an efffective β that is explicitly determined by β_1 and β_2 [45]. Thus we have for this case, J = 0.1 cm^{-1} since $\beta_{eff} = (6x\ 0.5)^{1/2}$ The important point here is that the calculation is only accurate to an order of magnitude, but provides a value for J (note B = 2zJ) and hence B that is orders of magnitude larger than the value calculated by Kopelman et al. [35] (2 x 10^{-8} cm^{-1}) for naphthalene and ''comparable'' with the value of KJ. For DBN see Ref. 65.

B. Population transfer

1. The kinetics model

The use of a kinetic model that decribes population transfer at finite temperatures was first suggested by us in Ref. 5. Here, we wish to make the model properly treat the phonon-induced breakdown of the threshold (here, by breakdown, we mean phonon assisted energy transfer to the host and back to other impurities or between impurities). The question we need to answer is, can we justifiably make approximations in the coupled nonlinear rate equations for the lattice (which we can write down but not solve) to produce a set of soluble rate equations which describe the important physics?

The applicability of kinetics is an old question and has been of concern to many investigators [46-48]. The real problem is due to the dispersion of the impurities in non-equivalent ways. Hence, the

interaction matrix elements are a function of r (intercluster separation). Statistically the system is not stationary (i.e., depends upon the choice of origin) and usually severe configurational averaging is required. If all the impurities have essentially the same separation, then the population scheme is adequate, otherwise, one must calculate probabilities of finding excitation on a subset of impurity sites and then average over all lattice configurations. Even in one-dimensional systems, the distribution function as a function of r is complex. Only recently has this problem been dealt with by Orbach and co-workers [47] to provide macroscopic dynamic rates in terms of microscopic quantities. For our steady state experiments we shall assume that the averaging simply gives rates that are products of population and rate constants.

2. System description

To obtain theoretical expressions relating the observed ratio of dimer to monomer phosphorescence emission to the temperature and the concentration we consider a model system consisting of a host band and two sets of impurity states, and consider transitions between all these levels. We consider that the triplet host band is populated by, e.g., intersystem crossing from the singlet manifold, while the impurity states are populated by a nonradiative phonon emission process from the host band. In addition, we also allow the possibility of the reverse phonon absorption process which serves to depopulate the monomer and dimer cluster states. These two nonradiative processes establish communication between the host and guest states, and indirectly betwen the guest states. In crystals with impurity concentrations above a

certain transition threshold, the guest states are ''extended'' and it becomes necessary to consider a direct communication between monomer and dimer clusters. This communication is also treated as a nonradiative transition involving phonon emission (for monomer-to-dimer transitions) and absorption (dimer-to-monomer).

The population of the monomer and dimer levels are found by solving a set of rate equations for the populations of the various levels. The observed emission ratio is simply related to the population ratio through the radiative rate constant. The rate constants for the phonon assisted transitions are calculated in a ''Golden Rule'' like form from a knowledge of the intersite coupling and the exciton-phonon coupling Hamiltonian and the phonon occupation numbers which contain the temperature dependence. As described before, the concentration dependence is contained in the spatial probabilities for finding host molecules, monomer or dimer clusters in a random lattice.

The energy level scheme we consider for the various processes under study is shown in Fig. 21. In this figure γ_S, γ_H, γ_M, and γ_D are the total decay rates to the ground state and contain the radiative and nonradiative contributions. All the other rates are represented by γ_{ij} which describe a process of excitation transfer from j into i (note the order of the subscripts, written in spirit of a matrix element where typically, the initial state is on the right and final states on the left) i and j label the host and impurity states. The singlet band is pumped by light, represented by a function $P_L(t)$, the number of transitions into the singlet state, S, per unit time. We assume that the triplet states are not pumped directly by the exciting

Figure 21. Level scheme used for kinetic equations (see text for explanation of symbols). This level scheme neglects trapping of singlet excitons, which is appropropriate if the intersystem crossing rate is greater than the singlet exciton trapping rate (see the work of L. J. Noe, E. O. Degenkolb and P. M. Rentzepis [63].)

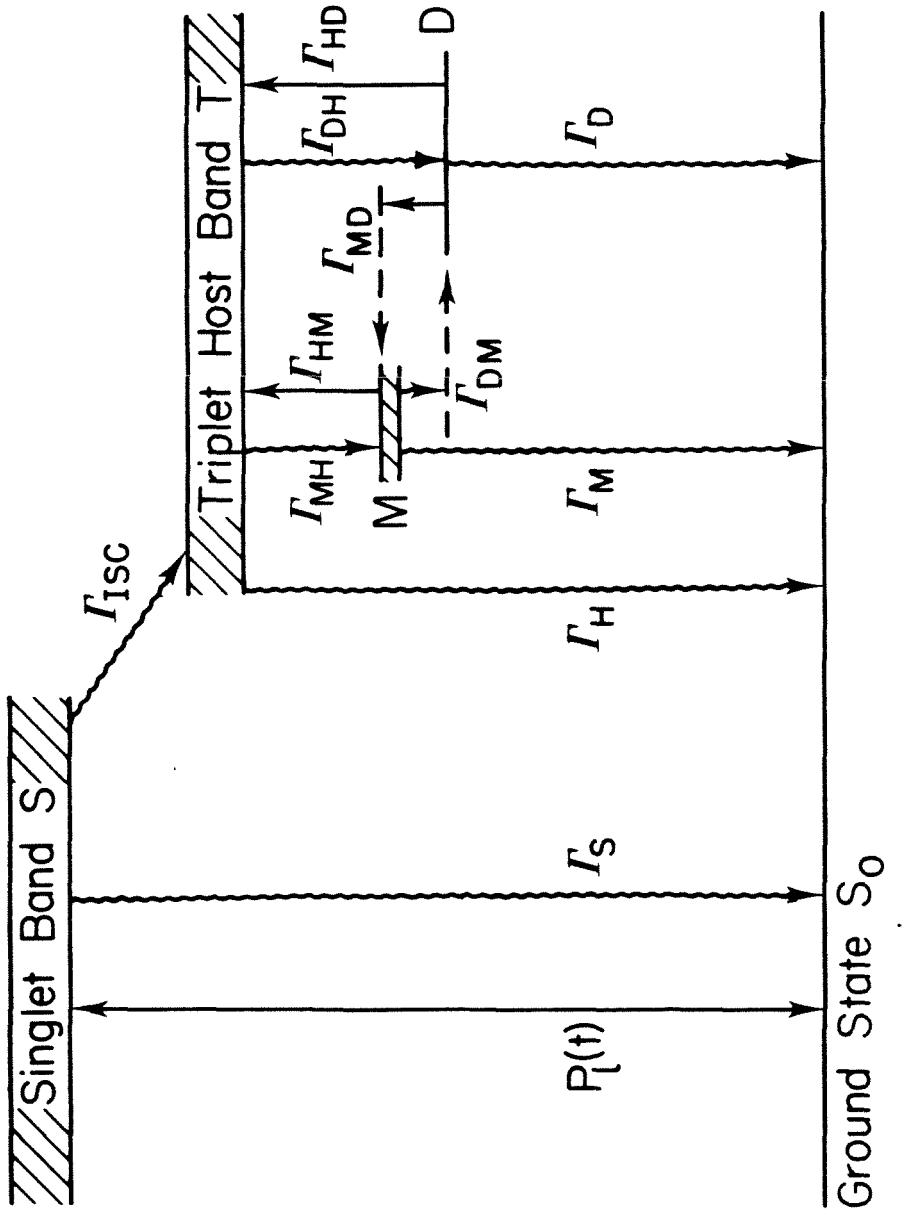
Singlet Band S
Triplet Host Band T
Ground State S_0
Γ_{ISC}
Γ_S
Γ_H
Γ_M
Γ_D
Γ_{MH}
Γ_{HM}
Γ_{MD}
Γ_{DM}
Γ_{DH}
Γ_{HD}
M
D
$P_l(t)$

light, and that the effect of spin splittings, which are much smaller than the inhomogeneous linewidth, is not important. Also, we ignore the effect of singlet traps.

3. Master expressions

Using the notation developed above, we arrive at the average rate equations describing population of the levels in Fig. 21:

$$\dot{n}_M(t) = \gamma_{MH} n_H(t) + \gamma_{MD} n_D(t) - \bar{\gamma}_M n_M(t) \tag{V.5}$$

$$\dot{n}_D(t) = \gamma_{DH} n_H(t) + \gamma_{DM} n_M(t) - \bar{\gamma}_D n_D(t)$$

$$\dot{n}_H(t) = \gamma_{ISC} n_S(t) + \gamma_{HM} n_M(t) + \gamma_{HD} n_D(t) - \bar{\gamma}_H n_H(t)$$

$$\dot{n}_S(t) = P_L(t) - (\gamma_S + \gamma_{ISC}) n_S(t) ,$$

where

$$\bar{\gamma}_i = \gamma_i + \sum_{i \neq j} \gamma_{ji} \qquad (i,j = M, D, H) \tag{V.6}$$

was used to simplify the notation by indicating the sum of all decay channels for the i^{th} level. All transition rates γ contain the information on the final density of states, temperature, and energy mismatch. We find the steady state solution to be

$$n_H = (\bar{\gamma}_M \bar{\gamma}_D - \gamma_{MD}\gamma_{DM})/\Theta \tag{V.7}$$

$$n_M = (\gamma_{DH}\gamma_{MD} + \gamma_{MH}\bar{\gamma}_D)/\Theta$$

$$n_D = (\gamma_{MH}\gamma_{DM} + \gamma_{DH}\bar{\gamma}_M)/\Theta,$$

where

(V.8) $$\Theta=\bar{\gamma}_S[\bar{\gamma}_H(\bar{\gamma}_M\bar{\gamma}_D - \gamma_{DM}\gamma_{MD}) - \gamma_{HM}(\bar{\gamma}_D\gamma_{MH} + \gamma_{MD}\gamma_{DH}) - \gamma_{HD}(\bar{\gamma}_M\gamma_{DH} + \gamma_{MH}\gamma_{DM})]/\gamma_{ISC}P_L.$$

The host singlet pumping and decay terms cancel upon taking the ratio of n_D and n_M, giving

(V.9) $$n_D/n_M = (\gamma_{MH}\gamma_{DM} + \gamma_{DH}\bar{\gamma}_M)/(\gamma_{DH}\gamma_{MD} + \gamma_{MH}\bar{\gamma}_D).$$

Equation (V.9) is the principal result by which we model the concentration and temperature dependence of the experiment. In the low concentration limit, where γ_{MD}, γ_{DM} tend to zero, one finds that equations (V.9) reduces to the following:

(V.10) $$n_D/n_M = \gamma_{DH}(\gamma_M + \gamma_{HM})/\gamma_{MH}(\gamma_D + \gamma_{HD}) \quad ,$$

which, at T ~ 0 K, further simplifies to the ratios of the feeding rate to the decay rate, a familiar result:

(V.11) $$n_D/n_M = (\gamma_{DH}/\gamma_D)/(\gamma_{MH}/\gamma_M) \quad .$$

At high concentrations and low temperatures (inefficient detrapping) (V.9) becomes

(V.12) $$n_D/n_M = [\gamma_{MH}\gamma_{DM} + \gamma_{DH}(\gamma_M + \gamma_{DM})]\gamma_{MH}\gamma_D \quad ,$$

which demonstrates that any increase in trap feeding rates will increase

n_D/n_M as all population ultimately ends up in the lowest lying state. Also, an increase in the dimer decay rate will reduce the dimer population relative to the monomer.

There are limitations to the kinetic description of the phenazine system--we enumerate a few: (1) The host band states are treated as one level, thus the nature of energy transport via host states is not known; (2) Use of discrete levels rather than inhomogeneously broadened levels which hopefully reflect effective energies for phonon assisted energy transfer; (3) Coherence effects are lost in a kinetic scheme, but they may not be important due to disorder; (4) Second and higher order electronic (e.g., multi-impurity energy exchange) and vibrational processes are omitted. Though the importance of the multiphonon processes has been demonstrated in other systems [49], we presume that the cross section for these processes in band-trap interactions is relatively small; and (5) The dimer (-) state has been omitted which has an undetermined role as an intermediate or final state in energy migration.

4. Role of exciton-phonon coupling: The rate constants

The parameters appearing in Eq. (V.5) are rate constants for two types of processes--transitions between impurity states and host states, and transitions between different impurity states. We adopt the point of view that these transitions are mediated by the electron-phonon interaction [50].

In the dilute crystal limit (say, one impurity per million host molecules) one may use the standard exciton-phonon formalism [51] of the

pure crystal (i.e., crystals with well defined exciton $\underset{\sim}{k}$ states) to describe the coupling terms explicitly. This has been recently done by Craig and his collaborators [52]. In the heavy doping limit this simple picture which utilizes the translational symmetry of the almost perfect lattice breaks down. Since there are no data that will allow us to compute the coupling terms [53,54] accurately, we shall not elaborate the point. Rather, we shall express the rates in terms of these coupling parameters like $\partial V/\partial R$, where V is the interaction potential and R the displacement for an electron-phonon interaction [54].

Using the above results, we can write the γ's at any temperature in terms of the concentration of the final species, assuming that the transition started from an averaged state. For example, for γ_{DM}, the rate involves transitions from equally averaged monomer states to all possible dimers. To conserve the energy a phonon must be emitted during this process. Thus for a single phonon process we may write

$$\text{(V.13a)} \quad \gamma_{DM} = \frac{2\pi}{(h/2\pi)} |\Omega_{DM}|^2 \rho(\eta_q + 1) C_D$$

$$\text{(V.13b)} \quad \gamma_{MD} = \frac{2\pi}{(h/2\pi)} |\Omega_{MD}|^2 \rho(\eta_q) C_M$$

$$\text{(V.13c)} \quad \gamma_{MH} = \frac{2\pi}{(h/2\pi)} |\Omega_{MH}|^2 \rho(\eta_q + 1) C_M$$

$$\text{(V.13d)} \quad \gamma_{HM} = \frac{2\pi}{(h/2\pi)} |\Omega_{HM}|^2 \rho(\eta_q) \quad ,$$

where Ω is the coupling matrix element [55] between, say, the monomer

and the host which results in transfer and emission of a phonon, q, with occupation number η. Note that γ_{DM} and γ_{MD} include J of equation (V.3). The phonon q has the appropriate energy to match H-M, H-D, or M-D energy separations. Finally,

$$\eta_q + 1 = (e^{(h/2\pi)\omega_q/kT} - 1)^{-1} + 1 \ . \tag{V.14}$$

Again, we should emphasize that we have assumed constant microscopic coupling constants between impurities and made the configurational average discussed before.

C. Numerical simulation of the experiment

In order to test the correctness of the model (described above) in predicting the steady state experiments, we have performed numerical simulations of D/M vs C and 1/T. An algorithm for the master rate equation (V.9) was written and plots to simulate the experimental data as a function of various parameters were generated. There are six parameters in the kinetic equation, all of which, in principle, can be determined spectroscopically. The parameters are (a) relaxation rates for the monomer, dimer, and host, and (b) coupling constants for transfer between all pairs of the three levels: monomer, dimer and host.

An attempt was made to fit the experimental curves, D/M vs concentration and temperature, by nonlinear regression for a fixed set of relaxation parameters and educated guesses for the coupling constants, but no convergence was obtained, indicating at least for the

starting guesses supplied, no unique solution existed (the kinetic expression is too complex to have ascertained this beforehand). Instead, we followed the behavior of the equations for reasonable parameters with self-consistency.

The best simulation of the experimental data using expression (V.9) is shown in Figs. 22 and 23. For phonon-induced transitions, the Hamiltonian for electronic distortion, $\partial V/\partial R$, is implicitly part of γ. Thus, in addition to J, the phonon occupation number and the concentration, the rate constants have an additional constant, K, that depends on the density of final states, Planck's constant, $\partial V/\partial R$, etc. This ''coupling'' constant K was the parameter (cm^2/sec) in our fit for a given communication channel.

As mentioned before, J depends on $\langle n \rangle$ and for phenazine this is given by

$$\langle n \rangle = (0.5/C^{1/2}) - 1 \quad .$$

In general, γ_{MD} and γ_{DM} are related by the ratio of phonon absorption and emission rates (at the energy of mismatch between M and D) and the total concentration of M and D. Monomer-to-monomer transfer is faster than M-to-D transfer partly due to the relative concentrations. For low C, approximately C of the monomers will be replaced by dimers. Monomer to dimer transfer will predominantly occur from monomers directly adjacent to dimers. For monomers not close to a dimer, M-to-M transfer will predominate, but this will not affect the steady state M-to-D transfer, as all monomers in the configuration

Figure 22. Theoretical simulation of D/M vs C for phenazine. Rate equation (V.9) was used with the following parameter set: $\gamma_H = 10^3$, $\gamma_M = 10^2$, $\gamma_D = 2\times10^2$, $K_{HM} = 10^{11}$, $K_{HD} = 2\times10^{12}$, $K_{MD} = 3\times10^8$. The monomer trap depth was 18 cm^{-1} (rather than 23 cm^{-1}, using the results of Fig. 14), dimer trap depth was 22.4 cm^{-1} and $\beta/\Delta = 4.4/18$). The actual rate constants are the product of the fitting parameter, a concentration and a phonon term. γ_H, γ_M, and γ_D are in sec^{-1}.

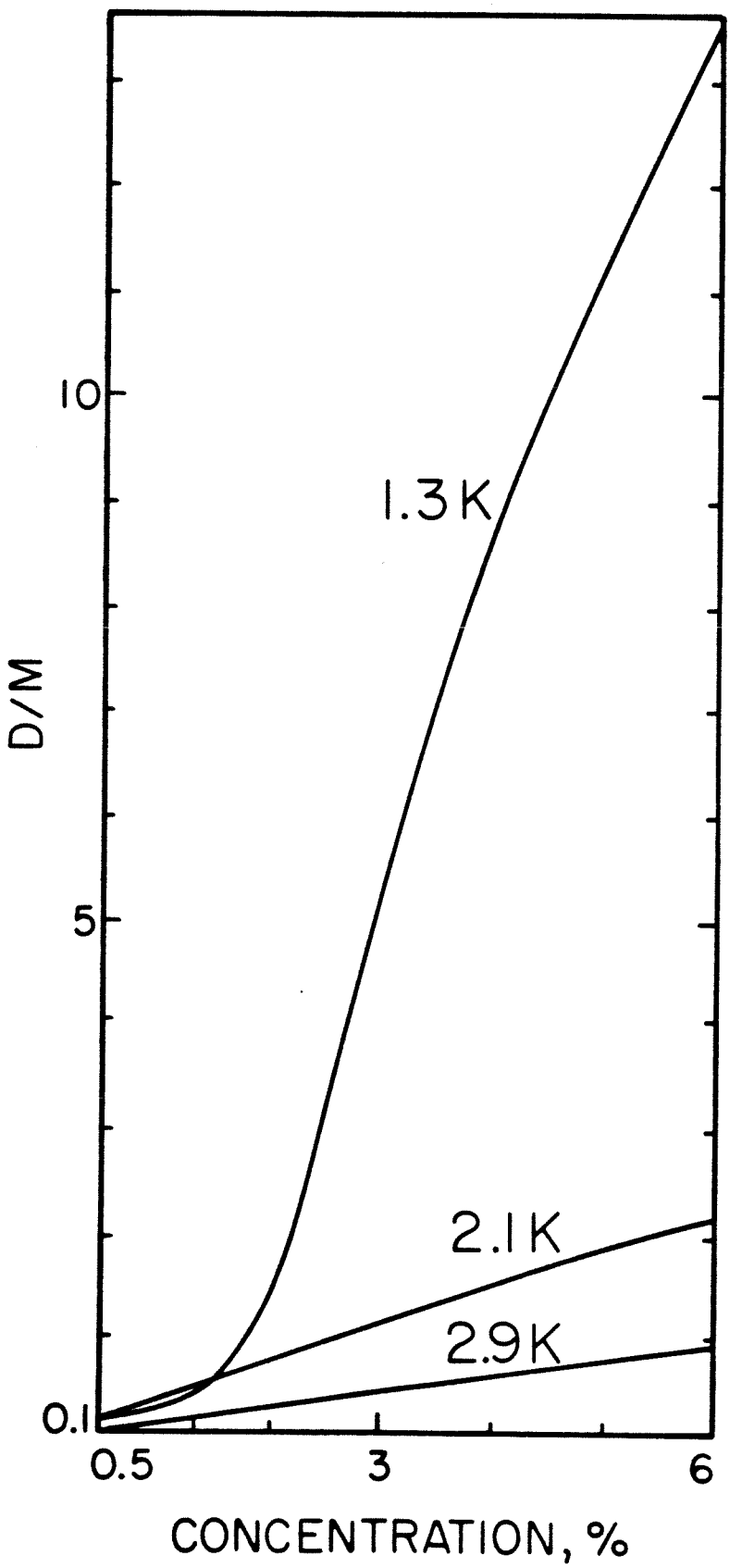
10
5
0.1
D/M
1.3K
2.1K
2.9K
0.5
3
6
CONCENTRATION, %

Figure 23. Theoretical simulation of D/M vs T^{-1} for phenazine using the same parameter set as that of Fig. 22.

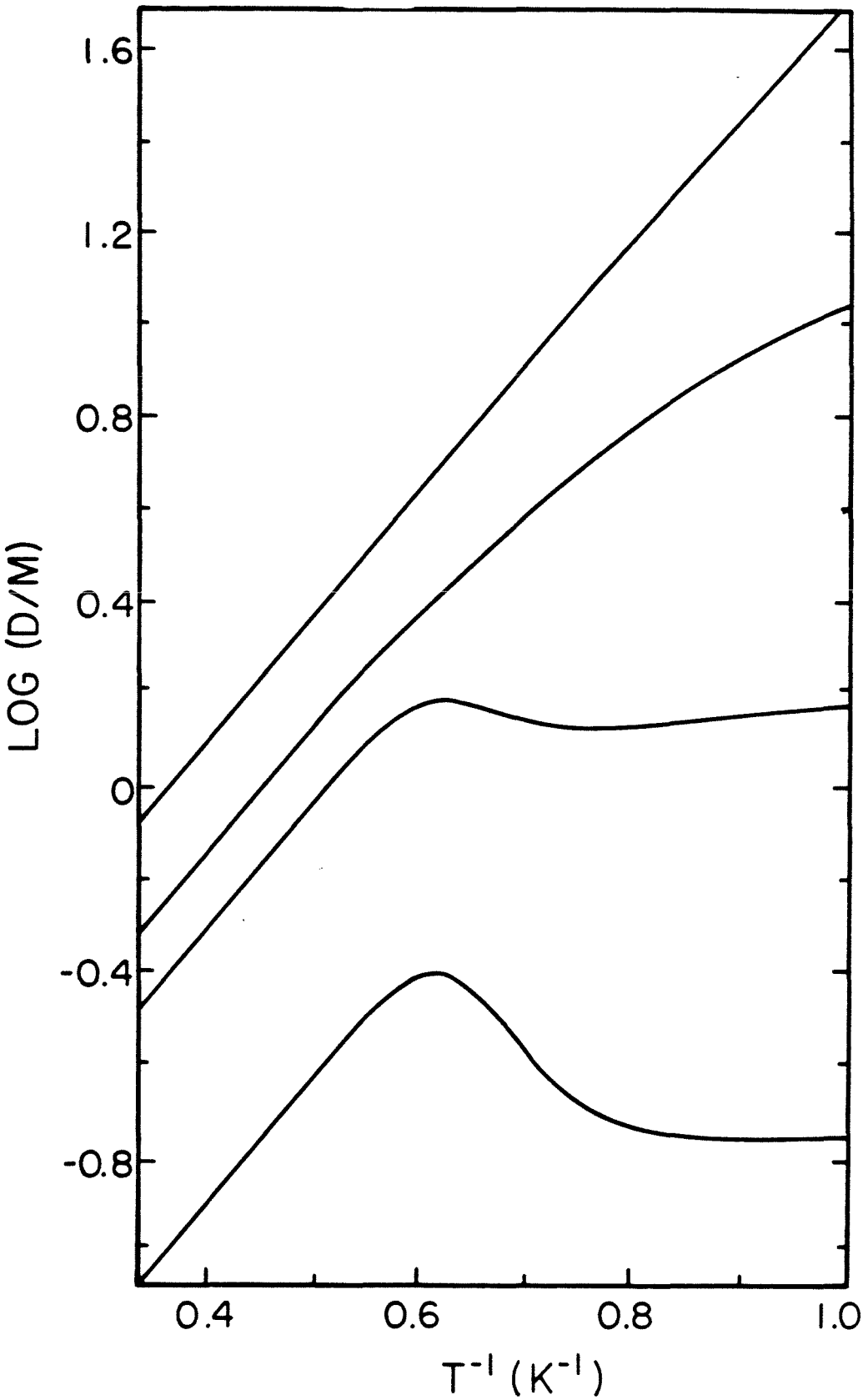
1.6
1.2
0.8
0.4
0
-0.4
-0.8
LOG (D/M)
0.4
0.6
0.8
1.0
T⁻¹ (K⁻¹)

averaged lattice have the same time-average probability of being excited. The claim that $r_{MD} \sim r_{MM}$ is substantiated by a Monte Carlo result of $r_{MM} = 2.1$, $\sigma_{MM} = 1$, $r_{MD} = 2.6$, $\sigma_{MD} = 1$ (all in units of lattice constants) for a 5% doped array [56]. Thus, as the monomer bandwidth increases, so does the monomer-dimer coupling. Recall in the concentration range we are interested in, C_D is much less than C_M (C_D/C_M ranges between 5×10^{-2} and 1×10^{-3}).

Figure 23 shows the theoretical log(D/M) vs 1/T for the same crystals as Fig. 10 (the two figures should be compared closely). Curve E(F) for the 0.5% crystal, represents the limit where monomer-dimer communication through the host band prevails. Indirect communication (illustrated by the results of Fig. 14 on D_s) is frozen out at low temperatures as is evidenced by the plateau for 1/T greater than 0.6 K^{-1} where the D/M ratio is determined by the statistical probabilities of finding the clusters and their feeding and decay rates [Eq. (V.10)]. Experimentally, the plateau is not completely established at 1/T = 0.8 K^{-1}, but it seems reasonable that the asymptotic behavior of theory and experiment will coalesce. Also, for the 0.5% crystal, the high temperature ''bump'' (A of Fig. 23) is predicted (~0.5 K^{-1}) but has yet to be experimentally verified due to the weak signal at high temperatures (bear in mind S/N greater than or equal to 100 is necessary to accurately measure the intensity of weak dimer satellite peak).

The importance of the 0.5% data at low temperatures is that they demonstrate the localized nature of the excitation and the departure from Boltzmann statistics. The usual partition function approach is no longer useful at these concentrations and temperatures. Furthermore, at

these low concentrations and temperatures the rate equations must include trap-''band'' interactions [57], especially in phenazine-type systems where Δ is relatively small.

The 2% crystal demonstrates a low temperature plateau but no bump as predicted theoretically. The plateau for the 2% case cannot be taken to imply ''locality'' of states, however. The physical significance of the lack of a bump in the high concentrated crystals lies primarily in the fact that the monomer and dimer communicate directly. These conclusions were arrived at by detailed inspection of the numerical results used to produce Fig. 23. For the 0.5% crystal at higher temperatures, the monomer indirectly feeds the dimer and to a much smaller extent the dimer feeds the monomer indirectly. The dimer to host detrapping resulting in the ''negative activation energy'' seen in the 0.5%. The plateau is due to freezing out of both channels of communication. The value of D/M at these low concentrations and at $T < 1$ K will be determined by Eq. (V.10).

The extreme nonlinearity of the phonon occupation number at ultralow temperatures is the key to understanding the changes. The monomer detrapping rate changes by 10 orders of magnitude from 1 to 4 K and the dimer changes by 12 orders of magnitude from 1 to 4 K. In the 2% crystal, the dimer is not truly isolated from the monomer (therefore no bump) and the kinetic equations dictate the largest D/M ratio should occur when there is no appreciable dimer to monomer back transfer (i.e., the low temperature plateau) which is jointly a function of the electronic matrix element, phonon occupation number, and final density of states.

For the 3% and 6.6% crystals, the increase in the tunneling matrix element is primarily responsible for the disappearance of the plateau at these temperatures. However, if one calculates D/M for T less than 1 K, one finds that even the 6.6% has an asymptotic temperature-independent value.

Theory predicts that at high temperatures, T > 2 K, the D/M ratio should be Boltzmann-like with an activation energy of 4.4 cm^{-1} for all crystals. This can be seen [from Eq. (V.9)] to occur as a result of direct (high-concentration) or indirect (low-concentration) communication between M and D. As an example, in the strong direct communication limit, equation (v.9) simply yields

$$n_D/n_M \propto e^{\Delta_{MD}/kT}$$

where Δ_{MD} is the monomer-dimer splitting. Note that the above findings are consistent with the results of Fig. 22 (D/M vs C at different temperatures) which reproduce the experimental observations. Further, the measured activation energy indicates that for first order detrapping processes, the dimer (-) state is not likely to be an important intermediate state.

We have thus advanced explanations for the D/M ratio as a function of concentration and temperature. A numerical simulation of the absolute cluster intensities as a function of concentration and temperature was also conducted in order to test the model. It is difficult, however, for the choice of the many parameters to place much certainty on such computation. Nevertheless, we shall make some heuristic

observations on the data.

One can see that for the monomer intensity as a function of temperature (Fig. 13) a trend of decreasing emission with increasing T dominates all samples and is most pronounced for the D_s phenazine crystal. For this ''pure'' D crystal, one has a steep decline in intensity that shows an 18 cm^{-1} activation energy (Fig. 14). The 18 cm^{-1} activation energy is less than the trap depth measured to the lowest available $\underset{\sim}{k} = 0$ state (21 cm^{-1}). This may be understood by noting that quasiresonance interactions create states below the band by several wave numbers [58]. Thus detrapping can occur to lower energy host states. The observed 18 cm^{-1} activation energy also implies that the population lost by detrapping to the host is lost forever to the monomer subsystem. This is intuitive insofar as the average monomer–monomer separation should be so large that transport between monomers via host states is not successful. The 0.5% phenazine crystal is unlike the ''pure'' D_s case in showing much less dependence on temperature, implying that to some extent, indirect monomer–to–monomer transfer [56] occurs and population is not irreversibly lost to the host. Looking at the remainder of the data in Fig. 13, one sees that the monomer system loss rate appears to decrease with increasing guest concentration (up to 2%). However, for a detailed description of the population of the monomer which lies between the band and the dimer, one must know all the direct and indirect communication parameters given in Θ of Eq. (V.8). We feel that a simulation is not useful at this point and only the ratio of M to D can be satisfactorily explained.

For the dimer emission as a function of temperature, the situation

is different (the dimer is the deepest trap under consideration). For the 0.5% phenazine crystal, dimer population increases with increasing temperature over the range 1.0 to 1.2 K (rather than decreasing as the monomer does). This behavior is correctly represented by the rate equations and can be undestood as indirect M to D transfer with little back transfer. The trend may only be exhibited over a narrow temperature range where the dimer detrapping rate is still small in comparison to the monomer detrapping rate and thus presents and ''irreversible'' sink for monomer population. The 2% and 6.6% cases would then represent situations where the dimer to monomer back transfer increases as temperature increases. The dimer and trimer in the 6.6% crystal appear to decrease in a linear fashion with increasing T. This is not explicable by a naive model where the ratio of the dimer feeding rate to dimer decay rate is written as $(\eta + 1)/\eta$. Such a model would predict exponential temperature dependence which is far beyond our error bars, even for a 4.4 cm^{-1} activation energy. In actuality, this behavior reflects the complexity involved in using absolute intensities which require knowledge of Θ. In other words, to describe this linearity quantitatively we must solve the full kinetic equation. As mentioned before, taking the ratio of D/M overcomes this problem.

For DBN, the log(D/M) vs. 1/T plots show the expected trends derived from the phenazine analyses, although we feel one must have more data over a wider temperature range before making quantitative interpretations (this is currently under investigation). It does appear, however, that the D/M ratio is roughly temperature independent for low concentrations and begins to show positive activation energies

for higher concentrations, in accord with direct communication between monomer and dimer.

The ''sluggishness'' of the D/M threshold in DBN with concentration (Fig. 9) is due largely to the smaller exponent for the superexchange coupling which goes as $(C^{-1} - 1)$ for 1-D and $[(0.5/C^{1/2}) - 1]$ for 2-D. As a means of illustrating this point, we have performed a simulation of D/M ratios for the phenazine system parameters, altering only the form of the macroscopic rate constants of Eq. (V.9) to represent a 1-D and 3-D system.

We compute D/M vs. C for the different dimensionalities and compare them in Fig. 24. In altering the rate constants for the 1-D and 3-D cases, one must change the exponent in the superexchange matrix element and the concentration of the final state. We use $\langle n \rangle = (C^{-1} - 1)$ in 1-D and $\langle n \rangle = (0.554\ C^{-3} - 1)$ in 3-D. The final specie concentration in 1-D follows the prescription in Sec. IV and in 3-D we use a simple cubic lattice [coordination number 6, monomer $\propto C(1 - C)^6$ and dimer $\propto C^2(1 - C)^{10}$]. The energy transfer threshold moves to decreasing concentration with increasing dimensionality largely due to the increased probability of finding a nearby impurity at short distance. However, the change in concentration of the final state as a function of dimensionality (at least with the form of rate equations we use) works against the effect of change in the superexchange exponent. That is, an increase in lattice dimensionality (or connectivity) increases the superexchange coupling but reduces final state concentrations due to terms of the form $C^n(1 - C)^h$ (n is the cluster size and h is the number of host molecules on the cluster perimeter, which increases with

Figure 24. Calculation of D/M vs C using the rate equation and parameters used to generate Fig. 22, but with rate constants modified to represent energy transfer for 1-D and 3-D topologies. Note that the energy transfer threshold moves to decreasing concentration with increasing dimensionality. For the 3-D calculation $\langle n \rangle = 0.554/(C)^3 - 1$, $C_m \propto C(1 - C)^6$ and $C_D \propto C^2(1 - C)^{10}$ (for a simple cubic lattice structure). Beyond the energy transfer threshold, $D/M \propto (C_D/C_M)e^{\gamma MD/kT}$ and the crossing of the curves 2-D and 3-D results from the terms of the form $(C_D/C_M) \propto C(1 - C)^4$ in 3-D and in 2-D $(C_D/C_M) \propto C(1 - C)^2$, which are important at higher concentrations.

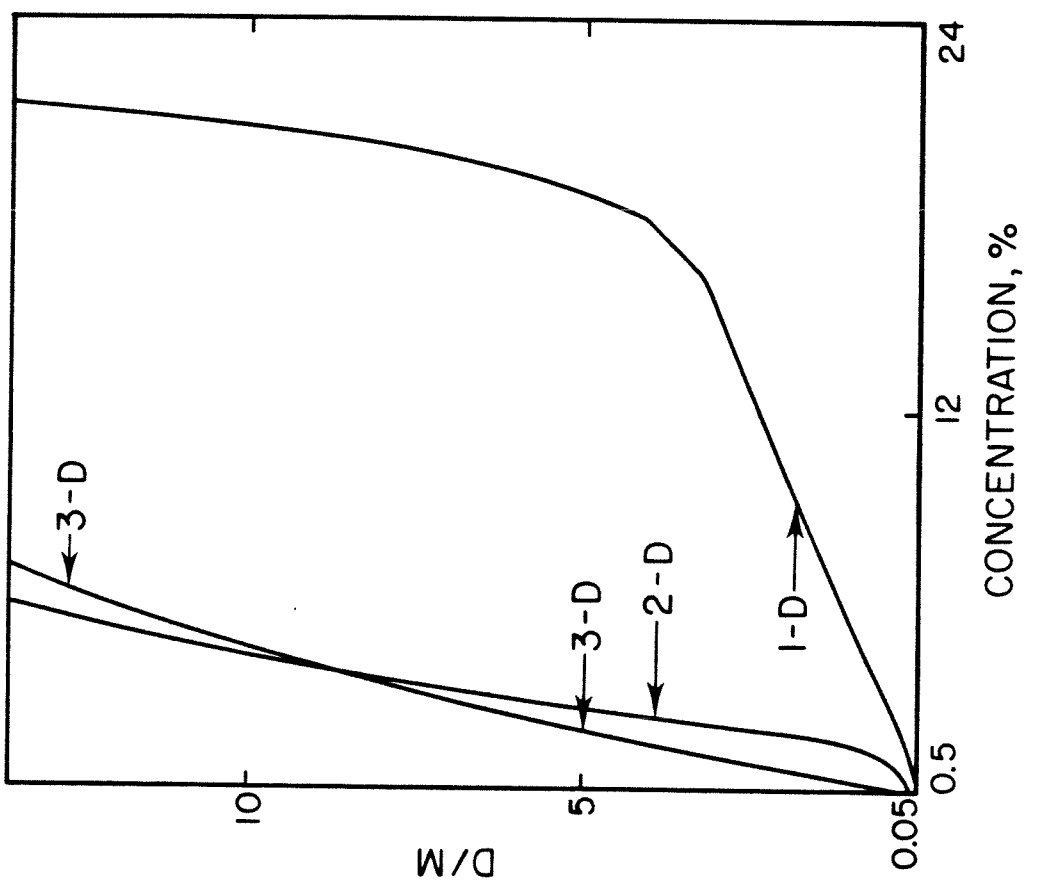
D/M
10
5
0.05
0.5
12
24
CONCENTRATION, %
3-D
3-D
2-D
1-D

dimensionality). The results of Fig. 24 are consistent with the results of ruby, phenazine and DBN.

Two important conclusions can now be drawn. First, the fact that we can fit the results at very low temperatures (no thermal assistance) with an effective tunneling matrix element between M and D indicates that the threshold concentration is most probably the result of this quantum effect. Second, from the parameters used in the simulation, at 5% and 1 K, $\gamma_{DM}\tau$ is 10^3, much larger than 1 (τ is the lifetime). Hence, the threshold is not lifetime limited. At higher temperatures this situation is different simply because of the back transfer discussed before (γ_{MD} at 2 K, 5% is about 8×10^5 sec^{-1}).

VI. SUMMARY AND CONCLUSIONS

We have presented data on isotopically doped phenazine (effective 2-D) and DBN (effective 1-D) concentration and temperature dependent optical emission. By use of an average-lattice rate equation and a numerical simulation of the data we have presented explanations for much of the data. To properly execute the simulation we have performed Monte Carlo calculations on cluster statistics in one and two dimensions and have calculated the eigenstates of relevant clusters.

From the studies made on phenazine and DBN the following conclusions were drawn: (1) Impurity state populations are sensitive to all communication channel rates and the host states must be included to understand the energy transfer dynamics between impurities, especially at low concentrations; (2) The role of the phonon bath

in ''masking'' the threshold at higher temperatures can now be understood; (3) One can understand many of the important processes at hand with a kinetic scheme; and (4) By explicit computation and comparison with experiment (DBN vs phenazine), the important role of dimensionality on threshold behavior is also explainable with the same kinetic model. In phenazine, M-D coupling has exponential turn on with concentration which can be modeled by a continuum particle separation distribution to a first approximation. This continuum averaging scheme, although a severe approximation to the discrete anisotropic lattice, appears to explain the steady-state experiments. In transient experiments this may not be the case [65].

The Boltzmann and non-Boltzmann regimes were delineated and individual trap intensity dependence on temperature and concentration in the 1-D and 2-D systems was experimentally shown and discussed. There are four distinct and limiting cases. In the low-concentration (below the abrupt transition), low temperature case, the dimer and monomer population are proportional to their statistical probabilities of occurrence. In the high-concentration, low-temperature limit, the monomer-to-dimer transfer is ''opened'' by monomer-to-monomer extension followed by trapping into a dimer of which there are fewer present (dimers are outnumbered by a factor of 20-1,000). Thus, in this case the population is nonstatistical in the number of clusters, but is statistical when the concentration is weighted by Boltzmann factors that are indicative of efficient and direct communication among clusters (using phonon absorption and emission). In the high-concentration, high-temperature limit, the back transfer

from D to M (which are in equilibrium due to direct communication) hinders the overall flow of population into the dimer, hence decreasing the ratio of D/M. In the low-concentration, high-temperature limit, indirect transfer again makes the dimer and monomer communicate. Because the monomer-dimer energy splitting is the same as the difference in trap depths of the monomer and dimer, phonon absorption and emission ensures the same ''activation'' energy for the high-concentration, high temperature and low-concentration, high-temperature regimes. Thus, as shown in Fig. 22 and as demonstrated experimentally, D/M vs C exhibits a straight line at high temperatures.

From the work reported here on DBN and phenazine we determined the temperatures at which phonon-assisted processes are negligible, and thus only the intrinsic effects of energy localization or delocalization are observed. Throughout the paper, only single phonon processes are considered at the temperatures of interest [59], and radiative transfer is not included [66].

Finally, we believe that at very low temperatures the monomer ''band'' is extended and wide (~0.1-0.01 cm^{-1}) near the transition. As noted in I, our measurement of w, the inhomogeneous site energy fluctuation (Gaussian distribution) and using Eq. (IV.3) predicts a transition from ''localized'' to ''delocalized'' states at ~ 5% concentration, when using the Klafter-Jortner model of the Anderson transition in the phenazine system. This result is consistent with the findings in Fig. 22, which does not include w explicitly. In other words, we explain essentially all the dynamics using the averaged rate equations approach and invoking the superexchange interaction which

includes the proper concentration exponent. This is one of the important conclusions of this paper. So, the only connection we can make with AT is at very low temperature since our result at 1.17 K is consistent with the KJ model. Experiments are now in progress to elucidate the role of w, especially at higher temperatures.

Note added in proof: Very recently A. Blumen and R. Silbey (private communication of preprint) have considered a simple kinetic scheme. Three things are different. (1) They consider the case of direct population of the monomer and no direct population of the dimer. In our 1977 note (see Ref. 5) and this work we considered the situation where the rates at which the monomer and dimer are populated are both finite. This is because the experiments on phenazine were performed at steady state by pumping the host states and not the monomer alone. (2) They describe the electronic energy transfer using the hopping model of Inokuti and Hirayama (J. Chem. Phys. 43, 1978 (1965)). (3) No host states are included in their model. Due to the omission of the host states it is unlikely that the model of Blumen and Silbey could treat the 0.5% phenazine data properly. At higher concentrations, however, their model fits the data well. As shown in this paper the host states of phenazine play a very important role in the energy transfer process, especially at low concentrations (2%, 0.5%, pure D_s). We believe that the communication channels described in Fig. 21 must be invoked since the trap depth is only 23 cm^{-1} and it is almost impossible to populate the monomer selectively. In contrast to the work reported here, neither our work in Ref. 5 nor the work of Blumen and Silbey have dealt with the effects of detrapping to host states.

REFERENCES

[1] For reviews see: G. W. Robinson, Ann. Rev. Phys. Chem. 21, 429 (1970); R. M. Hochstrasser, Int. Rev. of Science, Phys. Chem. Ser. 2, Vol. 3, edited by D. A. Ramsay (Butterworths, London, 1976).

[2] H. C. Wolf in Adv. At. Mol. Phys. 3, 119 (1967); R. Silbey, Ann. Rev. Phys. Chem. 27, 203 (1976); D. Zwemer and C. B. Harris (to be published).

[3] R. Kopelman, E. M. Monberg, F. Ochs, and P. Prasad, J. Chem. Phys. 62, 292 (1975); R. Kopelman, E.M. Monberg, and F. W. Ochs, Chem. Phys. 19, 413 (1977); 21, 373 (1977); R. Kopelman, E. M. Monberg, F. Ochs, and P. Prasad, Phys. Rev. Lett. 34, 1506 (1975).

[4] (a) S. D. Colson, S. M. George, T. Keyes, and V. Vaida, J. Chem. Phys. 67, 4941 (1977); ibid. 66, 2187 (1977), (b) T. L. Muchnik, R. E. Turner and S. D. Colson, Chem. Phys. Lett. 43, 570 (1976).

[5] D.D. Smith, R.D. Mead, and A.H. Zewail, Chem. Phys. Lett. 50, 358 (1977).

[6] J. Klafter and J. Jortner, Chem. Phys. Lett. 49, 410 (1977); J. Klafter and J. Jortner (to be published).

[7] P.W. Anderson, Phys. Rev. 109 , 1492 (1958).

[8] N.F. Mott, Phil. Mag. 29, 613, (1974); Comm. Phys. 1, 203

(1976).

[9] G.L. Pollack, Rev. Mod. Phys. 41, 48 (1969).

[10] F.H. Herbstein and G.M.J. Schmidt, Acta Cryst. 8, 399 (1955); 8, 406 (1955).

[11] A.H. Zewail, Chem. Phys. Lett. 33, 46 (1975); J.P. Lemaistre and A.H. Zewail, J. Chem. Phys. 72, 1055 (1980).

[12] R.H. Clarke and R.M. Hochstrasser, J. Chem. Phys. 47, 1915 (1967).

[13] J. Trotter, Can. J. Chem. 39, 1574 (1961).

[14] R.M. Hochstrasser and J.D. Whiteman, J. Chem. Phys. 56, 5945 (1972).

[15] R.M. Hochstrasser and A.H. Zewail, Chem. Phys. 4, 142 (1974).

[16] We have recently observed these and additional new lines as Raman scattering in time resolved laser experiments; unpublished results from this laboratory.

[17] T.G. Pavlopoulos, J. Chem. Phys. 51, 2936 (1969).

[18] S. Califano, J. Chem. Phys. 36, 903 (1962)

[19] A.H. Zewail, Chem. Phys. Lett. 29, 630 (1974).

[20] In DBN the D/M ratio in the 0,0 relative to 0, v is different from the phenazine case. This may be due to the extent to

which vibrational energy delocalization in the two cases occurs.

[21] L.A. Rebane and P.M. Saari, Sov. Phys. Sol. St. 12, 1547 (1971); S. Colson, Chem. Phys. Lett. 44, 431 (1976).

[22] J. Ph. Grivet and J.M. Lhoste, Chem. Phys. Lett. 3, 445 (1969).

[23] K.P. Dinse and C.J. Wincom, J. Chem. Phys. 68, 1337 (1978).

[24] R.B. McQuistan, J. Math. Phys. 12, 2113 (1971).

[25] D. Stauffer, J. Stat. Phys. 18, 125 (1978).

[26] P.L. Leath, Phys. Rev. B 14, 5046 (1976).

[27] M.E. Fisher and J.W. Essam, J. Math. Phys. 2, 609 (1961).

[28] (a) J.P. Lemaistre, Ph. Pee, R. Lalanne, F. Dupuy, Ph. Kottis, and H. Port, Chem. Phys. 28, 407 (1978). A private communication with J. Lemaistre revealed that their figure was in error and one should see Ph. Pee, R. Brown, F. Dupuy, Ph. Kottis, J.P. Lemaistre, Chem. Phys. 35, 429 (1978), (b) J. Hoshen and R. Kopelman, Phys. Rev. B. 14, 3438 (1976).

[29] E.N. Economou and M.H. Cohen, Phys. Rev. B 4, 396 (1971); 5, 293 (1972); Mat. Res. Bull. 5, 577 (1970).

[30] G. Theodorou and M. H. Cohen (preprint); E.N. Economou and M.H. Cohen, Phys. Rev. B 4, 396 (1971); Phys. Rev. Lett. 25, 1445

(1970).

[31] J. Koo, L.K. Walker, and S. Geschwind, Phys. Rev. Lett. 35, 1669 (1975); C. Hsu and R.C. Powell, ibid. 35, 734 (1975).

[32] E.N. Economou and M.H. Cohen, Phys. Rev. B 5, 2931 (1972); Phys. Rev. Lett. 25, 1445 (1970).

[33] S.R. Broadbent and J.M. Hammersley, Proc. Camb. Phil. Soc. 53, 629 (1957).

[34] S. Kirkpatrick, Rev. Mod. Phys. 45, 574 (1973); V.K.S. Shante and S. Kirkpatrick, Adv. Phys. 20, 325 (1971).

[35] E. Monberg and R. Kopelman, Chem. Phys. Lett. (to be published).

[36] J. Heinrichs, Phys. Rev. B 16, 4365 (1977); D. Wearie and A.R. Williams, J. Phys. C 10, 1239 (1977)

[37] H. Hong and R. Kopelman, J. Chem. Phys. 55, 724 (1971).

[38] A. Ralston and H. Wilf, Mathematical Methods for Digital Computers, Vol. II (Wiley, New York, 1967).

[39] For phenazine the Davydov splitting of H_s and D_s is the same implying the same β. For DBN we can fit all the aggregate SP spectra using nearest neighbor approximation, justifying the short range nature of the interaction.

[40] P. Hertz, Math. Ann. 67, 387 (109).

[41] S. Chandrasekhar, Rev. Mod. Phys. 15, 1 (1943).

[42] G.C. Nieman and G.W. Robinson, J. Chem. Phys. 37, 2150 (1962).

[43] D.A. Zwemer and C.B. Harris, J. Chem. Phys. 68, 2184 (1978).

[44] M.T. Lewellyn, A.H. Zewail, and C.B. Harris, J. Chem. Phys. 63, 3687 (1975).

[45] M.H. Cohen, private communication.

[46] W. Grant, Phys. Rev. B 4, 648 (1971); D.L. Huber, D.S. Hamilton, and B. Barnett, Phys. Rev. B 16, 4642 (1971); D.S. Hamilton, P.M. Selzer, and W.M. Yen, Phys. Rev. B 16, 1858 (1977); F. Fong and D.H. Diestler, J. Chem. Phys. 56, 2875 (1972); V.P. Sakun, Sov. Phys. Solid State 14, 1906 (1973); S. Haan and R. Zwanzig, J. Chem. Phys. 68, 1879 (1978); G.W. Robinson (unpublished results); J.A. Altmann, G. Beddard, and G. Porter, Chem. Phys. Lett. 58, 54 (1978); M.J. Schaffman and M. Silver (preprint); J.P. Lemaistre, Ph. Pee, R. Lalanne, F. Dupuy, Ph. Kottis, and H. Port, Chem. Phys. 28, 407 (1978).

[47] J. Bernasconi, S. Alexander, and R. Orbach, Phys. Rev. B. 17, 4311 (1978); see also D.D. Dlott, M.D. Fayer, and R.D. Wieting, J. Chem. Phys. 67, 3808 (1977).

[48] A. Szabo, Phys. Rev. Lett. 25, 924 (1970); 27, 323 (1971). L.A. Riseberg, Phys. Rev. A 7, 671 (1973); D.L. Huber,

D.S. Hamilton, and B. Barnett, Phys. Rev. B 16, 4642 (1977); D.S. Hamilton, P.M. Selzer, and W.M. Yen, Phys. Rev. B 16, 1858 (1977).

[49] T. Holstein, S.K. Lyo, and R. Orbach, Phys. Rev. Lett. 36, 891 (1976); T. Holstein, S.K. Lyo, and R. Orbach, Comments on Solid State Phys. (to be published).

[50] Electron-phonon coupling is usually used to refer to the interaction between localized excitation on molecules and phonons (even though there is no free elctron).

[51] A.S. Davydov, Theory of Molecular Excitons (Plenum, New York, 1971).

[52] D.P. Craig and L.A. Dissado, Chem. Phys. Lett. 44, 419 (1976); Chem. Phys. 14, 89 (1976).

[53] D. Smith, D. Millar, and A. Zewail, unpublished results.

[54] R.M. Hochstrasser and P.N. Prasad, J. Chem. Phys. 56, 2814 (1972).

[55] The $\partial V/\partial R$ term represents a ''distortion'' in the lattice which results in the absorption or emission of phonons, hence a transition amongst crystal states (trapping and detrapping). For H-M and H-D the coupling term Ω is given in terms of $\partial V/\partial R$ (and possibly the higher order derivatives) in addition to the single jump resonance interaction matrix element between H and M or D. For D-M, Ω contains the effective electronic coupling matrix elements, which

depend on concentration, and the distortion terms, i.e., $\partial V/\partial R$, that will lead into phonon absorption and emission between the monomer and the dimer.

[56] There is a simple physical picture for the average impurity sublattice and it is as follows. Construct a 2-D net with lattice constant $\langle r_{MM} \rangle = 0.5C^{-1/2}$, placing monomers at every corner. Then replace approximately C of the monomers by dimers. Alternatively, superimpose a dimer impurity net with lattice constant $0.5C^{-1}$ which gives a ratio of areas covered by the dimer relative to the monomer of C^{-1} (which is what one expects since the ratio of TE dimers to monomers is $C^2(1 - C)^8/C(1 - C)^6 \sim C$ for low C). One can see two things; (a) for low C, most monomers will not be near a dimer, and (b) as one increases the concentration, the monomer net shrinks but the dimer net shrinks faster. Thus, for a monomer not near a dimer, fewer m-m steps are required to reach a dimer with increasing concentration (the shrinking net effect is contained in the rate equations' density of states). Further, one should note that the monomer-monomer transfer is probably more efficient than monomer-dimer transfer [65] much as in the case of ruby (G.F. Imbusch, Phys. Rev. 153, 326 (1967)). Note that $\langle r_{MM} \rangle \sim 5$ lattice constants for 1% in contrast to 2.2 lattice constants for the 5% crystal.

[57] M.D. Fayer and C.B. Harris, Phys. Rev. B 9, 748 (1974).

[58] In addition to the host-guest mixing which produces levels below the host band, partially deuterated species (unavoidably

present in relatively low concentrations) will have lower energy than that of the perduetero host. For example, in phenazine there is a detectable ~ 17% D_7 and ~ 3% D_6 (Table I). If the isotopic energy shift is roughly (δ = 2.6 cm^{-1}) per deuterium, then the D_6 will be 5.2 cm^{-1} below the lowest k = 0 level. Thus, a trap depths for D_6 and D_7 from the H_8 monomer are simply 16 and 18.5 cm^{-1}, respectively. Note that the sample does not contain detectable amounts of D_5, D_4, D_3, D_2, or D_1.

[59] Multiphonon processes, although of lower probability than single phonon processes, may dominate, especially when the density of phonon states is low at the one-phonon energy and the ''coherence'' lengths, λ_c, of the phonon is much larger than the spatial separation of the imputities, with energy mismatch Δ. The former, density of states (and population), depends on Δ and the temperature. The latter, λ_c, depends on the velocity of sound (v) in the crystal; $\lambda_c = hv\Delta^{-1}$. Thus, if λ_c exceeds the separation between, say, the monomer and dimer, then the two impurities will be phonon-modulated to the same extent and the single phonon process becomes inefficient. For DBN, e.g., taking v = 1 x 10^5 cm/sec and Δ = 5.5 cm^{-1}, we obtain λ_c = 60 Å. At 5% concenration, the separation of $\underset{\sim}{c}$ axis impurities is roughly 80 Å. Thus, single phonons may efficiently assist the transfer. As Δ gets smaller or the concentration gets higher, one expects that this criterion becomes less applicable.

[60] A. Burns and C. B. Harris (unpublished results; private communication). These authors have found from the heat capacity measurement on 1,2,4,5-tetrachlorobenzene crystals at 1.4-2.2 K that

the Debye temperature is 81 K (52 cm^{-1}) and hence v = 1.58 x 10^5 cm/sec.

[61] I. Guttman, S. Wilks, and J.S. Hunter, Introductory Engineering Statistics, (Wiley, New York, 1971).

[62] M.F. Sykes and M. Glen, J. Phys. A 9, 87 (1976) and references therein.

[63] L.J. Noe, E.O. Degenkolb, and P.M. Rentzepis, J. Chem. Phys. 68, 4435 (1978).

[64] U. Doberer, Diplomarbeit, University of Stuttgart, Stuttgart, Germany (1978).

[65] D. Smith, R. Powell, and A.H. Zewail, Chem. Phys. Lett. (in press).

[66] Phenazine, in contrast to DBN, has a smaller oscillator strength, such that no radiative self-absorption effects were seen when comparing emission of the (0,0) and vibronic transitions.

CHAPTER II.

LINE NARROWING LASER SPECTROSCOPY IN DISORDERED QUASI-ONE DIMENSIONAL 1,4-DIBROMONAPHTHALENE CRYSTALS: MOBILITY EDGES?*

---

*D. D. Smith, R. C. Powell and A. H. Zewail, Chem. Phys. Lett. 68 (1979) 309.

ABSTRACT

Presented are measurements of excitation transport in quasi-one dimensional 1,4-dibromonaphthalene (DBN) using time-resolved laser spectroscopy. Energy migration as a function of temperature and dopant concentration in isotopically disordered DBN is describable in terms of step-wise incoherent transfer using a 1-D sampling function. The data indicate the effect of a superexchange interaction between the impurity clusters and no mobility edges in the inhomogeneously broadened trap profile. It is proposed that there will be no mobility edges in cases where superexchange dominates the transfer Hamiltonian.

I. INTRODUCTION

A great deal of theoretical and experimental effort has been put forth to understand trap-trap energy transfer in doped molecular [1a] and ionic crystals [1b], but only in the past few years have any data on time and spectrally resolved energy transfer become available. It has become a loose generalization to refer to these studies as dealing with impurity band transport (although $\underset{\sim}{k}$ is no longer a good quantum number) since the band picture is a convenient vehicle for description. Concepts such as the Anderson transition, mobility edges, spectral vs. spatial transfer, coherent tunneling, etc., are all unique to the impurity band, and the author hastens to add, still quite topical. The experiments described herein are direct time resolved measurements of electronic energy transfer between traps in lightly and heavily doped DBN. Since the

experiments deal with low lying electronic triplet states, the excitation is long lived and the transfer Hamiltonian is moderately ''weak'', resulting in slow tunneling times. (The energy transfer is not, in the strictest Quantum Mechanical sense, tunneling since superexchange coupling between the traps is mediated by mixing of the host and guest wavefunctions and is not tunneling through a potential barrier.) To the author's knowledge, the 1-D studies we report are unique in that all relevant spectroscopic parameters are well known and one can perform ab initio calculations of the energy transfer rates, finding good agreement with the data.

II. EXPERIMENTAL PROCEDURE

Details on the time-dependent measurements are presented in Chapter III. A picture of the apparatus is shown in Fig. 1.

II. EXPERIMENTAL RESULTS

DBN was chosen because the interaction between molecules is short range and the disorder can be ''controlled'' by doping DBN-H_6 with DBN-D_6, thus forming barriers in the crystal. In the limit of heavy disorder, we find that the transport of DBN-H_6 triplet excitation and effective dimensionality can be described by (a) a sampling function with time-dependent ($t^{-1/2}$) energy-transfer rate, and (b) a 1-D configuration-weighted average superexchange matrix element and (c) there is no evidence of a mobility edge if superexchange is the dominant transfer Hamiltonian.

The crystals were grown by Bridgman techniques using zone

Figure 1. A functional block diagram of the experimental set-up used for low-temperature time-resolved laser spectroscopy. In some cases, where high accuracy was required, an optical delay line for the laser was set up to compensate for the electronic delay.

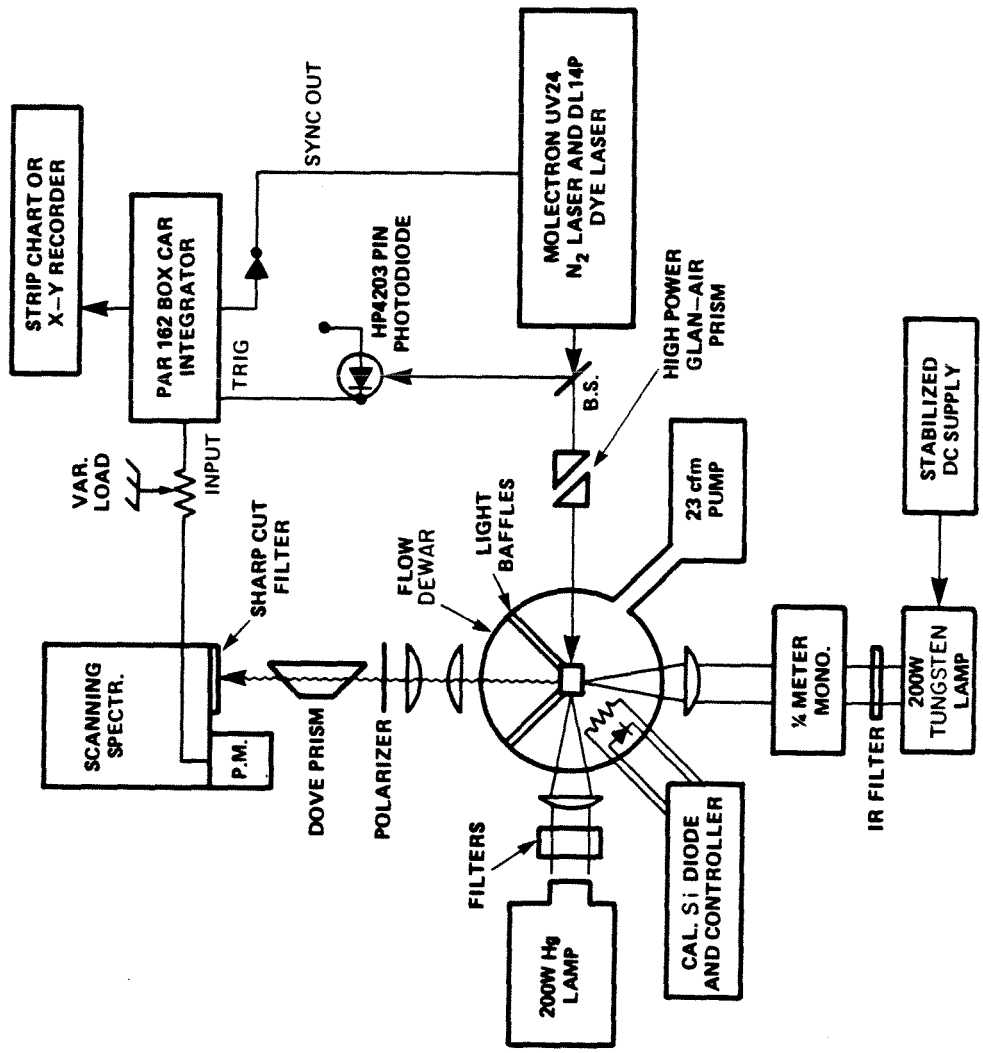
STRIP CHART OR X–Y RECORDER
PAR 162 BOX CAR INTEGRATOR
SYNC OUT
MOLECTRON UV24 N_2 LASER AND DL14P DYE LASER
HP4203 PIN PHOTODIODE
TRIG
B.S.
HIGH POWER GLAN–AIR PRISM
VAR. LOAD
INPUT
SHARP CUT FILTER
FLOW DEWAR
LIGHT BAFFLES
23 cfm PUMP
STABILIZED DC SUPPLY
SCANNING SPECTR.
P.M.
DOVE PRISM
POLARIZER
¾ METER MONO.
200W TUNGSTEN LAMP
IR FILTER
FILTERS
200W Hg LAMP
CAL. Si DIODE AND CONTROLLER

refined starting material. Samples were investigated with concentrations, C, of 0.1, 4.8, 8.2, 11.9, and 24.1% H_6 in DBN-D_6. Though the electronic properties of crystalline DBN were discussed in the previous chapter, we shall briefly review the important facts. The molecules align themselves in linear chains [2] with in-chain coupling ($\beta = -6.2$ cm^{-1}) several orders of magnitude larger than cross-chain coupling ($|\beta'| < 0.01$ cm^{-1}) [2,3]. Isolated protonated molecules (monomers) have a trap depth, Δ, of 65 cm^{-1} from the fully deuterated molecules. In-chain H_6 dimers have a triplet state 5.5 cm^{-1} below the monomer. We assume random substitution of D_6 by H_6 and statistically predict the probabilities of each of the n-mers. These statistics have been derived and correlate well with recent steady-state experiments [4] that indicated monomer-to-dimer transfer occurs in samples with $C \geq 11.9\%$.

A typical set of spectra is shown in Fig. 2. As time increases, the dimer emission increases relative to the monomer. Fig. 3 plots the time-dependent dimer-to-monomer phosphorescence intensity ratio for several samples at temperatures of 1.3, 1.8, and 4.2 K. At all three temperatures, the 11.9% and 24.1% samples exhibit time-dependent ratios, while in the lightly doped samples time dependence can be detected only at the highest temperature. In the lightly doped samples, the monomer and dimer lifetimes were found to be of the order of ~4 msec and independent of temperature from 1.3 to 4.2 K (more accurate measurements are available from ODMR studies and show that the dimer lifetime is very close to being half of the monomer lifetime).

Figure 2. Moderate resolution time resolved spectrum for 11.9% H_6/D_6 DBN at 1.3 K.

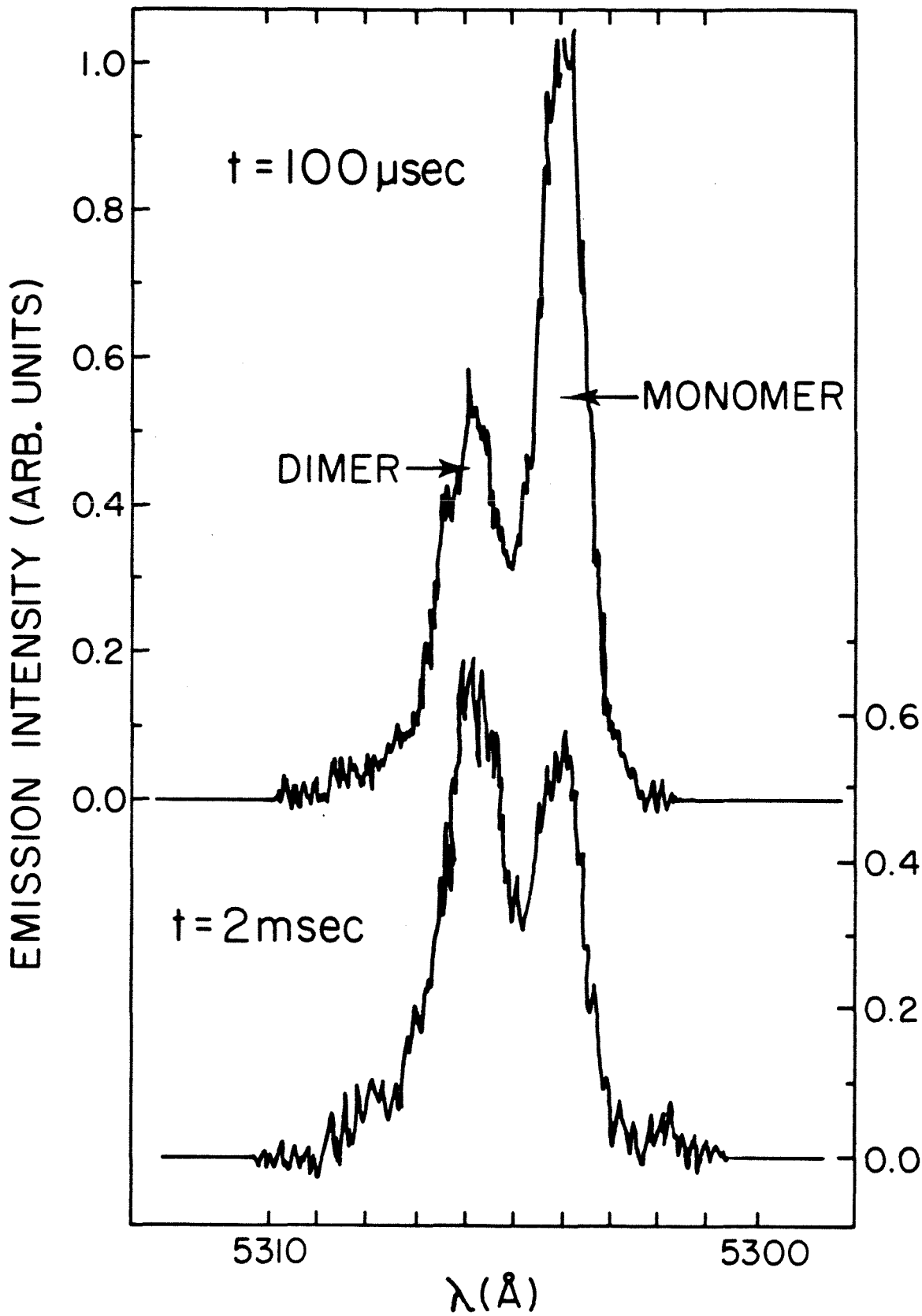
t = 100 μsec
t = 2 msec
DIMER
MONOMER
EMISSION INTENSITY (ARB. UNITS)
1.0
0.8
0.6
0.4
0.2
0.0
0.6
0.4
0.2
0.0
5310
5300
λ(Å)

Figure 3. Computer fit (solid lines) of the experimental (squares, triangles and circles) D/M for pumping the center of the monomer [(a), (b) and (c)] and the dimer (d).

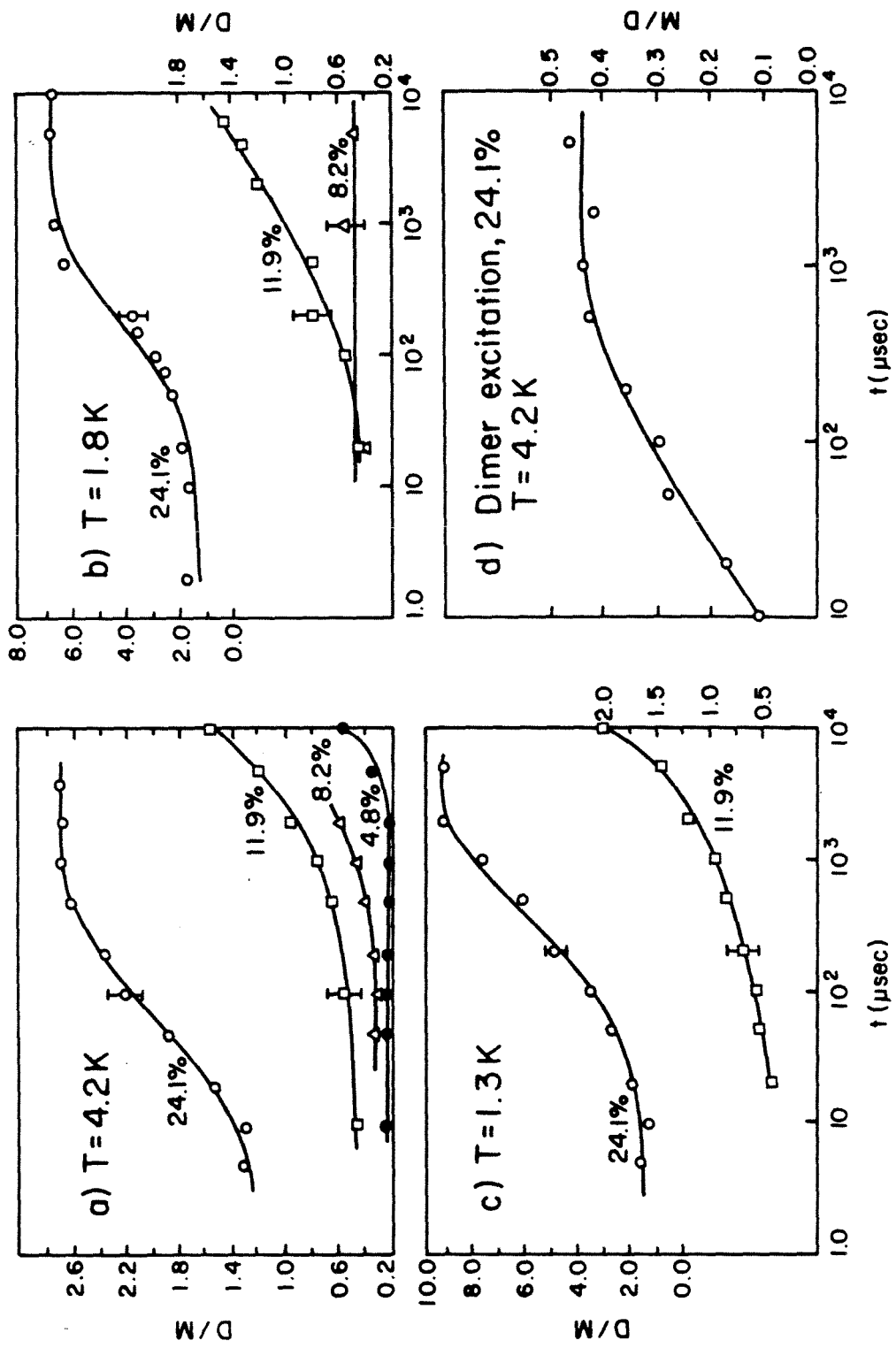
a) T=4.2K
24.1%
11.9%
8.2%
4.8%
b) T=1.8K
24.1%
11.9%
8.2%
c) T=1.3K
24.1%
11.9%
d) Dimer excitation, 24.1%
T=4.2K
D/M
M/D
t (μsec)

IV. THEORETICAL INTERPRETATION

The model used to interpret the data is as follows. The number of excited monomers and dimers are denoted by n_m and n_d and the rates of direct pumping of these states by the laser are P_m and P_d. the intrinsic decay rates of the monomers and dimers are given by γ_m and γ_d. The energy-transfer rate from d-to-m is ω_{dm} and the m-to-d rate is ω_{md}. The linearized rate equations for the populations of the excited states are therefore given by

$$(1) \quad \dot{n}_m(t) = -(\gamma_m + \omega_{md})n_m(t) + \omega_{dm}n_d(t) + P_m$$

$$(2) \quad \dot{n}_d(t) = -(\gamma_d + \omega_{dm})n_d(t) + \omega_{md}n_m(t) + P_d.$$

In order to solve these equations, one must know, a priori, the time dependences of the energy transfer rates. Neglecting correlated motion, excitation migration among the monomers, with the eventuality of being trapped at a dimer, may be describable as a random walk. In such case, the energy-transfer rate can be expressed in terms of the rate at which sites are sampled in the random walk [6]: $\omega_{md} = C_d\dot{S}(t)$ where C_d is the fraction of dimers and $S(t)$ is the so-called sampling function. In the limit of many steps and uniform step time, $\dot{S}(t)$ has the asymptotic form [7] $\dot{S}_{1-D} \sim (2/\pi\tau)^{1/2} + \ldots$ where τ is the mean hopping time. The leading term in the transfer rate becomes $\omega_{md} = C_d(2/\tau t\pi)^{1/2} = \omega t^{-1/2}$, with $\omega = C_d(2/\tau t\pi)^{1/2}$.

Thus with the rate ω_{md} from $\dot{S}(t)$ and postulating a $t^{-1/2}$ rate for

ω_{dm}, one can solve the system of differential equations (1) and (2) to determine $n_d(t)/n_m(t)$. In obtaining an exact solution, we assume delta function excitation (valid for time scales herein) and set the dominant monomer and dimer decay rates equal to one another, as observed experimentally. However, in order to perform an unbiased test, we have fit the data to models with (a) ω_{md} and $\omega_{dm} \propto t^{-1/2}$, (b) ω_{md} and ω_{dm} = constants, (c) $\omega_{md} \propto t^{-1/2}$, ω_{dm} = constant and (d) ω_{md} = a constant + a term proportional to $t^{-1/2}$ and $\omega_{dm} = 0$. (The solutions to the differential equations are presented in Appendix V.) The solution with both rates time dependent produces good fits with the smallest errors for the monomer and dimer pumping experiments (24.1%). For C $\leq$ 11.9%, models with or without back-transfer ($\omega_{dm} = 0$) give similar forward transfer rates (ω_{md}). Further, allowing ω_{md} to be equal to a constant + a $t^{-1/2}$ term, the fits clearly favor the time-dependent rate. It is worthwhile to note that fitting our data with $\omega_{md} \propto t^{-1/2}$ and ω_{dm} = constant does not change the value of the extrapolated rate constants beyond fitting errors, but the fits have larger errors due to the larger number of parameters. One will know the exact time-dependence when the narrow-band excitation (transient experiments with very high S/N) is complete, and more accurate tests of the model become available.

The solution for $n_d(t)/n_m(t)$ with both rates proportional to $t^{-1/2}$ predicts the observed intensity ratio to be

$$(3)\quad D/M = (\gamma_d^r \omega/\gamma_m^r \omega' R)\ \left[\frac{1+R-(1-R\omega'/\omega)\exp[-2(\omega+\omega')t^{1/2}]}{[1+R^{-1}+(\omega/\omega' R-1)\exp[-2(\omega+\omega')t^{1/2}]}\right.$$

where ω' is the d-to-m transfer rate parameter and $R = n_d(0)/n_m(0)$ is the initial condition for direct pumping of monomers and dimers. A nonlinear regression determined the best fit of eq. (3) to the data, treating $n_d(0)/n_m(0)$, ω and ω' as adjustable. The fits are shown in figure 2 and the parameters are listed in Table I.

We wish to calculate theoretical values for the rate parameter ω. For the m-to-d transfer we treat all n-mers with $n \geq 2$ as identical traps for the monomer excitation. For C_d one then has the statistical prediction $C_d = (C^2 + C^3 + ...)(1-C^2)^2$ [4]. In measuring the 'dimer' emission intensity from the data, we therefore include the contribution of the larger aggregates' emission.

Since the monomers are weakly coupled (as we shall demonstrate), the golden rule dictates the excitation hopping time to be

$$\tau^{-1} = [(2\pi)^2/h]|J|^2\rho_f$$

where ρ_f is the final density of states and J is the matrix element of the interaction causing the hop. If the homogeneous width, ω_{hom} is such that $\omega_{hom} > J$, the motion is incoherent and one must use the golden rule, not the inverse coupling time. For this type of system it has been proposed [8] that superexchange between two isolated impurities separated by n hosts is the transfer mechanism. Thus, $J = \xi\beta(\beta/\Delta)^n$, where ξ represents the effect of the number of paths (equal to <u>one</u> in 1-D), the Franck-Condon factors between

TABLE II

DBN ENERGY TRANSFER PARAMETERS FROM COMPUTER FIT OF DATA TO EQ. (3) [a]

Concentration h_6/d_6, %	T K	$\left[\frac{n_d(0)}{n_m(0)}\right]_{exp}$	ω_{exp} $sec^{-\frac{1}{2}}$	ω'_{exp} $sec^{-\frac{1}{2}}$	$\langle J_{mm} \rangle$ cm^{-1}	$\omega(\langle J_{mm} \rangle)$ [b] $sec^{-\frac{1}{2}}$	$\langle n \rangle$	$J(\langle n \rangle)$ cm^{-1}	$\omega(\langle n \rangle)$ $sec^{-\frac{1}{2}}$
24.1	1.3	1.14±.35	47.±8.	5.1±1.1					
	1.8	.9±.4	54.±13.	7.8±2.1					
	4.2	.9±.1	63.±11.	24.±4.4	.23	60.0	2.98	$5.6X10^{-3}$	121
11.9	1.3	.43±.07	6.3±2.	2.2±1.6					
	1.8	.35±.14	12.±5.	7.9±5.					
	4.2	.44±.03	3.8±.3	.95±.3	.14	10.3	5.1	$3.8X10^{-5}$	0.2
8.2 [c]	4.2	.24±.03	2.6±.6	——	.10	3.6	7.1	$3.4X10^{-7}$	10^{-3}
4.8 [c]	4.2	.16±.05	1.2±.4	——	.05	0.6	11.7	$6.8X10^{-12}$	$7X10^{-9}$

[a] The calculated errors are 85% confidence limits; [b] $\chi = 1.2X10^{-2}$; [c] fit to eq. (3) with $\omega_{dm}=0$.

impurities and host states and possible necessity of phonon emission or absorption (the principal shortcoming of the sampling function for applications such as the DBN case is that it does not include the effects of off-resonance coupling or dispersion in the intercluster separations). Put another way, the last step upon which the excitation is trapped may require a different rate constant than the monomer-monomer steps. Furthermore in a more exact treatment, the possibility of regenerating the random walk by detrapping from the dimer should be included. That is a random walk with trapping and biased regeneration, since once in the neighborhood of the dimer, trapping will occur more rapidly.

The density of final states is approximated from Lorentzian lineshapes, i.e. $(2\pi hc\omega_{hom})^{-1}$. Although ω_{hom} has not yet been measured for DBN traps, a sensible estimate is 0.5 cm^{-1} measured for pure crystals [2a, 2n, 9]. One thus finds

$$(4)\quad \langle\omega_{md}\rangle = [2\xi C_d, \beta(\beta/\Delta)^{n}\rangle(c/\omega_{hom})^{1/2}]t^{-1/2}.$$

One now needs the ensemble-averaged J, for which we have performed a 10^5 site linear chain Monte Carlo calculation [10]. An appropriate 1-D random array is generated and the distribution of m-m and m-d separations is measured. $\langle J_{mm}\rangle$ and $\langle J_{md}\rangle$ are calculated as the configuration weighted average of all observed J's. The $\langle J_{mm}\rangle$ are summarized in Table I.

For 4.8% DBN, $\langle J\rangle$ calculated with a weighted average differs by 10^{-10} from $\langle J\rangle$ calculated by $\beta(\beta/\Delta)^{\langle n\rangle}$, using $\langle n\rangle$ from the same

Monte Carlo run. Using the Monte Carlo $\langle J_{mm} \rangle$ and the known spectral paramters, one can predict the forward-transfer rate from eq. (4). The results are in Table I. With $\xi=1.2 \times 10^{-2}$, the predictions agree quite well with the observations. Note that predictions using $\omega(\langle n \rangle)$ are poor, supporting our analysis of superexchange.

The agreement between theory and experiment becomes slightly worse for concentrations. This is as one might expect if for dilute samples, the transport had increasing amounts of 3-D character (e.g. $\langle J_{mm} \rangle$ for a 4.8% chain is 0.053 cm^{-1}, comparable to the interchain J). This can be seen qualitatively from continuum models which show the 1-D coupling to be a steeper function of C than the 3-D coupling. However, before relative contributions of 3-D and 1-D transport topologies [11] (as a function of concentration and superexchange anisotropy) can be quantified, the homogeneous line widths and D/M for times shorter and longer than those investigated here must be probed.

Thus, in short form, the data were modeled the following way. One first calculates the ensemble-averaged impurity to impurity hop time, giving a microscopic rate. Then one calculates the macroscopic m-to-d rate constant by using the sampling function whose sole input is the ensemble averaged coupling matrix element.

Since the relevant spectroscopic constants for DBN are known from experiment, we have calculated, in an <u>ab initio</u> manner, the configurationally averaged coupling with no adjustable parameters. If the backtransfer is zero, as in the dilute samples, there is but

one adjustable parameter, ξ, in the fits. Indeed, ξ yielded by the fits is very reasonable (~0.01) for the known DBN molecular properties, albeit not known exactly. Where there is backtransfer, there are two adjustable parameters in the fits. However, whether or not there was backtransfer, the fitted forward transfer rate concentration dependence followed theoretical prediction to within Monte Carlo and experimental error. The fact that (a) the theoretical and experimental transfer rates scaled similarly, (b) the fitting errors were small, and (c) the same final parameter set was obtained for widely varying initial guesses supports the self-consistency of the procedure and to some extent, the uniqueness of the fits.

It is very important to mention the methods used to calculate the ensemble average superexchange coupling between monomers. In the first method used, <u>all</u> m-m coupling energies were counted and the first moment of the resulting distribution was calculated. By all, it is meant that if a monomer is bounded by monomers on the left and the right which are unequal distances away, both the weak and the strong couplings are recorded. For the second method used to calculate the configurationally weighted coupling, only the weakest of the two couplings would be recorded. In the third method, the stronger of the couplings would be recorded. The outcome was somewhat surprising in that the three methods gave very similar results. The similarity is understandable when one considers that for these experiments, one is dealing with heavy disorder (12 to 24%) and the anticipated fluctuations in inter-impurity distances (even from a continuum model)

is small. This is an important point since in systems where the transport threshold occurs at much lower concentrations, the dispersion in coupling energies is large and the analysis promulgated by Orbach and coworkers would be most appropriate. Their analysis assumes that in the steps among the traps to reach the supertrap, the slowest step will be crucial in determining the observed macroscopic rate. However, for heavily disordered DBN, it is clear that our analysis is able to explain the data.

V. Trap depth dependence of the energy transfer rate: Mobility edges?

For the 11.9% sample at 1.3K, we have investigated m-to-d transfer as a function of the position of the laser pump within the inhomogeneously broadened monomer line (see Fig. 4). The experimental ω has a Δ^{-2} trap depth dependence. If there were few hops or hops occurred at uniform Δ, then a simplified treatment of the Monte Carlo $\langle J_{mm} \rangle = 0.138\ cm^{-1}$ would predict a $\Delta^{-1.6}$ dependence, which is within expected error. Two things are significant about the Δ dependence. First, the experiments are consistent with a superexchange Hamiltonian for impurity-impurity coupling with a clear Δ-dependence at fixed n. Second, the transfer rate is a decreasing function of Δ and no mobility edges were observed. It may be that a different concentration would show mobility edges or homogeneous broadening serves to obscure it. But on the basis of the available data, it is reasonable to propose that there will be no mobility edges if the superexchange dominates the transfer Hamiltonian. This can be simply and intuitively supported. The reason for localized states in the wings of the inhomogeneously

Figure 4. The trap depth dependence of the energy transfer rate coefficient, ω (from two points in time with $\omega' = 0$) for 11.9% H/D DBN at 1.3 K. A high resolution spectrum is shown to indicate the laser position within the inhomogeneous monomer line. The peak at 20,210.5 cm^{-1} is probably due to a double monomer (see ref. [4]). The Δ^{-2} dependence of ω appears linear due to the small range of Δ.

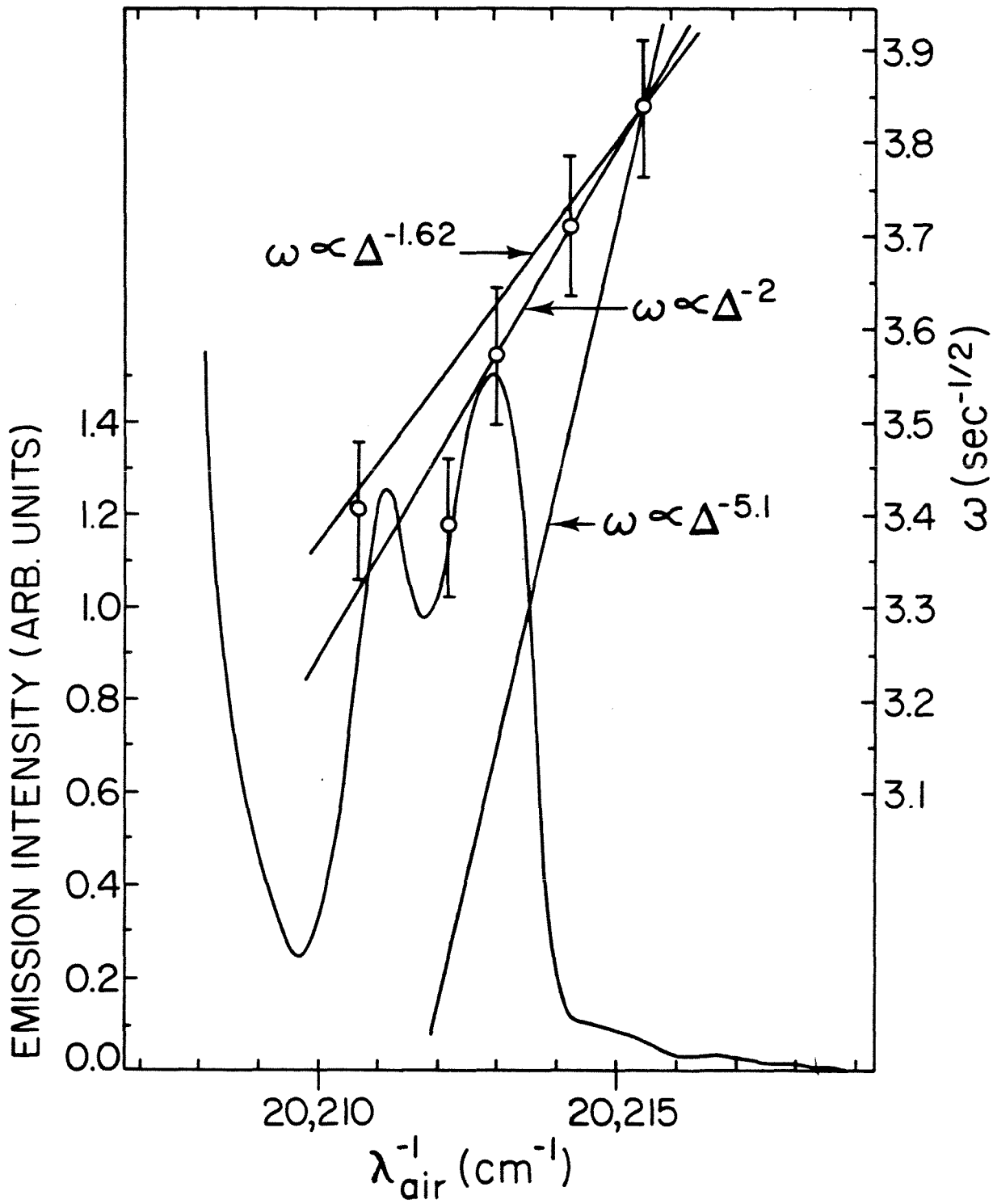
EMISSION INTENSITY (ARB. UNITS)
0.0
0.2
0.4
0.6
0.8
1.0
1.2
1.4
20,210
20,215
λ^{-1}_{air} (cm^{-1})
$\omega \propto \Delta^{-1.62}$
$\omega \propto \Delta^{-2}$
$\omega \propto \Delta^{-5.1}$
3.1
3.2
3.3
3.4
3.5
3.6
3.7
3.8
3.9
ω (sec$^{-1/2}$)

broadened impurity lines is off-resonance coupling. Statistically, the most probable energy for a trap to have is in the middle of the inhomogeneous profile. If a trap site is situated in the wings of the profile, it will probably have to couple to a neighboring trap which is in the middle of the profile. Therefore, the resonance denominator will damp out the coupling. (All other things being constant, the problem would be less severe in 2 or 3-D since the number of available trap sites to choose from would be larger and the probability of a resonant match higher.) When superexchange is occurring, though, the perturbation expansion for the coupling is in terms of trap depth from the host states, and not in terms of the inhomogeneous profile width as in the derivations of Anderson (14), Mott (15), and Cohen, Fritzche and Ovshinskii (16) that is the fundamental difference. Therefore, the shallower the trap depth at a given site the faster the energy transfer is.

One may note that as Δ increases, the superexchange contribution to the total energy should damp out in comparison to the direct exchange or residual multipolar coupling. It would be extremely interesting to carry on these sorts of experiments in higher dimensionality systems and systems with different transfer Hamiltonians.

REFERENCES

[1] R. Silbey, Ann. Rev. Phys. Chem. 27 (1976) 203; D. Burland and A. H. Zewail, Adv. Chem. Phys. 40 (1979) 369.

[2] (a) R. M. Hochstrasser and A. H. Zewail, Chem. Phys. 4 (1975) 142(b); R. H. Hochstrasser and J. D. Whiteman, J. Chem. Phys. 56 (1972) 5945; (c) R. M. Hochstrasser, L. W. Johnson and C. M. Klimcak, J. Chem. Phys. 73, 156 (1980).

[3] R. Schmidberger and H. C. Wolf, Chem. Phys. Lett. 16 (1972) 402.

[4] D. D. Smith, D. P. Millar and A. H. Zewail, J. Chem. Phys. 72 (1980) 1187.

[5] J. Koo, R. Walker and S. Geschwind, Phys. Rev. Lett. 35 (1975) 1669; C. Hsu and R. C. Powell, Phys. Rev. Lett. 35 (1975) 734; D. S. Hamilton, P. M. Selzer and W. M. Yen, Phys. Rev. B 16 (1977) 1858.

[6] Z. G. Soos and R. C. Powell, Phys. Rev. B 6 (1972) 4035.

[7] E. W. Montroll, Proc. Symp. Appl. Math. Am. Math. Soc. 16 (1963) 193.

[8] G. C. Nieman and G. W. Robinson, J. Chem. Phys. 37 (1962) 2150.

[9] D. M. Burland J. Chem. Phys. 67 (1977) 1926.

[10] D. D. Smith and A. H. Zewail, unpublished results.

[11] R. M. Rich, S. Alexander, J. Bernasconi, T. Holstein, S. K.

Lyo and R. Orbach, Phys. Rev. B 18 (1978) 3048.

[12] EMI applications note on ''Photomultipliers - space charge effects and transit time spread'', reference R/P 064, 1977.

[13] J. J. Mitteldorf and D. O. Landon, Appl. Opt. 7, (1968) 1431.

[14] P.W. Anderson, Phys. Rev. 109 (1958) 1492.

[15] N.F. Mott, Metal Insulator Trnasitions (Taylor and Francis, London, 1974); Phil. Mag. 29 (1974) 613.

[16] E.N. Economou and M.H. Cohen, Mat. Res. Bul. 5 (1970) 577, and references therein (for Cohen, Fritzche and Ovshinskii).

CHAPTER III.

LINE NARROWING LASER SPECTROSCOPY OF ORDERED AND DISORDERED QUASI-ONE-DIMENSIONAL 1,4-DIBROMONAPHTHALENE: DEPHASING OF TRIPLET EXCITONS AND BAND TO BAND TRANSITIONS*

---

*Portions of this chapter are published in D. D. Smith and A. H. Zewail, J. Chem. Phys. 71 (1979) 3533; D. D. Smith, J. P. Lemaistre and A. H. Zewail, to be published

I. INTRODUCTION

In the last several years, advances have been made in the theory of optical dephasing of vibronic transitions. Stimulated by recent experimental work on the coherent optical transients of impurity molecules in solids, the theorists have attempted to relate the optical dephasing time (T_2) to the dynamics in the condensed phase. Specifically, some relationships between T_2 of the optical transition and the structure of the phonon bath or the anharmonicity of the potential energy surfaces in the impurity ground and excited states have been established. Under the approximation that we have two impurity levels interacting with a bath, the total linewidth of the transition is a sum of two contributions. The first is due to the adiabatic fluctuations in the energies of the initial (i) and final (f) states of the molecule by the phonons. Hence, with this adiabaticity, there is no change in the population of the levels and the associated relaxation time is called pure dephasing (T_2'). The second kind of dephasing is an energy relaxation or lifetime broadening where the population of state i or f can be irreversibly lost to the bath by decay rates T_{1i}^{-1}, T_{1f}^{-1}. Pure dephasing has been studied for vibrational transitions in liquids by several authors [1,2] and for vibronic transitions in solids by Jones et al. [3] and Diestler and Zewail, [4].

Recently, Harris and his coworkers [5] advanced a model for the dephasing of an optical transition if by nearby i'f' transitions through the well-known exchange model of Anderson [6]. The exchange idea is widely used in NMR and Schmidt et al. [7] have used it

successfully to describe the EPR and coherence of isotopic impurity dimers in naphthalene. The extension of the exchange idea to multiple-level optical transitions was realized by Zewail [8] when discussing spin vs. optical coherence.

Basically, in any exchange model, the bath induces population exchange among the levels through anharmonic coupling. Physically, it is postulated that the energy difference between the transitions if and i'f' is due to unequal ground and excited state phonon energies. Due to the energy difference one expects an Arrhenius-type dependence for the linewidth and lineshift and that their ratio is constant. This conclusion was roughly supported by available data which have large experimental uncertainties.

Jones and Zewail have formally considered the exchange model and concluded that (a) the same temperature dependence of the width and shift can still be obtained for two-level (not many-level) systems without the necessity of having other (i'f') transitions and (b) exchange that is a T_1 process (not T_1') usually has a lower cross section than T_2' type processes. Small [9] has reached the same conclusions by comparing the results of the exchange model with those of Sturge and McCumber [9]. Because the equations of Jones et al. become those of Sturge and McCumber when the lower order terms of the molecule-phonon potential interaction is used, the agreement between Jones et al. and Small's result is exact, for this particular limit, except the cross section for the coupling was not displayed in Small's treatment.

Fischer and Laubereau [10] in discussing vibrational dephasing have concluded that, in general, exchange will not contribute significantly to the linewidth in the condensed phase. The Chicago group [11] has recently examined this problem and concluded that available experimental results on durene are not sufficient to penetrate into the origin of the exchange. The real questions now are as follows; Does exchange really contribute to the linewidth of optical transitions? If it does, what is the contribution of T_2'-type broadening?

In this paper, we critically examine these two questions and in the subsequent paper we present new experimental results that support our earlier contention that T_2' processes are dominating the dephasing, especially at high temperatures, and at least in the system we present here.

II. Theory

A. Single optical transition: The two-level system.

In solids, the homogeneous linewidth ($1/T_2$) for an optical transition (made of the two levels i and f) may be displayed as follows:

$$(2.1) \qquad T_2^{-1} = 1/2\left[T_{1i}^{-1} + T_{1f}^{-1} \right] + T_2'^{-1}$$

where $1/T_{1i}$ and $1/T_{1f}$ are the decay rates of initial (i) and final (f) states respectively, and $1/T_2'$ is the rate of pure dephasing. Denoting by $\underset{\sim}{T}$ the transiton operator $\underset{\sim}{T} = V + VG_0\underset{\sim}{T}$ which couples

the state i and f to the thermal bath, the contributions of inelastic $(1/T_1)$ and elastic $(1/T_2')$ phonon-induced processes to homogeneous linewidth are

$$(2.2a)\quad 1/T_{1i} = \frac{2\pi}{(h/2\pi)} \sum_{\substack{p,p' \\ i\neq i'}} W_p |\langle i'p'|\underset{\sim}{T}|ip\rangle|^2 \delta(E_{i'p'} - E_{ip})$$

and

$$(2.2b)\qquad 1/T_2' = \frac{\pi}{(h/2\pi)} \sum_{p,p'} W_p |\langle ip'|\underset{\sim}{T}|ip\rangle - \langle fp'|\underset{\sim}{T}|fp\rangle|^2 \delta(E_p - E_{p'})$$

where p and p' are the composite phonon states. All the temperature dependence of $1/T_{1f}$, $1/T_{1f}$ and $1/T_2'$ is contained in $\sum W_p$ which depends on the density of phonon states and on their thermal occupation number. The $\underset{\sim}{T}$ operator contains all the degrees of freedom of both the intramolecular states (if, i'f') and the phonon states (p,p'). Because the cross-sections of pure dephasing may be large relative to that of T_1-type dephasing, it may be principally responsible for the homogeneous broadenings and frequency shifts of the optical transition as a function of temperature. For illustration let us retain only the first order term, V, in the expansion of the $\underset{\sim}{T}$ operator. Thus, equations 2.2a and 2.2b now take the following simple forms:

$$(2.3a)\quad 1/T_2' = \frac{\pi}{(h/2\pi)} \sum_{p,p'} W_p |\langle p'|\Delta V_{if}|p\rangle|^2 \delta(E_p - E_{p'})$$

where

$$(2.3b) \qquad \Delta V_{if} = \langle V \rangle_i - \langle V \rangle_f = \langle i|V|i\rangle - \langle f|V|f\rangle$$

is simply the disparity in the scattering rates between the initial and final states. The scattering matrix elements that we denote by $\langle V \rangle$ depend strongly on the electronic distribution of the involved states. As we shall see later, this adiabatic modulation of the difference ΔV_{if} may be very large, especially for optical transitions. Similar to the linewidth, an expression for the lineshift of the transition can be written in terms of ΔV_{if}.

The expressions for the linewidth and lineshift are quite general and do not require a specific phonon mode (i.e. acoustic or optical). For acoustic phonons obeying a three-dimensional Debye model, the temperature dependence of the width is the usual T^7-type process. On the other hand, the dephasing by an optical phonon (or quasi-local mode) with a frequency Δ leads to the following temperature dependence:

$$(2.6a) \qquad \gamma_{if} = \gamma_0 \exp(\Delta/kT)/(1-\exp(\Delta/kT))^2$$

and

$$(2.6b) \qquad \delta_{if} = \delta_0 \exp(\Delta/kT)/(1-\exp(\Delta/kT))^2$$

where γ_0 is simply the product of $|\langle \Delta V_{if} \rangle|^2$ and a constant. It is now clear that γ_{if}/δ_{if} is constant, and this constant is close to one. Furthermore, in the low temperature limit, we recover the Arrhenius-type plot for both the shift and width for T_2' (elastic) dephasing of two levels interacting with a bath.

B. Multiple transitions: The exchange problem.

When spectral lines overlap, the isolated two level theory given in section A becomes less appropriate simply because the spectral overlap could lead into significant exchange coupling. We shall first consider two two-level transitions and then generalize the results in section III to many two-level transitions.

It can be shown that for two overlapping resonances (if and i'f') the eigenvalues of the following matrix determine the width and shift caused by elastic and exchange couplings:

$$(2.7) \quad \underset{\sim}{L} = \begin{bmatrix} \omega_{if}+\delta_{if}-i\gamma_{if} & -i\gamma_{if,i'f'} \\ -i\gamma_{i'f'if} & \omega_{i'f'}+\delta_{i'f'}-i\gamma_{i'f'} \end{bmatrix}$$

Where the diagonal δ and γ describes the shift and width, respectively, while the off-diagonal γ describe the matrix element connecting the two overlapping resonances. The different γ's can be related as follows:

$$\gamma_{i'f',if} = \gamma_{if,i'f'} e^{-\Delta/KT} \tag{2.8}$$

where Δ is the energy difference and γ is simply the golden rule rate for transitions between if and i'f':

$$\gamma_{if,i'f'} = \frac{\pi}{i} \sum_{p,p'} W_p |\langle V \rangle|^2 \delta(E_{fp} - E_{f'p'}) + \frac{\pi}{i} \sum_{p,p'} W_p |\langle V' \rangle|^2 \delta(E_{ip} - E_{i'p'})$$

It is now a simple matter to diagonalize the matrix and calculate the lineshape parameters. Several points are worth mentioning here. First, the pure dephasing of each transition is contained in γ_{if} and $\gamma_{i'f'}$. This pure dephasing is temperature dependent and in fact has exactly the same functional dependence as that of equation 2.8 in the low-temperature limit. Second, clearly, the exchange is a T_1-type process that contributes to the homogeneous width of if and i'f', but is not contained in the γ's when exchange is absent. Third, the effect of the exchange is to bring an ''interference term'' that depends on the relative magnitude of pure dephasing of the two resonances. In the limit where the relative pure dephasing is very large, the exchange contribution to the overall dephasing is negligible. Finally, there is no reason that the pure dephasing is constant at all temperatures while δ_1 and δ_2 are changing with temperature according to eq. 2.8. This is an important point recognized by us in reference 3 and more recently by

Abbot and Oxtoby in reference 11.

In the low temperature limit and assuming that the two resonances have comparable T_2' values, we obtain

$$(2.9) \qquad (1/T_2)_{if}^{total} = (1/T_2)_{if} + (1/T_2)_{exc.}$$

where

$$(2.10) \quad (1/T_2)_{exc.} = \frac{\gamma_{if,i'f'}(\omega_{if} + \delta_{if} - \omega_{i'f'} - \delta_{i'f'})^2}{(\omega_{if} + \delta_{if} - \omega_{i'f'} - \delta_{i'f'})^2 + \gamma_{i'f'if}^2}$$

Now if we use the notation of previous work, where ω refers to $\delta_{if,i'f'}$ and $\tau^{-1} = \delta_{i'f',if}$ and the square of the frequency difference as δ^2, then we get

$$(2.11) \qquad (1/T_2)_{exc.} = \frac{\omega\delta^2}{\delta^2} = \frac{\omega\tau^2\delta^2}{1+\delta^2\tau^2}$$

which is identical to all the expressions previously derived for the low-temperature limit. Similarly, the shift is

$$(2.12) \qquad \delta_{exc.} = \frac{\delta\omega\tau}{1+\delta^2\tau^2}$$

The connection of the above results with those of Anderson is now clear. In the absence of intrinsic broadening, the lineshape is simply

$$I(\omega) = -\mathrm{Re}(\underset{\sim}{W\mu}\cdot\underset{\sim}{L}^{-1}\cdot\underset{\sim}{\mu}) \tag{2.13}$$

where

$$\underset{\sim}{W\mu} = (w_{if}\mu_{if},\ w_{i'f'}\mu_{i'f'}) \tag{2.14}$$

$$\mu = \begin{bmatrix} \mu_{if} \\ \mu_{i'f'} \end{bmatrix}$$

is eq. 2.7 without γ_{if} and $\gamma_{i'f'}$. $I(\omega)$, when computed, gives precisely the results (due to exchange only) in equations 2.11 and 2.12.

III. A test model: The linear chain

A. Preliminaries

The objective here is to test the relative importance of T_2 and $T_2^{exc.}$ in contributing to the overall dephasing. Imagine that we have a linear chain made of N molecules, as e.g. the case of 1,4-dibromonaphthalene triplet excitons. The resonance interaction ($\beta = -6.2\ cm^{-1}$) between the molecules lifts the degeneracy of the $\underset{\sim}{k}$ states. The eigenfunctions and energies of a finite chain are

$$|\underset{\sim}{k}\rangle = (2/n+1)^{1/2} \sum_{n=1}^{N} \sin(\underset{\sim}{k}n\theta)\,|n\rangle$$

$$E_{\underset{\sim}{k}} = E_n + 2\beta\cos(\underset{\sim}{k}\theta)$$

Where $\theta = \pi/N+1$ and $\underset{\sim}{k}$ runs from 1 to N. The ket $|n\rangle$ denotes the one-site function on molecule n.

Emission from the band to the ground state gives essentially a one-line transition while those to a vibrational band give a band-to-band transition. The band-to-band (BTB) transition contains overlapping resonances while the (0,0) displays essentially the region around $\underset{\sim}{k} = 0$. Therefore, if we know the rate of exchange among the $\underset{\sim}{k}$ states and we know the pure dephasing time as a function of temperature, we can isolate the contribution of exchange dephasing.

As we shall see, the ''$\underset{\sim}{k}$-to-$\underset{\sim}{k}$'' scattering time can be measure by pumping the $\underset{\sim}{k} = 0$ level and recording the BTB spectra as a function of time. This transient experiment is repeated at different temperatures to obtain the exchange rates as a function of temperature. This measurement provides δ. Now we measure the (0,0) width as a function of temperature to obtain γ.

Theoretically, we can handle the effect of exchange on the BTB transitions by increasing the size of the matrix in eq. 2.7 to include all transitions. In other words, eq. 2.14 becomes

$$W\mu = (w_1\mu_1, \ldots w_k\mu_k, \ldots w_n\mu_n): \quad \mu = \begin{bmatrix} \mu_1 \\ \mu_{\underset{\sim}{k}} \\ \mu_n \end{bmatrix}$$

and

$$\underset{\sim}{L} = i\underset{\sim}{D} + \underset{\sim}{\Pi}$$

where

$$D_{\underset{\sim}{kk}'} = (W_{\underset{\sim}{k}} + \delta_{\underset{\sim}{k}} - W)\delta_{\underset{\sim}{kk}'}$$

$$\Pi_{\underset{\sim}{kk}'} = \gamma_{\underset{\sim}{kk}'}(1-\delta_{\underset{\sim}{kk}'}) + \left[-(T_{2\underset{\sim}{k}})^{-1} - \sum_{\underset{\sim}{k}''} '\gamma_{\underset{\sim}{kk}'} \right] \delta_{\underset{\sim}{kk}'}$$

Therefore, as a result of overlapping resonances in the BTB transitions, the effect of temperature should indicate the relative roles of $T_{1\underset{\sim}{k}}$ and $\gamma_{\underset{\sim}{kk}'}$.

IV. EXPERIMENTAL PROCEDURE

A. Materials and methods for steady state experiments

Isotopically mixed crystals of approximately 5 and 16 mole percent perdeutero in perproto DBN were grown by standard Bridgman techniques. All starting materials were extensively zone refined. The pure H_6 DBN sample, taken from the zone refining tube, was exceptionally clear with no visible fractures, so was used in the experiments with no further treatment. The cylindrically shaped boules were 4 to 6 mm in diameter. Samples cleaved from the boule were gently held with black photographic tape against a flat sample holder. Temperatures between 1.4 K (flooding and pumping the sample chamber) and 100 K were achieved in a Janis model DT-10 super varitemp dewar. Temperatures were measured with a calibrated silicon diode situated in a copper block which supported the sample holder. The samples were no more than 45 mm from the sensing element to reduce any temperature gradient effects. A second sensor was attached to the helium nozzle with indium solder. For temperatures greater than 4.2 K, the temperature at the nozzle was regulated by a heater in a feedback loop with a Lakeshore Cryotronics DTC-500 temperature controller. Temperatures could also be regulated using the sample sensor to control the current supplied to the nozzle heater, but much greater stability was achieved using the nozzle sensor.

As a check to determine if the helium flow rate was adequate to dissipate the sample heat, the flow rate was increased beyond that recommended by the manufacturer to double the heater current, yet

keep the sample at a constant temperature. Within the S/N ratio, the band to band lineshape was unaltered. It is worth mentioning that the helium gas flow nozzle was a sintered brass filter and for large flow rates of helium gas it was very difficult to regulate the temperature. Presumably, turbulent flow through the nozzle and small amounts of snow swept into the helium leak valve limit the maximum flow rate. The maximum stable flow rate is not a severe limitation for laser experiments, since the few tens of milliwatts typical average laser power the sample must dissipate is well within the cooling capacity even at 6 K. However, for steady state absorption and emission experiments with broad band sources, one must be very cautious to avoid sample heating effects. A filtered arc lamp can easily put 3 watts of focussed UV on the sample. Since the heat capacity (thus the cooling capacity) of helium gas goes as (3/2)kT, one expects sample heating to be less of a problem at high temperatures. At lower temperatures (5 to 25 K) it was found that the most reliable results were obtained using high flow rates and a double set of IR and visible absorbing filters on the arc lamp, producing less than 1 watt of UV (measured with a Scientech thermopile).

Broadband excitation of the sample was produced by a 200 watt Oriel Hg-Xe arc lamp filtered by a $NiSO_4$ solution filter, two Corning 7-54 filters and a high energy UV cut-off filter. For the transient line narrowing experiments, the emission was collected at right angles , passed through a high energy sharp cut filter and focussed on the slits of a Spex 1402 double spectrometer with dual 2400 groove/mm holographic gratings. Light was detected with a Hammatsu

R955 PMT and fed into photon counting electronics or a PAR 162 boxcar with 164 and 163 modules. For the absorption experiments, an Oriel 100 watt Tungsten lamp passed through IR and UV absorption filters and a Bausch and Lomb 1/4 meter monochromator was used. The light was dispersed with a Spex 3/4 meter spectrometer with an 1800 groove/mm holographic grating and detected with a Varian VP-192 PMT. The transmitted light was chopped with a PAR 192 chopper and detected in quadrature mode (reducing phase fluctuation noise) with an Ortec 9505 lock-in amplifier.

B. Procedure for laser line narrowing transients

In all the time resolved experiments, great care was taken to insure that the observed time dependences were not distorted by slow system response time or detector nonlinearity. Scans using neutral density filters on the spectrometer slits, different load resistors, different excitation wavelength, etc. were done to insure reliability. A detailed discussion of potential sources of experimental artifact and their diagnosis follows.

In our transient experiments, (see Fig. 1) a Molectron UV 24 nitrogen laser was used to pump a DL14P dye laser and amplifier, producing 5-8 nsec pulses of ~9 Ghz spectral bandwidth. Energy per dye laser pulse was typically 0.5 mJ with peak power of approximately 50 kW, average powers of 5 mW. The signal was processed with a Princeton Applied Research model 162 boxcar integrator with a model 164 plug-in and model 163 sampling head plug-in with 350 psec risetime. To reduce unwanted scattered light , the emission was

analyzed with a Spex model 1402 double spectrometer with dual 2400 groove/mm holographic gratings. To reduce the resonance Raman scattering, the vibronic transition at 18,850 cm^{-1} was used. The experiment (phosphorescence site selection) reported here for the first time for molecular excitons resembles those done on inorganic systems (fluorescence line narrowing [5]).

It should be immediately pointed out that signal averaging in these experiments is a problem unto itself. Unlike the picosecond sync-pumped dye laser systems where one performs experiments at repetition rates in the Mhz region, the maximum rate these experiments can be performed at is 10 to 20 hz, due to triplet state lifetimes being of the order of tens of milliseconds. Thus, to obtain a reasonable S/N spectrum in a reasonable amount of time, one needs to collect as many emitted photons per pump pulse as is possible. However, one also wants to avoid nonlinear effects such as excitonic fusion and fission and false time-dependences, so one requires (a) low excitation density and (b) all the physics to finish before the next pump pulse arrives. Thus, good S/N without artifact requires attention to several experimental parameters.

There are several very important sources of experimental artifact that must be dealt with in the transient experiments: (1) the reduction of scattered light, (2) the prevention of photomultiplier saturation, system response time limitations including (3) electronics, (4) transit time spread and (5) space charge limitation. These five (among other) potential pitfalls must be unequivocally and quantitatively dealt with if the experimentalist

is to trust the data. We shall discuss each one.

1. Reduction of scattered light

For the problem of scattered light produced by unwanted reflections, it is imperative to have the highest possible optical quality crystal, avoiding mechanical imperfections that scatter the light. Moreover, the use of holographic gratings greatly reduces the scattered light problem within the spectrometer and increases throughput since (a) the grating produced by the photoresist process does not have glass shavings and chips left behind as does the conventionally-ruled grating, reducing ghosts and scatter and (b) as the grating is produced by interference fringes, it is close to being sine grating and most of the light is diffracted in to first order. A perfect sine grating can only diffract in first order, thus it does not distribute the intensity of the dispersed light among many orders. One should bear in mind, however, that for most uses other than transient experiments, the holographic grating has drawbacks versus the conventionally ruled grating. The present, commercially available holo grating clearly has an undesirable wavelength-dependent polarization response and diffraction efficiency. An additional limitation of the holo is that if one wants to use the second order diffracted light for higher resolution (which is very frequently the case) one requires an anomalously intense signal since the throughput in second order is very low. For a Spex 1800 groove/mm holographic grating, second order efficiency is at least a factor of 50 less than that of first order. (The author has recently learned that the American

Holographic Corporation has produced a grating which has a second order efficiency comparable to that of conventionally ruled gratings.)

2. Photomultiplier saturation

To prevent photomultiplier saturation, several caveats should be observed (see reference [12]). First, using as high a PMT bias as is possible will keep the transit time spread (vide infra) and space charge saturation effects minimized. (Note that the dynodes roughly obey the Child-Langmuir law which states the saturation current between two parallel plate electrodes goes as $V^{3/2}$ where V is the applied voltage.) Secondly, one must realize that with transient signals whose rise and fall times approach the rise and fall times of the PMT, the averaged maximum current must be 100 to 1,000 times less than the maximum average continuous current the manufacturer quotes. For instance, if the manufacturer rates the tube at ~100 μA (e.g. the Varian VP-192), the time-averaged (not peak) current should be 0.1 to 1 μA. Terminating the PMT into a high-input impedance digital multimeter in DC volts mode will typically integrate the current well enough to determine the safe limits (100 megΩ input impedance at 20 hz laser repetition rate). We have indeed found that if the current is > 1/50 of the maximum rating, lifetimes were too long, time-dependences were too slow with weak lines amplified and strong lines suppressed. Further, differences were found between different photomultipliers -- the Hamamatsu R955 and EMI 9659QB in particular. The Varian VP-192 did not saturate easily, possibly due to its opaque rather than semitransparent photocathode. Being opaque, the photocathode is thicker, having less resistivity and smaller voltage

drops across its face (more uniform and higher fields, to resist space charge effects and transit time spread). To reduce PMT saturation, one can reduce the gain (bias) of the tube and use electronic amplifiers on the anode output, losing only PMT response time which may be tolerable in certain measurements.

The newest technique for reducing PMT saturation as well being the most promising and costly is the switching PMT (e.g. the EMI 9810 series and ITT star-tracking tubes). Some switching tubes have a deflection grid directly between the photocathode and first dynode acting as a current gate in a triode tube. Though these tubes can prevent dynode saturation, they cannot prevent photocathode damage or fatigue. The grid-controlled tubes were originally developed for laser rangefinders where one wants to discriminate against near-field backscatter shortly after the laser pulse. The ITT star-trackers use magnetic and electric deflection coils behind the photocathode. Though the deflection coils were intended to scan the photocathode (looking for stars imaged on the photocathode), they can be used to deflect all the photoelectrons away from the first dynode, acting as a switch. The principal limitation of the switching method at present is the switching speed. The circuits which are reliable and do not cause a ''ringing'' in the gain of the tube have a switching time of ~ 1 μsec (vide infra).

3. System response time limitations: electronic

In regard to the third experimental artifact (having system reponse times short enough to avoid integrating previous history into

the signal) there are several quantitive tests one can perform. A poor response time can be the most serious pitfall of the DBN experiments, where the short time, high intensity spike of light shaped identical to the pump pulse that arises from Raman and reflected light swamps the photomultiplier or the signal processing electronics. If one had a detection system with infinitely fast response time, the delta function like scattering pulse would not interfere with the luminescence. However, with finite response times, the scattered light is temporally integrated and overlaps with the luminescence. The light scattered within the instrument can be multiply-diffracted as is typically the case with the Czerny-Turner type of mount [13] or can simply be spurious reflections. The idea is to discriminate against this scattered light which usually dominates the luminescence by insuring that the system RC (recovery from the spike) does not contribute any signal at the time that the boxcar gate is open. If one represents the boxcar input as a simple lumped RC circuit with a real impedance (not worrying about any phase shifts from capacitive impedance) and solves the differential equation for the transient recovery from a delta function current pulse at t=0 [12], one finds a voltage response function, V(t) roughly resembling exponential rise and decay. If the system response is rapid, then the tail of the delta function current pulse does not contribute at the delayed time that the boxcar gate opens. Therefore the signal voltage should be linear in the load resistance. Otherwise, the signal will scale exponentially with the load since it is dominated by the integrated short time current spike. For the DBN experiments, (tunneling and band-to-band experiments), we would scan the

emission spectrum at a given delay time then repeat the scan for several different values of load resistance. It was found that for RC's > 1/5 of the observation time, the signal intensity clearly was nonlinear in the load resistance. For RC's 1/8, 1/10 and 1/15 of the observation time, the signal varied linearly with the load. All the DBN experiments were performed with system response times < 1/10 of the observation time. For the case where the driving current is $I(t) = I\exp(-t/\tau)$, the decay will be distorted and appear as [12];

$$V(t) = \frac{IR\tau}{\tau - RC}\left[(\exp-(t/\tau)) - \exp-(t/RC)\right]$$

where I is the maximum current from the PMT, τ is the decay constant of the sample, R is the lumped resistance and C is the lumped capacitance.

4. Transit time spread

The system response time can be limited by the detector as well as the detection electronics (cf. previous section). If response is limited by PMT space charge effects (in contrast to an RC problem) or transit time spread, one should be able to detect it by putting neutral density filters on the detector and/or altering the PMT bias (all else the same). Space charge (see next section) and transit time effects can cause erroneous time-dependences and unreliable signal intensities.

Transit time spread is a result of the fact that the photoelectrons do not all leave the photocathode with the same

kinetic energy and trajectory as they travel to the first dynode where they will produce many secondary electrons (the amplification). Carried one step further, as secondary electrons leave the first dynode, not all of them have the same energy and trajectories, resulting in different arrival times at the second dynode. This goes on until the electrons reach the anode and are collected, but due to the distribution of arrival times the signal would be broader than a true delta function light pulse. This broadening is often called transit time spread. If the photomultiplier bias is low, the spread in arrival times can be large. Exactly how large depends on the dynode geometry and bias scheme. To keep the rise time as short as possible and transit time dispersion low, one should keep the bias voltage high and use a high current, nonlinear dynode chain. Further, since the total transit time in the PMT is a function of bias voltage, do not change the bias after establishing the apparent t=0! I have seen changes of ~50 nsec in the ''apparent'' position in time of the laser pulse when changing only the PMT bias. One should use a photomultiplier with electrostatically focused dynodes in these types of experiments to help minimize most of the above mentioned effects.

5. Space charge limitations

As for space charge limitation, tests with neutral density filters are usually adequate. Space charge limitation refers to the effect of having too large a number of secondary electrons (or for that matter, photoelectrons from the cathode) such that the repulsive potential within the ''electron cloud'' competes with the potential

between dynodes. In such a situation, not all electrons are able to reach the next dynode, exacerbated by a transit time dispersion that can be severe. The neutral density filters reduce the number of electrons (photoelectrons) in the ''cloud'' and therefore, intensities are truer (electrons don't get lost between dynodes) and the response time is faster since the effective dynode field felt by each electron is higher.

One should realize that ''saturation'' of the photomultiplier is distinct from space-charge limitation proper. Instead, saturation is an effect where the photocathode fatigues due to prolonged or intense illumination. This sort of problem is generally rare compared to space-charge limitation and is difficult to diagnose and quantify (see ref. [12]).

Tests with neutral density filters up to 0.6 O.D. units were carried out and no discernible change in signal time-dependence or lineshape was found. A larger range of neutral density filters could not be easily tested since good signal/noise was required to do a quantitative test. That is, if one is looking for distortions in the time-resolved spectrum as we were. I usually ran with the PMT bias voltage at or slightly beyond the limit of the manufacturer's specifications, which was 3 KV for the Varian VP-192. Further, in all the transient experiments, the manufacturer's recommended nonlinear dynode bias chain was used.

C. Raman scattering vs. emission

As well as understanding the character of the detectors and the

detection electronics, it is essential to observe the emission to a final state with a small Raman cross section. That is, in order to record the emission without interference from resonance Raman scattering, one should pick a molecular transition with as large as possible relative emission/scattering cross sections. This is easily accomplished by setting the boxcar gate coincident in time with the laser pulse and scanning the spectrometer over the total spectrum (producing, essentially, the Raman spectrum). Then one compares the scattered light spectrum with a CW emission spectrum and uses the transitions absent in the Raman spectrum. Simply, one is finding the resonance Raman inactive modes. This was the procedure used to select the 5305 Å transition in DBN for the tunneling and band to band experiments. One should note that due to the high powers involved (megawatts/cm^2) that Raman scattering can be a serious problem. From the data, it was clear that looking at the (0,0) emission (resonant with the pump laser) would not work due to light scatter, even using the highest quality crystals and a double spectrometer (with an effective PMT switching scheme, this should be feasible). This is in contrast to experiments on rare earth doped glasses where it is routine to look near resonance with the transition being pumped (due to the smaller electron-phonon coupling, less efficient radiationless decay channels and lower polarizability of the ion than molecules in molecular crystals). Further, with emission to ground state modes with resonance Raman activity, the scattering/emission cross section ratio was too large to get rid of the short-time laser scatter with any value of load resistor on the boxcar that gave a signal.

D. Accuracy in time delay measurements

In order to achieve accuracy in the recorded time delay spectrum, an optical delay line 20 meters long was used to compensate for the electronic delays (~60 nsecs) of a photodiode triggering the boxcar. Then, the boxcar was scanned in time over the laser to find an apparent ''t=0'' in terms of the boxcar knobs. In other cases, a pulse generator which produced a trigger and delayed trigger was used to compensate for the various instrumental delays but this method proved to be less desirable, since (a) the trigger generator provided a path for thyratron noise to the boxcar and (b) the method relied on the time and amplitude stability of the pulse generator (since the boxcar was leading edge triggered) as well as low jitter on the nitrogen laser thyratron. The photodiode clearly had none of these problems. It can only trigger the electronics when the light pulse is on its way to the sample and does not provide a direct path for high frequency electromagnetic interference from the laser to the boxcar. The photodiode was powered by a small 15 volt battery and the entire assembly was encased in a small metal box with a 2 mm hole for the laser. Two mm was chosen to diffraction limit any broadcasted interference finding its way to the diode. Triaxial cable was initially used between the photodiode and the boxcar but it was empirically determined that normal coax did as well.

E. Sources of noise in data acquisition

The three largest sources of noise in the transient DBN experiments were found to be (1) laser beam wander, (2) laser

amplitude stability (~5%) and (3) fluctuations in the laser repetition rate. Beam wander causes different portions of the sample to be irradiated, which in turn causes different portions of the optics to be illuminated and all the concomitant problems. Unfortunately, the long arm of the delay line aggravates the problem. Presumably the wander is due to index of refraction changes due to local heating of the dye by the pump laser. Running the laser at rep rates below 10 hz seemed to minimize but not eliminate the problem of beam pointing stability. When using the second harmonic of the dye laser, the pointing instability of the beam made it unusable with a 20 meter delay line.

When using the boxcar to look for signals that are 2% of full scale deflection or less, a small fluctuation in the rep rate (<< 1 hz) gives baseline drift of the order of several tenths of a percent. This is problematic, since in most of the tunneling and band-to-band experiments we never saw the meter on the boxcar move!!! A more frequency stable triggering system may help the apparent drift. At this writing, it is not known if the drift is exclusively rep rate dependent and can be rectified (a digital storage option on the boxcar <u>was</u> used to prevent ''droop'').

As for pulse to pulse amplitude stability, I know of no simple cure. Using two boxcar plug-ins where one samples the laser pulse, the other emission intensity and taking the ratio did not reduce the noise, possibly due to errors in the analog division.

V. EXPERIMENTAL RESULTS

The relevant spectroscopic parameters for DBN were discussed in chapter I. However, it is useful to summarize what is known to date about the lowest triplet exciton, and the data are presented in Table I.

To aid the reader, a brief summary of the experiments and the conclusions drawn from them follows. The experiments include (1) The measurement of the temperature dependent homogeneous line width and shift for the $\underset{\sim}{k} \sim 0$ region of the upper and lower sublattices from absorption experiments; (2) the steady state temperature dependent band to band transition (BTBT) lineshape, in pure and disordered crystals; (3) the transient BTBT lineshapes as a function of temperature for pure and disordered DBN.

The data led to four principal conclusions: (1) The intraband exchange time (among the $\underset{\sim}{k}$ states) is of the order of 10 μsec and is weakly temperature dependent from 20 to 55 K. (2) interband scattering is not responsible for the observed broadening of the $\underset{\sim}{k}$-states. (3) To a good approximation one can describe the dephasing of all band states by elastic scattering of ~ 42 cm^{-1} phonons. (4) The relaxation amongst the $\underset{\sim}{k}$ states and the dephasing mechanism are not strongly affected by heavy (16%) substitutional disorder.

We have measured the absorption linewidth and shift of the (0,0) transition to the lowest triplet state in DBN as a function of temperature. The (0,0) transition yields a low temperature lineshape

TABLE I.
SUMMARY OF SOME IMPORTANT DBN MATERIAL PARAMETERS

PHYSICAL

1,4-dibromonaphthalene $C_{10}H_6Br_2$, MW = 286.0
Density = 2.037 g/cc
Melting point: 83 Centrigrade
Crystal structure (at 275 C): monoclinic $P2_1/a_0(C_{2h}^5)$,
a=27.45 ± 0.08, b=16.62 ± 0.04, c=4.09 ± 0.01 Å [a]

SPECTROSCOPIC

Lowest triplet exciton origins at 4.2 K [b]:
lower sublattice: 20,192 cm^{-1}
upper sublattice: 20,245 cm^{-1}

Nearest neighbor interactions at 4.2 K:
along c-axis: -6.2 cm^{-1} [c]
along a,b axes: <0.01 cm^{-1} [d] (sign unknown)

Intrinsic triplet state lifetimes as a function of cluster size:

	1.8 K [e]		1.4 K [f]
	monomer	dimer	exciton
x-state:	79 ± 5 msec	41 ± 5 msec	unknown
y-state:	5.2 ± .3 msec	2 ± .2 msec	476 μsec
z-state:	3.5 ± .3 msec	4.5 ± .3 msec	95 μsec

Naturally occurring triplet trap states so far identified: (given in terms of trap depth from $\underset{\sim}{k}$ = 0 of the lowest sublattice)

I. 28 cm^{-1}
II. 38 cm^{-1}
III. 67 cm^{-1}
IV. 146 cm^{-1}

---

[a] J. Trotter, Can. J. Chem. 39 (1961) 1574.

[b] R. M. Hochstrasser and J. D. Whiteman, J. Chem. Phys. 56 (1972) 5945.

[c] R. M. Hochstrasser and A. H. Zewail, Chem. Phys. 4 (1974) 142.

[d] R. M. Hochstrasser, L. W. Johnson and C. M. Klimcak, J. Chem. Phys. 73 (1980) 156.

[e] A. H. Zewail, W. G. Brieland and C. B. Harris, unpublished results quoted in D. M. Burland and A. H. Zewail, Adv. Chem. Phys. 40 369.

[f] A. M. Nishimura, A. H. Zewail and C. B. Harris, J. Chem. Phys. 63 (1975) 1919.

that has been reported to be asymmetric with a long tail to higher energy [13] and is nearly ''half'' a Lorentzian [12] due to the $\underset{\sim}{k}=0$ state being on the bottom of the band and a Van Hove singularity in the density of states at the exciton band edge. The asymmetric Lorentzian is ostensibly homogeneous [14] though, to the author's knowledge, there is no <u>direct</u> experimental proof of its homogeneity (indirect transitions producing asymmetric lineshapes such as those observed in CdS exciton absorption, would not exclusively reveal the electronic dephasing).

In our experiments, the low temperature linewidth of the $\underset{\sim}{k}\sim 0$ absorption was found to be sensitive to the method of crystal preparation and thermal cycling; widths would vary between 0.5 and 1.5 cm^{-1}. Generally, our crystals were not as strain free as previous studies [12,13], thus the steep, low energy side of the absorption profile was broadened. To correct for the inhomogeneity, we fit the low energy side of the low temperature (1.4 K) line to Gaussian and Voigt functions [15]. The Voigt line shape is a Lorentzian convoluted with a Gaussian and was fit to the data in a convolute and compare procedure using a nonlinear regression (see Appendix IV). The convolution integral was calculated using the expansions of Armstrong [16a], which were checked against published tables [16b,c] and found to be within the accuracy quoted. Voigt fits yielded the Gaussian component of the low energy side, which within fitting error was the same as fitting a purely Gaussian function. The Gaussian component was then used as a fixed parameter in a Voigt fit to the <u>high energy side</u> of the line. We obtained a half Lorentzian of width 0.3

cm^{-1}, in agreement with earlier work [12,13] (all positions and widths reported here are from the wavelengths in air, not in vacuum).

In performing the experiments, care was taken to use crystals of DBN thin enough that the peak absorption was 10% or less to obtain accurate lineshapes from our single beam apparatus. We found reasonable agreement with the reported low temperature absorption coefficients [17]. For the low temperature experiments, platelets 100 to 300 microns thick were cleaved with extra thin razor blades from a boule of DBN. In the high temperature experiments ($T > 50$ K), it was necessary to use 0.5 to 3 mm thick crystals to obtain sufficient absorption. In all cases, the temperature dependent line widths of the thin and thick crystals were overlapped at 3 or 4 intermediate temperatures and found to be identical within fitting error (a few tenths of a wavenumber, typically).

The $\underset{\sim}{k}\sim 0$ absorption becomes a symmetric Lorentzian for $T > 20$ K. For $T > 60$ K, there is incipient asymmetry to <u>lower</u> energy, probably due to absorption from the ground state + a phonon. The fitted homogeneous width as a function of temperature is shown in Fig. 1. For comparison's sake, the total apparent width for a typical crystal is also shown. Fitting the homogeneous width to a two phonon Raman type scattering process, we find a phonon of 42 ± 10 cm^{-1}, which is close to a phonon state reported at 39 cm^{-1} [5b] (the 10 cm^{-1} error represents a 92% confidence limit of a double tailed student t statistic; 75% confidence limits gives an error of $\pm$ 4 cm^{-1}). The data clearly did not fit T^3 or T^7 and since

Figure 1. Temperature dependence of the homogeneous FWHM for the DBN triplet (0,0) from Voigt fits. The crosses are the data from the lower sublattice triplet (0,0) absorption experiments in pure H_6 DBN; squares represent the upper sublattice. Typical total FWHM are shown as filled circles. The solid line is the fit of the data to 42 cm^{-1} two phonon elastic scattering.

ABSORPTION, LOWER SUBLATTICE (0,0) DBN H_6

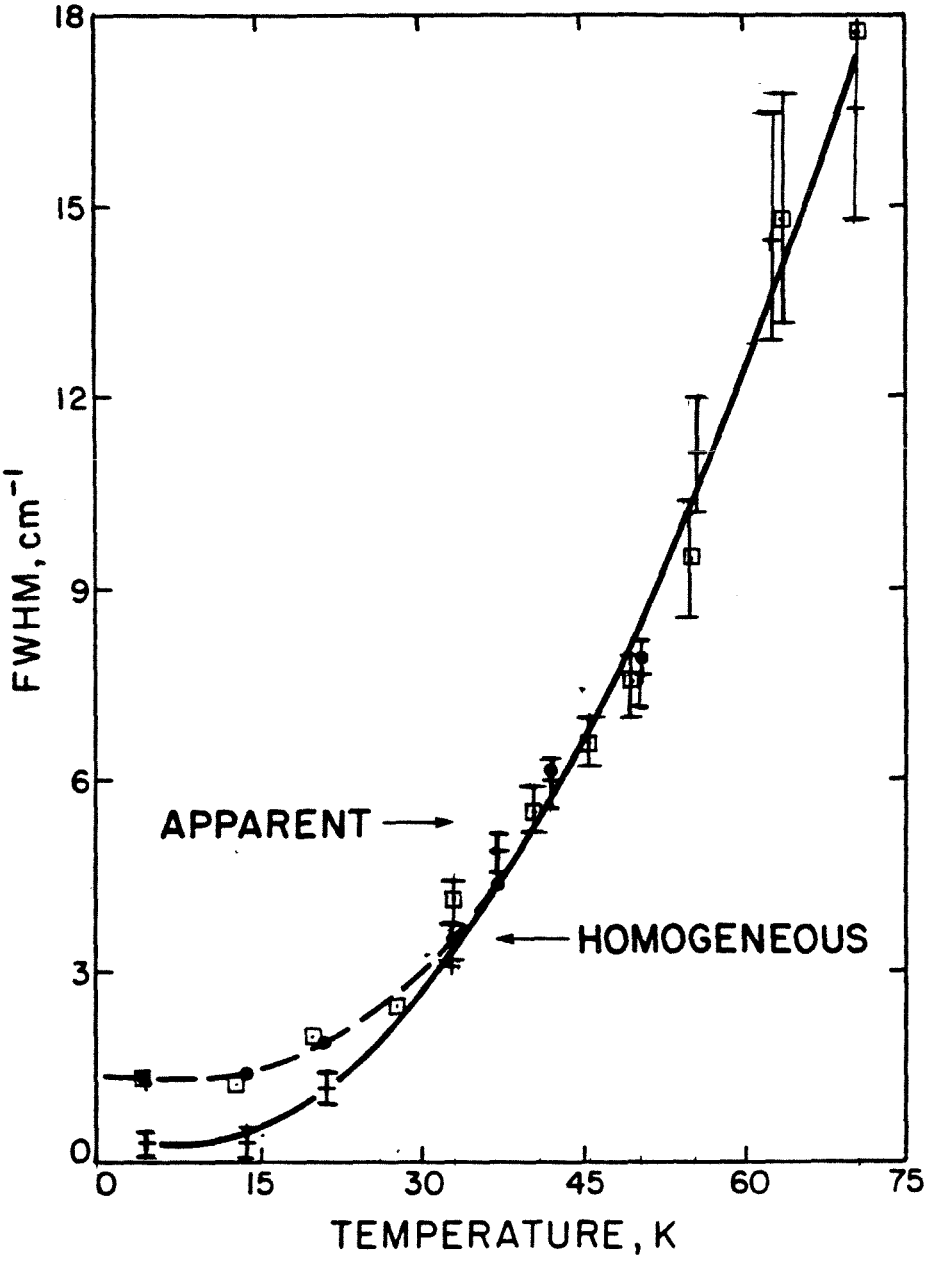

the lifetimes are of the order of at 100's of μsec (vide infra), one concludes the dephasing is not due to a single phonon process. If one were to use the total apparent width, the temperature dependence is less steep and a lower energy phonon (ca. 30 cm^{-1}) is obtained. We have also measured the temperature dependent emission lineshape of the (0,0). In all samples investigated, the emission was broader (typically 1 to 2 cm^{-1} FWHM at 4.2 K) and more symmetric than the absorption. Presumably, thermalization among the $\underset{\sim}{k}$~0 group has taken place (recall that even at 1.4 K, kT is greater than the absorption linewidth). Further, self reversal of the (0,0) [17] also makes study of the emission prone to error, so it was decided to use the absorption data for analysis.

In Fig. 2, the red shift of the (0,0) as a function of T is shown for each sublattice. Without correcting for the thermal expansion of the crystal, we find the red shift is well described by a single phonon process of 66 $\pm$ 8 cm^{-1} and fits T^3 and T^4 less well. Even though reasonable estimates of the volume thermal expansion and isothermal compressibility are available [18], the author knows of no measurements of the pressure dependent shift of the triplet electronic state, so correcting for the thermal expansion in the shift of the (0,0) is not yet possible. DBN might be expected to be similar to other soft organics (i.e. a low Debye Temperature) like crystalline alkanes [18], where the lattice expansion contributes a red shift to the total shift. In such a case, the actual single phonon describing the red shift would be lower energy than 66 cm^{-1}, conceivably around 42 cm^{-1}. From Fig. 2, at all temperatures, the

Figure 2. Shifts of the DBN triplet (0,0) absorption peaks for the upper and lower sublattices in pure H_6 DBN. Both shifts are to the red and the plot is only meant to show the shift magnitude. Lower sublattice shifts are denoted by crosses, the upper sublattice shifts by squares. The solid line is the fit to a single phonon occupation number for a 66 cm^{-1} mode.

ABSORPTION, LOWER SUBLATTICE (0,0) DBN H_6

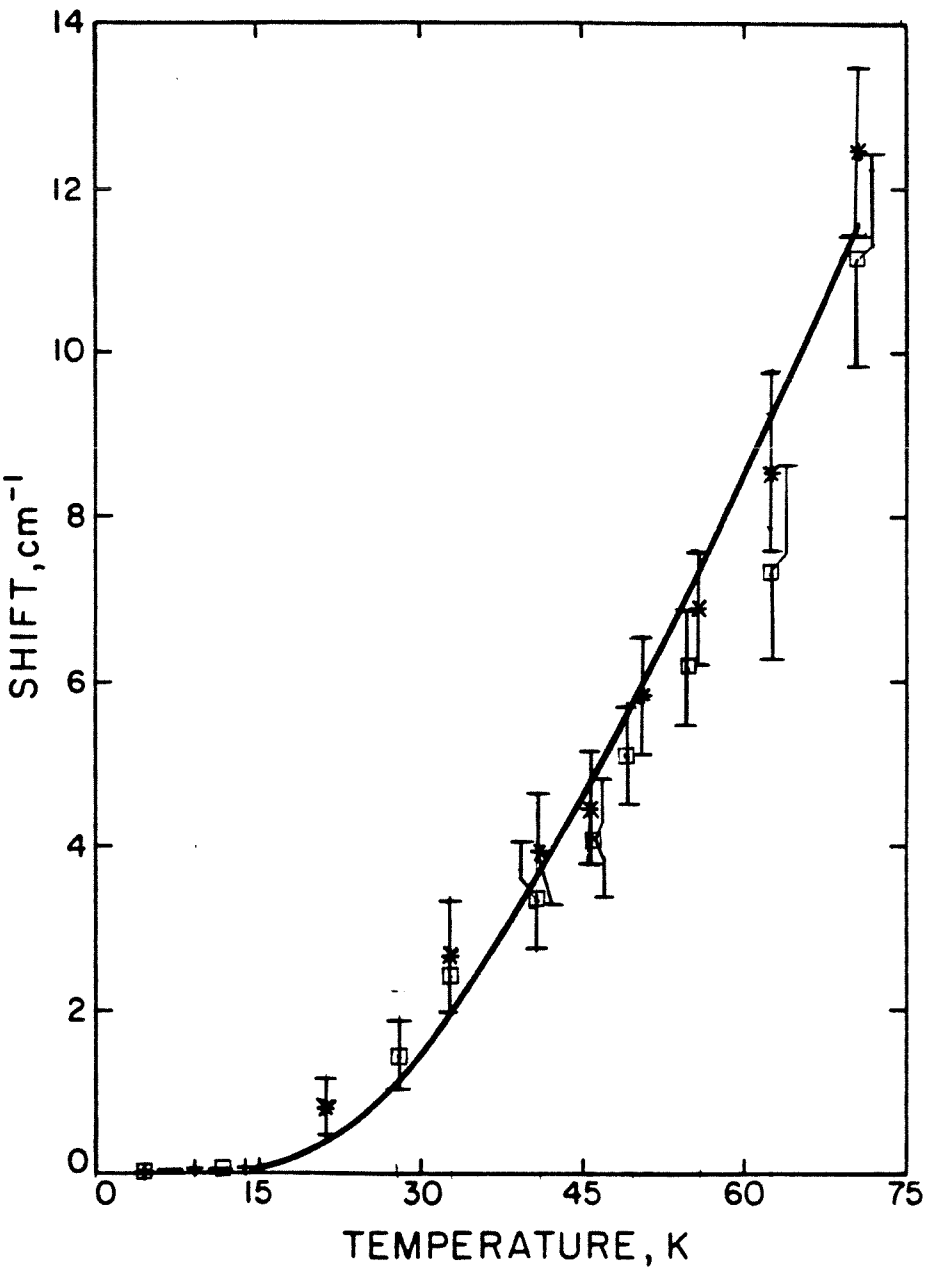

shift of the upper sublattice is seen to be within 2 cm^{-1} of the shift of the lower sublattice, in contrast with earlier work [12]. The discrepancy in the shift data is not understood. Possibly, the shift is affected by the strain in our crystals. The splitting between the two sublattices is 54 $\pm$ 2 cm^{-1}. Due to the large apparent broadening of the two $\underset{\sim}{k} \sim 0$ absorptions and lack of relative shift towards one another, one concludes that <u>interband</u> exchange is slow compared to the primary dephasing mechanism.

Though we have performed the absorption experiments for T > 70 K, it is of questionable usefulness, since phonon sidebands to the red and the blue make reliable baseline analysis difficult. To illustrate this, Fig. 3 shows a broad scan of the absorption spectrum of the two sublattices at high temperatures. The result is that beyond 70.5 K, the size of the error bars for the width make the data vanishingly useful.

We have also measured the absorption and photoexcitation spectra of 16% D_6/H_6 DBN (see Fig. 4). Though the $\underset{\sim}{k}\sim 0$ absorption in these samples is asymmetric at low temperatures, it is about an order of magnitude broader ($\sim$ 3 cm^{-1}) than the pure H_6 sample, which is likely due to the disordered linear chains. Since the shorter chains have their ''$\underset{\sim}{k}$''=0 states at higher energy than the infinite chains, their absorption produces inhomogeneity in the spectrum. Due to the inhomogeneity, it is not useful to plot the doped sample linewidth vs. T.

In order to investigate any effects of <u>intraband</u> exchange, we

Figure 3. Scans of the (0,0) absorption spectra of the two sublattices in H_6 DBN at high temperatures. The sloping linear baseline is due to the instrument response and is not a true spectral feature. The build up of the sidebands to the red and the blue of the $\underset{\sim}{k}\sim 0$ absorption is very pronounced at 70.5 K.

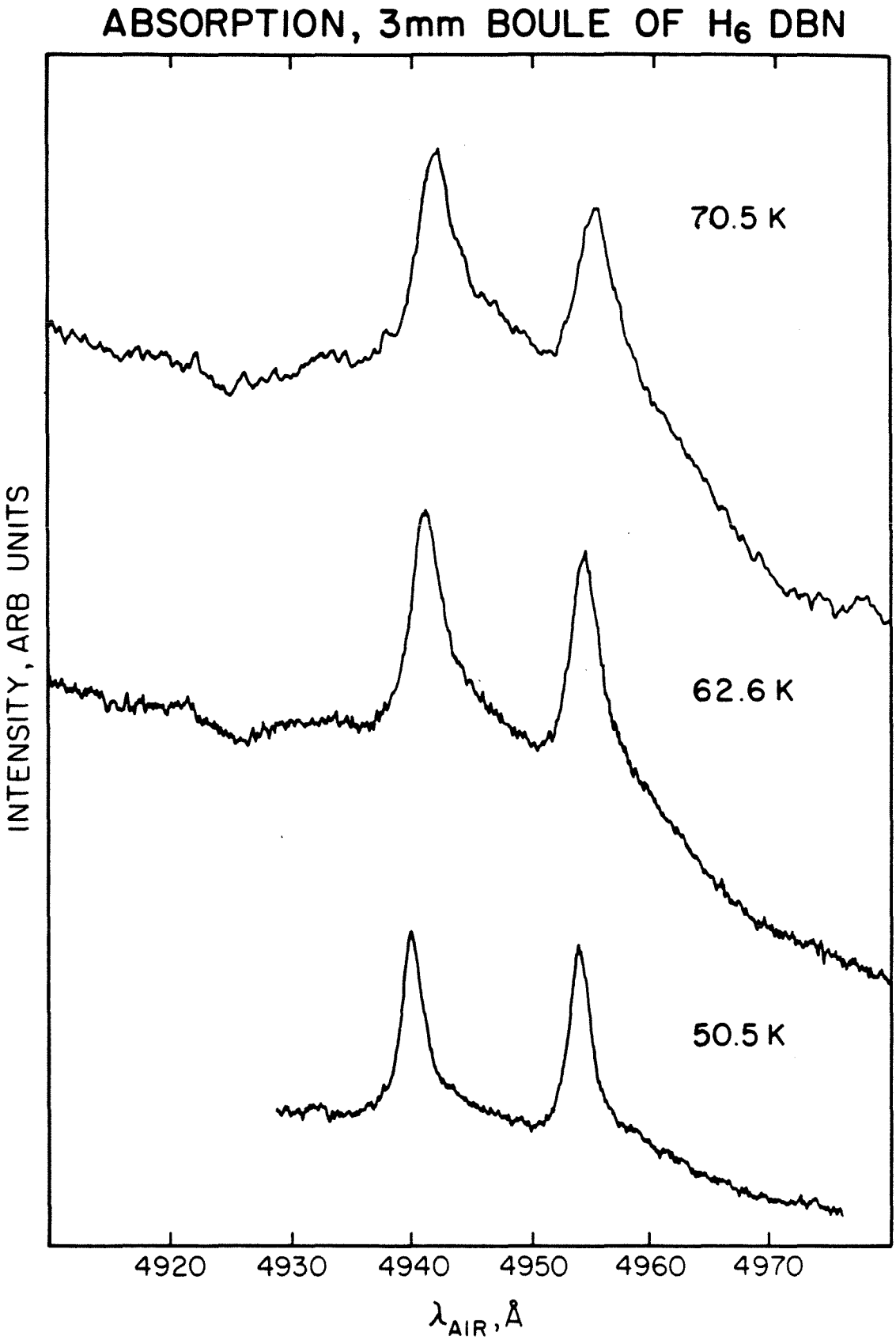
ABSORPTION, 3mm BOULE OF H_6 DBN
70.5 K
62.6 K
50.5 K
INTENSITY, ARB UNITS
4920
4930
4940
4950
4960
4970
λ_{AIR}, Å

Figure 4. The laser photoexcitation spectrum of the lower sublattice (0,0) transition in 16% D_6/H_6 DBN at 1.4 K. The spectrum was recorded by observing the (0,1350) BTBT with low resolution so as to gather emission from all the $\underset{\sim}{k}$ states. The laser bandwidth was 0.3 cm^{-1} and emission in a window 500 to 550 nsec after the laser pulse was collected. The FWHM is ~ 3 cm^{-1}.

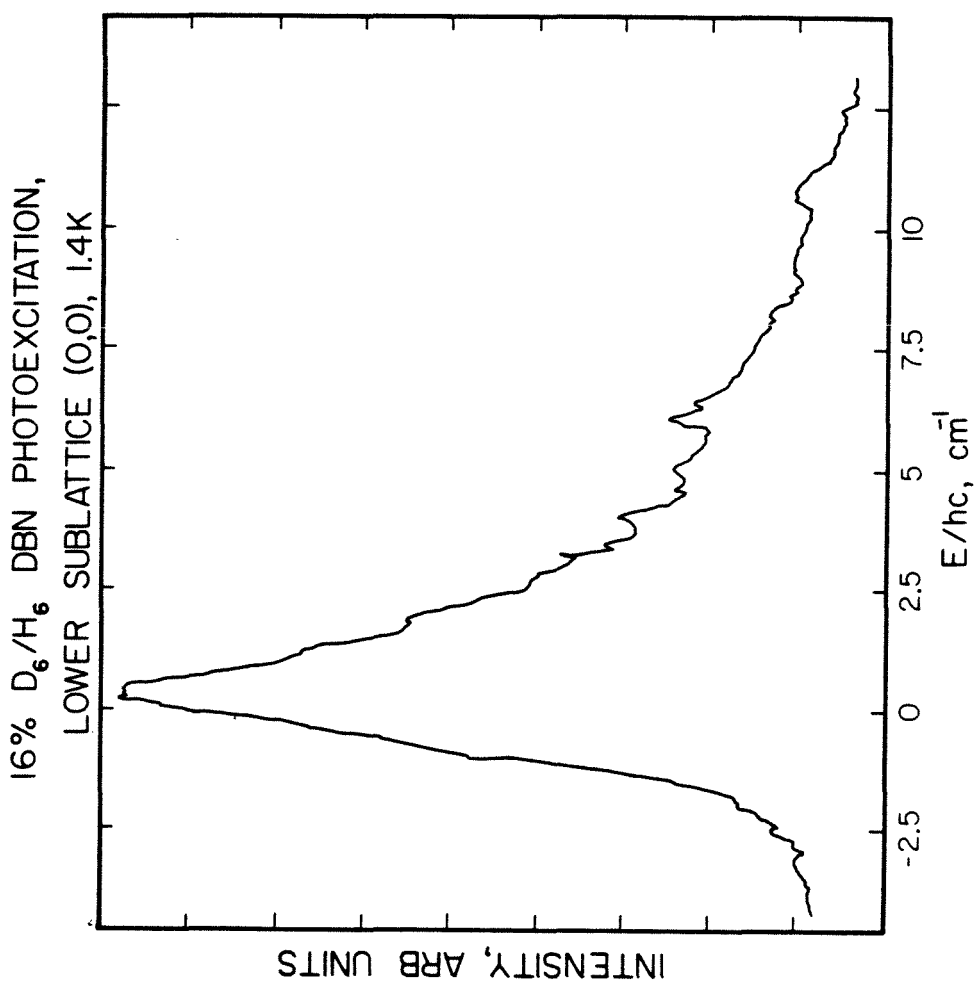
16% D_6/H_6 DBN PHOTOEXCITATION,
LOWER SUBLATTICE (0,0), 1.4K
INTENSITY, ARB UNITS
-2.5
0
2.5
5
7.5
10
E/hc, cm^{-1}

have measured the temperature-dependent steady state and transient BTBT spectra. Moreover, these measurements have been performed in pure and doped crystals. One should note that most of the molecular vibrations in DBN exhibit a BTBT, which implies that the vibrations are not completely local and must, to an extent, form vibrational exciton bands. One can qualitatively see the growth of the BTBT on many of the molecular modes by looking at the broadening of the transitions in Fig. 5. For the purposes of this work, we shall concentrate on the BTBT corresponding to the molecular (0,1350) transition (at ~ 5305 Å), since this transition has little resonance Raman activity and is ideal for the time resolved studies discussed below. The (0,1350) transition is well suited for the temperature dependent studies since self absorption would not be a problem as it is in the (0,0) transition.

Measurement of the BTBT spectrum offers information different from and complementary to the (0,0) transition. The (0,0) line is transition from a dispersionless, local state to a band state, and as such, only the $\underset{\sim}{k}\sim 0$ region is optically accessible. However, in the BTBT, initial and final states are band states and outside of symmetry restrictions, one needs only to conserve momentum in the transition, i.e. labeling the upper states by wavevector $\underset{\sim}{k}$, lower states by $\underset{\sim}{q}$ and the photon by $\underset{\sim}{j}$, $\underset{\sim}{k}+\underset{\sim}{q}+\underset{\sim}{j} = 0$. The difference between the (0,0) and the BTBT is schematized in Fig. 6.

From the steady state BTBT data, one arrives at three conclusions. (1) The BTBT lineshape broadens and shifts to the red as temperature increases, implying that <u>intraband</u> exchange is not

Figure 5. Broad, moderate resolution scan of the lowest triplet emission spectrum of 16% D_6/H_6 DBN at low and high temperatures. The apparent broadening of many of the transitions is due to the growth of the BTBT's which are built on the molecular vibrational modes.

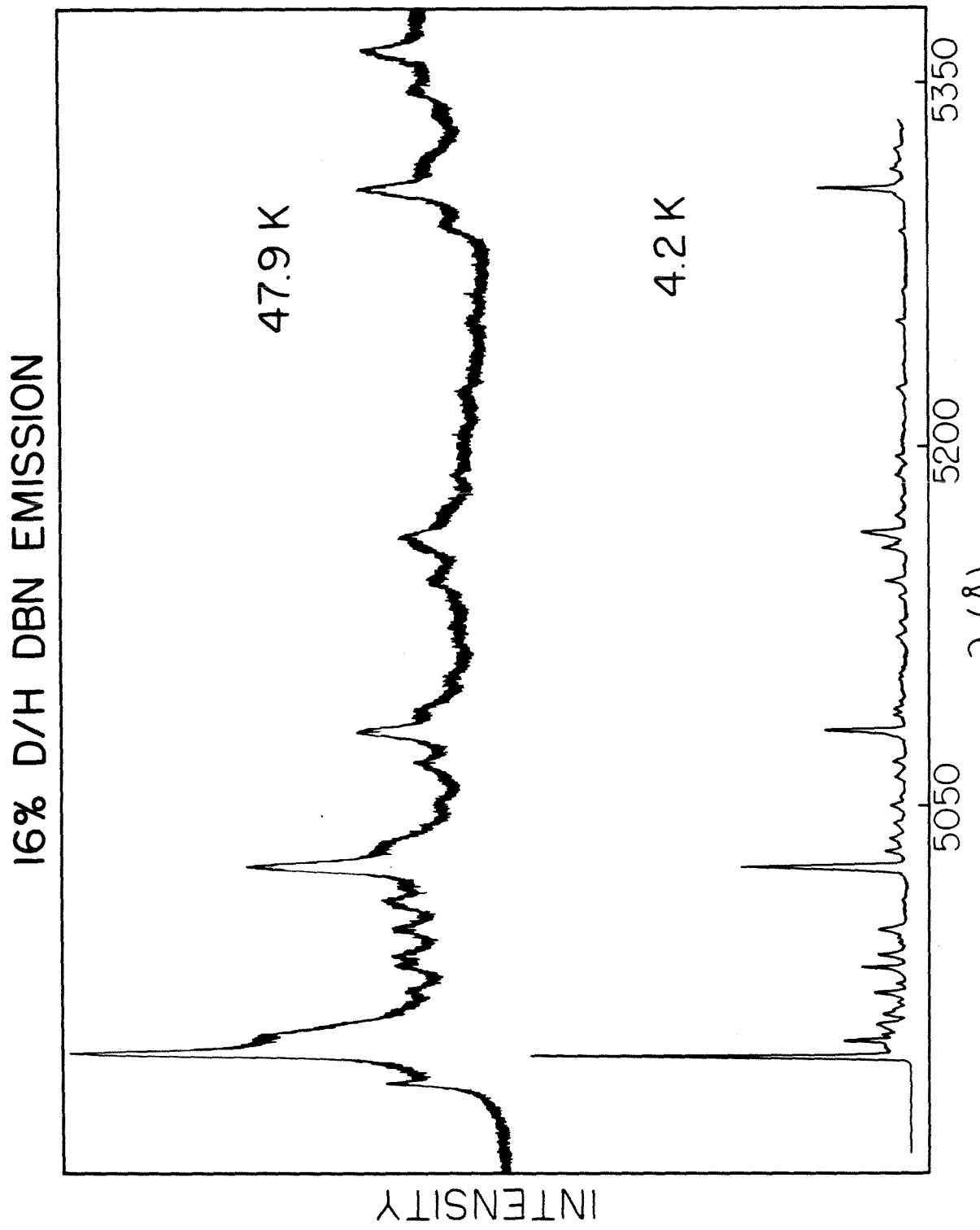
16% D/H DBN EMISSION
47.9 K
4.2 K
INTENSITY
5050
5200
5350
λ (Å)

Figure 6. A schematic representation of the BTBT and (0,0) transition in terms of energy, wavevector $\underset{\sim}{k}$ (electronic exciton) and wavevector $\underset{\sim}{q}$ (vibrational exciton). Note that for the BTBT, emission from all $\underset{\sim}{k}$ states to the ground vibrational exciton is allowed and the different $\underset{\sim}{k}$ states are energetically resolvable. For the (0,0) transition, only the $\underset{\sim}{k}\sim 0$ state is observable.

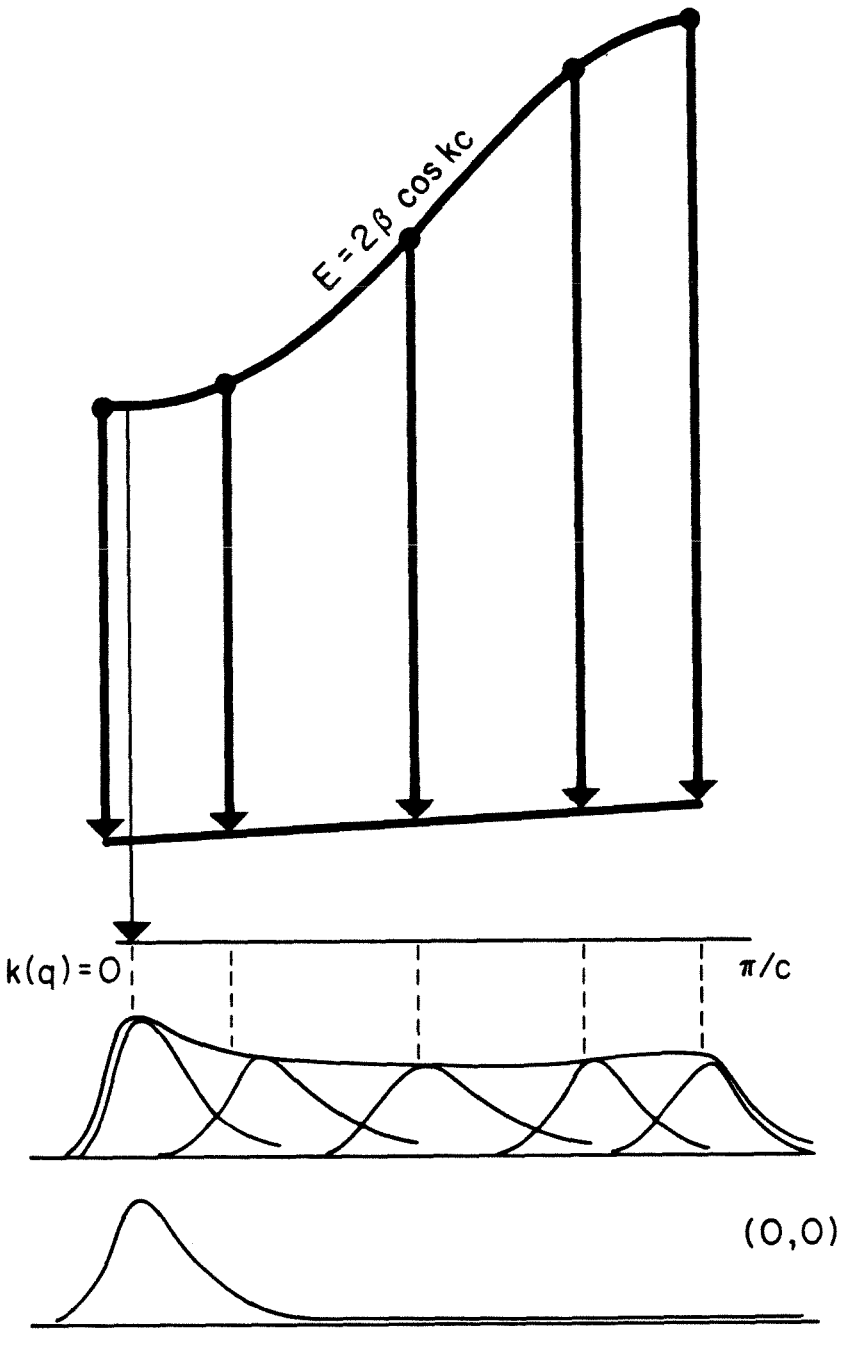
E=2β cos kc
k(q)=0
π/c
(0,0)

important. Inasmuch as there is intraband exchange, there should be collapse of the BTBT lineshape. The shift and broadening of the BTBT is shown in Fig. 7 for a crystal of pure H_6 DBN. (2) Heavy disorder (up to 16% barriers) has no detectable effect on the BTBT lineshape (and implicitly little effect on the dephasing mechanism). A few of the temperature dependent line shapes are shown for the 16% D_6/H_6 sample in Fig. 8. (3) The vibrational exciton originating from the 1350 cm^{-1} molecular mode has a nearest neighbor interaction that is negative in sign and of the order of 1 to 2 cm^{-1}. Since the nearest neighbor interaction of the triplet excitons is -6.2 cm^{-1}, a 24.8 cm^{-1} bandwidth is predicted, whereas the apparent $\underset{\sim}{k}=0$, $\underset{\sim}{k}=\pi/\underset{\sim}{c}$ splitting of the BTBT is ~17 cm^{-1}. Given that the selection rule $\underset{\sim}{k}+\underset{\sim}{q}+\underset{\sim}{j}=0$ holds, one is forced to conclude that $\underset{\sim}{q}=0$ lies at the bottom of the vibrational exciton band (one should note that the 1 to 2 cm^{-1} bandwidth is reasonable in view of typical molecular crystal vibrational factor group splittings from IR dichroism and mixed crystal studies [19]). Moreover, the (0,1350) BTBT lineshape is not polarization dependent and is strongly polarized horizontally with respect to the vertical growth axis (see Fig. 9), consistent with an out of molecular plane electronic moment and totally symmetric vibrational mode assignment [13].

We have directly measured the population exchange rate among the different $\underset{\sim}{k}$-states by looking at the transient BTBT lineshape [20] as a function of temperature. From the transient experiments, one arrives at three conclusions. (1) The population exchange rate among the $\underset{\sim}{k}$ states is of the order of 10 μsec and is weakly

Figure 7. The steady state (0,1350) BTBT emission spectrum for pure H_6 DBN as a function of temperature. The data clearly show the growth of the emission from the $\underset{\sim}{k}=\pi/\underset{\sim}{c}$ states with temperature (producing the characteristic ''double hump'' density of states for 1-D systems). At higher temperatures, the BTBT shifts to the red and broadens rapidly into a structureless asymmetric band.

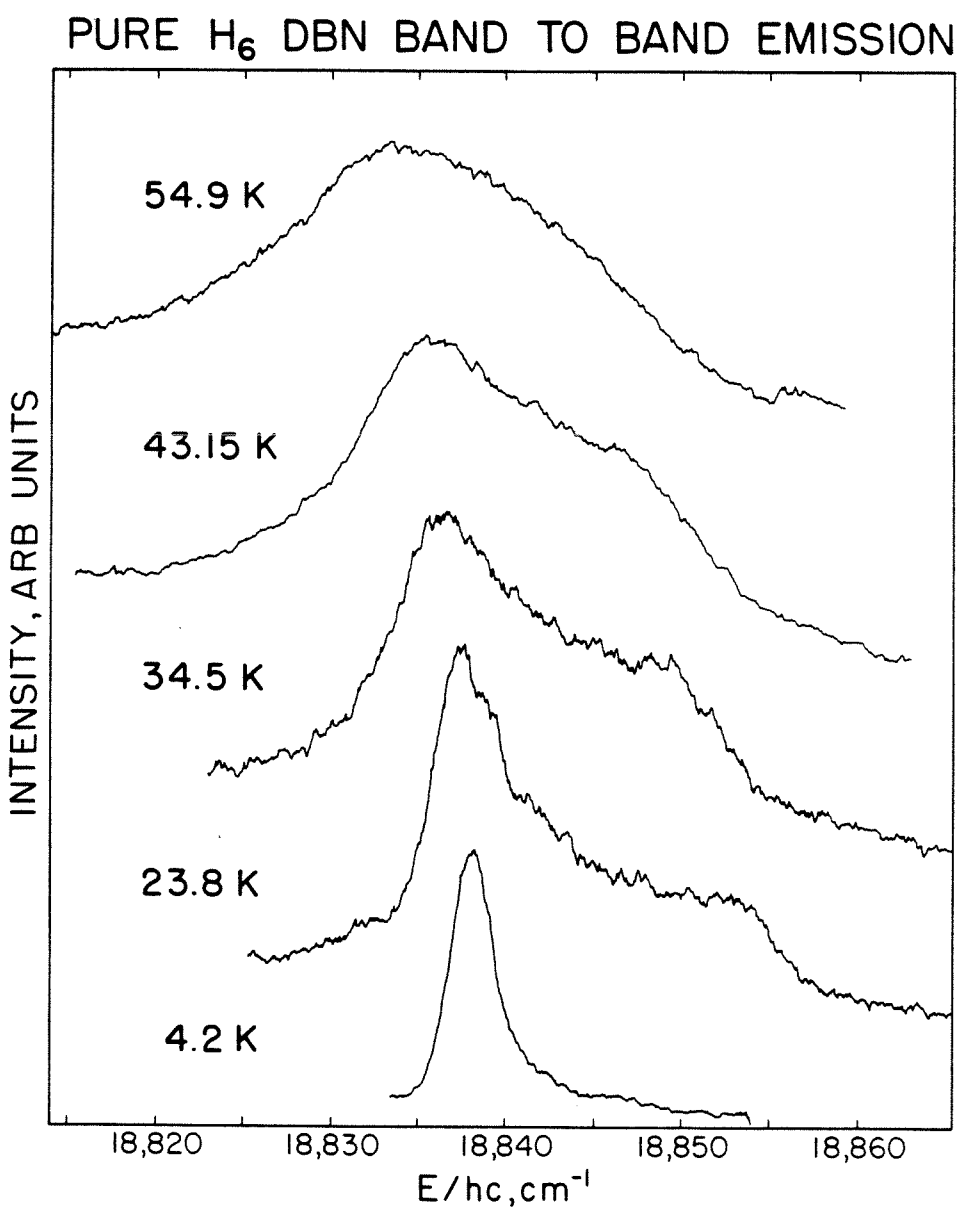
PURE H_6 DBN BAND TO BAND EMISSION
54.9 K
43.15 K
34.5 K
23.8 K
4.2 K
INTENSITY, ARB UNITS
18,820
18,830
18,840
18,850
18,860
E/hc, cm^{-1}

Figure 8. The steady state (0,1350) BTBT emission of 16% D_6/H_6 DBN at 4.2, 17 and 62.2 K.

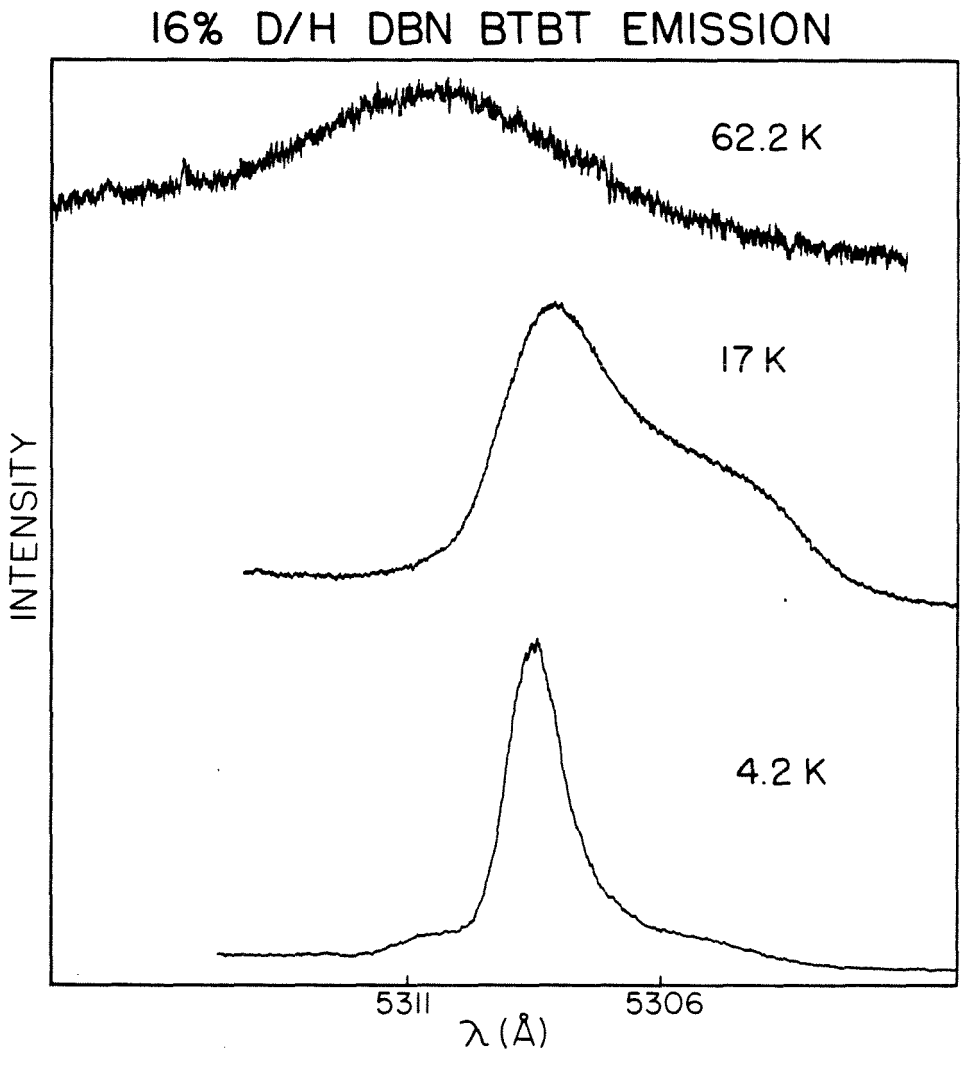
16% D/H DBN BTBT EMISSION
62.2 K
17 K
4.2 K
INTENSITY
5311
5306
λ (Å)

Figure 9. The polarized steady state (0,1350) BTBT emission of H_6 DBN at intermediate temperature, 34.5 K. The vertically polarized emission was 5–10 times weaker than the horizontally polarized emission and is therefore noisier.

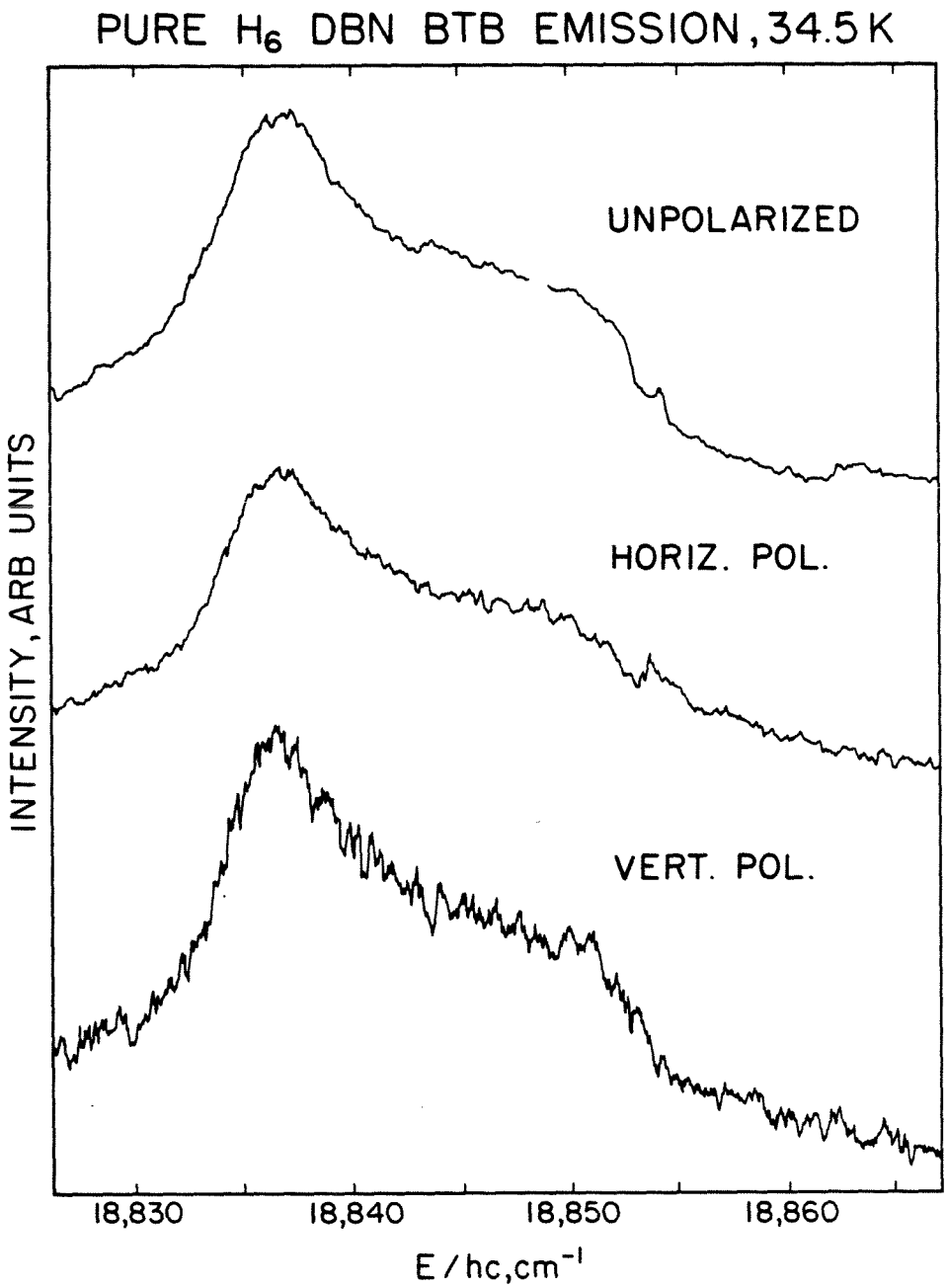
PURE H_6 DBN BTB EMISSION, 34.5 K
UNPOLARIZED
HORIZ. POL.
VERT. POL.
INTENSITY, ARB UNITS
18,830
18,840
18,850
18,860
E / hc, cm^{-1}

temperature dependent. (2) The inelastic scattering time amongst the $\underset{\sim}{k}$ states is essentially unaffected by up to 16% substitutional disorder. (3) Relaxation between the two sublattices is rapid and does not scramble the $\underset{\sim}{k}$ states (i.e. the relaxation obeys a $\Delta\underset{\sim}{k}=0$ ''selection'' rule).

The idea behind the transient BTBT experiments is that one prepares only the $\underset{\sim}{k}\sim 0$ state by ground state absorption of a laser pulse. Then one monitors the evolution of <u>all</u> $\underset{\sim}{k}$ states by observing the BTBT (see Fig. 10). The transient BTBT spectrum of pure H_6 DBN at 20 K is shown in Fig. 11. About ~20 μsec is required for the band states to reach thermal equilibrium with one another (cf. the steady state spectra in Fig. 7). The data unequivocally illustrate that the intraband inelastic scattering rate (intraband exchange) is slow and of the order of 10 μsec. Figure 11 demonstrates the beauty of the transient BTBT experiments in directly revealing the dynamical evolution of all $\underset{\sim}{k}$ states, rather than inferring it through the (0,0) transition (as all previous experiments have done). Figures 12 and 13 show the transient BTBT spectra at the same temperature (20 K), but for 5% and 16% D_6/H_6 DBN. Within the signal to noise ratio, the inelastic scattering time in the pure H_6, 5% and 16% D_6/H_6 samples is the same. Figure 14 is a plot of the time dependent emission intensity ration of the $\underset{\sim}{k}=\pi/\underset{\sim}{c}$ and $\underset{\sim}{k}=0$ states for 5% D_6/H_6 DBN at 20 K. The error bars are large, but using a simple two level model with time-independent transfer rates one obtains a scattering rate constant of the order of 10 μsec. However, until we obtain higher S/N data for the BTBT transients (on the 5% doped and other samples), we cannot seriously test different

Figure 10. The scheme of the transient BTBT experiments. A laser pulse prepares exclusively $\underset{\sim}{k}\sim 0$ eigenstates via the (0,0) transition. Then, elastic and inelastic scattering occur. The inelastic scattering transfers population to $\underset{\sim}{k} \neq 0$ states, which is monitored by the BTBT emission lineshape.

TRANSIENT BAND-TO-BAND SCATTERING

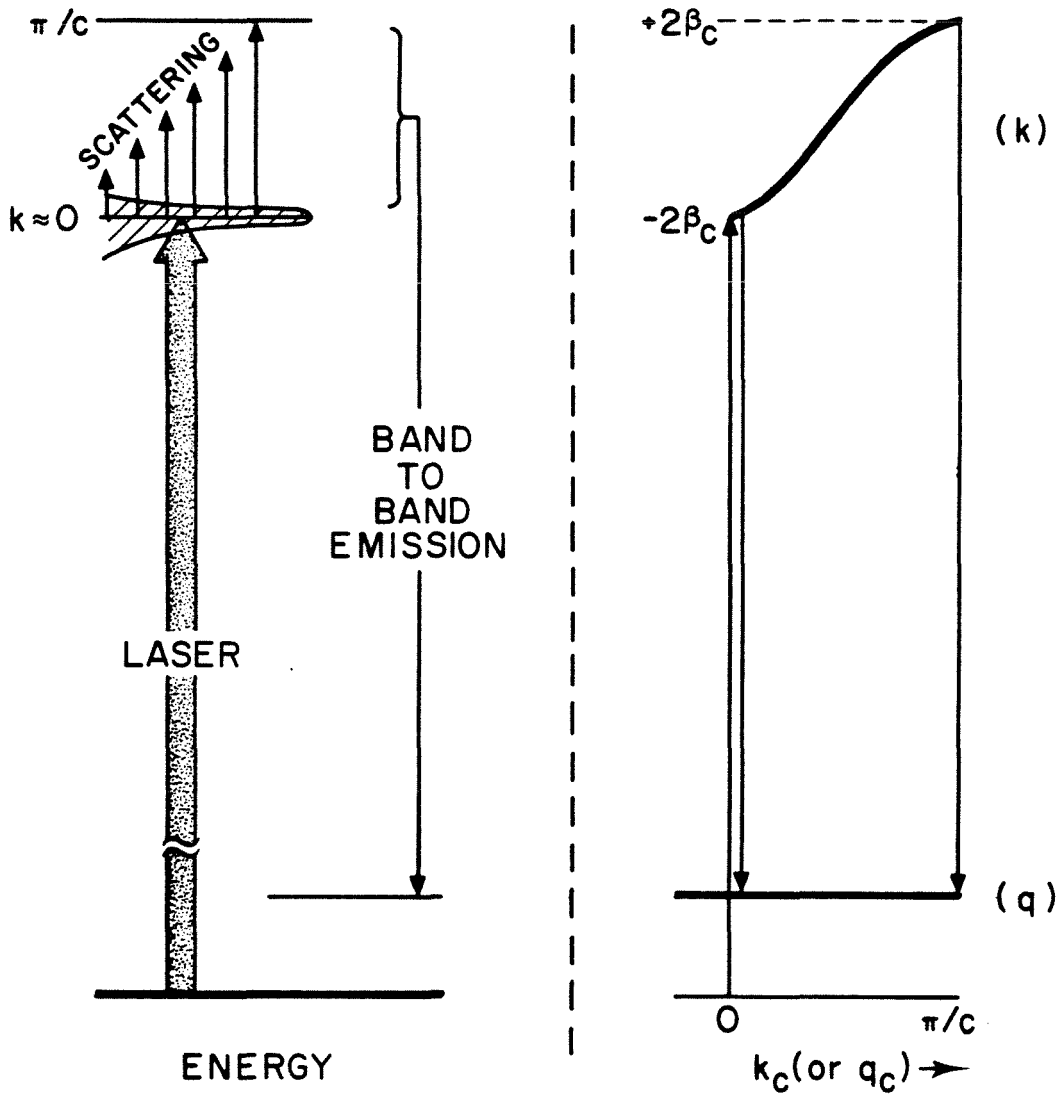

Figure 11. Transient BTBT spectra of H_6 DBN at 20 K. One can clearly see that 500 nsec after the laser pulse, primarily the $\underset{\sim}{k}=0$ region is populated. At 10 μsec, much of the population has been scattered to $\underset{\sim}{k} \neq 0$ states and the band has reached thermal equilibrium by 100 μsec.

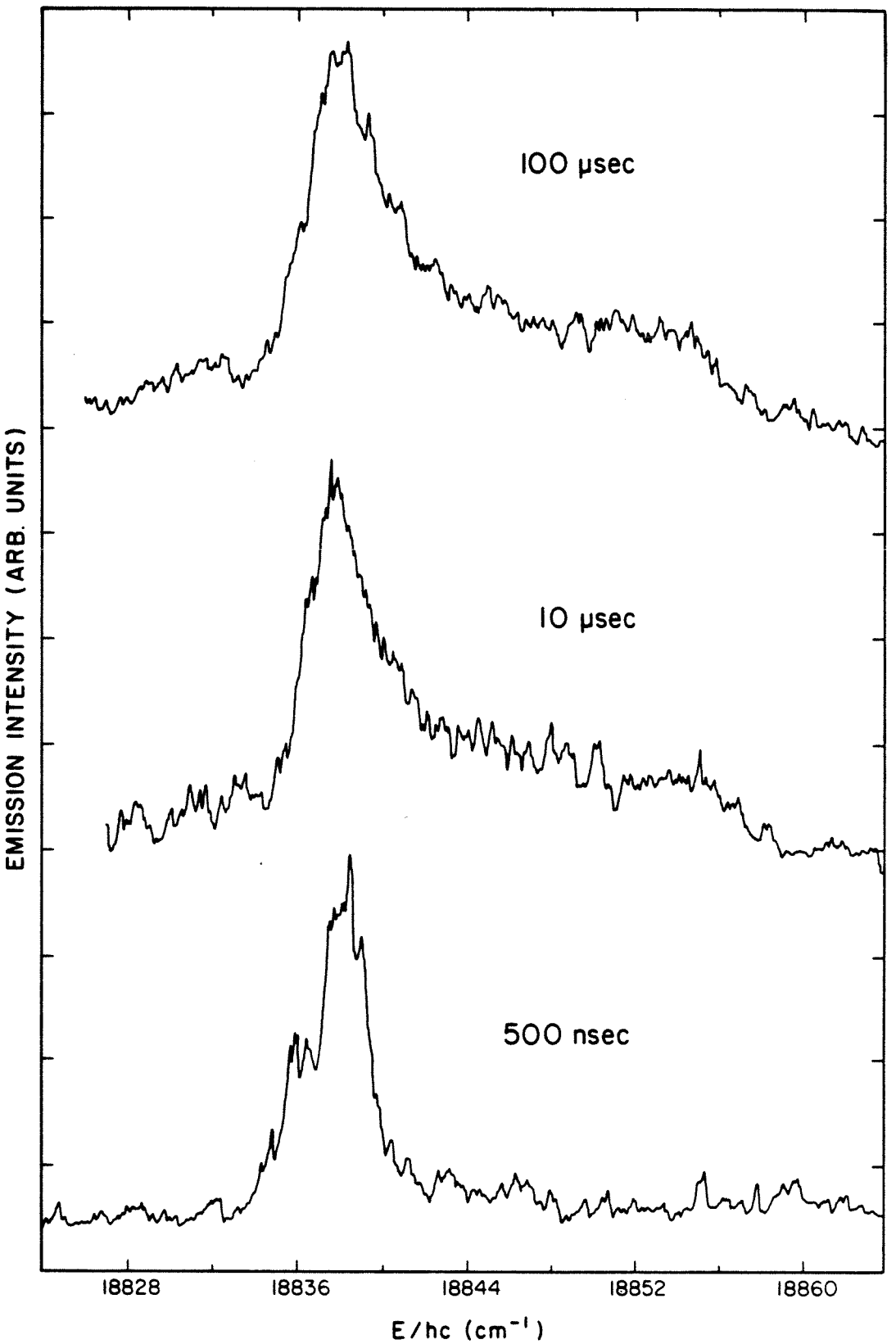
DBN-H6 BTBT PUMP LOWER SUBLATTICE, 20K
100 μsec
10 μsec
500 nsec
EMISSION INTENSITY (ARB. UNITS)
18828
18836
18844
18852
18860
E/hc (cm⁻¹)

Figure 12. Transient BTBT spectra of 5% D_6/H_6 DBN at 20 K. Comparing the data of this figure with those of Fig. 11, one can easily see there is little or no change in the inelastic scattering rate upon doping.

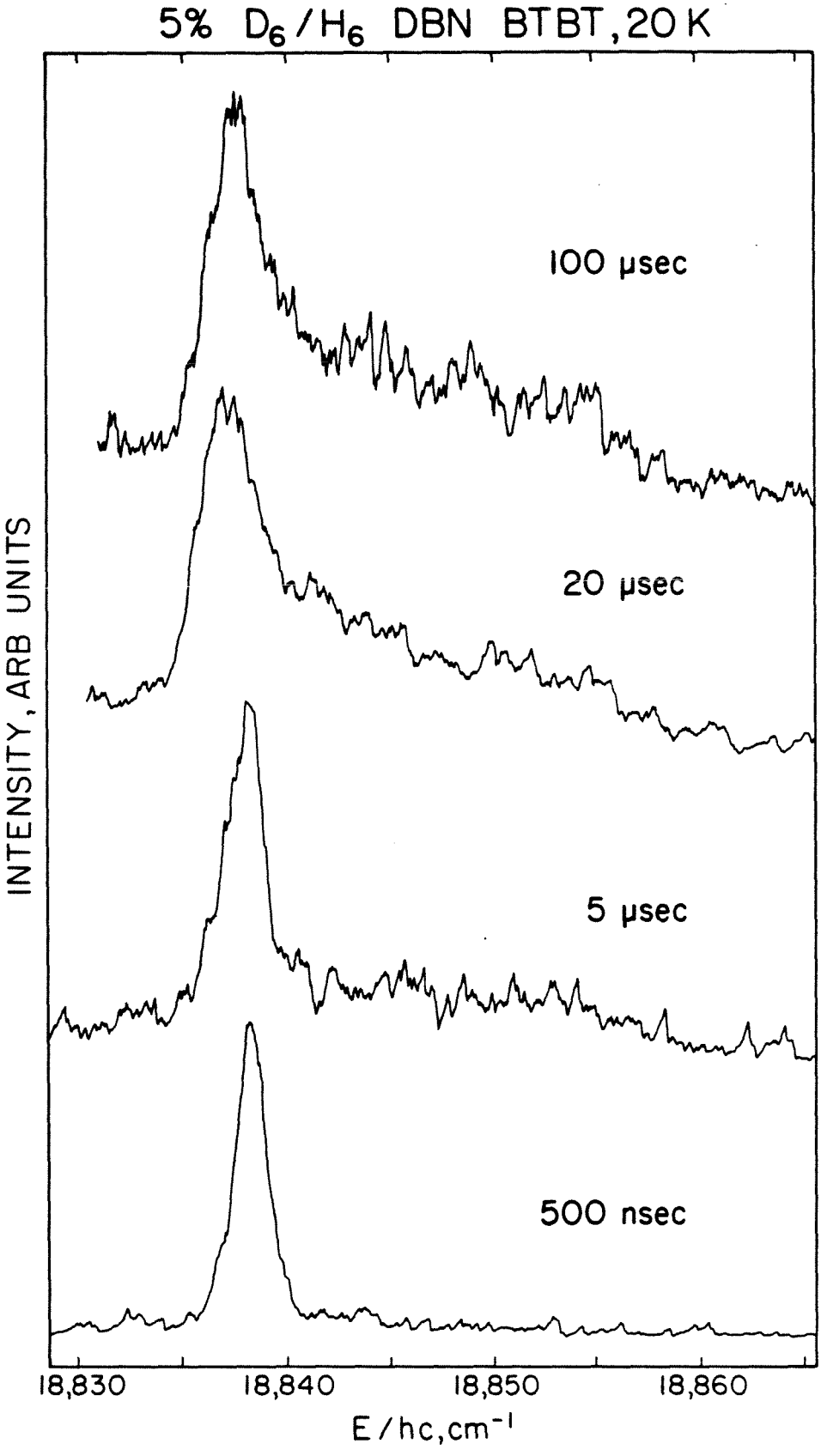
5% D_6/H_6 DBN BTBT, 20 K
100 μsec
20 μsec
5 μsec
500 nsec
INTENSITY, ARB UNITS
18,830
18,840
18,850
18,860
E/hc, cm^{-1}

Figure 13. Transient BTBT spectra of 16% D_6/H_6 DBN at 20 K. This figure should be compared with the transient data on the pure and 5% crystals to demonstrate that the inelastic scattering has not been dramatically affected by disordering the crystal with up to 16% of 65 cm^{-1} barriers! It is worth mentioning that the 16% doped samples always yielded better signal to noise ratios for the transients than the pure or 5% samples, probably due to the barriers preventing the excitation from reaching traps and defects in the crystal.

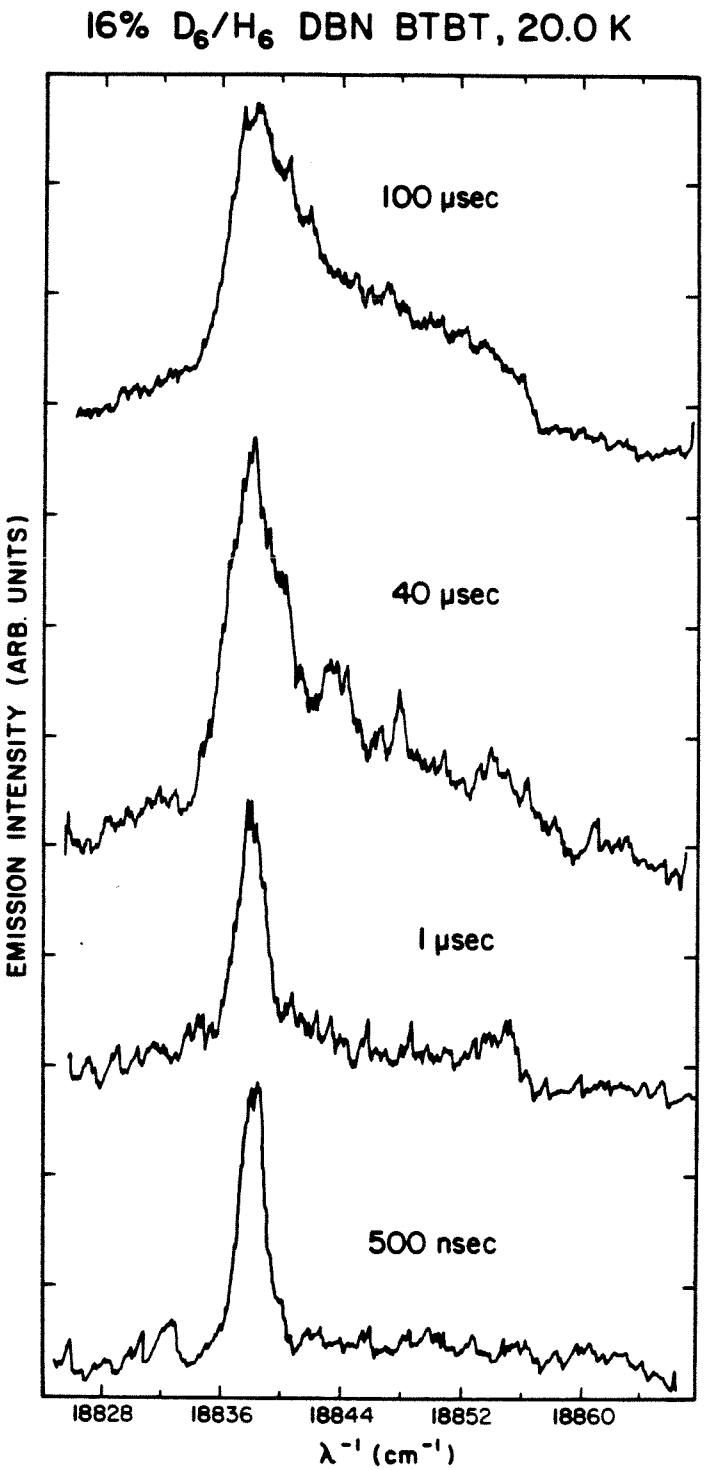
16% D_6/H_6 DBN BTBT, 20.0 K
100 μsec
40 μsec
1 μsec
500 nsec
EMISSION INTENSITY (ARB. UNITS)
18828
18836
18844
18852
18860
λ^{-1} (cm^{-1})

Figure 14. Time-dependent emission intensity ratio of the $\underset{\sim}{k}=\pi/\underset{\sim}{c}$ and $\underset{\sim}{k}=0$ BTBT's in 5% D_6/HJh6 DBN at 20 K.

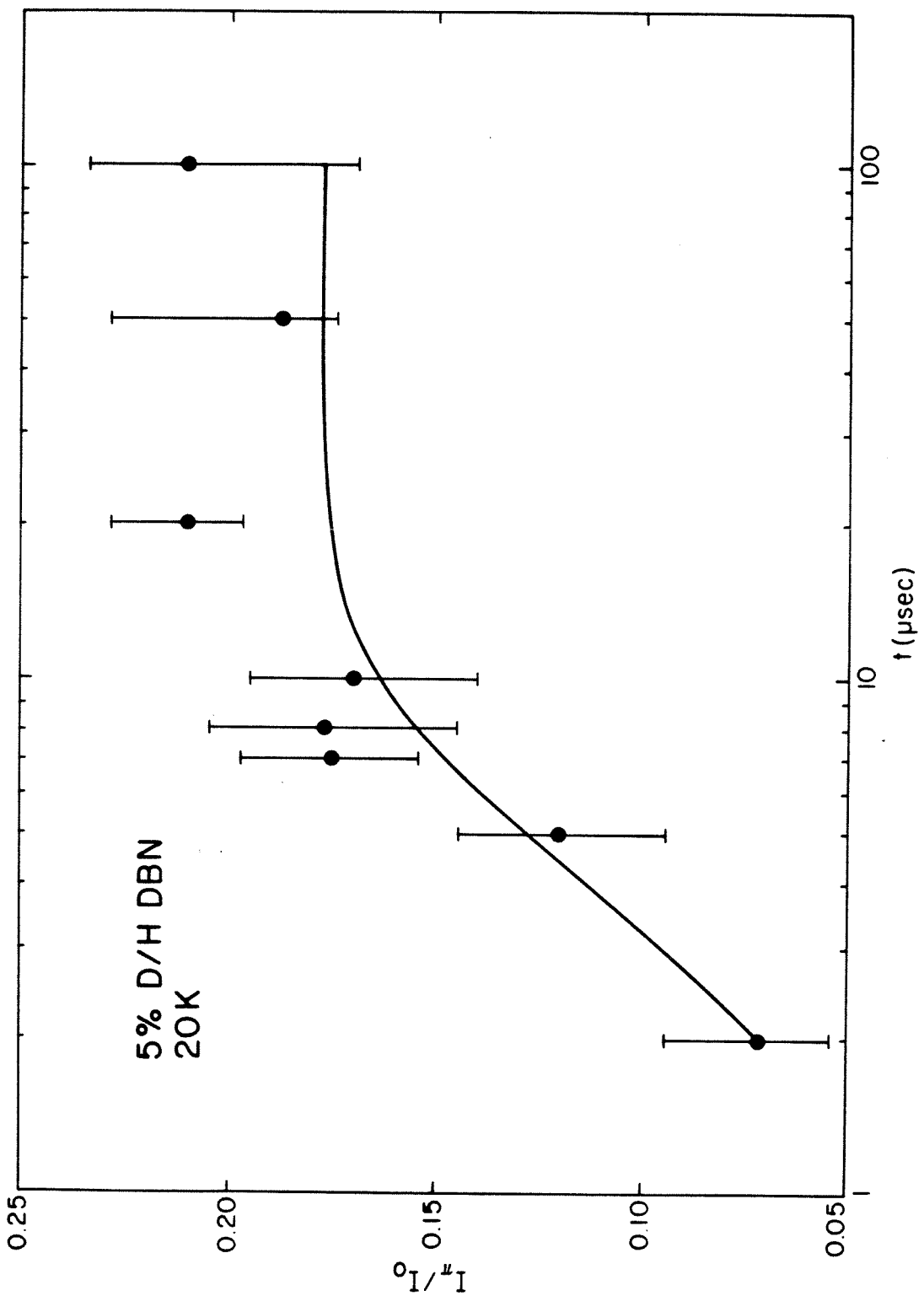
5% D/H DBN
20K
I_π/I_o
0.25
0.20
0.15
0.10
0.05
1
10
100
t (μsec)

scattering models.

To measure the effects of interband scattering, we have performed transient BTBT experiments where the laser is in resonance with the $\underset{\sim}{k}\sim 0$ state of the upper sublattice and ground state as shown in the energy level diagram of Fig. 15. It was found that all the population had relaxed from the upper sublattice $\underset{\sim}{k}\sim 0$ to the lower sublattice in less than 500 nsec and that all the population was deposited in the $\underset{\sim}{k}=0$ region of the lower sublattice (see Fig. 16). This indicates that the relaxation rate from the upper sublattice is much faster than the inelastic scattering rate in the upper sublattice and that scattering between the two lattices may be a single phonon process, as has been suggested before [12]. Relaxation between the sublattices is not likely to be a multiphonon process, since multiphonon relaxation would tend to populate many of the $\underset{\sim}{k}$ states in the lower sublattice due to the increased number of allowed relaxation paths. The short time linewidth of the BTBT from pumping the upper sublattice in Fig. 16 is slit-limited.

In addition to measuring the time resolved spectra of the BTBT, we have measured the decay of the BTBT as a function of time. However, the decays are very complex since there are three triplet sublevels and other processes making the apparent lifetimes highly non-exponential. Pumping the origin and observing the decay of the total BTBT (wide slits) at 4.2 K in pure H_6 DBN, the decay appeared to be roughly the sum of two exponential with decay constants of 99 and 463 μsec, which is in good agreement with

Figure 15. An abbreviated energy level diagram of the ground and lowest triplet states of crystalline DBN. E1 is the lower sublattice exciton, E2 is the upper sublattice exciton and v indicates a vibrational mode. The wavy lines indicate the different resonances pumped in the transient BTBT experiments and the broad, dark arrow denotes the BTBT used to monitor the inter- and intraband scattering dynamics.

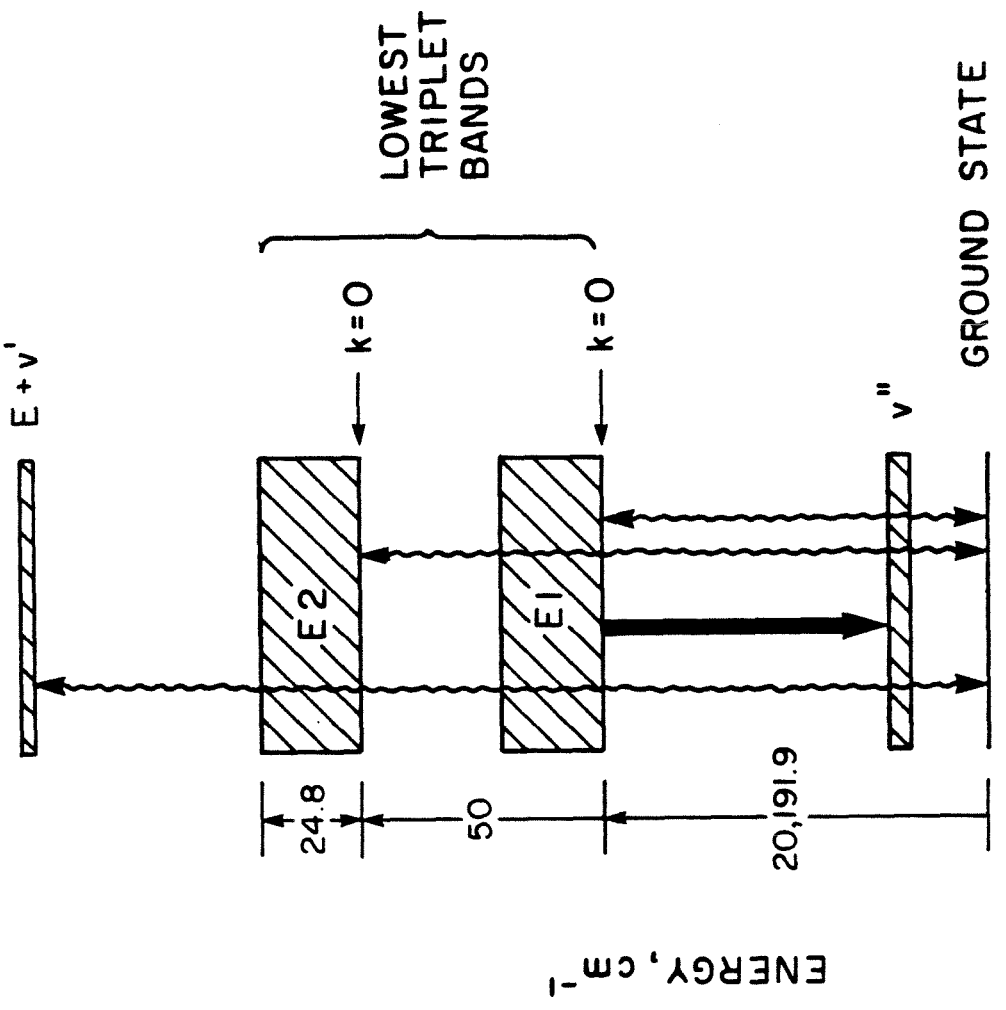
LOWEST TRIPLET BANDS
k=0
k=0
E+v'
E2
E1
v"
GROUND STATE
24.8
50
20,191.9
ENERGY, cm⁻¹

Figure 16. Transient (0,1350) BTBT spectra of 5% D_6/H_6 DBN when pumping the upper and lower sublattice. Within signal to noise ratios, the relaxation between the sublattices is complete in less than 500 nsec and does not scramble the $\underset{\sim}{k}$ states. After relaxation to the lower sublattice, inelastic scattering in the lower sublattice proceeds as if its own $\underset{\sim}{k}\sim 0$ state had been pumped. The short-time linewidth that occurs from pumping the upper sublattice is slit-limited. The wider slits were necessary to get comparable S/N as when pumping the lower sublattice.

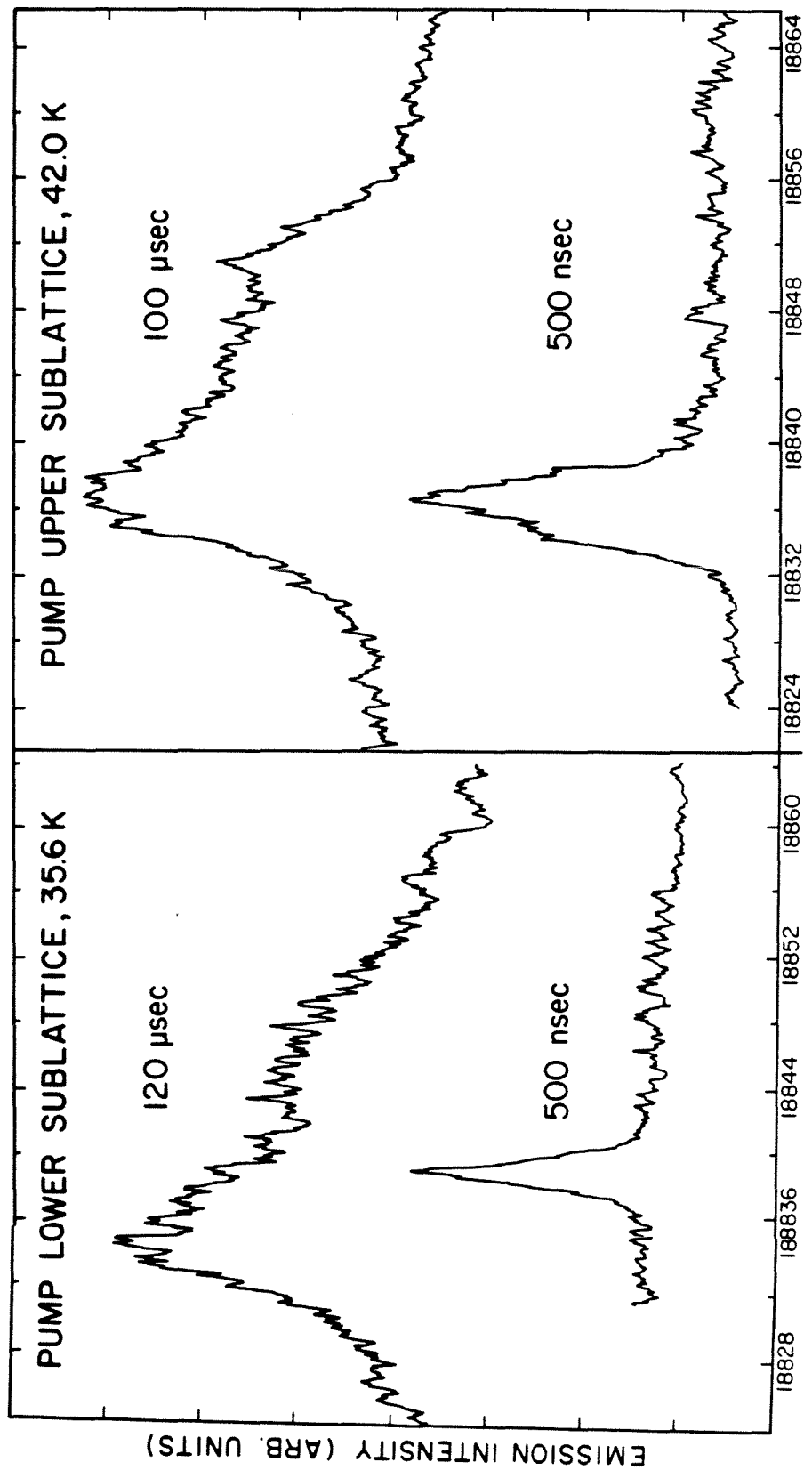
5% D_6/H_6 DBN BTBT TRANSIENTS
PUMP LOWER SUBLATTICE, 35.6 K
120 μsec
500 nsec
PUMP UPPER SUBLATTICE, 42.0 K
100 μsec
500 nsec
EMISSION INTENSITY (ARB. UNITS)
18828
188836
18844
18852
18860
18824
18832
18840
18848
18856
18864
E / hc (cm⁻¹)

the work of Nishimura et al. [21]. However, as the temperature was raised, the slits narrowed or the lattice was doped, the decays become more complex than a sum of two exponentials, making reliable interpretation difficult or impossible. A multiple resonance method, such as PMDR or ODMR on the BTBT is the only reasonable way the author is aware of to untangle the complex decay patterns. Microwave-optical resonance studies have been done [22], but only on the (0,0) transition. For the purposes of this work, however, what is important about the decays is that on the time scale of the intraband inelastic scattering, the intrinsic radiationless decay rates are not drastically affected and this is shown in Fig. 17.

VI. THEORETICAL SIMULATION OF STEADY STATE BTBT

Using the multilevel exchange theory developed earlier, we have simulated the experimental steady state BTBT spectra. To this end, we have taken a model linear chain, 10 molecules long, and used the known nearest neighbor interaction and Boltzmann factors to calculate the spectrum. Chains longer than 10 were tried, but no visible change in the simulated BTBT spectrum was obtained. Using different values of the off-diagonal coupling matrix elements at two temperatures, we generated the theoretical BTBT spectra shown in Fig. 18. One should note that even for off-diagonal coupling of 0.1 cm^{-1}, the BTBT narrows rather than broadens with temperature. The observed BTBT broadens and it is clear that exchange can only narrow the BTBT. However, if one assumes that each of the $\underset{\sim}{k}$-states is broadened by the same elastic scattering mechanism, the simulated BTBT broadens with temperature (cf. Fig. 19) and in fact fits the

Figure 17. BTBT decays of the $\underset{\sim}{k}\sim 0$ region of the H_6, 5 and 16% D_6 H_6 DBn at 4.2 K. The nonlinearity of the decays in a semilog plot helps demonstrate the complexity of the decay law. The data show that on a time scale of 1 msec the radiationless decay of the pure and doped samples are not drastically different from one another.

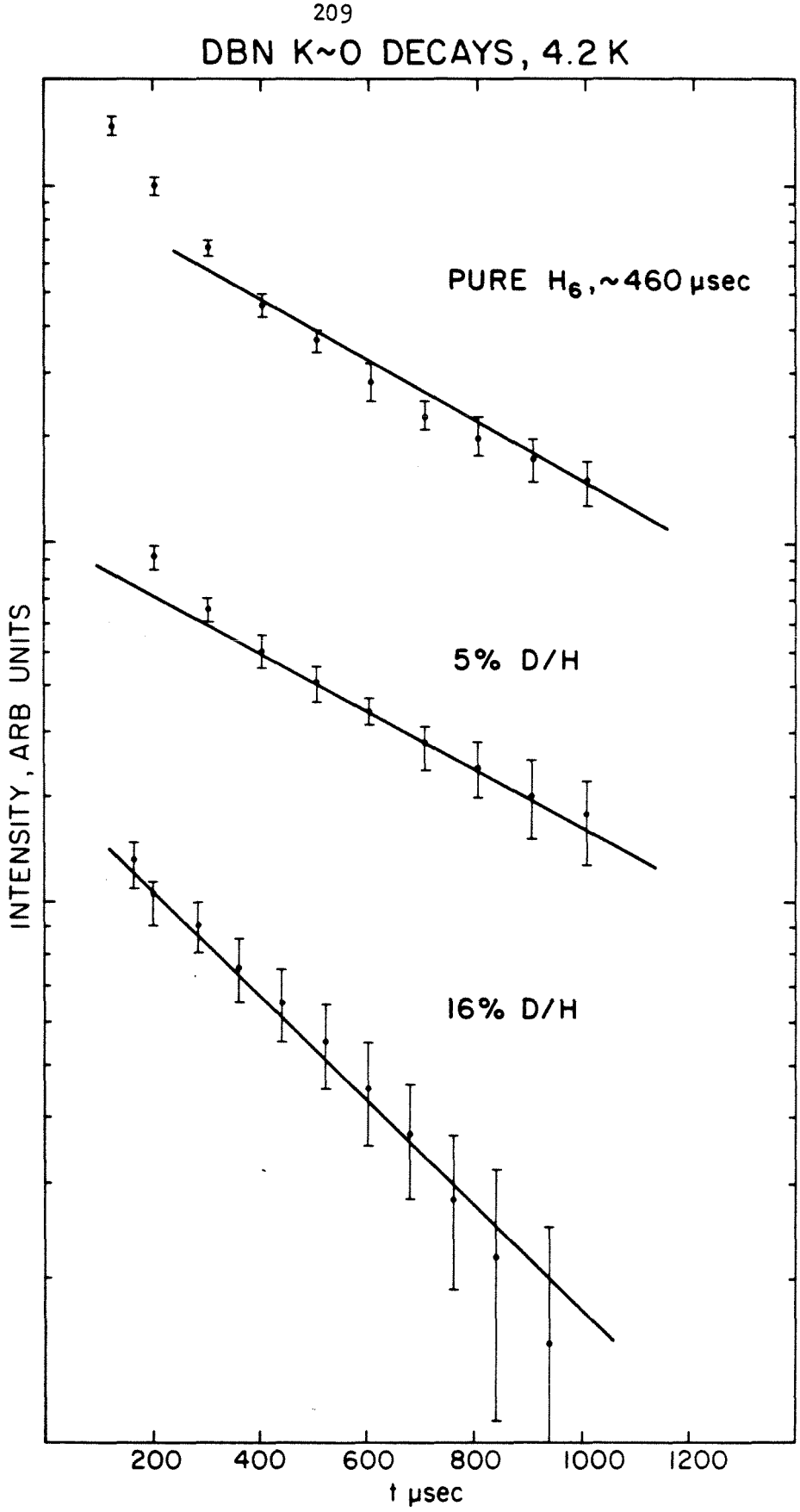
DBN K~O DECAYS, 4.2 K
PURE H_6, ~460 μsec
5% D/H
16% D/H
INTENSITY, ARB UNITS
200
400
600
800
1000
1200
t μsec

Figure 18. Theoretical calculation of the BTBT spectra in DBN using the multilevel relaxation matrix. The spectra are calculated for different values of the coupling matrix element, γ_0. The zeros on the horizontal axis for the spectra at 20 and 60 K correspond to the energy of the unperturbed $\underset{\sim}{k}$=0 state.

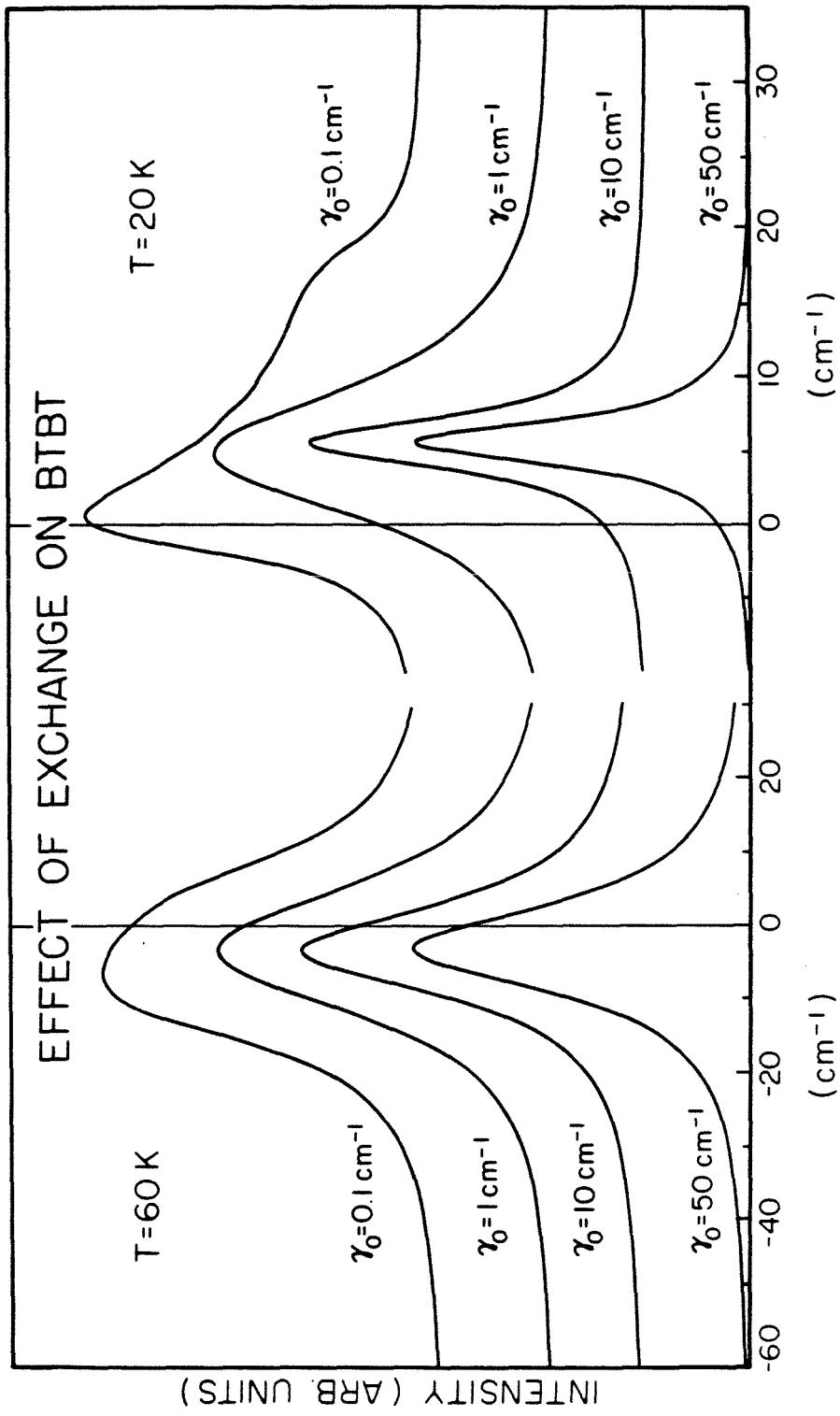
EFFECT OF EXCHANGE ON BTBT
T=60 K
T=20 K
γ_0=0.1 cm^{-1}
γ_0=1 cm^{-1}
γ_0=10 cm^{-1}
γ_0=50 cm^{-1}
INTENSITY (ARB. UNITS)
(cm^{-1})
(cm^{-1})
-60
-40
-20
0
20
0
10
20
30

Figure 19. Calculation of the (0,1350) BTBT lineshape as a function of temperature (with elastic phonon scattering as the dephasing mechanism). A linear chain 10 molecules long and Raman dephasing by a 42 cm^{-1} phonon are the only assumptions. Note the horizontal scale change for the high temperature spectra.

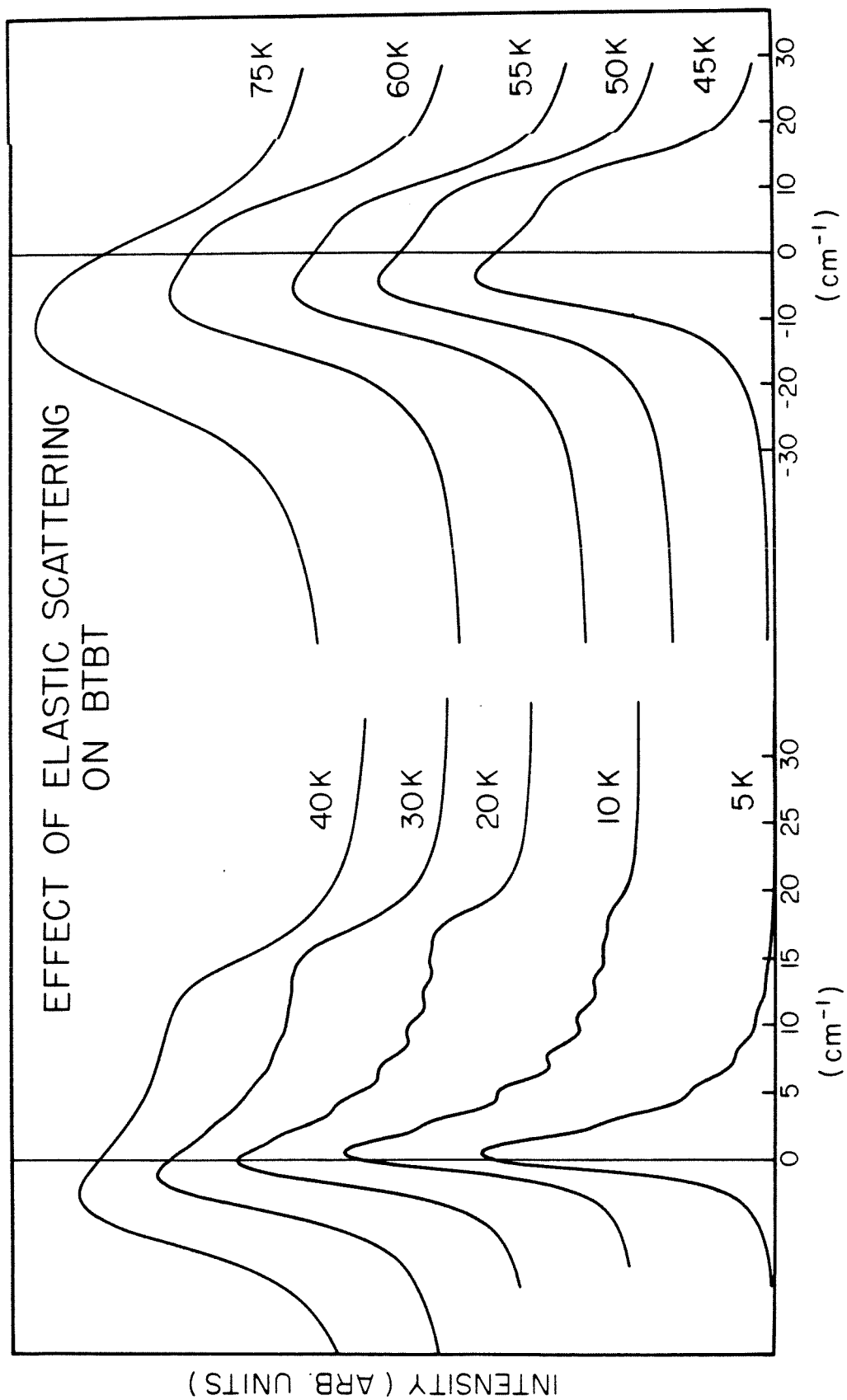
EFFECT OF ELASTIC SCATTERING
ON BTBT
75K
60K
55K
50K
45K
40K
30K
20K
10K
5K
INTENSITY (ARB. UNITS)
(cm⁻¹)
(cm⁻¹)

data remarkably well, using the same phonon energy used to fit the (0,0) temeperature dependent homogeneous linewidth (i.e. no parameters in the simulation). The theoretical fits to the data at two temperatures are shown in Fig. 20.

VII. CONCLUSIONS

From the steady state absorption experiments, the temperature dependent shift and width of the (0,0) are well described by Raman scattering and single phonon processes involving a 42 cm^{-1} phonon. Further, from the broadening and absence of a relative shift of the two sublattices towards one another, one concludes that interband exchange is negligible. Assuming the same 42 cm^{-1} phonon dephases <u>all</u> $\underset{\sim}{k}$ states, one can simulate the CW BTBT, which broadens rather than narrows with increasing temperature. The significance of the steady state results is that pure dephasing and not interband or intraband exchange is dominating.

From the transient BTBT experiments, one has the first direct and unequivocal measurement of inelastic (intraband exchange) scattering rates amongst the $\underset{\sim}{k}$ states. $T_{1\underset{\sim}{k}}$ is found to be of the order of 10 μsec at 20 K. In contrast, the elastic scattering time, $T_{2\underset{\sim}{k}}$, is ~ 10 psec at 20 K and one has a clear separation of time scales.

Pumping the upper sublattice in the transient BTBT experiment, one finds that the relaxation between the sublattices is a single phonon, does not scramble the $\underset{\sim}{k}$ states and is extremely rapid (lineshapes imply 50 psec relaxation times [12] and an upper limit from our transient measurements is 500 nsec). Moreover,

Figure 20. Comparison of the theoretical (no parameter) and experimental BTBT lineshapes in DBN.

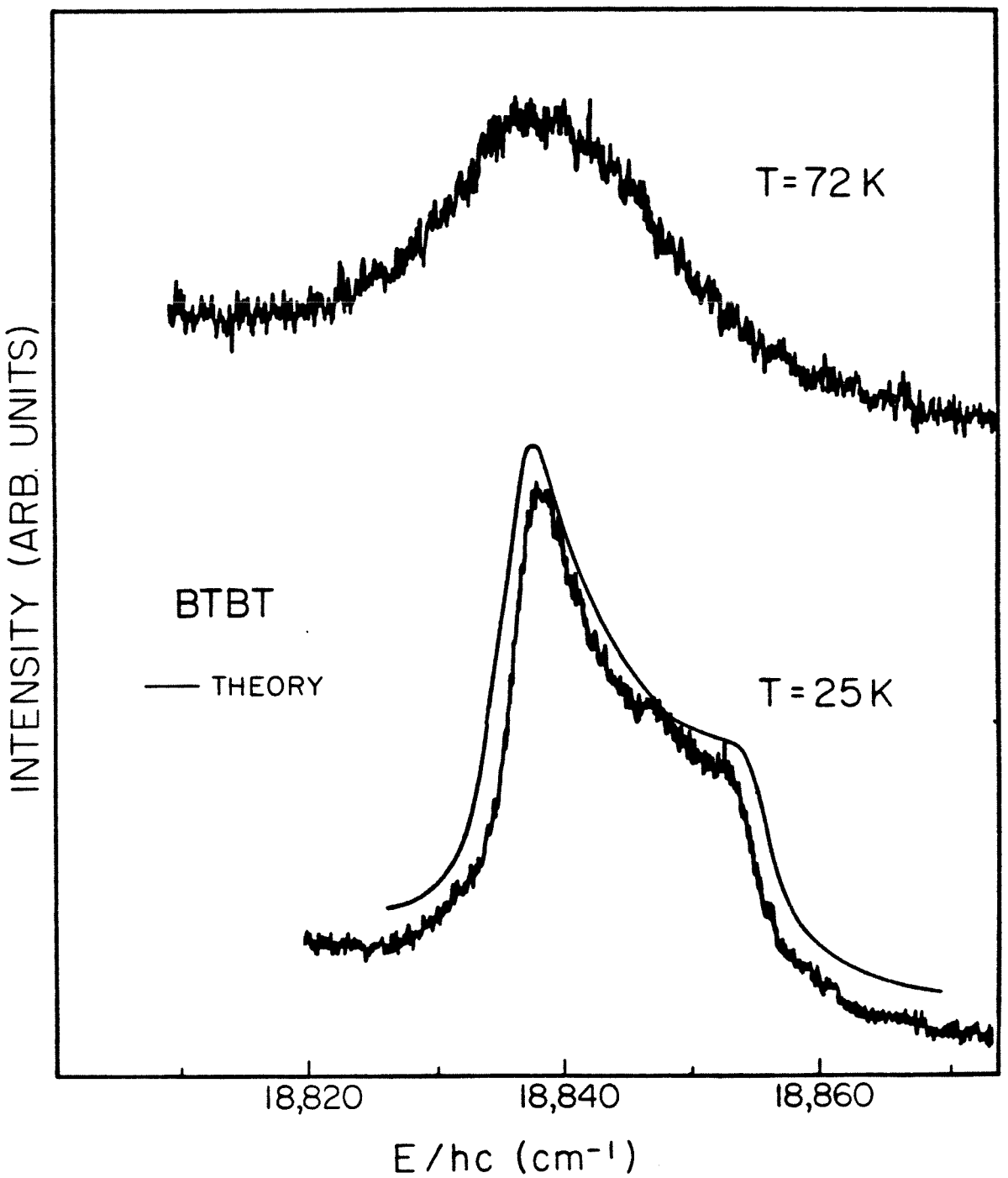
T=72 K
BTBT
THEORY
T=25 K
INTENSITY (ARB. UNITS)
18,820
18,840
18,860
E/hc (cm⁻¹)

performing the transient BTBT experiments with up to 16% D_6 DBN (65 cm^{-1} barriers), no change in the inelastic scattering time was observable. It may be that reflection from the potential barriers surrounding the chains of H_6 DBN does not alter the $\underset{\sim}{k}$, though from the experiments herein, one cannot reach such a conclusion.

REFERENCES

[1] D. W. Oxtoby, Adv. Chem. Phys. 40 (1979) 1.

[2] R. M. Shelby, C. B. Harris and P. A. Cornelius, J. Chem. Phys. 70 (1979) 34.

[3] K. E. Jones, A. H. Zewail and D. J. Diestler, Advances in Laser Chemistry, Springer-Verlag, Berlin 1978, pg. 258; K.E. Jones and A.H. Zewail, loc. cit., pg. 196.

[4] D. J. Diestler and A. H. Zewail, J. Chem. Phys. 71 (1979) 3103; 71 (1979) 3113.

[5] (a) C. B. Harris, J. Chem. Phys. 67 (1977) 5607; (b) Chem. Phys. Lett. 52 (1977) 5.

[6] P. W. Anderson, J. Phys. Soc. Jap. 9 (1954) 316.

[7] B. J. Botter, A. J. Van Strien and J. Schmidt, Chem. Phys. Lett. 49 (1977) 39; B. J. Botter, C. J. Nonhoff, J. Schmidt and J. H. Van derWaals, Chem. Phys. Lett. 43 (1976) 210.

[8] A. H. Zewail, J. Chem. Phys. 70 (1979) 5759.

[9] G.J. Small, Chem. Phys. Lett. 57 (1978) 501 and references therein.

[10] S. F. Fischer and A. Laubereau, Chem. Phys. Lett. 55 (1978) 189.

[11] R. J. Abbot and D. W. Oxtoby, J. Chem. Phys. 70 (1979) 4703.

[12] D. M. Burland, U. Konzelmann and R. M. Macfarlane, J. Chem. Phys. 67 (1977) 1926.

[13] R. M. Hochstrasser and J. D. Whiteman, J. Chem. Phys. 56 (1972) 5945.

[14] Y. Toyozawa, Prog. Theor. Phys. 20 (1958) 53; 27 (1962) 89; J. Phys. Chem. Solids, 25 (1964) 59.

[15] W. Voigt, Munch. Ber. 1912, pg. 603.

[16] (a) B. H. Armstrong, J. Quant. Spec. Rad. Trans. 7 (1967) 61. (b) D. G. Hummer, Mem. Roy. Astr. Soc. 70 (1965) 1. (c) B. D. Fried and S. D. Conte, ''The Plasma Dispersion Function'', prepared for the USAF, 1960.

[17] R. M. Macfarlane, U. Konzelmann and D. M. Burland, J. Chem. Phys. 65 (1976) 1022.

[18] M. N. Sapozhnikov, Phys. Stat. Sol. 75 (1976) 11 and references therein.

[19] S. Califano, Mol. Phys. 5 (1962) 601.

[20] D. D. Smith and A. H. Zewail, J. Chem. Phys. 71 (1979) 3533.

[21] A. M. Nishimura, A. H. Zewail and C. B. Harris, J. Chem. Phys. 63 (1975) 1919.

[22] A. H. Zewail, W. G. Brieland and C. B. Harris, results quoted in D. M. Burland and A. H. Zewail, Adv. Chem. Phys. 40, p 369.

CHAPTER IV.

OPTICAL DEPHASING OF F AND F_2^{2+} CENTER TRIPLET STATES IN CaO*

---

*D. D. Smith, M. Glasbeek and A. H. Zewail, to be published.

ABSTRACT

We have measured the temperature dependent emission lineshapes of CaO F and F_2^{2+} centers. Using lifetime data and homogeneous linewidths from Voigt profiles, it is concluded that the F center zero phonon line shift and width are best described as one and two phonon (elastic) scattering by effective oscillators of 70 $\pm$ 10 cm^{-1} and 89 $\pm$ 6.5 cm^{-1}, respectively. The same processes are consistent with the F_2^{2+} center width and shift, but for modes of 151 $\pm$ 8 and 139 $\pm$ 7 cm^{-1} respectively.

I. INTRODUCTION

Recently, the problem of vibronic dephasing of an optically active probe in an optically inactive medium has received considerable attention. In the case where the probe is a molecule (possessing localized modes and/or librational motions in the host) the formal theory requires treatment of the intra- and intermolecular interactions that contribute to dephasing [1,2,3]. On the other hand, if the probe lacks internal, localized motions, then the optical dephasing is solely determined by direct coupling of the probe levels to the bath; intramolecular (anharmonic) oscillators with or without exchange interactions with a reservoir are not involved.

We wish to consider dephasing of the latter type for two simple Schottky defects in an ionic solid, namely F and F_2^{2+} centers in CaO (cf. Fig. 1). We have measured the homogeneous line broadening of the zero-phonon transitions in the phosphorescence spectra of both centers as a function of temperature. The results represent phase relaxation due to coupling of defect electronic states and

Figure 1. A portion of the 100 plane in a CaO crystal showing an F-center. The filled circles represent O^{2-}; open circles represent Ca^{2+} ions. The F-center is an oxygen vacancy occupied by two electrons. The electrons are confined by the potential field of near neighbor ions in what is essentially an ''octahedrally dented'' spherical well. An F_2^{2+} center is two nearest neighbor O^{2-} vacancies occupied by only two electrons and has a net charge of 2+.

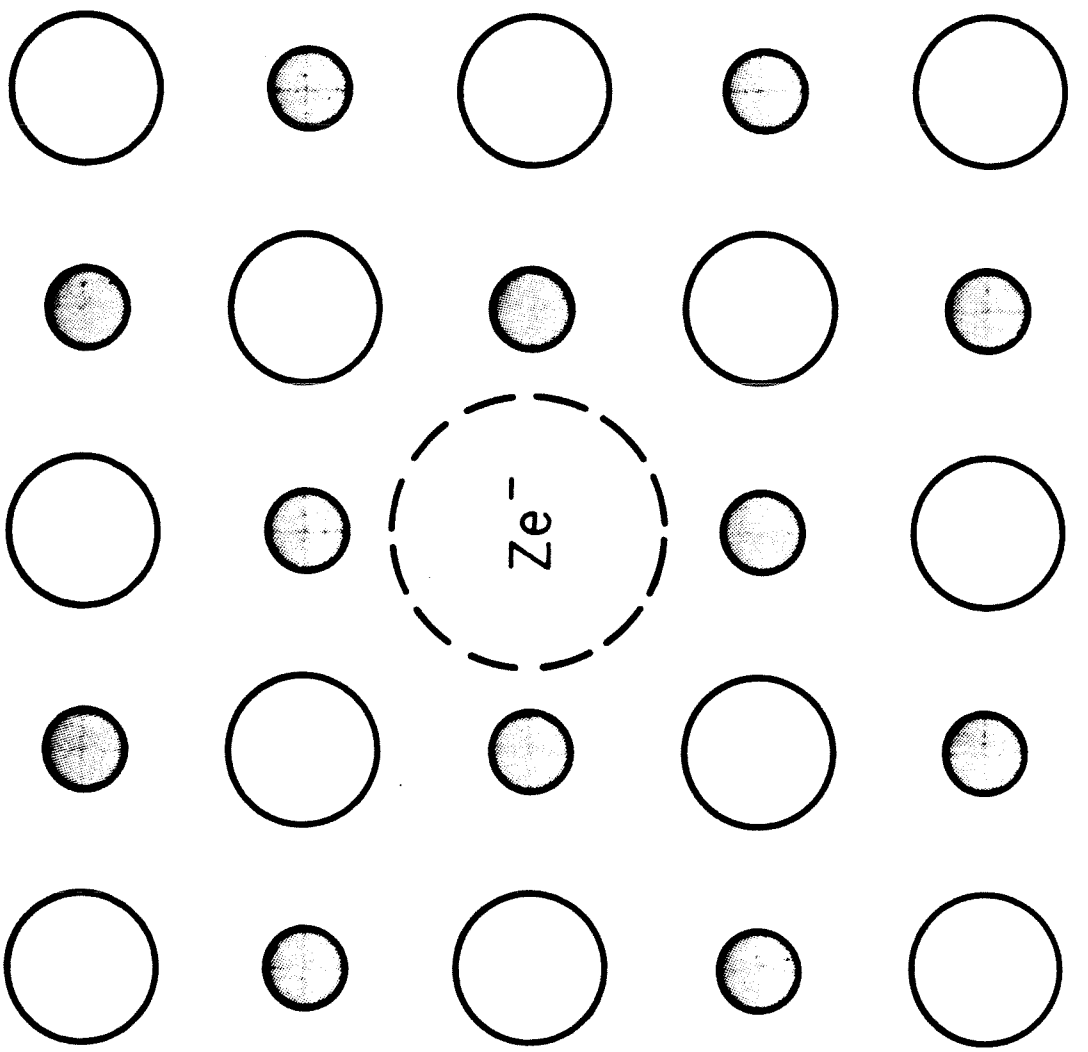
Ze⁻

low-frequency quasilocal modes. The optical dephasing is due to modulation of the optical transition frequency by elastic scattering of quasi-local phonons and/or anharmonic damping among the quasilocal modes.

For the chemist, CaO color center point defects may be a paradigm system to investigate vibrational relaxation and ergodicity due to the inferred slow interconversion rates between the Jahn-Teller distortions [4a], a moderate number of relevant modes and a uniquely simple electronic structure. Unlike most alkalai halides, CaO has a zero phonon line which persists over a range of low temperatures. Having a zero phonon line, one can directly study the defect center dynamics as opposed to an indirect moment analysis of a sideband. Although moment analysis of a phonon sideband offers a great deal of information [5], to the author's knowledge, such analyses do not include the effects of optical dephasing.

II. EXPERIMENTAL PROCEDURE

Cubic samples of CaO approximately 2 and 3 mm on a side were cut with 100 faces. The samples were mounted with a thin film of vacuum grease on a temperature sensing probe inside a Janis DT-10 supervaritemp dewar. Since the dewar cools by helium gas flow, several different flow rates (all else being the same) were tried to insure that the flow (cooling) rates were adequate. Temperatures were measured and regulated to $\pm$ 0.5 K using a calibrated silicon diode and DT-500 temperature controller from Lakeshore Cryotronics. The samples were optically pumped by a Molectron DL 14P nitrogen pumped dye laser

with a 0.2 cm^{-1} bandwidth and a typical pulse energy of 0.5 mJ when exciting the F-center at 574.3 nm. The CaO was of good optical quality and in order to collect more of the emission, a dove prism was used to rotate the image of the laser beam through the crystal (horizontal) such that it would be parallel to the entrance slits of the spectrometer (vertical). The light was dispersed with a Spex 3/4 meter spectrometer using an 1800 groove/mm holographic grating and detected with a Varian VP-100PMT with a GaAs photocathode. A Princeton Applied Research 162 boxcar was used to measure lifetimes and time-resolved spectra. The spectra were digitized using a Houston Instrument HiPad digitizer interfaced to a PDP 11/03 and fit by nonlinear regression on an IBM 370/3032.

III. RESULTS

The zero-phonon line (ZPL) emission in CaO at 683 nm has been shown [4b] to be due to the $^3B_1$ to ^1A transition in the F_2^{2+} centers (also known as M-centers). In the present experiments, the narrow emission of the M center could be isolated from the relatively strong, broad background emission of the F-center sideband after selective narrow-band excitation at 576 nm (just below the F-center). Pumping at 576 nm, we have observed three lines in the short time emission spectrum at 605, 658 and 696 nm. These lines are weak or absent at delay times greater than 1 msec and to our knowledge have not previously been reported in the literature. Presently, the nature of these lines is unknown. At increased temperatures, the M-center ZPL broadens rapidly and at about 90 K distinct resolution from the phonon-assisted emission is difficult. For all practical

purposes, the ZPL is absent at 120 K. Representative ZPL and phonon sideband lineshapes at 3 temperatures are shown in Fig. 2. The low temperature M center ZPL is shown in Fig. 3.

Line shape fitting shows that above 30 K, the M-center ZPL becomes Lorentzian. At lower temperatures, however, the emission line is best fit as a Voigt profile [6], which is a Lorentzian convoluted with a Gaussian. The Voigt fits yield the ratio of the homogeneous and inhomogeneous broadening (HB and IB), where the best fit at 4.2 K gave a Gaussian width of 1.5 $\pm$ .3 cm^{-1}. (The fits were done with several different sets of initial guesses to insure reliability.) The remainder of the M center data was fit to Voigt functions with a fixed IB of 1.5 cm^{-1}. Fitting was done by convolute-and-compare using the algorithm of B. H. Armstrong [7] to calculate the Voigt function. The accuracy of the Armstrong algorithm was checked by comparison with published tables [8] and found to be well within the accuracy quoted. The convolution, as expected, yields an HB that differs from apparent linewidths only when the broadening is small. Our procedure assumes that the HB and IB mechanisms are uncorrelated and that the inhomogeneity is temperature independent. For CaO, there is presently no experimental evidence that the broadenings are or are not correlated (though there are systems where the homogeneous and inhomogeneous broadening <u>are</u> correlated [9], the relatively small inhomogeneity in the CaO ZPL would introduce little error in our analysis if the two broadening mechanisms are inseparable).

The homogeneous widths and shifts of the best Voigt fits to the experimental lineshapes as a function of temperature are plotted in

Figure 2. Temperature dependence of the emission lineshape of the M-center ZPL and phonon sideband.

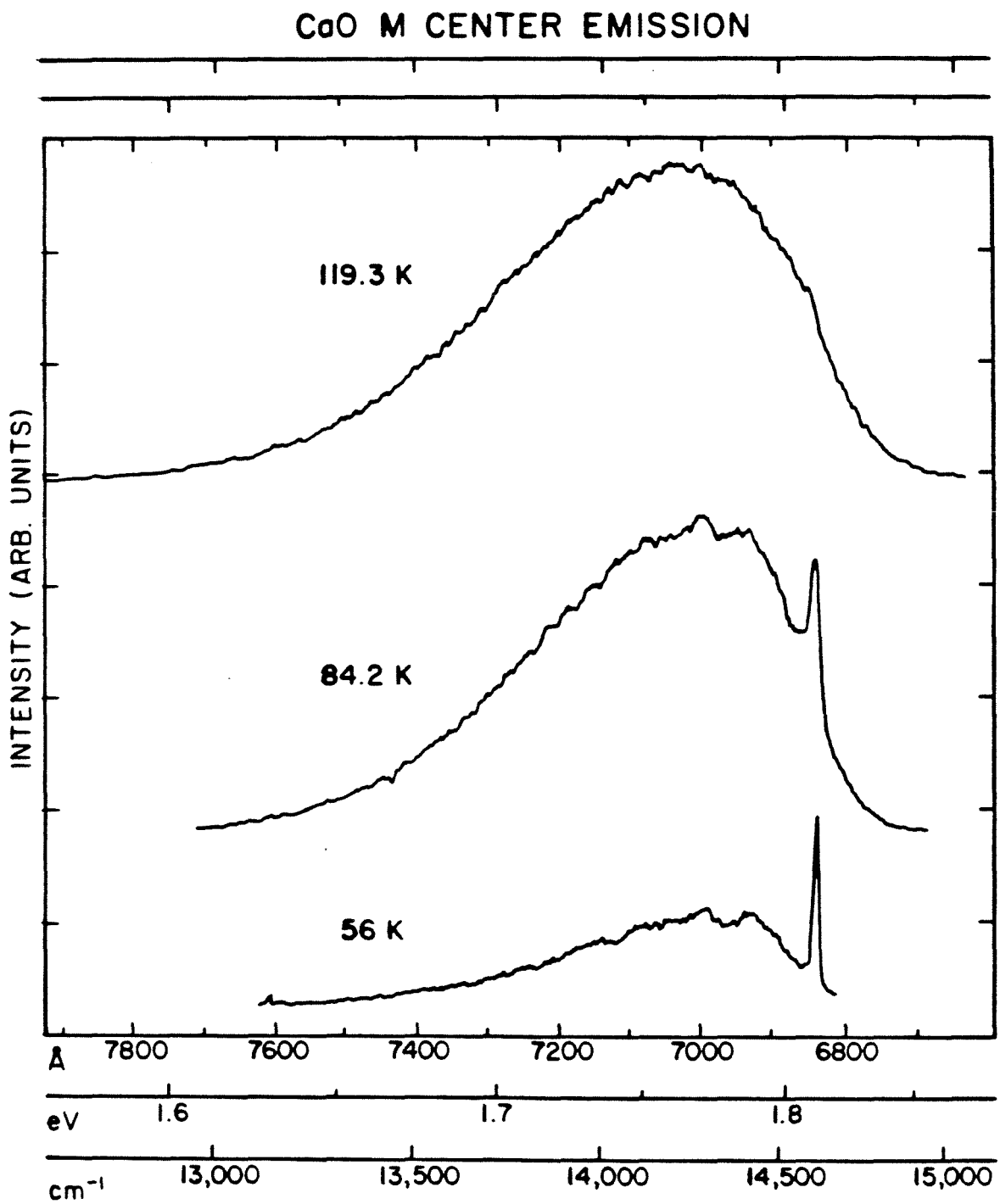
CaO M CENTER EMISSION
INTENSITY (ARB. UNITS)
119.3 K
84.2 K
56 K
A
7800
7600
7400
7200
7000
6800
eV
1.6
1.7
1.8
cm⁻¹
13,000
13,500
14,000
14,500
15,000

Figure 3. M center lineshape, 4.2 K.

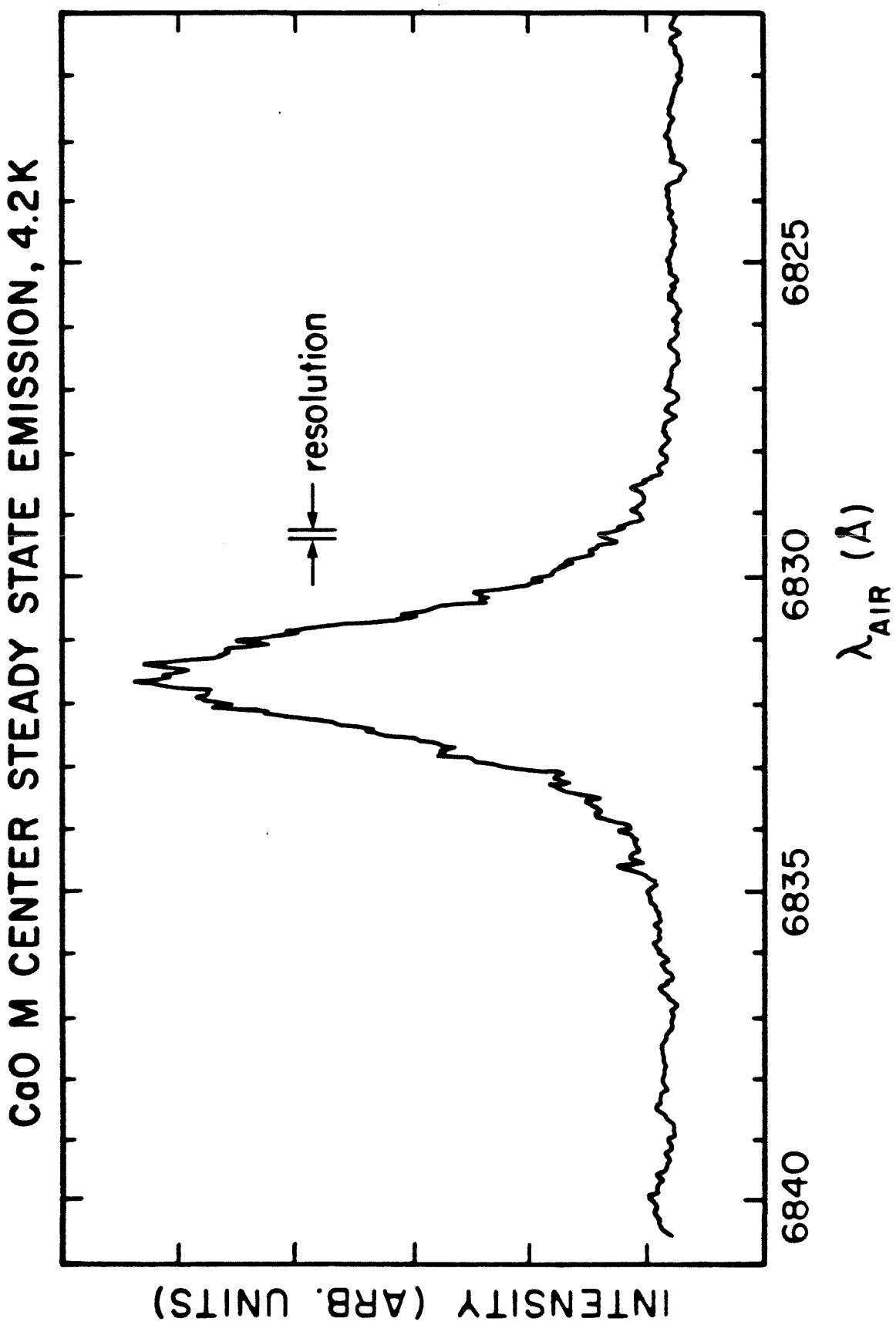
CaO M CENTER STEADY STATE EMISSION, 4.2K
resolution
INTENSITY (ARB. UNITS)
6840
6835
6830
6825
λ_{AIR} (Å)

Fig. 4. For comparison, the total apparent linewidth vs. T is also shown. The homogeneous width vs. T is best discribed by Raman scattering of a 139 ± 7 cm^{-1} phonon. The width clearly does not fit T^3 or T^7. It is useful to note that fitting the total apparent linewidth to n(n+1) yields a 163 cm^{-1} phonon. The implied asymptotic T = 0 K width of 1.4 cm^{-1} may be limited by S/N or insensitivities of Voigt fitting to non-ideal lineshapes. With known spin dephasing times, it is difficult to explain the total HB (spin + orbital) of 1.4 cm^{-1} (in case that as T approaches 0 K, hyperfine and fine contributions dominate the dephasing). Experiments such as optical hole burning or photon echoes need to be done to accurately measure the low temperature orbital dephasing rate. The red shift is best fit by a one phonon process of 151 ± 8 cm^{-1}, though fitting statistics indicate T^3 is also a fit within error. Therefore, within the accuracy of the data, an effective 145 cm^{-1} quasilocal mode is responsible for the shift and width of the M center ZPL. We say effective since the observed 145 cm^{-1} may represent a composite behavior of several local modes.

Much as in the case of the M-center, a significant line broadening effect was observed for the F-center ZPL emission at 574.3 nm. The 574.3 nm line, excited by pumping at 571.1 nm [10], is a transition from $^3T_{1u}$ to $^1A_{1g}$ orbital symmetry [11]. At temperatures lower than 20 k, the ZPL is asymmetrically shaped with a typical FWHM of 4.6 cm^{-1} (see Fig. 5). The asymmetry is ostensibly due to splitting of the triplet states by intrinsic strain fields in the crystal [12]. Over several days of experimentation, the 4.6 cm^{-1} FWHM increased ~1.5 cm^{-1}, probably due to strain induced by thermal

Figure 4. The shift and width of the M-center as a function of temperature. The circles are the homogeneous widths and shifts from the Voigt profiles and the crosses are the total apparent linewidth. The shift of the line center is actually to the red and the plot only shows the magnitude of the shift. The solid lines are theoretical fits.

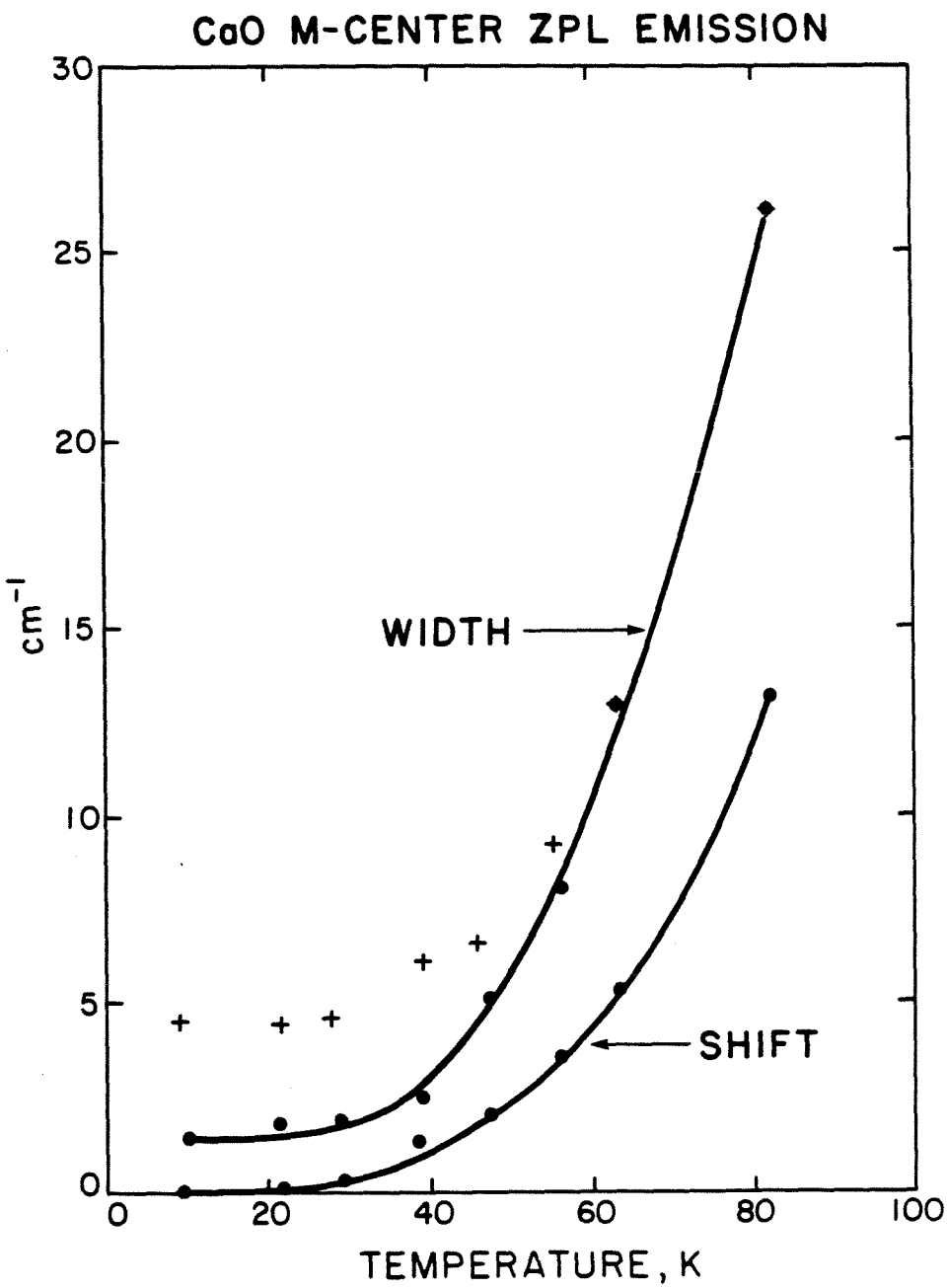
CaO M-CENTER ZPL EMISSION
30
25
20
15
10
5
0
cm⁻¹
WIDTH
SHIFT
0
20
40
60
80
100
TEMPERATURE, K

Figure 5. F center lineshape, 4.2 K.

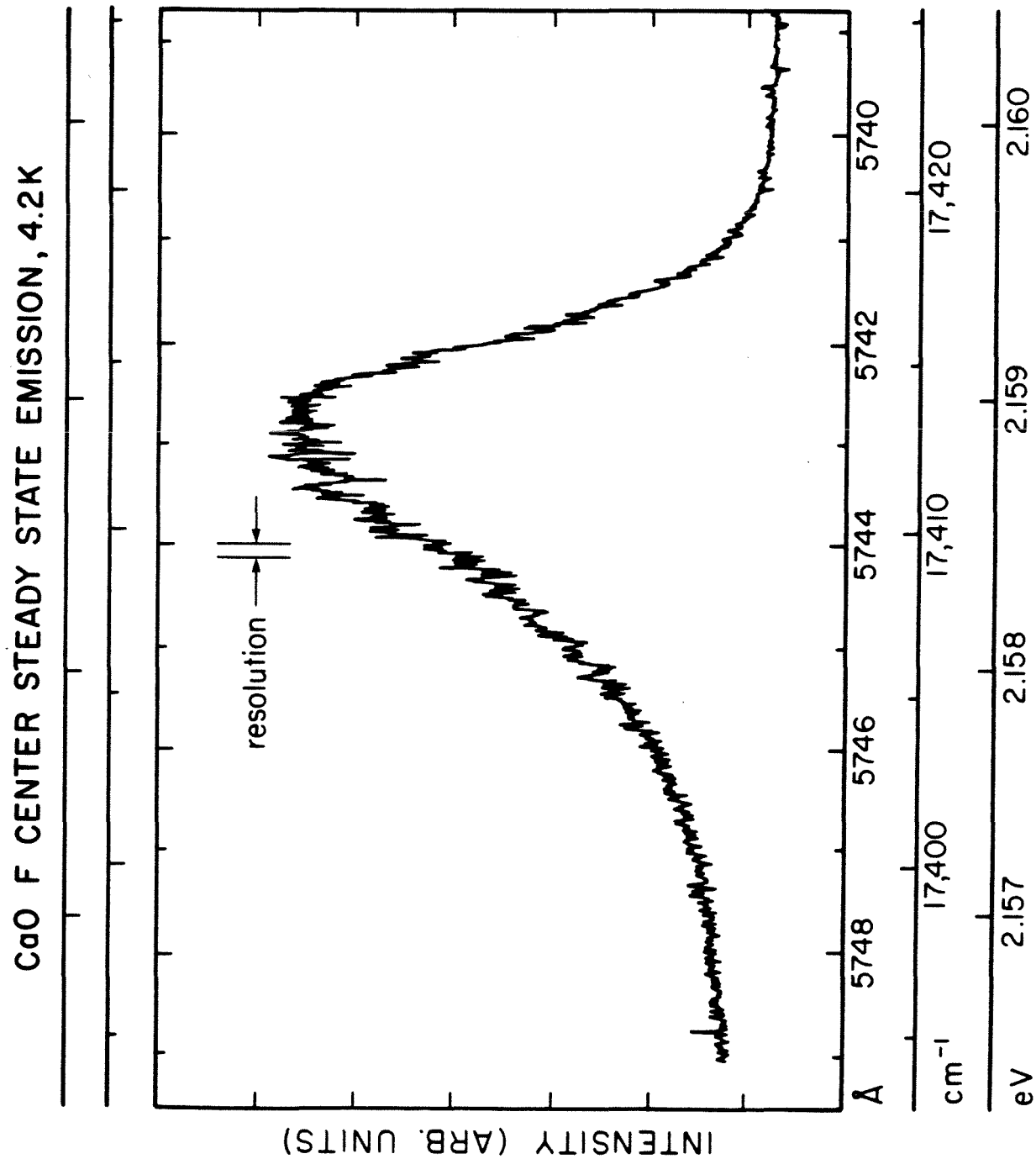
CaO F CENTER STEADY STATE EMISSION, 4.2K
INTENSITY (ARB. UNITS)
resolution
Å
5748
5746
5744
5742
5740
cm⁻¹
17,400
17,410
17,420
eV
2.157
2.158
2.159
2.160

cycling. As the temperature increases, the line becomes more symmetric and is a good Lorentzian for T > 40 K. Overlap with the phonon sideband is negligible for temperatures < 50 K and severe for temperatures > 65 K, imposing an upper limit of 65 K for the F-center ZPL study (as opposed to 85 K for the M-center, which has a weaker electron phonon coupling). To determine the low temperature inhomogeneous width, we fit a Voigt function to the high energy side of the line, which was the steepest edge. Using the steep edge gave an upper limit on the IB of 1.3 $\pm$ .5 cm^{-1}. It yields an upper limit since the spectrometer function may exaggerate the actual Gaussian component and the wings of the lineshapes are distorted by the other triplet substates, resulting in too small a Lorentz component for the low temperature spectra. Thus, the fits may yield slightly too low an energy for the phonon. The temperature dependence of the homogeneous width of the F-center ZPL is presented in Fig. 6 as well as the apparent FWHM and thermally induced shifts of the line center. The Voigt fits imply a homogeneous width of ~1.8 cm^{-1} at 8.9 K and lower temperatures. This would imply a 5.6 psec electronic dephasing time at 0 K! It may be that the accuracy of the implied T = 0 K dephasing is in error in the same manner the M-center rate is (vide supra). The HB fits T^3 and a two phonon process of 89 $\pm$ 6.5 cm^{-1} equally well -- T^7 clearly does not work. If the total apparent width is used, a phonon energy of 152 cm^{-1} is obtained. The small 4.5 cm^{-1} red shift is best described by a single 70 $\pm$ 10 cm^{-1} phonon and less well by T^3. From the data one therefore concludes that approximately an 82 cm^{-1} phonon is involved in the dephasing and shift of the F-center.

Figure 6. The shift and width of the F-center as a function of temperature. The circles are the homogeneous widths and shifts; crosses are the total apparent width. The shift of line center is actually to the red and the graph only illustrates the magnitude of the shift. The solid lines are theoretical fits.

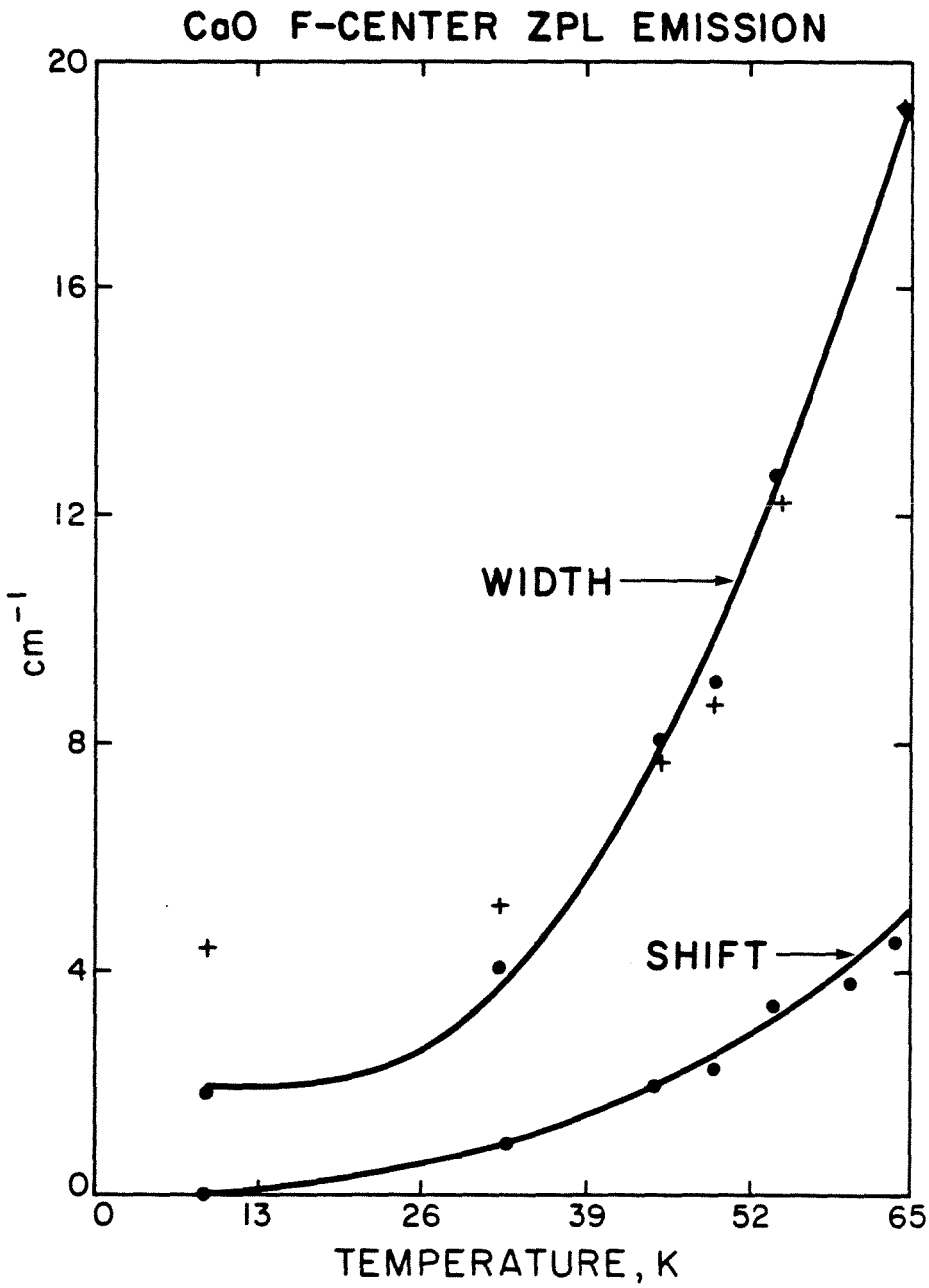
CaO F-CENTER ZPL EMISSION
20
16
12
8
4
0
cm⁻¹
WIDTH
SHIFT
0
13
26
39
52
65
TEMPERATURE, K

IV. DISCUSSION

In discussing the origin of the observed line broadening effects, it is useful to note that the Lorentzian component for both centers, at temperatures between 4.2 K and 80 K, is representative of homogeneously broadened lines with characteristic dephasing times ranging from 7 psec (1.4 cm^{-1}) to 0.4 psec (26 cm^{-1}). Since the lifetimes of the emitting triplet levels in both centers remain of the order of milliseconds, even at 80 K [13,14], one concludes that 'pure' dephasing and not population decay is responsible for the observed line broadening.

The general expression for the pure dephasing rate can be written as [3]:

$$(1a) \quad (1/T_2') = \frac{\pi}{(h/2\pi)} \sum_p W_p \sum_{p'} |\langle p|\Delta T|p'\rangle|^2 \delta(E_p - E_{p'})$$

$$(1b) \quad \Delta T = \langle i|T|i\rangle - \langle f|T|f\rangle$$

Here, T is the transition operator [1] for the coupling of the defect electrons to the lattic vibrational modes, initial (i) and final (f) states are the electronic levels of the optical transition, p and p' are the perturbing reservoir states and W_p is the occupation probability of state p. From eqn. (1a), it is apparent that in solids, pure dephasing involves isoenergetic phonon states p and p', whereas the population of the electronic levels remains unchanged. T satisfies

Dyson's equation:

$$(2)\quad T = V + VG^{o}T.$$

Where G^{o} is the zero-order resolvent operator and V is the potential for the electron-lattice interaction. Now, V can be expanded as a power series in the motional displacements $U_{\alpha}(1k)$ of the atoms from their equilibrium positions which exist in the absence of crystal defects, k denotes the k^{th} atom in the 1^{th} unit cell and α is the cartesian component of its displacement. One can write [15a]:

$$(3)\quad V = V_0^{(0)} + \sum_{1k\alpha} V^{(1)}_{1k\alpha} U_{\alpha}(1k) + (1/2!) \sum_{\substack{1k\alpha \\ 1'k'\beta}} V^{(2)}_{1k\alpha,1'k'\beta} U_{\alpha}(1k)U_{\beta}(1'k')$$

$$+(1/3!) \sum_{\substack{1k\alpha \\ 1'k'\beta \\ 1''k''\xi}} V^{(3)}_{1k\alpha,1'k'\beta,1''k''\xi} U_{\alpha}(1k)U_{\beta}(1'k')U_{\xi}(1''k'') + \ldots$$

The first term characterizes the electronic state of the defect. The terms linear in the $U_{\alpha}(1k)$ operators arise because the equilibrium positions of the nuclei (around the defect) vary in the electronic transition, the second sum is the harmonic potential and the remainder is anharmonic terms. Now one may invoke the lowest Born approximation, i.e., T=V. In this (first order) approximation, several dephasing mechanisms may be considered. By far the most important of these is due to the harmonic terms of eqn. (3),

which when used for the evaluation of the matrix elements of eqns. (1a) and (1b) are responsible for elastic scattering of phonons by the defect levels (the terms linear in the $U_\alpha(1k)$ operators also contribute to the elastic scattering process, but only in second order, which is not considered here). Retaining only the harmonic terms of eqn. (3), one can derive [3] that the optical dephasing rate is given by

$$(4) \quad \gamma_h^{(2)} = \frac{\pi}{(h/2\pi)^2} \sum_\mu \sum_{\mu\neq\lambda} |D_{\mu\lambda}^{(0)}|^2 n_\mu (n_\lambda+1) \delta(\omega_\mu - \omega_\lambda).$$

In eqn. (4), μ and λ are indices for the normal lattice modes in the harmonic approximation, n_μ is the thermally averaged occupation number of mode μ, while the scattering matrix elements are given by

$$(5) \quad D_{\mu\lambda}^{(0)} = \sum_{\substack{1k\alpha \\ 1'k'\beta}} (\langle i|V_{1k\alpha,1'k'\beta}|i\rangle - \langle f|V_{1k\alpha,1'k'\beta}|f\rangle) C^*_{1k\alpha;\mu} C_{1'k'\beta;\lambda}$$

where the $U_\alpha(1k)$ are transformed in the creation (b_μ^+) and destruction (b_μ) operators of the normal modes by

$$(6) \quad U_\alpha(1k) = \sum_\mu (C_{1k\alpha;\mu} b_\mu + C^*_{1k\alpha;\mu} b_\mu^+)$$

Note from eqn. (5) that in harmonic systems (or in any system where the potential goes as $U_\alpha(1k)^{2n}$ where n=1,2,3,...), the dephasing arises from a disparity in the elastic force constant between the ground and excited electronic states. Two limiting cases may now be considered. First, elastic scattering takes place for all phonons in the acoustic branches. In the Debye approximation, and assuming $T<<T_D$, one then finds [3]: $\gamma_h \propto T^7$, where T_D and T denote the Debye temperature and temperature respectively. In ionic solids, such a temperature dependence for the line width has been found for a number of cases long ago [16]. On the other hand, one may consider coupling to a quasilocal mode. In this (second) case, the coupled modes exhibit a sharply peaked density of states for $\omega_\mu \sim \omega_0$ and the temperature dependence becomes [17] $\gamma_h \propto n(n+1) \propto \coth^2(h\omega/4\pi kT)$. The latter temperature dependence is not uncommon in line broadening studies of impurity molecules in molecular crystals [18].

As can be seen from Figs. 4 and 5, the widths of the zero phonon transitions can be fitted to a function of the form $\gamma = \gamma_0 + n(n+1)$. This result demonstrates that Raman type acoustic phonon scattering does not dominate the dephasing process. We remark that T in our experiments was indeed always less than the Debye temperature (T_D (CaO) = 605 K at 0 K [19]). From the close fit between the simulated curve and the experimental points in Figs. 4 and 5, one infers that the observed IB is produced by elastic scattering of low-frequency quasilocal phonons with effective mode frequencies of 89 and 139 cm^{-1} for the F and M centers respectively.

To our knowledge, low frequency quasilocal phonon modes in defect containing alkaline earth oxides have not been reported before. However, it is interesting to note that recent experiments performed in the microwave region give independent support of their existence. In these experiments [14], the spin-lattice relaxation within the $^3B_1$ state of the M-center in CaO was studied as a function of temperature. It was found that the mechanism is an activated (Orbach type) process in which a thermally induced excitation takes place to a low-lying intermediate state, some 40 cm^{-1} above the $^3B_1$ state. It is likely that the intermediate level may be associated with a quasilocal mode state.

In the dephasing mechanisms considered so far, dephasing is generated by the harmonic terms of V. However, from the substitution of V given by eqn. (3) into eqn. (1b), it is seen that within the Born approximation, optical dephasing occurs by virtue of phonon dephasing during the optical transition (i.e., they are mutually disruptive). Anharmonic interactions which lead to phonon decay or phonon exchange should be considered as well. Here we restrict ourselves to the effects of cubic and quartic terms of V. Cubic anharmonic interactions give rise to a T_1 type phonon decay into two other phonons. The linewidth of the optical transition results from this process is given by [15]

$$(7)\qquad \gamma_a^{(3)}(\omega) = \frac{18\pi}{(h/2\pi)^2} \sum_{\lambda,\lambda'} |\Delta V_{\mu\lambda\lambda'}|^2 \{(n_\lambda + n_{\lambda'} + 1)\delta(\omega - \omega_\lambda - \omega_{\lambda'})$$

$$+ (n_{\lambda'} - n_\lambda)[\delta(\omega - \omega_\lambda + \omega_{\lambda'}) - \delta(\omega + \omega_\lambda - \omega_{\lambda'})]\}$$

where

$$\Delta V_{\mu\lambda\lambda'} = \langle i|V^{(3)}_{\mu\lambda\lambda'}|i\rangle - \langle f|V^{(3)}_{\mu\lambda\lambda'}|f\rangle$$

with $V_{\mu\lambda\lambda'}$ is the anharmonic coupling coefficient of the cubic terms in V when V is written as an expansion of the normal coordinates. Clearly, the temperature and time dependence eqn. (7) implies is incompatible with the data. One concludes, therefore, that two phonon decay is irrelevant to our observations. On the other hand, the quartic anharmonic interactions produce higher order elastic scattering or a three phonon decay which contains contributions of the type [18]

$$(8)\qquad \gamma_a^{(4)} = \frac{\pi}{(h/2\pi)^2} \sum_{q_1 s_1 s_2} |V_{qs,-qs,q_1 s_1,-q_1 s_2}|^2$$

$$\times\, n_{q_1 s_1}(n_{-q_1 s_2} + 1)\delta(\omega_{q_1 s_1} - \omega_{-q_1 s_2})$$

In eqn. (8), a lattice phonon of wave vector $\underline{q}$, branch index s, is scattered by a quasilocal phonon $\underline{q}_1$, s_1 which is coupled to another quasi-local mode $\underline{q}_1$, s_2. On comparison of eqn. (8) with eqn. (4), one finds phonon scattering by quasilocal modes also may contribute to the observed temperature dependence of the zero-phonon linewidths, though to a much lower extent than the previously discussed elastic scattering process.

V. CONCLUSIONS

In summary, from the temperature dependent homogeneous linewidths, the F and M centers are elastically dephased by quasilocal modes of 89 and 139 cm^{-1} respectively. For the F-center the emission line at 571.1 nm is approximately 89 cm^{-1} from the ZPL and since it is strongly coupled to the ZPL, it may be the F-center Jahn-Teller state with one quantum of excitation.

REFERENCES

[1] K. E. Jones and A. H. Zewail, in Springer Series in Chemical Physics, Vol. 3: Advances in Laser Chemistry, ed. by A. H. Zewail, (Springer, Berlin, Heidelberg, New York, 1978), p. 196.

[2] R. M. Shelby, C. B. Harris and P. A. Cornelius, J. Chem. Phys. 70 (1979) 34.

[3] D. J. Diestler and A. H. Zewail, J. Chem. Phys. 71 (1979) 3103.

[4] (a) C. J. Krap, M. Glasbeek and J. D. W. Van Voorst, Phys. Rev. B

17 (1978) 61; (b) D. J. Gravesteijn and M. Glasbeek, Phys. Rev. B 19 (1979) 5549.

[5] See, e.g., C. Escribe and A. E. Hughes, J. Phys. C 4 (1971) 2537, and references therein.

[6] W. Voigt, S. B. Bayer Akad. Wiss. 1912, p. 603.

[7] B. H. Armstrong, J. Quant. Spect. Rad. Trans. 7 (1967) 61.

[8] (a) B. D. Fried and S. D. Conte, ''The Plasma Dispersion Function'', published for the USAF, 1960; (b) D. G. Hummer, Mem. Roy Astr. Soc. 70 (1965) 1.

[9] Ph. Avouris, A. Campion and M. A. El-Sayed, Proc. SPIE 113 (1977) 57.

[10] The 571.1 nm line may belong to the F-center. When pumping at 574.3 nm, prompt emission at 571.1 nm is observed as a doublet as well as the fitted phonon for elastic scattering equaling the energy difference of the 571.1 and 574.3 nm states. This implies the 571.1 line is the Jahn-Teller mode with one quantum of excitation.

[11] B. Henderson and J. E. Wertz, Defects in the Alkaline Earth Oxides, (Taylor and Francis, London, 1977).

[12] L. S. Dang, Y. M. D'Aubigne, Y. Rasoloarison, J. Physique, 39 (1978) 760; P. Edel, Y. M. D'Aubigne and R. Louat, J. Phys. Chem. Sol. 35 (1974) 67.

[13] L. S. Welch, A. E. Hughes and G. P. Summers, J. Phys. C Solid St. Phys. 13 (1980) 1791.

[14] R. Hond and M. Glasbeek, to be published.

[15] (a) A. A. Maradudin, Solid St. Phys. 18 (1966) 273, (see pp. 395 and 396); (b) A. A. Maradudin, Solid St. Phys. 19 (1966)(see eqn. 10.43).

[16] (a) D. E. McCumber and M. D. Sturge, J. Appl. Phys. 34 (1963) 1682, (b) G. F. Imbusch, W. M. Yen, A. L. Schawlow, D. E. McCumber and M. D. Sturge, Phys. Rev. 133 (1964) A 1029; (c) R. J. Elliot, W. Hayes, G. D. Jones, H. F. MacDonald and C. T. Sennett, Proc. Roy. Soc. A 289 (1965) 1.

[17] M. N. Saposhnikov, Phys. Stat. Sol. B 75 (1976) 11.

[18] J. C. Bellows and P. N. Prasad, J. Chem. Phys. 70 (1979) 1864.

[19] E. Gmelin, Z. Naturforsch. 24a (1969) 1794; Z. Naturforsch. 25a (1970) 887.

CHAPTER V.

CO-STRETCH VIBRATIONAL OVERTONES OF BENZOPHENONE MATRIX ISOLATED IN DDE: RELAXATION AND DEPHASING OF AN ANHARMONIC OSCILLATOR IN THE CONDENSED PHASE*

---

*D. D. Smith and A. H. Zewail, J. Chem. Phys. 71 (1979) 540.

ABSTRACT

By observing the optical emission spectrum of benzophenone matrix isolated in DDE at 2 K, it has been determined that the ground state CO stretch vibrational overtone linewidth is linear in the CO quantum number. This implies vibrational relaxation rates linear in the CO quantum number, consistent with proposed theoretical models. The data are interesting in that (1) they reveal carbonyl vibrational relaxation mechanisms rather than CH stretches as most commonly studied, (2) benzophenone may represent a ''two-mode'' molecule in that the CO stretch and phenyl torsions may be the most strongly coupled modes.

I. INTRODUCTION

The concept of local modes in polyatomic molecules has recently been under examination, both theoretically [1-5] and experimentally [4-7]. Bond locality has direct relevance to various interesting phenomena such as multiphoton dissociation of molecules and laser induced chemistry. The characterization of local vs. normal modes in moderate sized molecules has been addressed theoretically by Gelbart and his group [1,2]. Experimentally, the question of local vs. normal modes in liquids [5], gases [6] and cooled solids [7] has been dealt with by observing the absorption spectra of the different overtones. A plot of ΔEv^{-1}, the energy divided by the vibrational quantum number, v gives a straight line consistent (but not proof of) the idea of a simple Morse oscillator. These experimental results have been confined mostly to

CH stretches in molecules.

Here, we use emission rather than absorption spectroscopy, as used in all previous work, and we explore a different type of molecule that may be useful for detailed theoretical inspection. The idea is quite simple -- using a high sensitivity spectrophotometer (e.g. one that utilizes photon counting) one scans the optical emission spectrum (say, the singlet-triplet transition) that has ground vibrational overtones as final states. Knowing the energy of the (0,0) transition, one can deduce the energy of the mode as a function of v along with the anharmonicity and transition linewidths. Because we are using the emission and not the absorption (which requires long path length or dense media), several advantages can be realized. First, mixed crystals at low temperatures (or molecules in molecular beam nozzle sources) can be studied with very small concentrations (10^{-4} to 10^{-6} mol/mol), thus avoiding possible intermolecular perturbations (or in the case of a beam, collisional effects). Second, polarization techniques can be used to assign bands. Third, measurement of linewidths can be done easily, since the v transitions will be in the visible, as opposed to absorption experiments where IR detection is required in the low energy region. The method, however, relies on a finite and useful value for the Franck-Condon factor between the upper vibronic state and the ground one.

The system studied here is benzophenone isolated in 4,4'-dibromodiphenyl ether (DDE) from 1.4 to 60 K (the high temperature studies will be reported elsewhere, here we only deal with T < 4.2 K). These mixed crystals exhibit a ''clean'' spectrum consisting of a

carbonyl (CO) progression with (presumably) torsional modes of the two phenyls. Since electronic excitation is highly localized on the CO moiety, vibrational progressions corresponding to complex vibrational modes of the phenyl groups do not congest the spectrum. The v=1 and 2 transitions have been characterized before [8].

II. EXPERIMENTAL

The crystals were grown from the melt by standard Bridgman techniques. The benzophenone was dissolved in the DDE up to its limit of solubility. Samples were held in a helix and supported from underneath by a piece of tape. Low temperatures were obtained in a Janis 10 liter immersion dewar or in a Janis super varitemp flow dewar (10 liter capacity). The temperature was regulated with a Lakeshore Cryotronics DTC-500 controller in a feedback loop with a silicon diode soldered with indium to the helium gas flow nozzle. Temperatures were measured with a calibrated Silicon diode situated in a copper block 1 cm above the sample. Broadband UV excitation was supplied by a heavily filtered 150 watt Hg-Xe arc lamp. The flow rate of the helium gas was varied to determine that the cooling rates were adequate. Emission was collected with f1 Tessar configuration collection optics and focussed on the slits of a Spex 1402 double spectrometer with dual 2400 groove/mm holographic gratings. The light was detected with a Hammatsu R955 PMT and Spex photon counting electronics. Emission from the sample was copious so that narrow slits and high resolution was possible for all scans.

Figure 1 displays the overtone spectra of the benzophenone CO stretch at 2 K. (The detection sensitivity was enhanced approximately 10^4 to observe v=5; but note that the concentration of the benzophenone was only about 10^{-4} molar.) From the spectra we have learned several things; (a) when ΔEv^{-1} vs. v is plotted for the CO overtones, we obtain a nearly straight line (see Fig. 2); (b) as one goes to higher overtones of CO, the apparent linewidth increases. In fact, at v=5, all lines (CO and torsional) overlap, yielding a much broader resonance (CO width greater than 20 cm^{-1}); (c) the torsional progression exhibits a similar trend in linewidth with increasing quantum number.

From the plot of ΔEv^{-1} we find a fundamental frequency of 1670 $\pm$ 5 cm^{-1} and an anharmonicity constant of -12.5 $\pm$ 1.5 cm^{-1} [9]. These data raise an interesting point. Probably due to the electronic excitation being highly localized on the CO [8], the progression in the ground states appears to have the nature of a ''local'' mode. Which further, has appreciable anharmonicity. This suggests that the extent to which these modes couple to other modes should be evident from the line broadening as v increases. For v=5, an experimental estimate of the linewidth will be on the order of 50 cm^{-1} [10]. It is perhaps accidental that this line has a width approximately half that of naphthalene (100 cm^{-1}) v=5 transition of the CH stretch and that the ratio of the CH stretch frequency to the CO enone, the torsional mode may prove to be the accepting mode for energy relaxation. This would be an example of vibrational relaxation due to the forces imposed by the neighboring CC

Figure 1. The overtone spectra of benzophenone in DDE at 2 K. The numbers in boxes denote the CO vibrational quantum number. Note the broadening and shift of the CO and torsional bands. The v=1 line is an uneven doublet [12] and the relative intensities are resolution limited.

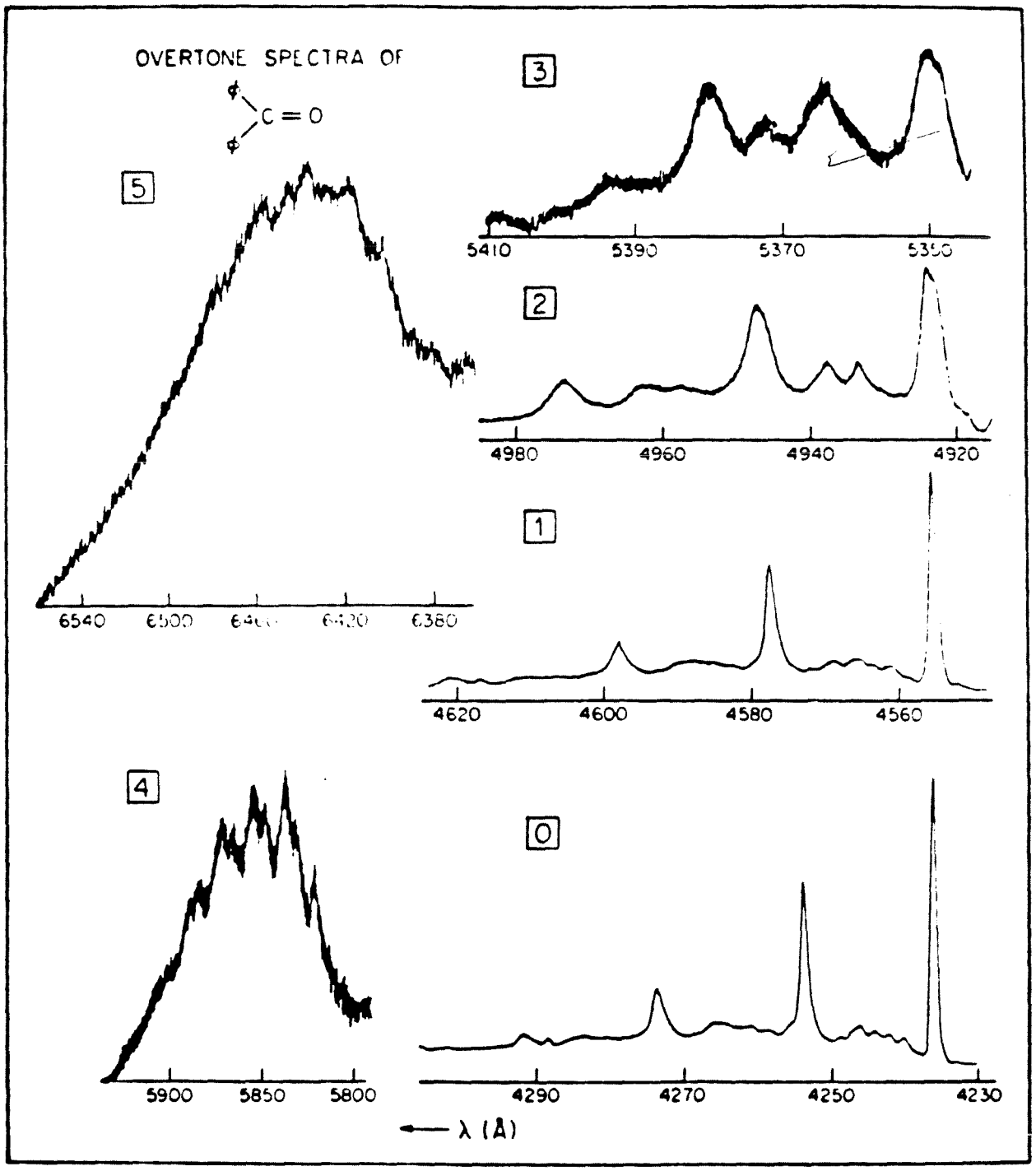
OVERTONE SPECTRA OF
C = O
5
6540
6500
6380
3
5410
5390
5370
5350
2
4980
4960
4940
4920
1
4620
4600
4580
4560
4
5900
5850
5800
0
4290
4270
4250
4230
λ (Å)

bonds on the CO. As suggested by Shobatake et al. [11] this kind of interaction yields a relaxation rate linear in v (see Fig. 2). However, one must first demonstrate the inhomogeneity of the overtone resonances and measure the contribution of pure dephasing to the linewidth before deducing the energy relaxation rate accurately from the lineshape [12].

III. CONCLUSIONS

In conclusion, by using simple optical techniques, one can obtain the widths, the anharmonicity, and the energies of the overtones. Comparison between absorption and emission data will be extremely important tests for current theoretical work. Finally, benzophenone offers an opportunity to unravel some of the ''local'' mode relaxation processes. Extension of these ideas to CH modes and to molecules in beams will be reported later. Similar to emission, Raman scattering into overtones should also prove feasible.

Figure 2. A plot of $\Delta E v^{-1}$ vs. v for benzophenone (CO stretch) in DDE at 2 K. The straight line is a linear least squares fit (see also footnote 9). The point for v=1 seems to be at lower energy than predicted by the best straight line fit. However, our uncertainty at the moment is large. The insert is a plot of the apparent width, $\Delta\omega$, vs. the energy of excitation. The 6477 cm^{-1} point is uncertain due to spectral overlap, and the width of the v=1 includes the shoulder.

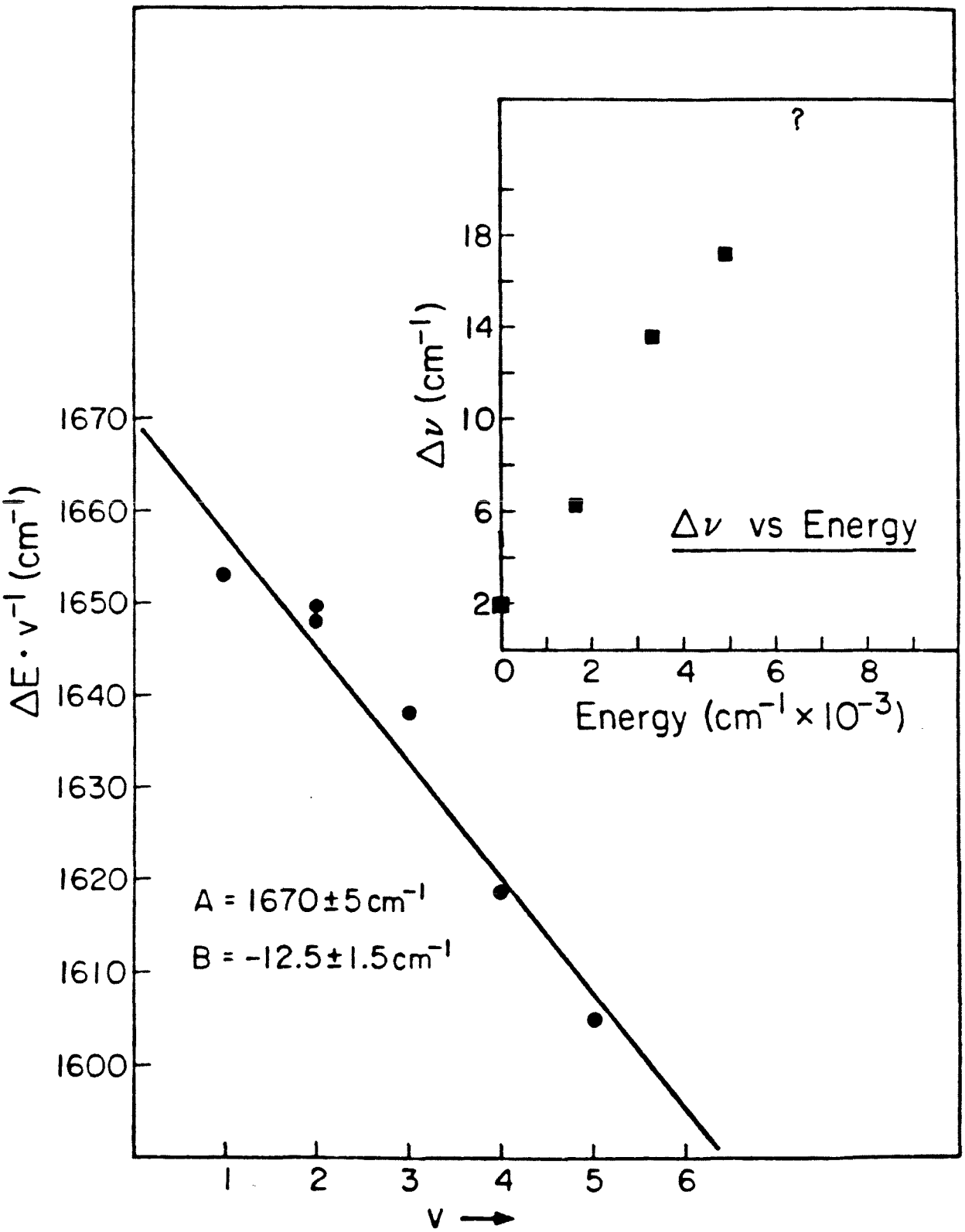
?
18
14
10
6
2
$\Delta\nu$ (cm^{-1})
$\Delta\nu$ vs Energy
0
2
4
6
8
Energy (cm^{-1} × 10^{-3})
1670
1660
1650
1640
1630
1620
1610
1600
$\Delta E \cdot v^{-1}$ (cm^{-1})
A = 1670 ± 5 cm^{-1}
B = −12.5 ± 1.5 cm^{-1}
1
2
3
4
5
6
v →

REFERENCES

[1] M. Elert, P. Stannard, and W. Gelbart, J. Chem. Phys. 67 (1977) 5395.

[2] W. M. Gelbart, P. Stannard, and M. Elert, Int. J. Quant. Chem. 14 (1978).

[3] P. Nagy and W. Hase, Chem. Phys. Lett. 54 (1978) 73.

[4] B. R. Henry, Acc. Chem. Res. 10 (1977) 207.

[5] A. Albrecht in ''Advances in Laser Chemistry'', edited by A. H. Zewail, Springer Series in Chemical Physics, 3 (Springer-Verlag, Berlin 1978), p. 235; and references therein.

[6] K. V. Reddy, R. G. Bray and M. J. Berry, in ref. 5, p. 48.

[7] J. W. Perry and A. H. Zewail, J. Chem. Phys. 70 (1979) 582.

[8] A. H. Zewail, Ph.D. thesis, University of Pennsylvania, Philadelphia, PA; R. M. Hochstrasser, G. W. Scott and A. H. Zewail, Mol. Phys. 36 (1978) 475.

[9] From another set of data we obtained 1672 $\pm$ 6 cm^{-1} and 14 $\pm$ 2 cm^{-1}. These uncertainties are due to the broadening of the high energy overtones and the error in the baselines.

[10] G. W. Robinson in Proceedings of the R. A. Welch Conference on Chemical Research, Vol. XIX Photon Chemistry, Houston, TX 1975. The author mentioned that the high energy CH modes were observed in benzene at long wavelengths from the singlet-

triplet origin. He estimated the relaxation time to be 10 psec.

[11] K. Shobatake, S. A. Rice and Y. T. Lee, J. Chem. Phys. 59 (1973) 2483; see also D. Micha, Chem. Phys. Lett. 46 (1977) 188. The idea for the v-linear dependence arose during a conversation with Professor S. Rice.

[12] D. D. Smith and A. H. Zewail, to be published.

PROPOSAL I.

PREPARATION OF $\underset{\sim}{k}$ NOT EQUAL TO 0 ELECTRONIC EXCITONS: MEASUREMENT OF T_1 AND T_2 AS A FUNCTION OF $\underset{\sim}{k}$

ABSTRACT

The author proposes methods to excite and measure the dynamics of $\underset{\sim}{k} \neq 0$ electronic exciton states. Further that the experiments use the lowest triplet state of a molecular crystal of 1,4-dibromonaphthalene (DBN), which has a well-defined quasi-1-D transport topology. The impetus for preparing the $\underset{\sim}{k} \neq 0$ state is to measure the exciton population relaxation rate (characterized by the constant T_1^{-1}) and phase relaxation rate (T_2^{-1}) as a function of the quasimomentum $\underset{\sim}{k}$. After preparing the $\underset{\sim}{k}$ not equal to 0 eigenstates, one would measure the total (spin + total) T_1 and T_2 using the time-dependent lineshape of the band to band transitions [1]. Or, in the proposed many-wave mixing experiments one measures T_2 by the spectrum of the probe beam. To the author's knowledge, no such condensed matter experiments have been performed and the results would provide the first $\underset{\sim}{k}$ dependent data on coherence, spectral and spatial transport in a simple system with a 1-D transport topology and well characterized spectroscopic parameters.

I. INTRODUCTION

If the proposed experiments are successful, the gain in understanding ''dense'' n-level relaxation and coherence (ill-defined as n-level coherence is) may be greater than the gain in understanding the 1-D exciton dynamics. N-level coherent phenomena involving order parameter descriptions (e.g. liquid crystals, superfluidity), radiationless relaxation, photodissociation, etc.

have many n body - n level formal equivalences. What is missing, however, is data on the evolution of all n-levels of which the optically accessible $\underset{\sim}{k}=0$ state is only 1 of n states.

The methods proposed herein to prepare the $\underset{\sim}{k} \neq 0$ eigenstates can be broadly classified into two categories; (1) those involving single particle excitation (exciton only), and (2) those involving multiple particle excitations (exciton + phonon). Each spectroscopic method has advantages and disadvantages. Rather than describing the best method alone, the author feels it is heuristically useful to discuss each of the techniques. Ultimately, it may be necessary to corroborate the results of several of the proposed methods to unequivocally establish the Physics.

II. DIRECT, ONE-PARTICLE EXCITATION

Briefly, there are three ways to directly excite $\underset{\sim}{k}$ not equal to 0 states; (1) a photon using prism coupling, (2) particle excitation (such as electron impact-beam foil spectroscopy), (3) surface grating coupling of photons. The principal limitation of the prism coupling method (also known as Attenuated Total Reflection--ATR) as first performed by Otto [2] is that it allows excitation of a very limited range of $\underset{\sim}{k}$ values near $\underset{\sim}{k}=0$. The strength of ATR is its simplicity and freedom from artifacts when compared to the two particle excitation methods. Surface grating coupling has similar limitations in the range of $\underset{\sim}{k}$ values it can optically couple to. The shortcoming of charged particle excitation is the lack of resolution and crystal damage, whereas its advantage is a larger range

of $\underset{\sim}{k}$ that is accessible. A brief description of each one particle excitation technique ensues.

Space does not allow a detailed discussion of the prism coupling method (ref. [2] is quite lucid), but ATR allows one to cover only about 2% of the range of $\underset{\sim}{k}$ states between the center ($\underset{\sim}{k}$=0) and edge ($\underset{\sim}{k}\sim 10^7$ cm^{-1}) of the Brillouin zone! Thus only $\underset{\sim}{k}$ very nearly equal to ''zero'' is accessible. [One does mean $\underset{\sim}{k}$ <u>near</u> zero since with or without the prism coupling $\underset{\sim}{k}$ is greater than 20,000 cm^{-1}. Theoretically, there are states with wavevectors <u>smaller and larger</u> than the photon that the photon cannot excite while simultaneously conserving energy and momentum.]

Therefore in the case of DBN, ATR is vanishingly useful since the inhomogeneous broadening for triplet excitons is typically 2% of the exciton bandwidth. That only 2% of the zone is accessible can be seen by examining Fig. 1. One can see the line $(\omega/k)=c$ only intersects the triplet exciton dispersion curve at 20,192 cm^{-1}, which on a linear scale from 0 to 10^7 cm^{-1} appears to be very near zero. When using the ATR method one uses a high index of refraction prism to increase the apparent wavevector (decrease the wavelength) with which one can at best increase the wavevector about a factor of two for a given energy photon. The factor of 2 limit holds since it is difficult to make a glass prism with n>2 (e.g. Schott IRG-2 glass, which is exceptional, has n=1.95 in the relevant visible region). For n=2, the apparent wavelength is shortened to ~2,500 Å which is far away from $(\underset{\sim}{k})^{-1}=(\pi/\underset{\sim}{c})^{-1}\sim 1.25$ Å!! In the ATR method the apparent $\underset{\sim}{k}$ can be shortened somewhat more than a factor of two since the light comes in at

Figure 1. Superimposed dispersion curves of photons and triplet excitons in the first Brillouin zone of DBN. (N.B. the scales for the vertical and horizontal axes are broken.) In the diagram, c is the speed of light and n is the index of refraction. The lowest triplet exciton in DBN starts at 20,192 cm^{-1} and is 24 cm^{-1} wide.

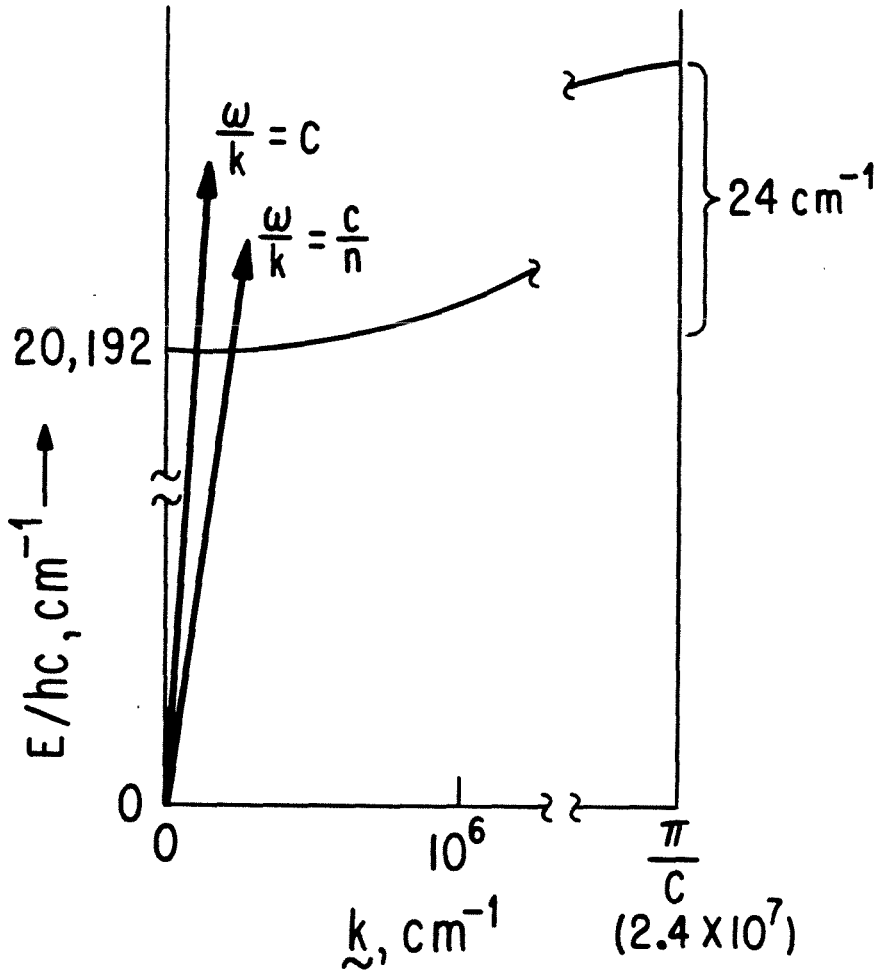
ω/k = c
ω/k = c/n
24 cm⁻¹
20,192
E/hc, cm⁻¹
0
0
10⁶
π/c
(2.4 x 10⁷)
k, cm⁻¹

an angle with respect to the surface normal and it is the projection of the wave on the crystal-spacer-prism interface that is used. However, due to total external reflection from the prism, one cannot make the angle arbitrarily large.

The principal usefulness of the ATR method lies in studies of surface excitation (see, e.g. [3]) where one makes use of the evanescent waves whose penetration depth is controlled by selecting different angles and prism indices of refraction. For the study of surface plasmons [4], ATR is generally adequate since the dispersion curve becomes asymptotically flat for small $\underset{\sim}{k}$ and a wider range of $\underset{\sim}{k}$ is unecessary. Unfortunately, for solids with tight binding type band structures, it is rarely the case that the dispersion reaches a plateau so close to the zone center.

The surface grating coupling method [4] uses an inscribed grating to alter the apparent wavevector of the exciting photon, but as in the case ATR, it is difficult to get more than a factor of 2 or 3 increase in the wavevector. The factor of 2-3 obtains since the absorption intensity from using the higher orders of the Ronchi grating (having square shaped grooves) are small. In principle, different grating geometries could be used to get higher order absorption, but to the author's knowledge, this has not been investigated.

Electron and α particle beam excitation of organic crystals has been attempted [5], but unlike the beam-foil electron energy loss experiments [6] used to study metal plasma resonances, there is severe crystal damage and the resonances are too narrow for a

detailed study with present technology (submillivolt resolution is mandatory). The bottom line is that none of the one particle excitation methods is desirable.

III. TWO PARTICLE EXCITATION METHODS

This class of techniques is distinguished by the fact that to create the $\underset{\sim}{k} \neq 0$ state, an exciton is created concomitantly annihilating or creating a phonon, thus two particles are involved. There are three such techniques that the author is aware of that may be practicable; (1) ''thermally assisted absorption'' (2) stimulated Raman scattering, (3) phonon-laser double resonance.

In the first method, one would use a laser which is in resonance with a band to band absorption where the initial state is a ground electronic state vibrational exciton of wavevector $\underset{\sim}{q}$. The final state is an electronic exciton of wavevector $\underset{\sim}{k}$. The disadvantage of thermally assisted absorption is that one must work at temperatures high enough to populate the ground vibrational exciton, which (a) reduces the quantum yield for emission and (b) makes difficult temperature dependent studies that would determine if there are $\underset{\sim}{k}$ dependent exciton-phonon scattering mechanisms. Once the $\underset{\sim}{k} \neq 0$ state has been prepared by the BTBT absorption one would observe the time dependent band to band emission [1] directly obtaining T_1 and T_2. Then, changing the pump wavelength, one would prepare different $\underset{\sim}{k}$ states, measuring T_1 and T_2 as a function of the quasimomentum, $\underset{\sim}{k}$.

Band to band absorption has been done on naphthalene [7]. It

is sensible, then for reasonable temperatures (~40 K) and low energy ground vibrational excitons, that the experiment may be tractable in DBN. Of course, the signal will depend exponentially on the temperature and energy of the vibrational exciton (i.e. a Boltzmann factor for population of the ground state mode). In the author's opinion, the thermally assisted absorption experiment is the most likely to work with the least effort and should be tried first.

A wave mixing resonance Raman experiment may also be a viable way to measure T_2 as a function of $\underset{\sim}{k}$. With the sample at low temperature, one laser is tuned to excite the $\underset{\sim}{k} \neq 0$ state via ground state absorption, the other laser is tuned to excite the same final $\underset{\sim}{k} \neq 0$ state, but with the ''initial'' state being a ground vibrational exciton (see Fig. 2). The signal of interest would be on scanning the lower energy laser (or higher energy, but scanning just one laser at a time). As the lower energy laser became resonant with BTBT using the same $\underset{\sim}{k}$ state as the high energy laser there should be gain, with the concomitant annihilation of a lattice phonon (required for energy conservation and phase-matching). Experiments similar to the proposed scattering experiment have been done in organic crystals [8], the principal difference being that the proposed experiment exclusively involves band states.

In the phonon-laser double resonance method, the idea is to inject monochromatic phonons into the sample, say continually, and pulse the laser, producing a simultaneous phonon-photon absorption. Such phonon-photon double resonance has been performed in organic crystals [9] but for electron spin resonance transitions where a low

Figure 2. Wave mixing Raman experiment proposed for DBN excitons. The wavevector $\underset{\sim}{k}$ is for the electronic exciton and wavevector $\underset{\sim}{q}$ is for the vibrational exciton. Laser 1 is in ''resonance'' with a $\underset{\sim}{k} \neq o$ 0 state and laser 2 is resonant with the BTBT to the same $\underset{\sim}{k} \neq$ 0 state. Emission of a phonon $\underset{\sim}{q}$ causes gain in probe beam (laser 2).

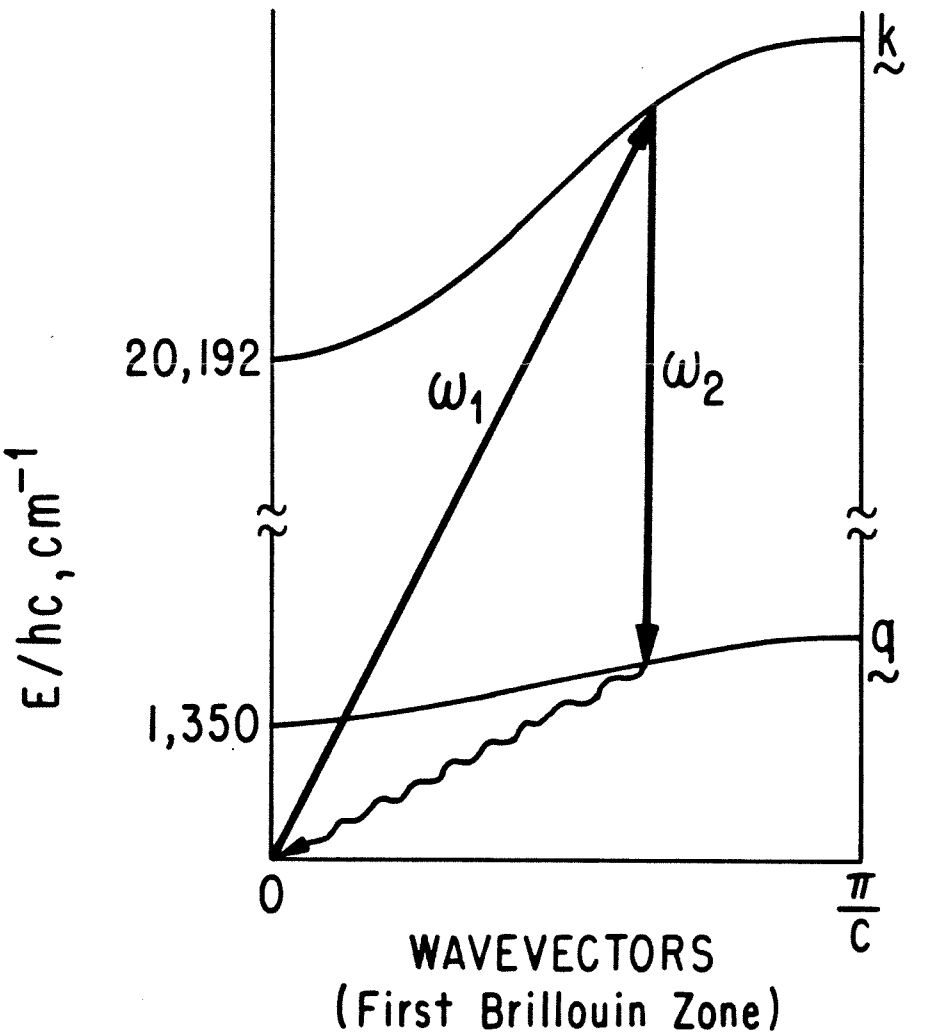
E/hc, cm⁻¹
20,192
1,350
0
k
q
π/c
ω1
ω2
WAVEVECTORS
(First Brillouin Zone)

energy phonon was used. That is to say, low energy in comparison to those needed to populate the $\underset{\sim}{k} \neq 0$ states of DBN (tenths of wavenumbers vs. 24 cm^{-1}). There are two ways to inject the phonons; (1) mechanically coupling a transducer such as a Josephson junction, producing intermediate energy phonons in the hundreds of Ghz [10] or irradiating the crystal with millimeter waves where the induced polarization excites the phonons via electron-phonon coupling. Both methods have been used, but the technology for such experiments is very primitive. A potential problem with the injection of phonons is that the organic crystals are typically monoclinic. Being monoclinic, it is difficult to inject a phonon along a pure mode axis, meaning decay of the phonon and crystal heating may be problematic [11], especially at phonon excitation densities that may be needed for the simultaneous absorption of phonons and photons.

IV. CONCLUSIONS

In summary, the two particle excitations are best suited to the measurement of T_1 and T_2 as a function of the quasimomentum, $\underset{\sim}{k}$. Of the two particle excitation methods, thermally assisted absorption is extremely promising (on the basis of previous experiments) and the many wave mixing experiments, though complex, should yield the most information with the fewest limitations.

REFERENCES

[1] D. D. Smith and A. H. Zewail, J. Chem. Phys. 71 (1979) 3533.

[2] A. Otto, Z. Physik, 216 (1968) 398.

[3] D. Guidotti and S. A. Rice, Phys. Rev. B 15 (1977) 2984; K. Tomoika, M. G. Sceats and S. A. Rice, J. Chem. Phys. 66 (1977) 2984; M. G. Sceats, K. Tomoika and S. A. Rice, J. Chem. Phys. 66 (1977) 4486; R. T. Holm and E. D. Palik, Laser Focus, August 1979, pg. 60.

[4] B. Fischer, N. Marschall and H. J. Quiesser, Surf. Sci. 34 (1973) 50, and references therein.

[5] G. Klein, Mol. Cryst. and Liq. Cryst. 44 (1977) 125; 47 (1978) 39.

[6] A. Krauss and R. Gomer, Phys. Rev. (to be published).

[7] S. D. Colson, D. M. Hanson and G. W. Robinson, J. Chem. Phys. 48 (1968) 2215.

[8] R. M. Hochstrasser, G. R. Meredith and H. P. Trommsdorf, J. Chem. Phys. 73 (1980) 1009.

[9] A. I. Attia, M. J. Buckley, R. M. Panos and J. M. Raney, Phys. Rev. B 15 (1977) 1239.

[10] Duane D. Smith, Candidacy report proposition, Caltech.

[11] Private communication, A. H. Francis, Univ. of Mich., Ann Arbor.

PROPOSAL II.

INVESTIGATION OF VIBRATIONAL OVERTONE DEPHASING AND RELAXATION IN GASEOUS AND CONDENSED PHASES.

ABSTRACT

Using laser Optical-Optical Double Resonance (OODR) and picosecond CARS experiments, it is proposed to measure T_1^{-1} and T_2^{-1} relaxation rates for carbonyl vibrations (principally the CO stretch) as a function of relevant molecular quantum numbers. Further, it is proposed to measure the relaxation rates in the gaseous and condensed phases, providing valuable information on intramolecular and molecule-bath energy transfer.

I. INTRODUCTION

Intense theoretical and experimental effort is being directed towards the study of vibrational relaxation and dephasing. However, to the author's knowledge, there are no unequivocal measurements of overtone T_1 (population relaxation) and T_2 (phase relaxation) parameters. The physical impetus to study overtones is to understand the quantum mechanical features of mode-mode coupling, ''ergodicity'' and the spatial extent of a mode (all may be a function of the quantum numbers and molecule-specific). The chemical impetus is to understand the effect of vibrational dynamics on unimolecular reactions (e.g. multiphoton dissociation) and reactive collisions (e.g. entrance and exit channel relaxation effects).

II. EXPERIMENTAL

Preliminary work on CO stretch overtone lineshapes in matrix-isolated benzophenone [1] from 1.4 to 100 K has been carried out. The data are consistent with CO relaxation rates linear in

the CO quantum number and Raman (lattice-induced) dephasing. Benzophenone is a model ''two-mode'' molecule in that the ring torsions are believed to be the dominant accepting mode for the CO stretch. Rather than use traditional overtone emission, absorption or scattering lineshapes, it is proposed to use the highly selective and sensitive technique of laser multiple optical resonance (see Fig. 1). For an intermediate level with good oscillator strength, slow decay and narrow homogeneous linewidth [1], the origin of the CO $^3\pi\pi^*$ electronic state would be used.

Specific experiments would be (a) CW high resolution optical-optical double resonance (OODR) and (b) transient coherent (wave vector matched, measures T_2) and incoherent (no phase match, measures T_1) stimulated Raman scattering [2]. The CW experiments would use two collinear single-mode dye lasers; the higher energy, ω_1, being fixed in energy while ω_2 is scanned. Monitoring the forward gain for ω_2 would measure the homogeneous linewidth of the overtone. Moving ω_1 in the absorption profile would allow investigation of the total dephasing of different sub-doppler or ''strain field'' components. The transient stimulted Raman scattering experiments, though technologically complex, should be feasible if one can prepare the coherent, vibrationally excited state. One might do this using the higher order Stokes components of a Raman generator [3] (see Fig. 2) containing a carbonyl compound which would be near resonant with a CO overtone when used in conjunction with the parent pump frequency (for instance, a doubled, mode-locked Nd:glass laser). Such a pumping scheme may limit one to the first

Figure 1. Energy level scheme depicting the proposed OODR experiment.

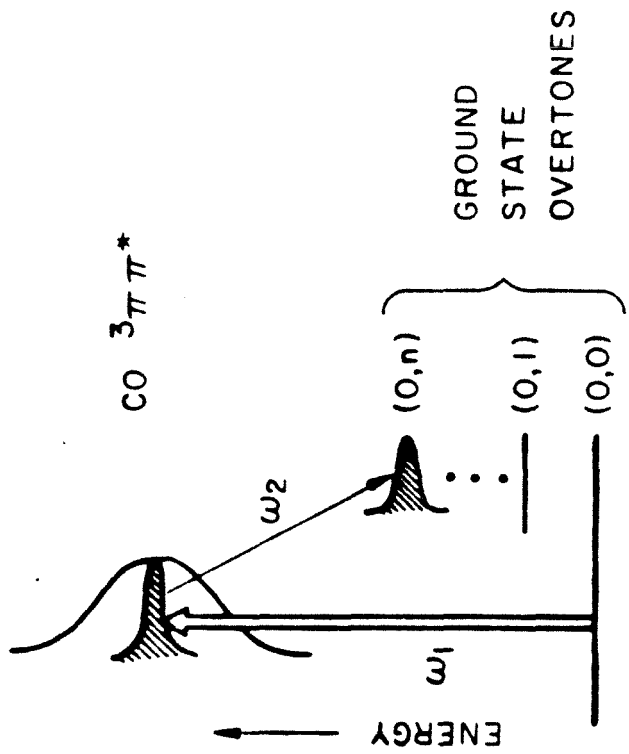
GROUND STATE OVERTONES
(0,n)
(0,1)
(0,0)
CO $^3\pi\pi^*$
ω_2
ω_1
ENERGY

Figure 2. A simplified block diagram of the transient Raman scattering experiment proposed to measure vibrational overtone coherence and relaxation.

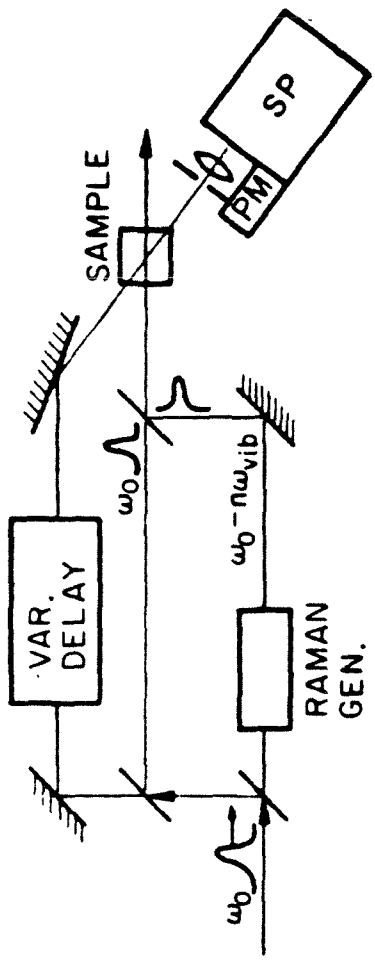
SP
PM
SAMPLE
VAR. DELAY
RAMAN GEN.
ω_0
$\omega_0 - n\omega_{vib}$
ω_0

few overtones, due to anharmonicity. Alternatively, one might use tunable, synchronously pumped dye lasers to take advantage of electronic resonance enhanced scattering to populate the overtones. Such experiments, to the author's knowledge, have not been performed and would also yield information on electronic state coherence. It should be pointed out that populating (much less coherently preparing) the overtone state by direct absorption from the ground state is impractical due to vanishingly small absorption cross-sections. However, the optical pumping scheme with an intermediate, allowed electronic level represents a viable way of preparing the level.

III. CONCLUSION

In summary, the OODR homogeneous linewidth, together with transient T_1 and T_2 measurements, would give a detailed view of carbonyl vibrational dynamics. From an experimental standpoint, the protypic molecule may not be benzophenone or the other extreme H_2CO, but a system with an intermediate density of states for accepting modes, thereby putting the experiment on a time scale to avoid effects such as stimulted Brillouin scattering and transit times across the probing beams.

REFERENCES

[1] D. D. Smith and A. H. Zewail, J. Chem. Phys. 71 (1979) 540; D. D. Smith and A. H. Zewail, to be published.

[2] A. Penzkofer, A. Lauberau and W. Kaiser, Prog. Quant. Elect. 6 (1979) 55 and references therein.

PROPOSAL III.

SEARCH FOR SUBNATURAL LINEWIDTHS USING TRANSIENT LINE NARROWING SPECTROSCOPY.

ABSTRACT

The author proposes development of a laser technique with spectral resolution less than the natural transition linewidth. The method is generically known in the quantum optics literature as Transient Absorption Line Narrowing (TALN). TALN allows measurement of the difference of the natural linewidths (thus phase and population decay) of the two levels involved in the transition rather than the traditional sum of the widths (decays). Thus, one can obtain ultra high resolution if the widths of the two levels are nearly commensurate. No such experiments have been performed on atoms or molecules and it is proposed that the protypical experiments are performed on a Na atom beam, say from a Zacharias type nozzle, not a supersonic nozzle to avoid long range dephasing effects (see proposal IV).

I. INTRODUCTION

In order to more fully understand reactive scattering, energy transfer or unimolecular dynamics (photodissociation, radiationless relaxation, etc.) the chemist is perpetually searching for new tools. Some of the most powerful probes have evolved from the use of lasers: laser induced fluorescence, picosecond spectroscopy, CARS and so on. TALN, with possibilities for exceptional spectral resolution and versatility in a number of experimental applications, can yield a wealth of dynamical information about intra and intermolecular relaxation. However, due to the complexity of TALN experiments, the author expects that TALN's use in the short term

would be limited, and that long term implications are the greatest.

Theoretically, it is well known (e.g. [1] problem 2-7, pg. 28) that in the transient regime, the spectrum for induced transitions in a two level system has a width of $(\gamma_c-\gamma_b)/2$ vs. $(\gamma_c+\gamma_b)/2$, where b and c are the two levels in the transition and the γs are the linewidths. However, there is no experimental proof that one can indeed see such a narrowed line. The author hastens to point out that TALN is different than selecting oscillators that have survived beyond their mean life (e.g. [2] and references therein) or delayed level crossing experiments [3]. TALN relies upon the coherent evolution of states driven and mutually coupled by a monochromatic radiation field.

II. METHODOLOGY

The most practicable form of TALN uses a three level scheme (see Fig. 1). With a picosecond pulse (frequency ω_1) one excites $|b\rangle$. The purpose of the picosecond pulse is to prepare $|b\rangle$ with a well defined phase (this requires the total dephasing time of $|b\rangle$ be longer than the pulse). Population inversion (i.e. a $\pi/2$ pulse) is not necessary. Then, continuously, one coherently drives the b-c transition (frequency ω_2) with a tunable monochromatic field (e.g. a ring laser). It is to be emphasized that coherent pumping of the b-c transition with the steady state monochromatic field is crucial to TALN. However, rather than recording the absorption spectrum of the laser driving the b-c transition, one measures the population in $|c\rangle$ by emission or absorption from $|c\rangle$ to a fourth level. The population in $|c\rangle$ can be measured with another picosecond pulse or the

Figure 1. Level scheme for the proposed TALN experiments. The decay rates for state $|b\rangle$ and $|c\rangle$ are γ_b and γ_c. The frequencies of the $|a\rangle$ to $|b\rangle$ and $|b\rangle$ to $|c\rangle$ transitions are ω_1 and ω_2.

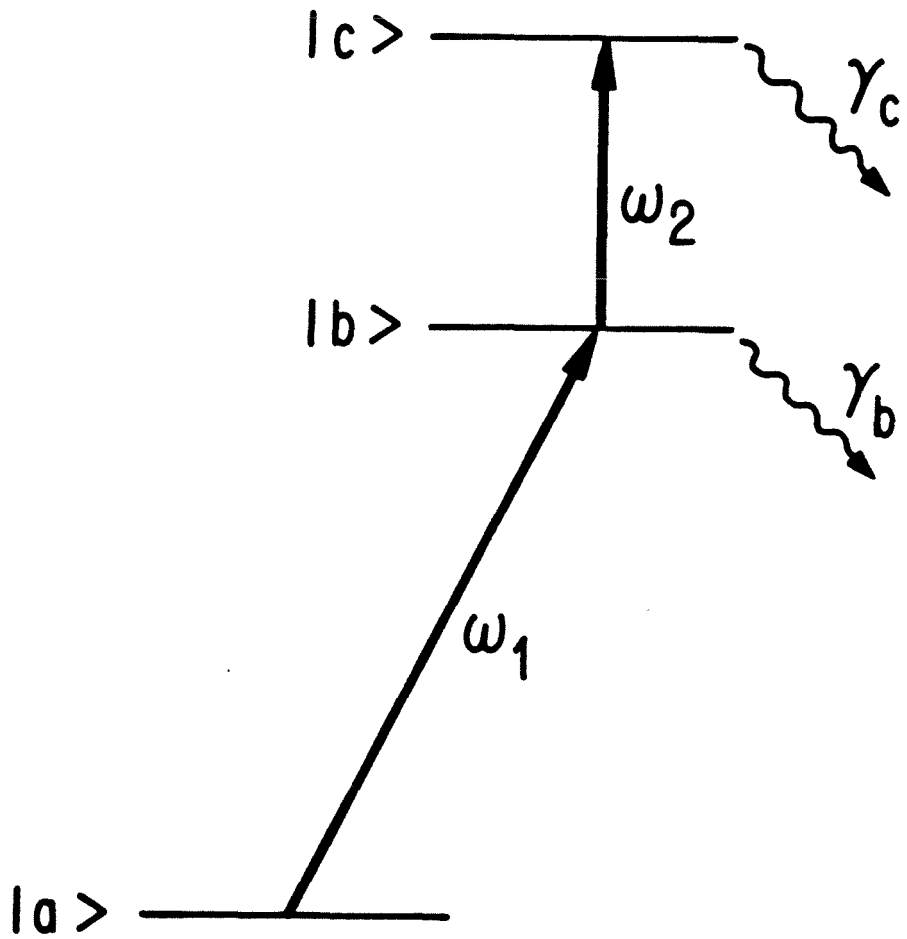
|c>
|b>
|a>
ω_1
ω_2
γ_c
γ_b

time integrated emission from $|c\rangle$ to a fourth level. The shortcoming is that one must wait longer than mean decay time of $|b\rangle$ or $|c\rangle$ to measure the population. But one does not need to wait ''n'' lifetimes nor will waiting infinitely long infinitely narrow the TALN spectrum as in the case of selecting long lived oscillators. The best one can do is to obtain the difference in the widths. Importantly, one can use low spectral resolution to record the decay or absorption from $|c\rangle$, making TALN uniquely powerful. Another notable advantage of TALN is that there are no oscillations in the wings of the narrowed line as is the case for selecting long lived species or in delayed level crossing.

III. DISCUSSION

The physical interpretation of the TALN effect is not yet fully understood [4]. However, at present, the theoretical mechanism for the TALN would appear to be due to interferences between the prepared b-c substates (a substate can loosely be described as an oscillator and a single mode of the field forming an infinitely narrow mixed state [7,8]). The fact that TALN should occur is confirmed by three different mathematical approaches; (1) solution of two coupled linear equations of motion (two pages of simple algebra) [1], (2) solution of a three level density matrix [5] (one day of tedious algebra) and (3) the full quantum field theoretical treatment [6].

Despite the incomplete theoretical understanding of TALN, the promise of the method is great enough to warrant investigation. It is proposed that TALN first be tried on a Na atom

beam (to reduce collisional redistribution effects). For Na, there is a large number of convenient states for the a–b, b–c transitions which would use two visible lasers and do not have largely different decay rates [9]. For molecules, TALN may be expected to be most useful for very small species where the intramolecular relaxation between levels corresponding to $|b\rangle$ and $|c\rangle$ is slow. Thus only diatomic and triatomic molecules (or an atom used as a probe in collisions with molecules) may profitably be used. Put another way, in molecules where there is little or no single vibronic level fluorescence, the decay rates of two upper states may differ widely so that the sum and difference of the widths are essentially the same, in which case, standard high resolution spectroscopy would do as well.

IV. CONCLUSIONS

It has been proposed to look for subnatural transition linewidths using transient absorption line narrowing, which has not yet been experimentally demonstrated. The advantages of TALN over standard high resolution spectroscopy include: (1) resolution less than the natural transition line width and (2) no need for high resolution detection methods such as long path length spectrometers or interferometers. The disadvantages are: (1) the dephasing rates of the two levels must be nearly commensurate or else TALN is no better than standard high resolution laser spectroscopy and (2) one must wait longer than γ_b^{-1} or γ_c^{-1} to collect signal, which may be prohibitive in certain experimental situations.

The ultra high resolution this method affords may be useful in

analyzing the states of projectiles before and after collisions in a molecular beam configuration similar to that of Wittig and coworkers [10], which spatially and spectrally filters the collected light around the scattering region, obtaining energy transfer information on the product species. Alternatively, optical-molecular beam methods similar to those of Kinsey and colleagues [11] may be well suited to TALN. Coupling the atomic and molecular beam methods with TALN, one could in principle obtain unprecedented accuracy in the translational energy distribution and other energy deposition paths.

REFERENCES

[1] M. Sargent, M. O. Scully, W. E. Lamb, ''Laser Physics'', published by Addison-Wesley, Reading, Massachusetts, 1974.

[2] G. zuPutlitz, Comm. Atom. Mol. Phys. 1 (1969) 74.

[3] G. Copley, B. Kibble and G. Series, Phys. Rev. Lett. 31 (1973) 189.; T. Andersen, S. Isaksen, D. B. Iversen and P. S. Ramanujam, Phys. Rev. A 18 (1978) 1079.

[4] M. O. Scully, private communication.

[5] P. Meystre, M. O. Scully, and H. Walther, Opt. Comm. 33 (1980) 153.

[6] M. O. Scully, preprint, to be published.

[7] For a clear but highly simplified discussion see R. Woolley and D. W. N. Stibbs, ''The Outer Layer of a Star'', Oxford University Press, 1953, Chapters VII and VIII.

[8] The ''substate'' jargon has nearly the same physical significance as the intermediate state in the Heitler effect (W. Heitler, ''The Quantum Theory of Radiation'', Oxford University Press, 1953, Chap. V, section 20), or resonance scattering (F. A. Novak, Ph.D. thesis, University of Pennsylvania, 1977).

[9] C. Fabre, S. Haroche and P. Goy, Phys. Rev. A 18 (1978) 229, and references therein.

[10] T. A. Watson, S. Mangir, C. Wittig and M. R. Levy, preprint.

[11] E. J. Murphy, J. H. Brophy and J. L. Kinsey, J. Chem. Phys. 74 (1981) 331.

PROPOSAL IV.

MEASUREMENT OF LOW ENERGY ELASTIC AND INELASTIC COLLISION CROSS SECTIONS FOR ELECTRONIC EXCITED SPECIES USING SUPERSONIC JETS

ABSTRACT

Using the hydrodynamic flow region of an underexpanded supersonic jet, one can adjust collision energies between the seed and carrier gas from about 100 to 1 cm^{-1} (for He gas, say). It is proposed to measure the electronically elastic and inelastic collision cross sections of a seed molecule (atom) as a function of collision energy using high resolution photoexcitation spectra. Further, using simple atomic or molecular Rydberg states, to determine the functional dependence of the cross section on the principal and angular electronic quantum numbers. Using different carrier gases (e.g. He, Ne and Ar) one may be able to develop simple propensity rules for the elastic and inelastic cross sections as a function of relative seed and carrier polarizabilities and/or similar material properties.

I. INTRODUCTION

Much of the early interest in supersonic jet studies was due to the promise of ''collisionless'', internally cold molecules. However, it is becoming clear (at least for unskimmed, single chamber jets) that inelastic collision cross sections for very low energy collisions are orders of magnitude larger than room temperature cross sections (for underexpanded jets with small cones of silence, this can be serious). Studies by Rice and coworkers [1] have shown low energy collisions greatly enhance vibrational relaxation, possibly by orbiting resonances rather than Landau-Teller (''fly-by'') interactions. Microwave experiments have shown a speed

dependent cross section for rotational relaxation [2]. Jouvet and Soep [3] have shown that cross sections for rotational relaxation and collision induced intersystem crossing are as large as 400 $Å^2$ for low energy helium-glyoxal collisions. Other workers in the field [4] have mentioned the care with which one must address such a ''collisionless'' environment and to an extreme way of thinking, one might even suggest that the usefulness of the bare jet lies in complex formation and spectral cooling alone. Even for certain types of common optical experiments on static gas in a bulb, averaging the collision cross section over a large range of energies may be in serious error.

It is proposed to measure the electronic elastic and inelastic collision cross sections for the Na atom and small molecule (methylbenzene) Rydberg states at low energies. Rydberg states were chosen for the preliminary studies since the wavefunctions are exceptionally diffuse and should be most susceptible to dephasing from low energy collisions. To the author's knowledge, no systematic measurements of the electronic cross sections have been carried out and such information should prove valuable. As an example, the electronic line broadening mechanisms would affect engineering of resonance multiphoton ionization experiments used in isotopic enrichment [5]. Another interesting application is towards the study of relaxation pathways for molecular Rydberg states, which may have little real vibrational identity and poor oscillator strength.

II. EXPERIMENTAL

The jet and optical configuration is simple (too simple to warrant a figure): one has the jet, laser and collection optics all perpendicular to one another. Pumping with a narrow bandwidth source (such as a single mode ring laser) and collecting emission to lower energy of the laser, one obtains a high resolution photoexcitation profile. In the event of poor quantum yield for total emission from the state, one might consider multiphoton ionization or intracavity absorption detection schemes. The experiment is performed as a function of distance from the nozzle (selecting the collision frequency and energy) and stagnation pressure and temperature (determining the range of collision energies and frequencies). The collision energy and frequency are well enough understood and calculable from the position dependent jet translational temperature and density [6].

Interpreting the photoexcitation spectra must be done with caution, however, since collecting emission from all points down stream will reveal only the cumulative collisional effects. One can circumvent the problem by masking off the remaining portion of the jet or alternatively, doing absorption studies. However, absorption studies are not practical since for typical jet densities (2×10^{19} cm^{-3}) and circular jet absorption path lengths (100 to 200 microns) absorption is less than 1%, even for large cross sections (10^{-18} cm^2/molecule).

In obtaining the high resolution photoexcitation spectrum, one measures the line broadening effects as a function of collision energy and collision partner, extracting the sum of the elastic and

inelastic cross sections. To separate the pure dephasing and population decay contributions, one needs to determine the total radiative and radiationless decay rates, which can be reasonably well measured with knowledge of the true radiative lifetime and quantum yield measurements, as has been done by Behlen and Rice [7] for naphthalene.

It is proposed that the preliminary experiments be performed on methylbenzene, for which the multiphoton ionization spectroscopy of the 3p Rydberg state has been investigated [8]. Extension to other principal electronic quantum numbers should be straightforward. Done with a variety of carrier gases, the experiments will help determine to what extent that external heavy atom effects [9] (spin orbit coupling and mutual polarizabilities), coulombic interactions, etc. are involved in the low energy cross section. Similar experiments are proposed for the Rydberg states of Na, which can be conveniently prepared using two visible lasers as in the work of Fabre et al. [10]. Moreover, Fabre's work has measured the polarizabilities of the n=23 to 41 Rydberg states, which would be useful in calculation of the cross sections. Hartmann and coworkers [11] are actively involved in rare gas perturber effects in Na as well and the experiments proposed herein should prove highly complementary.

III. CONCLUSIONS

Measurement of T_1 and T_2 is propsed for low energy collisions for electronically excited atomic (Na) and molecular (methylbenzene)

Rydberg states. The goal is to obtain simple propensity rules for oscillator-perturber elastic/inelastic collision cross sections. Moreover, quantum number and energy dependences for the cross section are sought. Ultimately, such information may be useful in resonant multiphoton ionization studies and optical spectroscopy in beams.

REFERENCES

[1] J. Tusa, M. Sulkes and S. Rice, J. Chem. Phys. 73 (1980) 5987; M. Sulkes, J. Tusa and S. A. Rice, to be published.

[2] S. L. Coy, J. Chem. Phys. 73 (1980) 5531.

[3] C. Jouvet and B. Soep, J. Chem. Phys. 73 (1980) 4127.

[4] T. D. Russel, B. M. DeKoven, J. A. Blazy and D. H. Levy, J. Chem. Phys. 72 (1980) 3001.

[5] For a review, see V. S. Letokhov, Phys. Today 33 (1980) 34.

[6] Wade L. Fite, Extranuclear Lab. Inc. Research Note 1, ''Expansion of Gases from Molecular Beam Sources''; D. A. McQuarie, ''Statistical Mechanics'', Harper and Row Pub. Inc., New York, 1973.

[7] F. M. Behlen and S. A. Rice, J. Chem. Phys. in press.

[8] G. O. Uneberg, P A. Campo and P. Johnson, J. Chem. Phys. 73 (1980) 1110.

[9] B. Meyer, ''Low Temperature Spectroscopy'', American Elsevier, New York, 1971.

[10] C. Fabre, S. Haroche and P. Goy, Phys. Rev. A 18 (1978) 229.

[11] A. Flusberg, R. Kachru, T. Mossberg and S. R. Hartmann, Phys. Rev. A 19 (1979) 1607; R. Kachru, T. Mossberg and S. R. Hartmann, Phys. Rev. A 21 (1980) 1124.

PROPOSAL V.

SCATTERING OF STATE SELECTED AND ORIENTED MOLECULAR PROJECTILES FROM CLEAN SINGLE CRYSTAL SURFACES: DIRECT MEASUREMENT OF ANISOTROPY FOR SCATTERING AND CHEMICAL REACTIONS

ABSTRACT

It is proposed to scatter state selected and oriented formaldehyde from well characterized low index single crystal surfaces. By time, angle and mass resolved inelastic scattering, one will be able to gather information on the orientation effects on the elastic and inelastic scattering (reactive + nonreactive). Of greatest interest are those inelastic scattering events which result in energy transfer to the surface and/or chemical decomposition.

I. INTRODUCTION

In the past few years there has been a flurry of papers on surface scattering of neutral particles produced by supersonic beams. The work has dealt mostly with scattering as a probe of surface phonons, surface structure, physisorption potentials and so on. Using helium atoms, for example, it is possible to couple to more energetic phonons than by electron scattering and the surface penetration (i.e. multiple scattering) is less of a problem. Recent studies have found evidence that the helium scatters principally from one phonon [1]. Carried one step further, the studies of Janda et al. [2] have measured the detailed angle and time of flight distributions for scattering Ar from W, where the polarizability of Ar contributes to a stronger interaction and essentially all scattering is inelastic. A logical next step would be to deal with even stronger couplings, such as chemical bonds.

II. EXPERIMENTAL

It is now economically and technologically feasible to orient and state select molecules for use in molecule-surface scattering. Focussing and orienting symmetric [3] and asymmetric tops [4] has been done long ago. In particular, the asymmetric top formaldehyde has been focussed and oriented in a six pole inhomogeneous field followed by adiabatic passage into a homogeneous field [4]. (One might note that with present supersonic jet technology, orienting rotationally cool lighter polar diatomics in inhomogeneous quadrupolar fields [5] followed by homogeneous fields should be quite feasible, though to the author's knowledge, no experiments have utilized this.) In the spirit of previous measurements [2], it is proposed to measure the angle, time and mass resolved scattering of formaldehyde from surfaces as a function of surface temperature and surface structure (stepped, nicked, terraced, etc.). With such detailed data, one should in principle be able to elucidate reaction mechanisms and the shape of the potential surface responsible for the scattering.

III. DISCUSSION

Formaldehyde is a particularly interesting case, since it undergoes thermally activated decomposition on Pd [6] and W [7] and is believed to be an intermediate in the methanation of CO on Ni [8]. Catalytic methanation of CO has been studied theoretically [9] and a geometrically specific formation of the formyl radical is believed to be the important intermediate. Moreover, studies of thermal decomposition of CO and CO/H_2 chemisorbed on Pt/Au segregated alloys [10] has attracted interest for rate

controlled surface chemistry. Apart from purely scientific motivation, clearly there is good chemical/economic impetus to study the reactive scattering of formaldehyde from surfaces.

For the series of small oxygen containing organics, CH_3OH, CH_3OCH_3, H_2CO and $(CH_3)_2O$ (an alcohol, ether, aldehyde and ketone) absorbed on group VIII transition metal catalysts, the principal attachment method seems to be the oxygen lone pair [6] rather than π-type orbitals as in the case of unsaturated hydrocarbons [11]. It would appear, then, that surface-molecule collisions of formaldehyde with the oxygen towards the surface would result in the most energy transfer or chemistry. The proposed scattering experiments would yield information on the possibility of reorientation during the reaction.

However, there is potentially a problem. Interaction of the impinging dipole with its image dipole in the metal exerts a torque ($\underset{\sim}{T} = \underset{\sim}{\mu} \times \underset{\sim}{E}$) that may destroy orientation or state selection achieved with the hexapole and homogeneous fields. Of course, those projectiles which come in at the magic angle (57 degrees) or in the lowest energy configuration will tend to stay so. It is difficult to estimate the image dipole interaction energy since there is dispute that the classical field theory will work at short distances. The data of Harris and coworkers [12] indicates that at least for electronic energy transfer, classical treatment works, where other studies indicate that near field effects may be important [13].

As an order of magnitude estimate of the dipole-image dipole

interaction, a situation with two dipoles, 2 debye each (formaldehyde is 2.39 D [4]), 30 Å apart, the potential is about 5 cm^{-1} and the largest rotational quantum of formaldehyde is ~ 8 cm^{-1} [14]. It may be that different orientations of the impinging dipole will result in differing amounts of rotational excitation, thus selecting different entrance and exit channels for scattering! However, since the molecule moves 10 Å in 1 psec (using a supersonic stream velocity of 1 km/sec) and other short range interactions are starting to come in to effect for the close approach, the dipolar interactions may not alter the orientation or become less important. Ideally, if one could use a molecule with a vanishingly small electric moment that could be oriented magnetically, the problem may be alleviated.

IV. CONCLUSIONS

Using oriented and state selected formaldehyde scattered from well characterized single crystal surfaces, it is proposed to measure the angle, time and mass resolved distributions of the scattered particles as a function of surface temperature and structure. The experiments will help determine (1) the decomposition mechanism of H_2CO and companion reactions, (2) the stereospecificity for chemistry and energy transfer to and from the surface and (3) the shape of the molecule–surface scattering potential.

REFERENCES

[1] B. Feuerbach and M. A. Adriaens, Surf. Sci. 94 (1980) L171.

[2] K. C. Janda, J. Hurst, C. Becker, J. Cowin, D. Auerbach and L.

Wharton, J. Chem. Phys. 72 (1980) 2403.

[3] K. H. Kramer and R. B. Bernstein, J. Chem. Phys. 42 (1965) 767.

[4] E. Jones and P. Brooks, J. Chem. Phys. 53 (1970) 55.

[5] H. Bennewitz, W. Paul and Ch. Schlier, Z. Physik 141 (1955) 6.

[6] H. Luth, G. Rubloff and W. Grobman, Surf. Sci. 63 (1977) 325.

[7] R. Gasser, G. Jackson and F. Rolling, Surf. Sci. 67 (1977) 317.

[8] V. M. Vlasenko and G. E. Yuzefovich, Russian Chem. Rev. 38 (1969) 728; G. A. Mills and F. W. Steffgen, Catal. Rev. 8 (1973) 159.

[9] W. Goddard, S. Walch, A. Rappe and T. Upton, J. Vac. Sci. Tech. 14 (1977) 416.

[10] J. A. Schwartz, R. S. Polizzotti and J. J. Burton, J. Vac. Sci. Tech. 14 (1977) 457.

[11] J. Demuth and D. Eastman, Phys. Rev. Lett. 32 (1974) 1123; Jap. J. Appl. Phys. supp. 2, part 2 (1974) 827.

[12] A. Campion, A. R. Gallo, C. B. Harris, H. J. Robota and P. M. Whitmore, Chem. Phys. Lett. 73 (1980) 447.

[13] See, e.g., the review of T. E. Furtak and J. Reyes, to be published.

[14] G. Herzberg, ''Electronic Spectra and Electronic Structure of Polyatomic Molecules'', Van Nostrand Reinhold Co., New York, 1966, table 66 page 612.

APPENDIX I.

ANALYTIC EXPRESSIONS AND MONTE CARLO PROGRAM FOR SIMULATION OF IMPURITY CLUSTER PROBABILITIES IN RANDOM 1-D CHAINS

APPENDIX I.

In this appendix we use Lagrange multipliers to determine the probabilities of isolated impurity n-mers and ''contiguous'' impurity n-mers in a randomly substituted one-dimensional chain.

Given a linear array of N sites to be randomly occupied by G guests and H hosts, we calculate the number of guest clusters of length n isolated on both sides by a host (the remaining lattice configuration being unspecified).

Define q_n as the number of guest clusters containing n contiguous guests, where n=0,1,2,... By definition, we choose n=0 to represent the single host specie, when n=1, one has a monomer and so on. To formulate the problem, define a guest cluster as n guests terminated only on the right by a host. Using a basis of clusters constructed in this manner, placing n-mers side by side will give a least one spacer between clusters, producing isolated n-mers.

Using the notation developed above it is obvious that

$$\sum_{n=0}^{\infty} nq_n = G \tag{A1.1}$$

and

$$\sum_{n=0}^{\infty} q_n = H = N - G. \tag{A1.2}$$

(Recall in doing sums (A1.1) and (A1.2) the sum starts with the zero

cluster). To find the cluster distribution, one wants to maximize the ''entropy'' of the quantity

$$(A1.3) \qquad \frac{\left[\sum_{n=0}^{\infty} q_n\right]!}{\left[\prod_{n=0}^{\infty} (q_n)!\right]} = \frac{(N - G)!}{\prod_{n=0}^{\infty} (q_n)!}$$

Which is the number of permutations of all n-mers divided by the number of ways all clusters of a particular size can be permuted among themselves (which would not yield a distinguishable configuration). Equation (A1.3) can be maximized subject to the constraints

$$\sum_{n=0}^{\infty} nq_n - G = 0$$

$$\sum_{n=0}^{\infty} q_n - (N - G) = 0.$$

Thus, the Lagrangian would be

$$L = \ln\left[\frac{(N-G)!}{\prod_{n=0}^{\infty} (q_n)!}\right] - \lambda\left(\sum_{n=0}^{\infty} nq_n - G\right) - \eta\left(\sum_{n=0}^{\infty} q_n - (N-G)\right)$$

Using Stirling's approximation for the log of a factorial

$$(A1.4) \qquad \frac{\partial L}{\partial q_n} = 0 = -\ln(q_n) - n\lambda - \eta$$

$$q_n = e^{-(n\lambda + \eta)}$$

We wish to find expressions for the exponentials of the Lagrange multipliers in (A1.4) in terms of N, G and H. From (A1.4) and (A1.2);

$$(A1.5) \qquad \sum_{n=0}^{\infty} q_n = e^{-\eta} \sum_{n=0}^{\infty} e^{-n\lambda}$$

$$(A1.6) \qquad e^{-\eta} = \frac{(N-G)}{\sum_{n=0}^{\infty} e^{-n\lambda}}$$

With manipulation of (A1.5) (too lengthy to be demonstrated here), one can show $e^{-\lambda} = G/N$. Therefore

$$\sum_{n=0}^{\infty} \left[e^{-\lambda} \right]^n = 1/(1 - (G/N)).$$

Using the last two results and substituting eqn. (A1.6) into (A1.4), one obtains

$$(A1.7) \qquad q_n = N (1 - (G/N))^2 (G/N)^n.$$

Or, in terms of guest concentration, the number of clusters of n impurities in a chain N long is

$$(A1.8) \qquad q_n = N(1-C)^2 C^n.$$

Equation (A1.8) is the principal result we sought.

Now we want to find the probability of n-contiguous i-mers, d_{in}, in 1-D

(A1.9) $$N - G - q_i = \sum_{n}^{\infty} d_{in}$$

(A1.10) $$\sum_{n=1}^{\infty} n d_{in} = q_i$$

maximize

(A1.11) $$\frac{(N - G - q_i)!}{\prod_{n=0}^{\infty} (d_{in})!}$$

subject to the constraints (A1.9) and (A1.10);

(A1.12) $$L=(N-G-q_i)\ln(N-G-q_i)- \sum_{n=0}^{\infty} d_{in}\ln(d_{in}) - d_{in}n + \lambda(N-G-q_i- \sum_{n=0}^{\infty} d_{in})$$

$$\eta(q_i - \sum_{n=0}^{\infty} n d_{in})$$

Optimize the Lagrangian with respect to a particular d_{in}

(A1.13) $$\frac{\partial L}{\partial d_{in}} = -\ln(d_{in}) - \lambda - n\eta = 0$$

(A1.14) $$d_{in} = e^{-\lambda - n\eta}$$

(A1.15) $$\sum_{n=0}^{\infty} d_{in} = e^{-\lambda} \sum_{n=0}^{\infty} e^{-n\eta}$$

Using (A1.9) and noting that the geometric sum in (A1.15) is equal to $1/(1-e^{-\eta})$,

$$e^{-\lambda} = (N-G-q_i)(1-e^{-\eta}) \tag{A1.16}$$

Use (A1.16) in (A1.15);

$$d_{in} = (N-G-q_i)(e^{-n\eta} - e^{-(n+1)}) \tag{A1.17}$$

$$\sum_{n=0}^{\infty} nd_{in} = (N-G-q_i)\left(\sum_{n=0}^{\infty} ne^{-n\eta}\right)(1-e^{-\eta}) \tag{A1.18}$$

$$\sum_{n=0}^{\infty} nd_{in} = (N-G-q_i)(1-e^{-\eta})\frac{e^{-\eta}}{(1-e^{-\eta})^2} \tag{A1.19}$$

Use (A1.19) and (A1.10) solving for $e^{-\eta}$;

$$q_i = (N-G-q_i)e^{-\eta}/(1-e^{-\eta})$$

$$q_i = (N-G-q_i)e^{-\eta} + q_i e^{-\eta}$$

$$\frac{q_i}{N-G} = e^{-\eta} \tag{A1.20}$$

Substitute (A1.20) and (A1.16) into (A1.15);

$$d_{in} = (N - G - (q_i/N-G))((q_i/N-G)^n \tag{A1.21}$$

Or, in terms of the concentration (using the expressions above derived for q_i, the cluster probabilities;

$$(A1.22)\quad d_{in} = \left[N(1-(G/N)) - (1-C)^2 C^i N \right] \left[1 - \frac{C^i(1-C)^2 N}{(1-(G/N))N} \right]$$

$$X \left[\frac{C^i(1-C)^2 N}{(1-(G/N))N} \right]^n$$

$$(A1.23)\quad d_{in} = N\left[(1-C) - C^i(1-C)^2\right] \left[1 - C^i(1-C)\right] \left[C^i(1-C)\right]^n$$

Which is number of n contiguous i^{th} mers in a 1-D lattice of N sites. e.g. for i=2, n=3 one has the following configuration; G = guest and H = host.

Listing of program used to count impurity clusters in a randomly substituted 1-D chain.

```
      INTEGER A(10000),B,C,D,E,F,G,H,I,J,K,L,M,N,O,P,Q,R,S,T,U,V
      INTEGER M1,M2,M3,D1,D2,D3,T1,T2,T3,MONDIM
      INTEGER OTHER,MM,MULTID
      INTEGER MON,DIM,TRI,TET,PENT,HEX,SEPT,NON,DEC,UNDEC
      DIMENSION LINEAR(10000)
      INTEGER LM(10000)
      WRITE (5,5)
5     FORMAT( ' INPUT NUMBER OF IMPURITIES (OUT OF 10000)')
      READ(5,10)N
10    FORMAT (15)
C     THE DO LOOP DEFINED BY STATEMENT 11 FILLS THE ARRAY
C     LM WITH -1'S SO THAT IN LOOPS 450 AND 550, WHICH
C     COUNT THE NUMBER OF CONTIGUOUS MONOMERS AND DIMERS
C     RESPECTIVELY, ONE CANNOT ACCIDENTALLY FIND A
C     NUMBER GREATER THAN OR EQUAL TO ZERO, WHICH WOULD
C     BE MISTAKEN FOR A CLUSTER, FURTHER IT ALLOWS THE
C     COMPUTER TO DECIDE WHEN IT CAN STOP SEARCHING
C     THE ARRAY LM FOR CLUSTERS
      DO 11 I=1,10000
      A(I)=I
      LM(I)=-1
      LINEAR(I)=0
11    CONTINUE
      WRITE (5,13) A(N)
13    FORMAT (I6)
C     THE DO LOOP DEFINED BY STATEMENT NUMBER 20 POPULATES THE
C     ARRAY LINEAR AT RANDOM WITH 1'S WHICH ARE TO REPRESENT
C     IMPURITIES.  EVERY ELEMENT IN THE ARRAY LINEAR WAS PREVIOUSLY
C     SET TO ZERO.  ONLY N IMPURITIES ARE PLACED IN THE ARRAY.
C     THE DO LOOP DEFINED BY STATEMENT 15 IS TO INSURE THAT THE
C     SAME RANDOM NUMBER IS NOT CHOSEN TWICE AND THE RANDOM
C     NUMBER GENERATOR CANNOT TRY TO PLACE TWO OR MORE IMPURITIES
C     ON ONE SITE.
      DO 20 I=1,N
      H=RAY(DUM)*(10000-I+1)
      LINEAR(A(H))=1
      INT=10000-I
      DO 15 J=H,INT
      A(J)=A(J+1)
15    CONTINUE
20    CONTINUE
      B=0
      M=1
C     THE DO LOOP DEFINED BY STATEMENT NUMBER 100 COMPUTES
C     A LINEAR ARRAY CONTAINING THE CLUSTER SIZES,  IN
C     SEQUENCE.  FOR EXAMPLE, IF THE MONTE CARLO CALCULATION
C     GAVE THE SEQUENCE ...01011010001..., (WHERE 1 IS AN IMPURITY
C     AND 0 IS A HOST) WHICH IS MONO-DIMER-MONO-HOST-HOST-MONO,
C     THE ARRAY LM WOULD CONTAIN ....121001...  KEEP IN
C     MIND THAT WHEN ONE SPECIFIES A MONOMER YOU SPECIFY ONE
```

```
C       IMPURTIY AND ONE (ONLY) HOST, SO A MONOMER IS ...01... AND A
C       DIMER IS ...011... ETC>
        DO 100 I=1,10000
        IF (LINEAR(I) .EQ. 0) GO TO 30
        B=B+1
        IF (I  .EQ. 10000) GO TO 30
        GO TO 100
30      LM(M)=B
        B=0
        M=M+1
100     CONTINUE
        B=0
        M1=0
        M2=0
        M3=0
        MM=0
C       DEFINITION OF VARIABLES:  M1 IS THE NUMBER OF MONOMERS
C       WHICH DO NOT HAVE A NEIGHBORING IMPURITY CLUSTER WHICH
C       IS A MONOMER (ANY OTHER CLUSTER IS ACCEPTABLE).  M2 IS THE
C       NUMBER OF DOUBLE MONOMERS (TWO CONTIGUOUS MONOMERS).
C       M3 IS THE NUMBER OF TRIPLE MONOMERS (THREE CONTIGUOUS
C       MONOMERS).  MM IS ALL MULTIPLE MONOMERS WITH GREATER
C       THAN THREE CONTIGUOUS MONOMERS.  THE SAME NOMENCLATURE
C       IS USED BELOW FOR DIMERS, WHERE MULTID IS THE NUMBER
C       OF MULTIPLE DIMERS HAVING GREATER THAN THREE DIMERS
C       IN A ROW.
        DO 450 I=1,10000
        IF(LM(I).NE.1) GO TO 400
        B=B+1
        IF(I.EQ.10000) GO TO 400
        GO TO 450
400     IF(B.EQ.1) M1=M1+1
        IF(B.EQ.2) M2=M2+1
        IF(B.EQ.3) M3=M3+1
        IF(G.GE.4) MM=MM+1
        IF(LM(I).EQ.-1) GO TO 475
        B=0
450     CONTINUE
475     D1=0
        D2=0
        D3=0
        MULTID=0
        C=0
        DO 550 I=1,10000
        IF(LM(I).NE.2) GO TO 500
        C=C+1
        IF(I.EQ.10000) GO TO 500
        GO TO 500
500     IF(C.EQ.1) D1=D1+1
        IF(C.EQ.2) D2=D2+1
        IF(C.EQ.3) D3=D3+1
        IF(C.GE.4) MULTID=MULTID+1
        IF(LM(I).EQ.-1) GO TO 575
```

```
      C=0
550   CONTINUE
575   MON=0
      DIM=0
      TRI=0
      TET=0
      PENT=0
      HEX=0
      SEPT=0
      OCT=0
      NON=0
      DEC=0
      UNDEC=0
      OTHER=0
      DO 698 I=1,10000
      IF(LM(I).EQ.1) MON=MON+1
      IF(LM(I).EQ.2) DIM=DIM+1
      IF(LM(I).EQ.3) TRI=TIR+1
      IF(LM(I).EQ.4) TET=TET+1
      IF(LM(I).EQ.5) PENT=PENT+1
      IF(LM(I).EQ.6) HEX=HEX+1
      IF(LM(I).EQ.7) SEPT=SEPT+1
      IF(LM(I).EQ.8) OCT=OCT+1
      IF(LM(I).EQ.9) NON=NON+1
      IF(LM(I).EQ.10) DEC=DEC+1
      IF(LM(I).EQ.11) UNDEC=UNDEC+1
      IF(LM(I).GE.12) OTHER=OTHER+1
      IF(LM(I).EQ.-1) GO TO 699
698   CONTINUE
c     THE DO LOOP DEFINED BY STATEMENT NUMBER 704 SEARCHES
C     THE ARRAY LM FOR A MONOMER NEXT TO A DIMER, I.E.
C     A CONFIGURATION OF EITHER ...01011... OR ...01101...
c     (AGAIN THE 0 IS A HOST AND A 1 IS AN IMPURITY SITE)
C     NOTE CAREFULLY THAT THIS ALGORITHM CANNOT DISTINGUISH THE
C     CONFIGURATION ..0101101.. AND ..01011..01011..  THAT
C     IS TO SAY THAT IF YOU HAVE A MONOMER-DIMER-MONOMER SEQUENCE
C     THIS ALGORITHM CALLS THAT SEQUENCE TWO MONO-DIMER PAIRS.
      MONDIM=0
699   DO 704 I=1,10000
      IF (LM(I).EQ.-1) GO TO 750
      IF (LM(I).NE.1) GO TO 701
      GO TO 702
701   IF (LM(I).NE.2) GO TO 704
      GO TO 703
702   IF (LM(I+1).NE.2) GO TO 704
      MONDIM=MONDIM+1
      GO TO 704
703   IF (LM(I+1).NE.1) GO TO 704
      MONDIM=MONDIM+1
704   CONTINUE
750   ANS=FLOAT(N)/FLOAT(10000)
      WRITE (5,775) ANS
775   FORMAT ('FRACTION OF LATTICE DOPED IS',F8.4)
```

```
      WRITE (5,8000 M1,M2,M3,MM,D1,D2,D3,MULTID
800   FORMAT (' M1=',I5,',M2=',I5,',M3=',I5,',MM=',I5,
1     ',D1=',I5,',D2=',I5,',D3=',I5,',MULTID=',I5)
      WRITE (5,815) MONDM,MON,DIM,TRI,TET,PENT,HEX
815   FORMAT ('MONDIM=',I5,',MON=',I5,',DIM=',I5,',TRI=',
1     I5,',TET=',I5,',PENT=',I5,',HEX=',I5)
      WRITE (5,820) SEPT,OCT,NON,DEC,UNDEC,OTHER
820   FORMAT ('SEPT=',I5,',OCT=',I5,',NON=',I5,',DEC=',
1     I5,',UNDEC=',I5,',OTHER=',I5)
      STOP
      END
```

APPENDIX II.

MONTE CARLO FOR SIMULATING QUANTUM MECHANICAL MOTION OF OPTICAL EXCITATION ON A RANDOMLY DOPED 1-D CHAIN WITH A SUPEREXCHANGE HAMILITONIAN.

APPENDIX II.

This program generates excitation on a trap in a randomly doped 1-D chain. Then the program calculates the superexchange coupling matrix element and hop time using the simulated nearest impurity neighbor distances (picking the largest). Hops occur until the excitation is trapped at an n-mer ($n \geq 2$). A large number of excitations are created and the distribution of number of steps before trapping and lifetime before trapping is computed. The competition between radiationless decay and trapping is also computed.

Glossary of Variables.

TAU--exciton lifetime (milliseconds are convenient).

NTRAPS--mole fraction of lattice sites occupied by supertraps.

CONC--mole fraction of lattice sites occupied by doant.

HOPTME--near-neighbor hoptime.

ATTEN--near neighbor hoptime divided by monomer trap depth (for calculating superexchange Hamiltonian).

NUMXIT--number of excitons created to go on the ''random'' walk.

TERLIF--number of excitons terminated by radiative decay.

TERIMP--number of excitons terminated by trapping on supertraps.

INTRAP--number of excitons created on supertraps (no random walk, then!).

ISTEP--number of steps a given exciton has taken.

RANREL--random real number uniformly distributed between 0 and 1.

NX--random integers distributed between 0 and 2^{31}.

RANDIS--random numbers distributed with the Hertz distribution.

RANHOP--random hopping time calculated with Hertz distribution and superexhcange Hamiltonian.

LIFTME--total lifetime of an exciton, later put into array TOTLIF.

MPURIT--if MPURIT=0, then no impurity supertrap is at that site, if MPURIT=1, then there is an impurity at that site.

SUMLIF--the sum of the total number of steps taken by each of the excitons (used to calculate the average exciton lifetime).

SUMSTP--the sum of the number of steps taken by each exciton (used to calculate the average number of steps taken).

RANIMP--random real numbers uniformly distributed between 0 and 1.

YLIF--array for bin-sort MC lifetimes.

YSTP--array for bin-sort for MC number of steps.

YSUPER--array for bin-sort of superexhange times from manufactured Hertz distribution.

YHERTZ--array for bin-sort of manufactured Hertz distribution.

In the following is a short mathematical description of the procedure used to generate the 1-D Hertzian distribution of random numbers from a uniform distribution of random numbers. This ''mapping'' procedure if you will, is of great practical importance since essentially all computer algorithms to generate random numbers produce a uniform distribution.

The 1-D distribution is exponential and this is a particularly simple case. One starts with a random number generator generating random numbers, U, uniformly between 0 and 1. Since the Hertzian distribution is normalized, one can set the two integrals equal to one another and solve for one random variable in terms of another. For more detail, the reader is referred to D. E. Knuth ''Seminumerical Algoithms for Digital Computers''.

$$U = \int_0^x \rho e^{-\rho x'} dx'$$

$$= -e^{-\rho x} + 1$$

Solve for x in terms of U;

$$x = \frac{-\ln(1-U)}{\rho}$$

Thus, one draws a uniformly distributed random number U, puts it in the equation above and obtains an exponentially distributed random number. One should be careful to pick a random number generator that will not exhaust itself before the program stops drawing random numbers. In this program, the IBM cataloged procedure power residue method described in manual C20-8011 was used. The procedure, NRAND, is specific to the system 370 and will produce 2^{29} terms before repeating. To insure uniqueness in choice of the random numbers, the day and date and time on the IBM 370 was used as the starting number in the sequence of random numbers that NRAND would generate (since the user must supply one number to start the random sequence).

Physically, the only shortcoming with this Monte Carlo that the author is aware of is that it would neglect the potentiality of correlated motion. That is, the excitation is spatially trapped by hopping between two impurities that are more strongly coupled to one another than to any other impurities.

```
c       This Monte Carlo was written to calculate the distribution of
c       arrival times at 'supertraps' for a randomly doped chain
c       where a superexchange potential is the coupling Hamiltonian.
c
      DIMENSION HERTZ(5000),SUPERX(5000),YHERTZ(10),XHERTZ(10)
      DIMENSION YSUPER(10),XSUPER(10),XHOP(10),YHOP(10),YSTP(10)
      DIMENSION XSTP(10),YLIF(10),XLIF(10),TOTLIF(1000),ISTEPS(1000)
      DIMENSION DOC(3)
      REAL  LIFTME,LIFMAX,LIFMIN,LIFINT
      REAL NTRAPS
      INTEGER TERIMP
      DATA DOC/0.,0.,1./
      READ(5,100) TAU,NTRAPS,CONC,HOPTME,ATTEN,NUMXIT
100   FORMAT(3(F10.3),E10.3,F10.3,I3)
      TERLIF=0
      TERIMP=0
      INTRAP=0
      NX=54321
      DO 500 J=1,NUMXIT,1
      LIFTME=0
      ISTEP=0
      DO 450 I=1,10000,1
      IF(I.EQ.10000) GO TO 510
410   NX=NRAND(NX)
      RANREL=NX/0.2147484E10
      RANDIS=-ALOG(1-RANREL)/CONC
      IF(RANDIS.LT.1.OR.RANDIS.GT.10) GO TO 410
      RANHOP=HOPTME*ATTEN**(RANDIS-1)
      LIFTME=LIFTME+RANHOP
      ISTEP=ISTEP+1
      NX=NRAND(NX)
      RANIMP=NX/0.2147484E10
      MPURIT=0
      IF(RANIMP.LE.NTRAPS) MPURIT=1
      IF(MPURIT.EQ.1) GO TO 475
      IF(EXP(-RANHOP/TAU).LT.0.37) GO TO 473
450   CONTINUE
473   TERLIF=TERLIF+1
      GO TO 480
475   IF(ISTEP.EQ.1) GO TO 485
      IF(ISTEP.GT.1) GO TO 477
477   TOTLIF(J)=LIFTME
      ISTEPS(J)=ISTEP
      TERIMP=TERIMP+1
      GO TO 500
480   TOTLIF(J)=LIFTME
      ISTEPS(J)=ISTEP-1
      GO TO 500
485   INTRAP=INTRAP+1
      ISTEPS(J)=0
      TOTLIF(J)=0
500   CONTINUE
      GO TO 525
```

```
510   WRITE(6,520)
520   FORMAT (1H0, 26('*****'))
      WRITE(6,521)
521   FORMAT(1H0 'ERROR--MORE THAN 10,000 STEPS TAKEN')
      WRITE (6,520)
525   SUMSTP=0
      SUMLIF=0
      DO 600 I=1,NUMXIT,1
      SUMLIF=TOTLIF(I)+SUMLIF
      SUMSTP=ISTEPS(I)+SUMSTP
600   CONTINUE
      AVELIF=SUMLIF/(NUMXIT-INTRAP)
      AVESTP=SUMSTP/(NUMXIT-INTRAP)
      DO 650 J=1,10,1
      YLIF(J)=0
      YSTP(J)=0
      YHERTZ(J)=0
      YSUPER(J)=0
650   CONTINUE
      CALL MAXMIN(TOTLIF,1000,LIFMAX,LIFMIN)
      LIFINT=(LIFMAX-LIFMIN)/10.
      DO 675 K=1,10,1
      XLIF(K)=(K-.5)*LIFINT+LIFMIN
675   CONTINUE
      DO 800 I=1,NUMXIT,1
      DO 700 J=1,10,1
      A=(J-1)*LIFINT+LIFMIN
      B=J*LIFINT+LIFMIN
      IF(TOTLIF(I).GE.A.AND.TOTLIF(I).LT.B) GO TO 750
      GO TO 700
750   YLIF(J)=YLIF(J)+1
      GO TO 800
700   CONTINUE
800   CONTINUE
      CALL MAXMIN(ISTEPS,-NUMXIT,ISTPMX,ISTPMN)
      STPMAX=ISTPMX
      STPMIN=ISTPMN
      STPINT=(STPMAX-STPMIN)/10.
      IF(STPMAX.LT.10) STPMAX=10
820   DO 825 J=1,10,1
      XSTP(J)=(J-.5)*STPINT+STPMIN
825   CONTINUE
      DO 1000 I=1,NUMXIT,1
      DO 900 J=1,10,1
      A=(J-1)*STPINT+STPMIN
      B=J*STPINT+STPMIN
      IF(ISTEPS(I).GE.A.AND.ISTEPS(I).LT.B) GO TO 850
      GO TO 900
850   YSTP(J)=YSTP(J)+1
      GO TO 1000
900   CONTINUE
1000  CONTINUE
      DO 1100 I=1,5000
```

```
1050  NX=NRAND(NX)
      RANREL=NX/.2147484E10
      HERTZ(I)=-ALOG(1-RANREL)/CONC
      IF(HERTZ(I).LT.1.OR.HERTZ(I).GT.10) GO TO 1050
      SUPERX(I)=HOPTME*ATTEN**(HERTZ(I)-1)
1100  CONTINUE
      CALL MAXMIN(HERTZ,5000,HRTZMX,HRTZMN)
      HRTZIN=(HRTZMX-HRTZMN)/10.
      DO 1200 J=1,10,1
      XHERTZ(J)=(J-.5)*HRTZIN+HRTZMN
1200  CONTINUE
      DO 1400 I=1,5000,1
      DO 1300 J=1,10,1
      A=(J-1)*HRTZIN+HRTZMN
      B= J*HRTZIN+HRTZMN
      IF(HERTZ(I).GE.A.AND.HERTZ(I).LT.B) GO TO 1350
      GO TO 1300
1350  YHERTZ(J)=YHERTZ(J)+1
      GO TO 1400
1300  CONTINUE
1400  CONTINUE
      CALL MAXMIN(SUPERX,5000,XSUPMX,XSUPMN)
      SUPRIN=(XSUPMX-XSUPMN)/10.
      DO 1425 I=1,10,1
      XSUPER(I)=(I-.5)*SUPRIN+XSUPMN
1425  CONTINUE
      DO 1600 I=1,5000,1
      DO 1500 J=1,10,1
      A=(J-1)*SUPRIN+XSUPMN
      B=J*SUPRIN+XSUPMN
      IF(SUPERX(I).GE.A.AND.SUPERX(I).LT.B) GO TO 1450
      GO TO 1500
1450  YSUPER(J)=YSUPER(J)+1
      GO TO 1600
1500  CONTINUE
1600  CONTINUE
      CALL MAXMIN(YLIF,10,YLIFMX,YLIFMN)
      CALL LABEL(0.,0.,LIFMIN,LIFMAX,15.,4,'LIFETIME',8,0)
      CALL LABEL(0.,0.,YLIFMN,YLIFMX,10.,4,'NUMBER OF EXCITONS',18,1)
      CALL PLOTXY(10,XLIF,YLIF,LIFMIN,LIFMAX,YLIFMN,YLIFMX,1,0,3,1,DOC)
      CALL MAXMIN(YSTP,10,YSTPMX,YSTPMN)
      CALL LABEL(0.,0.,STPMIN,STPMAX,15.,4,'NUMBER OF STEPS',15,0)
      CALL LABEL(0.,0.,YSTPMN,YSTPMX,10.,4,'NUMBER OF EXCITONS',18,1)
      CALL PLOTXY(10,XSTP,YSTP,STPMIN,STPMAX,YSTPMN,YSTPMX,1,0,3,1,DOC)
      CALL MAXMIN(YHERTZ,10,YHTZMX,YHTZMN)
      CALL LABEL(0.,0.,HRTZMN,HRTZMX,15.,4,'DISTANCE,LATTICE CONSTANTS',
     C26,0)
      CALL LABEL(0.,0.,YHTZMN,YHTZMX,10.,4,'NUMBER OF NEIGHBORS',19,1)
      CALL PLOTXY(10,XHERTZ,YHERTZ,HRTZMN,HRTZMX,YHTZMN,YHTZMX,1,0,3,1,D
     COC)
      CALL MAXMIN(YSUPER,10,YSUPMX,YSUPMN)
      CALL LABEL(0.,0.,XSUPMN,XSUPMX,15.,4,'SUPEREXCHANGE TIME',18,0)
      CALL LABEL(0.,0.,YSUPMN,YSUPMX,10.,4,'NUMBER OF HOPS',14,1)
```

```
      CALL PLOTXY(10,XSUPER,YSUPER,XSUPMN,XSUPMX,YSUPMN,YSUPMX,1,0,3,1,D
     COC)
      WRITE(6,520)
      WRITE(6,1700) NUMXIT
 1700 FORMAT(1H0,'NUMBER OF EXCITONS GENERATED=',I3)
      WRITE(6,1701) TAU
 1701 FORMAT(1H0,'EXCITON LIFETIME=',F10.3)
      WRITE(6,1702) HOPTME
 1702 FORMAT(1H0,'NEAR NEIGHBOR HOP TIME=',1PE10.3)
      WRITE(6,1703) CONC
 1703 FORMAT(1H0,'IMPURITY CONCENTRATION=',F8.3)
      WRITE(6,1704) ATTEN
 1704 FORMAT(1H0,'BETA/DELTA=',F7.3)
      WRITE(6,1705) NTRAPS
 1705 FORMAT(1H0,'NUMBER OF DEEP TRAPS=',F10.3)
      WRITE(6,1706) TERIMP
 1706 FORMAT(1H0,'NUMBER OF WALKS TERMINATED BY TRAPPING=', I3)
      WRITE(6,1707)TERLIF
 1707 FORMAT(1H0,'NUMBER OF WALKS TERMINATED BY RADIATIVE DECAY=', I3)
      WRITE(6,1708) INTRAP
 1708 FORMAT(1H0,'NUMBER OF EXCITONS CREATED ON A TRAP=', I3)
      WRITE (6,1709) AVELIF
 1709 FORMAT(1H0,'AVERAGE EXCITON LIFETIME=', 1PE10.3)
      WRITE (6,1710) AVESTP
 1710 FORMAT(1H0,'AVERAGE NUMBER OF STEPS=',F10.3)
      WRITE(6,1711)
 1711 FORMAT(1H0,'BIN-SORT')
      WRITE(6,1712)
 1712 FORMAT(1H0,'LIFETIME      NUMBER OF EXCITONS')
      WRITE(6,1713) ((XLIF(I),YLIF(I)),I=1,10)
 1713 FORMAT(1H0,1PE10.3,5X,1PE10.3)
      SUMEXC=0
      DO 1750 J=1,10
      SUMEXC=YLIF(J)+SUMEXC
 1750 CONTINUE
      WRITE(6,1800) SUMEXC
 1800 FORMAT(1H0,'TOTAL NUMBER OF EXCITON LIFETIMES=',1PE10.3)
      WRITE(6,1850) LIFMIN
 1850 FORMAT(1H0,'SHORTEST EXCITON LIFETIME=',1PE10.3)
      WRITE(6,1875) LIFMAX
 1875 FORMAT(1H0,'LONGEST EXCITON LIFETIME=',1PE10.3)
      WRITE(6,1711)
      WRITE(6,1900)
 1900 FORMAT(1H0,'TOTAL STEPS    NUMBER OF EXCITONS')
      WRITE(6,1950) ((XSTP(I),YSTP(I)),I=1,10)
 1950 FORMAT(1H0,1PE10.3,6X,1PE10.3)
      SUMEXC=0
      DO 2000 J=1,10
      SUMEXC=YSTP(J)+SUMEXC
 2000 CONTINUE
      WRITE(6,2050) SUMEXC
 2050 FORMAT(1H0,'TOTAL NUMBER OF EXCITONS THAT STEPS WERE COUNTED FOR='
     C,1PE10.3)
```

```
      WRITE(6,2060) STPMIN
2060  FORMAT(1H0,'SMALLEST NUMBER OF STEPS TAKEN=',1PE10.3)
      WRITE(6,2070) STPMAX
2070  FORMAT(1H0,'LARGEST NUMBER OF STEPS TAKEN=',1PE10.3)
      WRITE(6,1711)
      WRITE(6,2100)
2100  FORMAT(1H0,'HERTZ DISTRIBUTION    NUMBER OF NEIGHBORS')
      WRITE(6,2150) ((XHERTZ(J),YHERTZ(J)),J=1,10)
2150  FORMAT(1H0,1PE10.3,12X,1PE10.3)
      WRITE(6,1711)
      WRITE(6,2200)
2200  FORMAT(1H0,'SUPEREXCHANGE TIME       NUMBER OF PAIRS')
      WRITE(6,2250) ((XSUPER(J),YSUPER(J)),J=1,10)
2250  FORMAT(1H0,1PE10.3,15X,1PE10.3)
      WRITE(6,520)
      STOP
      END
//DATA   DD    *
   5.       .058       .24          1.0E-7      .095  10
```

APPENDIX III.

MONTE CARLO PROGRAM TO CALCULATE SUPEREXCHANGE COUPLING AND INTER-IMPURITY CLUSTER SEPARATION DISTRIBUTIONS IN RANDOMLY DISORDERED 1-D CHAINS

APPENDIX III.

I. The do loop defined by statement 300

This do loop constructs a contracted array (to be defined) called B(I).

II. The philosophy behind the contraced array

One first constructs an array containing zeroes and randomly replaces a certain number of the zeroes by ones (let 1=impurity, 0=host). 1's isolated by 0's on both sides are impurity clusters, 0's isolated on both sides are host clusters. Clearly, this array contains only two types of clusters, and they must occur alternately (this is crucial). One cannot find two guest or host clusters side by side since this would be one larger cluster. One can dramatically reduce the size of the array containing only 0's and 1's by constructing a new array from it containing only host and guest cluster sizes.

Consider the sequence 001000110001. One can define a contracted array (having no less information than the original array) to be 213231. This contraction is increasingly compact for small numbers of impurities (or hosts) where the host (or guest) clusters are enormous. Further, one knows that if the first number in the contracted sequence represents an impurity cluster size, then the 3^{rd}, 5^{th}, 7^{th},... numbers in the sequence are also impurity cluster sizes and the 2^{nd}, 4^{th},... are host cluster sizes.

The FORTRAN algorithm

The IBM random number generator NRAND produces uniformly distributed random numbers between 0 and 1. As many random numbers are drawn as there are impurity sites in the chain. As the n^{th} random number is drawn, it is compared to CONC (the concentration, also between 0 and 1). If the random number is less than CONC, then MPURIT (the FORTRAN variable in the program) is set=1 (i.e. an impurity is placed at the site). A counter, H, is set up to keep track of the number of consecutive 0's and 1's, thus recording the host or guest cluster size. The flag, K, is set to 1 for guest clusters and set to 0 for host clusters. The first cluster in B(I) is thus artificially set to a host cluster. This is to ensure that all even numbered sites in the contracted array are impurity clusters. This artificial start is inconsequential since do loop 500 starts searching the contracted array at the second impurity cluster to avoid end effects. The counter J keeps track of the total number of host and guest clusters counted.

The do loop defined by statement 500

This do loop searches the contracted sequence for m-m, m-to-nearest-d, and d-to nearest-m separations. The array element DIST(J,1) contains the total number of monomers separated by J hosts. DIST(J,2) contains the total number of monomers that are adjacent to a dimer with J intervening hosts. DIST(J,3) is the number of dimers next to a monomer with J intervening hosts. Special cases arise and they will discussed below.

Philosophy of the search algorithm

The computer looks only at the impurity clusters (even numbered elements in the contracted array) since we are presently only interested in the impurity cluster separations. For the purposes of this program, all impurity clusters with greater than or equal to 2 impurities are treated identically (at low temperatures, they are all traps). If the computer finds a monomer, it looks at the nearest impurity clusters to the left and to the right and finds one of three situations: (1) m-m-m, (2) m-m-d, or (3) d-m-d where d implies an n-mer with $n \geq 2$ and - implies some number of intervening hosts. If one subtracts the cluster size of the left and right impurity clusters and obtains zero one has case 1 or case 3, otherwise, it is situation 2 (it could be that a monomer is bounded by a trimer and dimer which we call case 3). So if the subtraction yields zero, one needs only to test one of the neighboring impurity clusters (either one) to see if it is a monomer. If it is a monomer, one has case 1, otherwise case 3. If the subtraction yields a negative or positive nonzero number, one immediately knows which of the neighboring impurity clusters is smaller and then tests it to see if it is a monomer. If it is a monomer, one has case 2, otherwise one has case c.

The neighbors of the dimer are characterized in the same manner. To summarize, there are a total of six possible situations: (1) m-m-m, (2) m-m-d, (3) d-m-d, (4) m-d-m, (5) d-d-m and (6) d-d-d. The six cases are treated in the following manner. Case 1, m-m-m: for the monomer in the middle, the separation is picked to be the smallest number of intervening hosts to the left or to the right and was placed in DIST(J,1). Case 2, m-m-d: the m-m

separation is the number of hosts to the left and the m-d separation is the number of hosts to the right. Case 3, d-m-d: the m-d separation is set to the smallest number of intervening hosts to the left or to the right and is placed in the array element DIST(J,2). Case 4, m-d-m: the d-m separation is recorded as the smaller number of intervening hosts and put into DIST(J,3). Case 5, d-d-m: the d-m separation is set to the number of intervening hosts to the right and no other distances are recorded. Case 6, d-d-d: nothing is recorded in any array element.

```
//FORT   DD    *
c      This is the program that generated unpublished results
c      on the inter-cluster distance statistics for dissimilar clusters.
c      That is, to simulate the average distance between the monomers
c      between the dimers and between monomers and dimers.
       DIMENSION DOC(3),SUMSUP(3),XSUPRX(50)
       INTEGER*4 B(100001) ,DIST(1000,3),CLUSTR,RMAX
       REAL AIST(1000,3),X(500)
       REAL MMAVE,MDAVE,DMAVE
       REAL MMMX,MDMX
       INTEGER DMMAX,DMMIN
       DATA DOC/0.,0.,1./
       READ(5,100) CONC
100    FORMAT(F10.6)
       RMAX=4./CONC
200    CALL ICLOCK(K)
       IF(MOD(K,2).EQ.0) GO TO 200
       NX=K
       J=1
       K=0
       H=0
       DO 300 I=1,100001
       NX=NRAND(NX)
       TEST=NX/.2147484E10
       MPURIT=0
       IF(TEST.LE.CONC) MPURIT=1
       IF(MPURIT.EQ.K) GO TO 250
       B(J)=H
       J=J+1
       K=0
       IF(MOD(J,2).EQ.0) K=1
       H=1
       GO TO 300
250    H=H+1
300    CONTINUE
       CLUSTR=J/2
       L=0
       M=0
       N=0
       DO 500 I=4,J,2
       IF(B(I).GE.2) GO TO 400
       L=L+1
310    IF(B(I+2)-B(I-2)) 325,350,340
325    IF(B(I+2).EQ.1) GO TO 330
       DIST(MIN0(B(I-1),B(I+1)),2)  =DIST(MIN0(B(I-1),B(I+1)),2) +1
       GO TO 500
330    DIST(B(I+1),1)=DIST(B(I+1),1)+1
       DIST(B(I-1),2)=DIST(B(I-1),2)+1
       GO TO 500
340    IF(B(I-2).EQ.1) GO TO 345
       DIST(MIN0(B(I-1),B(I+1)),2)=DIST(MIN0(B(I-1),B(I+1)),2)+1
       GO TO 500
345    DIST(B(I-1),1)=DIST(B(I-1),1)+1
```

```
      DIST(B(I+2),2)=DIST(B(I+2),2)+1
      GO TO 500
350   IF(B(I-2).EQ.1) GO TO 375
      DIST(MIN0(B(I-1),B(I+1)),2)=DIST(MIN0(B(I-1),B(I+1)),2)+1
      GO TO 500
375   DIST(MIN0(B(I+1),B(I-1)),1)=DIST(MIN0(B(I-1),B(I+1)),1)+1
      GO TO 500
400   M=M+1
      IF(B(I+2)-B(I-2)) 410,430,420
410   IF(B(I+2).EQ.1) GO TO 415
      GO TO 500
415   DIST(B(I+1),3)=DIST(B(I+1),3)+1
      N=N+1
      GO TO 500
420   IF(B(I-2).EQ.1) GO TO 425
      GO TO 500
425   DIST(B(I-1),3)=DIST(B(I-1),3)+1
      N=N+1
      GO TO 500
430   IF(B(I+2).EQ.1) GO TO 435
      GO TO 500
435   DIST(MIN0(B(I+1),B(I-1)),3)=DIST(MIN0(B(I+1),B(I-1)),3)+1
      N=N+2
500   CONTINUE
      WRITE(6,600)
600   FORMAT(1H0,130('*'))
      WRITE(6,610) CONC,L,M,CLUSTR
610   FORMAT(1H0,'CONCENTRATION=',F10.6,'#MONOMERS=',I5,'#DEEP TRAPS=',I
     C5,'TOTAL #CLUSTERS=',I5)
      FRACT=FLOAT(N)/FLOAT(L)
      WRITE(6,612) L,FRACT
612   FORMAT(1H0,'#MONOMERS=',I5,'FRACTION MONOMERS BY A DIMER=',1PE10.3
     C)
      MMSUM=0
      MMNUM=0
      MDSUM=0
      MDNUM=0
      DMSUM=0
      DMNUM=0
      DO 625 J=1,RMAX
      MMSUM=DIST(J,1)*J+MMSUM
      MMNUM=DIST(J,1)+MMNUM
      MDSUM=DIST(J,2)*J+MDSUM
      MDNUM=DIST(J,2)+MDNUM
      DMSUM=DIST(J,3)*J+DMSUM
      DMNUM=DIST(J,3)+DMNUM
625   CONTINUE
      MMAVE=FLOAT(MMSUM)/FLOAT(MMNUM)
      MDAVE=FLOAT(MDSUM)/FLOAT(MDNUM)
      DMAVE=DMSUM/DMNUM
      WRITE(6,626) MMAVE
626   FORMAT(1H0,'AVE M-M SEP IN CHAINS OF MS(MORE THAN 1M)=',F10.3)
      WRITE(6,627) MDAVE
```

```
627   FORMAT(1H0,'AVE M-D SEP FOR MS ADJACENT TO A D(IF 2DS, PICK SMALLE
     CST M-D',F10.3)
      WRITE(6,628) DMAVE
628   FORMAT(1H0,'AVE D-M SEP FOR DS ADJACENT TO AN M(IF 2 MS, PICK SMAL
     CLEST D-M',F10.3)
      DO 629 I=1,50
      XSUPRX(I)=6.5*.095**I
629   CONTINUE
      WRITE(6,620)
620   FORMAT(1H0,'#INTERVENING',T20,'SUPEREXCHANGE',T42,'M-M SEP,M CHAIN
     CS ONLY',T74,'M-D SEP',T106,'D TO NEAREST M SEP')
      WRITE(6,631)
631   FORMAT(1H0,'HOSTS',T20,'   cm-1')
      WRITE(6,630)((J,XSUPRX(J),DIST(J,1),DIST(J,2),DIST(J,3)),J=1,50)
630   FORMAT(1H0,I2,T20,1PE10.3,T42,I5,T74,I5,T106,I5)
      DO 640 I=1,500
      X(I)=FLOAT(I)
640   CONTINUE
      CALL MAXMIN(DIST(1,1),-RMAX,MMMAX,MMMIN)
      CALL MAXMIN(DIST(1,2),-RMAX,MDMAX,MDMIN)
      CALL MAXMIN(DIST(1,3),-RMAX,DMMAX,DMMIN)
      RMX=FLOAT(RMAX)
      MMMX=FLOAT(MMMAX)
      MDMX=FLOAT(MDMAX)
      DMMX=FLOAT(DMMAX)
      DO 700 I=1,3
      DO 650  J=1,RMAX
      AIST(J,I)=FLOAT(DIST(J,I))
650   CONTINUE
700   CONTINUE
      DO 725 I=1,3
      SUMSUP(I)=0
725   CONTINUE
      DO 800 J=1,3
      DO 750 I=1,50
      SUMSUP(J)= 6.5*.095**I*DIST(I,J)+SUMSUP(J)
750   CONTINUE
800   CONTINUE
      AVEMMS=SUMSUP(1)/FLOAT(MMNUM)
      AVEMDS=SUMSUP(2)/FLOAT(MDNUM)
      AVEDMS=SUMSUP(3)/DMNUM
      WRITE(6,850) AVEMMS,AVEMDS,AVEDMS
850   FORMAT(1H0,'AVE SUPERXCHNG,cm-1,FOR MM:',F10.3,'MD:',F10.3,'DM:',F
     C10.3)
      WRITE(6,600)
      CALL LABEL(0.,0.,1.,RMX,15.,4,'LATTICE CONSTANTS',17,0)
      CALL LABEL(0.,0.,0.,MMMX,10.,4,'MM SEPARATIONS',14,1)
      CALL PLOTXY(RMAX,X,AIST(1,1),1.,RMX,0.,MMMX,1,0,11,1,DOC)
      CALL LABEL(0.,0.,1.,RMX,15.,4,'LATTICE CONSTANTS',17,0)
       CALL LABEL(0.,0.,0.,MDMX,10.,4,'MD SEPARATIONS',14,1)
      CALL PLOTXY(RMAX,X,AIST(1,2),1.,RMX,0.,MDMX,1,0,11,1,DOC)
      CALL LABEL(0.,0.,1.,RMX,15.,4,'LATTICE CONSTANTS',17,0)
      CALL LABEL(0.,0.,0.,DMMX,10.,4,'DM SEPARATIONS',14,1)
```

```
      CALL PLOTXY(RMAX,X,AIST(1,3),1.,RMX,0.,DMMX,1,0,11,1,DOC)
      STOP
      END
//DATA   DD    *
```

APPENDIX IV.

COMPUTER PROGRAM TO FIT SPECTRAL AND OTHER DATA TO MATHEMATICAL MODELS

APPENDIX IV.

NONLIN, a Program to Fit Spectral and Other Data.

The purpose of this document is to describe the structure and use of NONLIN, so that it can be modified, if need be, and so that its strengths and limitations are clear. NONLIN is a program to fit spectral lineshapes (or any other data) to Gaussians, Lorentzians, Voigt functions (or any other mathematical entity that can be expressed in terms of calculable functions). The program in its first form was written by Roy Mead and Duane D. Smith in the summer of 1977. Since then, the program has been continually optimized for ease of use, versatility, readability and to a lesser extent, speed. The current version operates on an IBM 370/3032 and plots on a Versatec 1200A plotter. I/O and plotting have been engineered to be as flexible and user transparent as possible, all control is from the input data, so in most cases, code changes should be unnecessary.

The program is built around a subroutine named LSQENP which is a generalized nonlinear regression capable of fitting any model that can be described in terms of calculable functions. Fitting with the Voigt function has been tested by fitting published tables with NONLIN (see e.g., B. D. Fried and S. D. Conte, ''The Plasma Dispersion Function'', 1961, Physical Research Laboratories: G. D. Finn and D. Mugglestone Mon. Not. Roy Astr. Soc. vol. 129, p. 221, 1965: D. G. Hummer, Mem. R. Astr. Soc. vol. 70, p. 1, 1965). In using these tables, of Voigt functions one should be careful to keep track of factors of π, $(\pi)^{1/2}$. Fitting of Gaussians and Lorentzians has been tested by fitting calculated data as well.

On the usage of LSQENP: One should note that in using analytic (rather than numerically estimated) partials in the fit, the convergence is more rapid and accurate. In using numerical derivatives, the program must pick an interval size for the differential element, which may not be ideally suited to the function being fit, or the current values of the function's parameters.

Note that in subroutine PEAKVA when the Voigt function is calculated (B. H. Armstrong's algorithm, referenced below) it was necessary to (a) take the absolute value of x and (b) to take the absolute value of the ratio of the homogeneous and inhomogeneous widths. For the case of x, if a negative value is encountered, FUNCTION K, which chooses between subroutine K1, K2, and K3 can (but not in all cases) make the wrong choice. Armstrong wrote the algorithm only to calculate for positive x which is reasonable for the symmetric convolution integral. However when one translates

the origin to fit data in any sort of practical situation, one will encounter negative x values. Therefore, the absolute value. For the case of the ratio, if one is dealing with small values of the ratio, the nonlinear regresssion can shoot slightly past zero. If it does, the resulting function that is computed looks something like an Airy function, with oscillations in the wings. Therefore, to prevent the regression from fitting with unphysical ratios and additionally to speed convergence the absolute value of the ratio was computed.

When one is fitting data to functions where some of the parameters differ widely, convergence may be difficult to obtain. One such practical situation is in fitting T**7 to the homogeneous width vs. temperature. The preexponential factor in fitting such data in practical situations can be smaller than E-12, whereas the function has a severe exponential dependence on the parameter used in the exponent (i.e. the 7). It may be that using analytic derivatives will remedy this. This has not been investigated since in the data fit so far, it was readily apparent that T**7 would not be able to fit the data.

Core: 170 kilobytes

Typical execution times of compiled NONLIN using optimized Fortran H on the 370/3032:

10 iterations, Voigt fit	to 256 points:	16.5 seconds.
10 iterations, Gaussian fit	to 256 points:	6.0 seconds.
10 iterations, Lorentzian fit	to 256 points:	5.4 seconds.

Algorithms:

Nonlinear regression; Marquardt, D. W., ''An Algorithm for Least-Squares Estimation of Nonlinear Parameters''. Jour. Soc. Ind. and App. Math. vol. 11, no.2, June 1963 pp. 431-441.

Power series expansions of Voigt function: Armstrong, B. H., Jour. Quant. Spect. and Rad. Trans., vol. 7, 1967 p. 61.

All I/O by Duane D. Smith.

Plotting software: Versatec and Caltech.

FORMAT FOR DATA INPUT FOR LINESHAPE FITTING.

1. FITTST FORMAT(20A4)

Type of fit. If the first four characters are 'line' (uc or lc), the program will assume a lineshape fit and only Gaussian, Lorentzian and Voigt functions will be available to the user. If anything other than line appears here the user must supply a subprogram FUNCTION MODEL(X,B) to be fit to the data. Maximum of 80 characters. FITTST will be printed in the output to allow the user to more easily identify the output.

2. TITLE FORMAT(20A4)

Title of fit, to be printed at the top of the plot. Should be <62 characters if the plot is horizontally oriented and <41 characters is the plot is vertically oriented (see step 12 below).

3. NEWDAT, NEWPAR, IPRINT, IFP, IPLOT, IDVT, IQUIT FORMAT(6I1,I3)

Conditions of the fit--7 parameters for the I/O and nonlinear regression.

NEWDAT=0 Use previous data set.
=1 Read new data set.

NEWPAR=0 Use previous parameter set.
=1 Read new parameter set.

IPRINT=0 Short printout.
=1 Include table of observed and calculated values in output.
=2 Print the results of every iteration.

IFP =0 No line printer plot.
=1 Do line printer plot.

IPLOT =0 No Versatec plot.
=1 Do Versatec plot.

IDVT =0 Analytic partials used. User must supply partials in SUBROUTINE PCODE.

=1 Numerically estimated partials used. Currently, must use numerical partials when fitting any function other than Gaussian or Lorentzian. If one uses analytic partials and no algorithm exists, the initial guesses will not be improved upon, presumably since the analytic partials are left near zero.

IQUIT =N Maximum number of iterations, N, for fit. If the internal convergence criteria of the regression routine LSQENP are satisified, it will quit sooner (the criteria are very stringent

and described in the exhibit on LSQENP).

4. NPEAKS FORMAT(I1)

Number of peaks to be fit. Once the number of peaks is input, the data for each peak will take three lines (steps 5 through 7 below). Thus, one repeats steps 5 - 7 n times.

5. B(I) FORMAT(3E16.9)

Parameter values for peak position, height and width (in that order). The large E16.9 format was chosen for convenience and versatility. Recall that one can enter regular floating point numbers with the decimal point in an arbitrary position within the 16 character field. The exponential format is useful where very large or small numbers occur.

6. IVARY FORMAT(3I1)

Switches to fix or float the position, height and width (again, in that order). If IVARY=1, the parameter is floating, if anything else is there, the parameter is fixed. Using IVARY=0 is a handy way to fix the parameter.

7. FUNCT(I,J),INHOMO FORMAT(3A4,4X,F10.5)

An alphabetical description of the type of function to be fit to that peak. If the first four letters are 'gaus' (uc or lc), a Gaussian function will be fit to that peak. Similarly, if the first four lettters are 'lore', a Lorentzian will be fit, if they are 'voig', a Voigt function will be fit and if they are 'conv', a Romberg quadrature integration to calculate the Voigt function will be invoked (this is primarily used to check B. H. Armstrong's power series expansion of the Voigt function). The first 12 characters on this line are printed on the output to indicate to the user what function was used in the fit. If a Voigt function is being fit, the user must supply a value of the inhomogeneous (gaussian) FWHM, known as INHOMO, to be used as a fixed parameter in the fit. If one wants to fix the Lorentzian contribution and fit the Gaussian content, then one needs to modify function PEAKVA where function K(ZZ,RATIO) is called.

8. FITOFF, B(M-1) FORMAT(A8,8X,E16.9)

If the first six characters on this line are 'offset' then the offset of the baseline beneath the peak is fixed to the value read in field positions 17-33 with E16.9 format. Parameter B(M-1) is the offset parameter. If anything other than 'offset' is found, the baseline offset is optimized in the fit with the user supplied B(M-1) as the initial guess.

Usually one finds it convenient to spell out 'offset' and 'fit offset' to increase readability.

9. FITSLO, B(M) FORMAT(A8,8X,E16.9)

If the first five characters are 'slope', then the slope of the baseline under the peak is fixed to the value read in field positions 17-33 with E16.9 format. Parameter B(M) is the slope parameter. If anything other than 'slope' is found, the baseline slope is optimized in the fit using the supplied B(M) value as an initial guess. Usually one finds it convenient to write 'slope' and 'fit slope'.

10. HORSIZ,HORIZ FORMAT(I2,16A4)

HORSIZ is the number of characters in the title of the horizontal axis, FORMAT(I2). HORIZ is the array that contains the axis label and should occur directly after HORSIZ (no intervening spaces).

11. VERSIZ,VERT FORMAT(I2,16A4)

Same as step 10 above, but for the vertical axis.

12. ORIENT FORMAT(3A4)

An alphabetical switch which determines the orientation of the plot. If the first four characters are 'vert', then the plot will be generated with the horizontal axis on the short edge of 8 1/2 X 11 paper with thesis margins. If anything else is found, the horizontal axis will be along the 11'' edge, again with thesis margins. [Thesis margins are 1'' on the top and bottom, 1/2'' on the right and 1 and 1/2'' on the left.] Writing out 'horizontal plot' or 'vertical plot' on this line makes the input very readable.

13. N FORMAT(I4)

The number of data points. Will accept up to 9,999 x,y pairs, but LSQENP is currently dimensioned for a maximum of 500 data points. Was set up with 1024 point MCA output in mind.

14. X,Y FORMAT(2E16.9)

The data in ordered x,y pairs. This generously large format was chosen such that it could accept just about any input and is not limited by an IBM single precision calculation (unlikely as it is that your data will have that many significant figures). The E16.9 format was chosen since the standard modulo tab on a terminal is 8

spaces, making counting spaces unnecessary. Recall that a regular floating point number can be successfully read as long as it is within the 16 character field. If one does use the exponential format, it must be right justified.

15. TITLE FORMAT(20A4)

If the program finds anything on the next record, it assumes it is the title of the next data set to be fit and expects to find more data records. If this card is blank, then the program assumes there is no more data to fit, prints *****Last run completed***** and stops.

SAMPLE DATA INPUT FOR LINESHAPE FITTING.

```
lineshape fit
CaO M center emission, 50.9K,  75, Voigt fit
101111  5
1
14623.2         7.0              5.0
111
Voigt fcn         1.5
offset            1.0
slope             1.0
17wavenumbers, cm-1
20intensity(arb units)
vertical plot
 256
14620.0          1.234
14620.2          1.2345
          .
          .
  other data points
          .
          .
  (a blank card)
```

FORMAT OF DATA INPUT FOR NON-LINESHAPE DATA FITTING.

1. FITTST FORMAT(20A4)

Type of fit. The first four characters must not be 'line', or else the program assumes you want a Gaussian, Lorentzian or Voigt function. User must supply the special function in FUNCTION MODEL(X,Y,B). One usually supplies a message here that helps to identify the fit and fitting procdure.

2. TITLE FORMAT(20A4)

The title of the fit, to be written at the top of the plot. Title must be <62 characters if plot is horizontal, <41 characters if plot is vertical (see step 10 below).

3. NEWDAT, NEWPAR, IPRINT, IFP, IPLOT, IDVT, IQUIT FORMAT(6I1,I3)

Conditions for the fit and nonlinear regression.

NEWDAT=0 Use previous data set.
=1 Read new data set.

NEWPAR=0 Use previous parameter set.
=1 Read new parameter set.

IPRINT=0 Short printout.
=1 Include table of observed and calculated values in output.
=2 Print the results of every iteration.

IFP =0 No line printer plot.
=1 Do line printer plot.

IPLOT =0 No Versatec plot.
=1 Do Versatec plot.

IDVT =0 Analytic partials used. User must supply partials in SUBROUTINE PCODE.
=1 Numerically estimated partials used. Currently, must numerical partials when any function other than Gaussian or Lorentzian, if analytic partials are used and no algorithm exists to calculate them, the initial guesses will not be improved upon, presumably since all the partials are left near zero.

IQUIT =N Maximum number of iterations, N, for fit. If the internal convergence criteria of the regression routine LSQENP are satisified, it will quit sooner (the criteria are very stringent and described in the exhibit on LSQENP).

4. M FORMAT(I2)

Number of parameters in the fit (includes fixed and floating parameters). If the number of parameters is n, then one will repeat steps 5 through 7 n times, one time through for each parameter.

5. PARDES FORMAT(20A4)

A human language alphabetic description of the first parameter in the fit. Will be used in the output to label

the fitted value of the parameter. Maximum of 80 characters.

6. B FORMAT(E16.9)

The user supplied numerical value of the parameter in the fit.

7. FIXED FORMAT(2A4)

If the first four characters in the record are 'fixe', then the parameter value supplied by the user is fixed (i.e. not optimized in fitting the data). If anything else is encountered, the parameter is floating. Since FIXED is used to label the parameter in the output, it is usually useful to write out 'fixed' or 'floating'.

8. HORSIZ,HORIZ FORMAT(I2,16A4)

HORSIZ is the number of characters in the label for the horizontal axis. HORIZ is the array that contains the axis label and should occur directly after HORSIZ (no intervening spaces).

9. VERSIZ,VERT FORMAT(I2,16A4)

Same as in step 8, but for the vertical axis.

10.ORIENT FORMAT(3A4)

An alphabetical switch which determines the orientation of the of the plot. If the first four characters are 'vert', then the plot will be generated with the horizontal axis on the short edge of 8 1/2 X 11 paper with thesis margins. If anything else is found, the horizontal axis will be along the 11'' inch edge, again with thesis margins. [Thesis margins are 1 1/2'' on the left and 1'' on top and bottom and 1/2'' on the right]. Writing out 'horizontal plot' or 'vertical plot' makes the input file very readable.

11. N FORMAT(I4)

The number of data points. Currently, LSQENP is only dimensioned for 500 data points.

12. X,Y FORMAT(2E16.9)

The data in ordered x,y pairs.

13.TITLE FORMAT(20A4)

If the program finds anything on this record, it assumes it is the title of the next data set to be fit and expects to find more data. If this card is blank, then the program

assumes there are no more data to fit, prints out ******LAST RUN COMPLETED****** and stops.

SAMPLE DATA INPUT FOR FITTING NON-LINE SHAPE DATA.

```
Fit of n(n+1) to temp-dependent homogeneous FWHM of CaO M center
CaO M center emission, Raman T-dep fit
110111  5
2
preexponential factor
2.5
floating
phonon energy
30.0
fixed
14temperature, K
26homogeneous linewidth, cm-1
vertical plot
  15
1.3              1.2
4.2              1.4
        .
        .
(the rest of the data points).
        .
        .
(blank card if no more data to fit).
```

SAMPLE OF DATA OUTPUT FOR FITTING NON-LINE SHAPE DATA.

```
**************************************************************************

FIT OF N(N+1) TO TEMP-DEPENDENT HOMOGENEOUS FWHM OF CAO M CENTER.
CAO M CENTER EMISSION, RAMAN T-DEP FIT
PARAMETER NUMBER 1
        PREEXPONENTIAL FACTOR
                PARAMETER IS FLOATING
                INITIAL PARAMETER VALUE IS= 2.5
                FINAL   PARAMETER VALUE IS= 2.345
PARAMETER NUMBER 2
        PHONON ENERGY
                PARAMETER IF FIXED
                INITIAL PARAMETER VALUE IS= 30.0
                FINAL   PARAMETER VALUE IS= 30.0

**************************************************************************
******LAST RUN COMPLETED*****
```

PROGRAM LISTING FOR NONLIN, NONLINEAR LEAST SQUARES FOR FITTING LINESHAPES AND ARBITRARY DATA TO ARBITRARY FUNCTIONS.

```
// EXEC FORTXCL,PARM.FORT='OPT=2',PARM.LKED='LIST,NCAL,LET'
//FORT.SYSIN DD *
c      MAIN PROGRAM
       REAL*8 FITSLO,FITOFF,SLOPE,OFFSET,CONST(34),C(34)
       REAL*4 LINE,ORIENT(3),INHOMO,LORNTZ
       INTEGER HORSIZ,VERSIZ
       DIMENSION X(500,1),Y(500),B(50),BA(50),IB(50),IVARY(50)
       DIMENSION CNEW(100),Q(10),U(10),FIXED(2,50),PARDES(20,50)
       COMMON/AXSLBL/ HORIZ(16),VERT(16),HORSIZ,VERSIZ,ORIENT
       COMMON/NUMPK/NPEAKS,M2
       COMMON/NAME/FUNCT(3,12),INHOMO
       COMMON/HUMMER/C
       COMMON/XLIM/XMIN,XMAX
       COMMON/YLIM/IFP,YMIN,YMAX
       COMMON/VOIGT1/W(10),T(10),Y2
       COMMON/USRMSG/TITLE(20),FITTST(20)
       COMMON/FCN/IFCN(10)
       DATA LORNTZ,GAUSS,VOIGT,FIXTST/'LORE','GAUS','VOIG','FIXE'/
       DATA CONST/.1999999999972224,-.184000000029998,.1558399999965025,
      1-.1216640000043988,.087708159994039 1,-.0585141248086907,
      1.0362157301623914,-.0208497654398036,.0111960116346270,
      1-.56231896167109D-2,.26487634172265D-2,-.11732670757704D-2,
      1.4899519978088D-3,-.1933630801528D-3,.722877446788D-4,
      1-.256555124979D-4,.88620736841D-5,-.27876379719D-5,
      1.8566873627D-6,-.2518433784D-6,.709360221D-7,-.191732257D-7,
      1.49801256D-8,-.12447734D-8,.2997777D-9,-.696450D-10,.156262D-10,
      1-.33897D-11,.7116D-12,-.1447D-12,.285D-13,-.55D-14,.10D-14,
      1-.2D-15/
       DATA LINE,SLOPE,OFFSET,BLANK/'LINE','SLOPE','OFFSET','    '/
       DATA Q/4.62243670E-1,2.86675505E-1,1.09017206E-1,2.48105209E-2,
      13.24377334E-3,2.28338636E-4,7.80255648E-6,1.08606937E-7,
      14.39934099E-10,2.22939365E-13/
       DATA U/.245340708,.737473729,1.23407622,1.7385377,2.25497400,
      12.78880606,3.34785457,3.94476404,4.60368245,5.38748089/
       DO 20 I=1,34
       C(I)=CONST(I)
20     CONTINUE
       DO 25 I=1,10
       W(I)=Q(I)
       T(I)=U(I)
25     CONTINUE
       WRITE(6,26)
26     FORMAT(' Program to fit simple functions and convolutions to line
      1shapes as well as fit arbitrary fcns to arbitrary data.')
       WRITE(6,27)
27     FORMAT(' First written June, 1977. Last modified June 1980.')
28     READ(5,29) (FITTST(I),I=1,20)
29     FORMAT(20A4)
       IF(FITTST(1).NE.BLANK) GO TO 38
       WRITE(6,35)
```

```
35    FORMAT(1H-,'*****LAST RUN COMPLETED*****')
      STOP
38    READ(5,40) (TITLE(I),I=1,20)
40    FORMAT(20A4)
      READ(5,80)NEWDAT,NEWPAR,IPRINT,IFP,IPLOT,IDVT,IQUIT
80    FORMAT(6I1,I3)
      WRITE(6,90) IQUIT
90    FORMAT(1H1,'MAXIMUM NUMBER OF ITERATIONS=',I3)
      IPRNT=IPRINT-1
      IF(FITTST(1).NE.LINE) GO TO 510
c     Check for new parameters. Jump to parameter copy routine if old values  USED
100   IF(NEWPAR.NE.1)GOTO 650
      IP=0
125   READ(5,150)NPEAKS
150   FORMAT(I1)
c     Each peak has three parameters.  There are also two baseline parameters.
      M2=3*NPEAKS
      M=M2+2
      DO 350 I=1,NPEAKS
      IDX=3*(I-1)
      READ(5,200)(B(IDX+J),J=1,3)
200   FORMAT(3E16.9)
      READ(5,250)(IVARY(IDX+J),J=1,3)
250   FORMAT(3I1)
      READ(5,300) (FUNCT(J,I),J=1,3),INHOMO
300   FORMAT(3A4,4X,F10.5)
      IFCN(I)=4
      IF(FUNCT(1,I).EQ.LORNTZ) IFCN(I)=1
      IF(FUNCT(1,I).EQ.GAUSS)  IFCN(I)=2
      IF(FUNCT(1,I).EQ.VOIGT)  IFCN(I)=3
c     IVARY is a switch, IVARY=1 if parameter is varied.  Otherwise, tell
c     LSQENP the parameter is held constant.
      DO 400 J=1,3
      IF(IVARY(IDX+J).EQ.1)GOTO 400
      IP=IP+1
      IB(IP)=IDX+J
400   CONTINUE
350   CONTINUE
c     Punching 'offset' in the offset card fixes this parameter.
      READ(5,450) FITOFF,B(M-1)
450   FORMAT(A8,8X E16.9)
      IF(FITOFF.NE.OFFSET) GO TO 500
      IP=IP+1
      IB(IP)=M-1
c     Punching 'slope ' in the slope card fixes this parameter.
500   READ(5,450) FITSLO,B(M)
      IF(FITSLO.NE.SLOPE) GO TO 501
      IP=IP+1
      IB(IP)=M
501   READ(5,502) HORSIZ, (HORIZ(I),I=1,16)
502   FORMAT(I2,16A4)
      READ(5,502) VERSIZ, (VERT(I),I=1,16)
      READ(5,504) (ORIENT(I),I=1,3)
```

```
504   FORMAT(3A4)
      GO TO 550
510   IP=0
      READ(5,515) M
515   FORMAT(I1)
      DO 535 I=1,M
      IFCN(I)=4
      READ(5,520) (PARDES(J,I),J=1,20)
520   FORMAT(20A4)
      READ(5,525) B(I)
525   FORMAT(E16.9)
      READ(5,530) (FIXED(J,I),J=1,2)
530   FORMAT(2A4)
      IF(FIXED(1,I).NE.FIXTST) GO TO 535
      IP=IP+1
      IB(IP)=I
535   CONTINUE
c     Set the variable IDX=1, so when FUNCTION PEAKVA is called, it will
c     know how to make the logical test to find the correct function.
      IDX=1
      READ(5,540) HORSIZ,(HORIZ(J),J=1,16)
540   FORMAT(I2,16A4)
      READ(5,545) VERSIZ,(VERT(J),J=1,16)
545   FORMAT(I2,16A4)
      READ(5,548) (ORIENT(I),I=1,3)
548   FORMAT(3A4)
c     Save the parameters, since LSQENP changes them.
550   DO 600 I=1,M
600   BA(I)=B(I)
c     Get the old parameters, since they were changed by LSQENP.
650   DO 700 I=1,M
700   B(I)=BA(I)
725   IF(NEWDAT.EQ.0) GO TO 750
      CALL READ(X,Y,N)
c     Find the maximum and minimum values of the data for integ. β plotting.
      XMAX=X(1,1)
      XMIN=X(1,1)
      DO 730 I=2,N
      IF(X(I,1).LT.XMIN) XMIN=X(I,1)
      IF(X(I,1).GT.XMAX) XMAX=X(I,1)
730   CONTINUE
      YMAX=Y(1)
      YMIN=Y(1)
      DO 735 I=2,N
      IF(Y(I).LT.YMIN) YMIN=Y(I)
      IF(Y(I).GT.YMAX) YMAX=Y(I)
735   CONTINUE
750   CALL LSQENP(N,M,1,Y,X,B,IP,IB,IDVT,0,IQUIT,IPRNT)
c     Thus, the array CNEW contains the initial value of parameter one
c     in CNEW(1), final value of parameter one in CNEW(2), initial value
c     of parameter two in CNEW(3), final value of parameter two in C(4)
c     ad infinitum, ad naseumM.
c     The final value of a parameter is supplied by LSQENP if
```

```
c     the parameter is floating, otherwise, the initial guess or
c     value set in SUBROUTINE PEAKVA is used.
      DO 800 I=1,M
      CNEW(2*I-1)=BA(I)
      CNEW(2*I)=B(I)
800   CONTINUE
      IF(FITTST(1).NE.LINE) CALL FCNOUT(CNEW,M,FIXED,PARDES)
      IF(FITTST(1).EQ.LINE) CALL OUTPUT(CNEW,NPEAKS)
      IF(IPLOT.EQ.1)CALL PLOTPK(X,Y,N,B,M2)
      GO TO 28
      END
//LKED.SYSLMOD DD DSN=DDS.NONLIN(MAIN),
// DISP=OLD,VOL=SER=CITSL5
// EXEC FORTXCL,PARM.FORT='OPT=2',PARM.LKED='LIST,NCAL,LET'
//FORT.SYSIN DD *
c
c     function ymodel----------------------------------------------------------
c
      FUNCTION YMODEL(X,B)
c     This function subroutine is used only when fitting functions other than
c     Gaussian, Lorentzian or Voigt. The user can place any calculable fcn
c     here.
      DIMENSION B(50)
      REAL*4 POWER,K
      COMMON/USRMSG/TITLE(20),FITTST(20)
      DATA EXPONT,SINGLE,TWO,VOIGT,POWER/'EXPO','SING','TWO ','VOIG',
     ,'POWE'/
      IF(TITLE(1).EQ.SINGLE) GO TO 500
      IF(TITLE(1).EQ.TWO)    GO TO 400
      IF(TITLE(1).EQ.EXPONT) GO TO 300
      IF(TITLE(1).EQ.POWER)  GO TO 200
      IF(TITLE(1).EQ.VOIGT)  GO TO 600
100   GO TO 700
200   YMODEL = B(1) + B(2)*X**B(3)
      RETURN
300   YMODEL = B(1) + B(2)*EXP(-B(3)/(.6951*X))
      RETURN
400   BOSON  = 1./(EXP(B(3)/(.6951*X)) - 1.)
      YMODEL = B(1) + B(2)*BOSON*(BOSON+1.)
      RETURN
500   YMODEL = B(1) + B(2)/(EXP(B(3)/(.6951*X)) - 1.)
      RETURN
600   ZZ     = ABS((X-B(1))/B(3))
      RATIO  = ABS(B(2)/B(3))
      YMODEL = B(5) + B(4)*K(ZZ,RATIO)
      RETURN
700   WRITE(6,800)
800   FORMAT(' YOU MISSED, NO FCN WAS CHOSEN IN SUBROUTINE YMODEL.')
      RETURN
      END
//LKED.SYSLMOD DD DSN=DDS.NONLIN(YMODEL),
// DISP=OLD,VOL=SER=CITSL5
// EXEC FORTXCL,PARM.FORT='OPT=2',PARM.LKED='LIST,NCAL,LET'
```

```
//FORT.SYSIN DD *
c
c     function peakva-------------------------------------------------------
c
      FUNCTION PEAKVA(X,B,IDX)
      DIMENSION B(50),BN(50)
      COMMON/IDENT/ID
      COMMON/NAME/FUNCT(3,12),INHOMO
      COMMON/XLIM/XMIN,XMAX
      COMMON/FIT/BN
      COMMON/POSIT/XN
      COMMON/FCN/IFCN(10)
      EXTERNAL CONVOL
      REAL*4 LORE,GAUS,VOIGT,K,INHOMO
      DO 100 I=1,50
      BN(I)=B(I)
100   CONTINUE
      ID=IDX
      XN=X
      J=(IDX-1)/3 + 1
      IGO=IFCN(J)
      GO TO (300,200,400,450),IGO
150   GO TO 500
200   PEAKVA=B(IDX+1)*EXP(-2.77259*((X-B(IDX))/B(IDX+2))**2)
      RETURN
300   PEAKVA=(B(IDX+1)*(B(IDX+2)/2.)**2)/( (X-B(IDX))**2+(B(IDX+2)/2.)
     ,**2)
      RETURN
c     K(X,RATIO) is B. Armstrong's power series expansion of the Voigt fcn.
400   ZZ=(X-B(IDX))/INHOMO
      RATIO=ABS(B(IDX+2)/INHOMO)
      PEAKVA=B(IDX+1)*K(ZZ,RATIO)
      RETURN
c     DCADRE,an IMSL routine, computes the voigt function by Romberg integr.
c     It is slow β expensive, used only to check K(X,RATIO).
450   PEAKVA=DCADRE(CONVOL,XMIN,XMAX,0.03,0.03,ERROR,IER)
      RETURN
500   WRITE(6,600)
600   FORMAT(' No such function is in peakva now.  User either has an
     ,error in input or must supply a new function peakva')
      STOP
      END
//LKED.SYSLMOD DD DSN=DDS.NONLIN(PEAKVA),
// DISP=OLD,VOL=SER=CITSL5
// EXEC FORTXCL,PARM.FORT='OPT=2',PARM.LKED='LIST,NCAL,LET'
//FORT.SYSIN DD *
c
c     subroutine pcode------------------------------------------------------
c
      SUBROUTINE PCODE(P,X,B,F,I)
c     This is a routine required by LSQENP.  When possible or practical,
c     the user supplies the partial derivatives of the fcn to be fit here.
c     When the S/N is very high, analytic partials should improve the quality
```

```
c      of the fit.
       DIMENSION P(1),B(1),X(500,1)
       COMMON/FCN/IFCN(10)
       COMMON/NUMPK/NPEAKS,M2
       DO 250 J=1,NPEAKS
       ID=3*(J-1)+1
       IGO=IFCN(J)
       GO TO (100,200,300,300),IGO
 50    GO TO 300
100    WIDTH  = (B(ID+2)/2.)**2
       DENOM  = (X(I,1)-B(ID))**2+WIDTH
       P(ID)  = B(ID+1)*WIDTH*2.*(X(I,1)-B(ID))/DENOM**2
       P(ID+1)= WIDTH/DENOM
       P(ID+2)= B(ID+1)*(SQRT(WIDTH)/DENOM-WIDTH**1.5/DENOM**2)
       GO TO 250
200    EXPRES = EXP(-2.77259*((X(I,1)-B(ID))/B(ID+2))**2)
       P(ID)  = (2.*2.77259*B(ID+1)*(X(I,1)-B(ID))*EXPRES)/(B(ID+2)**2)
       P(ID+1)= EXPRES
       P(ID+2)= (2.*2.77259*B(ID+1)*((X(I,1)-B(ID))**2)*EXPRES)/
      ,(B(ID+2)**3)
250    CONTINUE
       P(M2+1)= 1.
       P(M2+2)= X(I,1)
300    RETURN
       END
//LKED.SYSLMOD DD DSN=DDS.NONLIN(PCODE),
// DISP=OLD,VOL=SER=CITSL5
// EXEC FORTXCL,PARM.FORT='OPT=2',PARM.LKED='LIST,NCAL,LET'
//FORT.SYSIN DD *
c
c      subroutine fcode-------------------------------------------------------
c
       SUBROUTINE FCODE(Y,X,B,F,I)
c      This subroutine is called by LSQENP.  It calculates the value
c      baseline and calls subroutine PEAKVA to calculate the peak's
c      contribution.  If not fitting line shapes, it calls YMODEL.
       REAL*4 LINE
       DIMENSION Y(1),X(500,1),B(50)
       COMMON/USRMSG/TITLE(20),FITTST(20)
       COMMON/NUMPK/NPEAKS,M2
       DATA LINE/'LINE'/
       IF(FITTST(1).NE.LINE) GO TO 300
       F=B(M2+1)+B(M2+2)*X(I,1)
       DO 200 IDX=1,M2,3
200    F=PEAKVA(X(I,1),B,IDX)+F
       RETURN
300    F=YMODEL(X(I,1),B)
       RETURN
       END
//LKED.SYSLMOD DD DSN=DDS.NONLIN(FCODE),
// DISP=OLD,VOL=SER=CITSL5
// EXEC FORTXCL,PARM.FORT='OPT=2',PARM.LKED='LIST,NCAL,LET'
//FORT.SYSIN DD *
```

```
c
c     function k-------------------------------------------------------------
c
      FUNCTION K(ZZ,RATIO)
c     This function is the real part of the complex probability
c     or the Voigt spectrum line profile.
      REAL K,K1,K2,K3
      COMMON/VOIGT1/W(10),T(10),Y2
c
c     One must use the ABS(ZZ) since Armstrong's routine does not calculate
c     the symmetric Voigt function for negative arguments (understandably).
c     Given a negative argument, function k will pick the wrong subroutine
c     (k1,k2,k3) and the subroutine will return the wrong value since many
c     of the statements are not even with respect to ZZ.
c
      A=ABS(ZZ)
      Y2=RATIO**2
      IF(RATIO.LT.1.0.AND.A.LT.4.0.OR.RATIO.LT.1.8/(A+1.0))GO TO 300
      IF(RATIO.LT.2.5.AND.A.LT.4.0) GO TO 200
100   K=K3(A,RATIO)
      RETURN
200   K=K2(A,RATIO)
      RETURN
300   K=K1(A,RATIO)
      RETURN
      END
//LKED.SYSLMOD DD DSN=DDS.NONLIN(K),
// DISP=OLD,VOL=SER=CITSL5
// EXEC FORTXCL,PARM.FORT='OPT=2',PARM.LKED='LIST,NCAL,LET'
//FORT.SYSIN DD *
c
c     function K1------------------------------------------------------------
c
      FUNCTION K1(A,RATIO)
      COMMON/HUMMER/C
      REAL*8 C(34),COEFF,BN01,BN02,BN,X1,F
      REAL K1
      F3(T)=EXP(T**2-A**2)
      Y2=RATIO**2
      IF((A**2-Y2).GT.70.0) GO TO 2
      U1=EXP(-A**2+Y2)*COS(2.*A*RATIO)
      GO TO 5
2     U1=0.0
5     IF(A.GT.5.0) GO TO 1000
c     Clenshaw'w algorithm as per Hummer.  From statement 5 TO 30,Dawson's
c     function is computed.  Chebyshev coeffs, C(I), are in COMMON/HUMMER/.
      BN01=0.0D0
      BN02=0.0D0
      X1=A/5.0D0
      COEFF=4.0D0*X1**2-2.0D0
      DO 20 I=1,34
      I1=35-I
      BN=COEFF*BN01-BN02+C(I1)
```

```
      BN02=BN01
20    BN01=BN
30    F=X1*(BN-BN02)
40    DN01=1.0-2.0*A*SNGL(F)
1100  DN02=SNGL(F)
      GO TO 1200
1000  DN01=-(.5/A**2+.75/A**4+1.875/A**6+6.5625/A**8+29.53125/A**10+
     1162.4218/A**12+1055.7421/A**14)
      DN02=(1.-DN01)/(2.*A)
1200  FCN=RATIO*DN01
      IF(RATIO.LE.1.0E-08)GO TO 2500
      Q=1.0
      YN=RATIO
      DO 2000 I=2,50
      DN=(A*DN01+DN02)*(-2.)/FLOAT(I)
      DN02=DN01
      DN01=DN
      IF(MOD(I,2))2000,2000,1500
1500  Q=-Q
      YN=YN*Y2
      G=DN*YN
      FCN=FCN+Q*G
      IF(ABS(G/FCN).LE.1.0E-08)GO TO 2500
2000  CONTINUE
2500  K1=U1-1.12837917*FCN
      RETURN
      END
//LKED.SYSLMOD DD DSN=DDS.NONLIN(K1),
// DISP=OLD, VOL=SER=CITSL5
// EXEC FORTXCL,PARM.FORT='OPT=2',PARM.LKED='LIST,NCAL,LET'
//FORT.SYSIN DD *
c
c     function K2-------------------------------------------------------
c
      FUNCTION K2(A,RATIO)
      REAL K2
      COMMON/VOIGT1/W(10),T(10),Y2
      G=0.0
c     Using S=T(I)+A is also correct since  -ARCTAN(Q)=ARCTAN(-Q)
      DO 100 I=1,10
      R=T(I)-A
      S=-T(I)-A
c     The next two statements are exactly as in Armstrong's program.
c     Though I believe the arguments of the logarithms to be wrong,
c     I have demonstrated the accuracy Armstrong quotes is still right.
100   G=G+(4.*T(I)**2-2.)*(R*ATAN2(R,RATIO)+S*ATAN2(S,RATIO)-.5*RATIO*
     ,(ALOG(Y2+R**2)+ALOG(Y2+S**2)))*W(I)
c     The following is 20 term Gauss-Hermite quadrature using the Voigt
c     fcn integrated by parts once, not twice.  Although less accurate, it's
c     faster.
c     G=G+(ATAN2(R,RATIO) + ATAN2(S,RATIO))*T(I)*W(I)*2.0
      K2=0.318309886*G
      RETURN
```

```
      END
//LKED.SYSLMOD DD DSN=DDS.NONLIN(K2),
// DISP=OLD,VOL=SER=CITSL5
// EXEC FORTXCL,PARM.FORT='OPT=2',PARM.LKED='LIST,NCAL,LET'
//FORT.SYSIN DD *
c
c     function K3-----------------------------------------------------------
c
      FUNCTION K3(A,RATIO)
      REAL K3
      COMMON/VOIGT1/W(10),T(10),Y2
      G=0.0
      DO 100 I=1,10
100   G=G+(1.0E0/((A-T(I))**2+Y2)+1.0E0/((A+T(I))**2+Y2))*W(I)
      K3=0.318309886*RATIO*G
      RETURN
      END
//LKED.SYSLMOD DD DSN=DDS.NONLIN(K3),
// DISP=OLD, VOL=SER=CITSL5
// EXEC FORTXCL,PARM.FORT='OPT=2',PARM.LKED='LIST,NCAL,LET'
//FORT.SYSIN DD *
c
c     function convol-------------------------------------------------------
c
      FUNCTION CONVOL(Z)
      DIMENSION BN(50)
      COMMON/IDENT/ID
      COMMON/FIT/BN
      COMMON/POSIT/XN
      FCN1=(BN(ID+1)*((BN(ID+2)/2)**2))/((XN-Z)**2+(BN(ID+2)/2)**2)
      FCN2=EXP(-2.77259*((Z-BN(ID))/1.8)**2)
      CONVOL=FCN1*FCN2
      RETURN
      END
//LKED.SYSLMOD DD DSN=DDS.NONLIN(CONVOL),
// DISP=OLD,VOL=SER=CITSL5
//  EXEC FORTXCL,PARM.FORT='OPT=2',PARM.LKED='LIST,NCAL,LET'
//FORT.SYSIN DD *
c
c     subroutine fcnout-----------------------------------------------------
c
      SUBROUTINE FCNOUT(CNEW,M,FIXED,PARDES)
c     This subroutine is called to display the results of fitting
c     non-lineshape data (i.e. if one fits data that are not spectra
c     to some functional form other than Gaussian, Lorentzian or Voigt).
      DIMENSION CNEW(100),PARDES(20,50),FIXED(2,50)
      COMMON/USRMSG/TITLE(20),FITTST(20)
      WRITE(6,100)
100   FORMAT(26(5H*****))
      WRITE(6,500)
      WRITE(6,125) (FITTST(I), I=1,20)
125   FORMAT(' THIS IS A ',20A4)
      WRITE(6,130) (TITLE(I), I=1,20)
```

```
130   FORMAT(' ',20A4)
      DO 1000 I=1,M
      WRITE(6,150) I
150   FORMAT(' PARAMETER NUMBER ',I1)
      WRITE(6,200) (PARDES(J,I),J=1,20)
200   FORMAT(10X,20A4)
      WRITE(6,250) (FIXED(J,I),J=1,2)
250   FORMAT(10X,'   PARAMETER IS ',2A4)
      WRITE(6,300) CNEW(2*I-1)
300   FORMAT(10X,'   INITIAL PARAMETER VALUE IS=',E14.7)
      WRITE(6,400) CNEW(2*I)
400   FORMAT(10X,'   FINAL   PARAMETER VALUE IS=',E14.7)
      WRITE(6,500)
500   FORMAT('  ')
1000  CONTINUE
      WRITE(6,100)
      RETURN
      END
//LKED.SYSLMOD DD DSN=DDS.NONLIN(FCNOUT),
// DISP=OLD,VOL=SER=CITSL5
// EXEC FORTXCL,PARM.FORT='OPT=2',PARM.LKED='LIST,NCAL,LET'
//FORT.SYSIN DD *
c
c     subroutine output-------------------------------------------------------
c
      SUBROUTINE OUTPUT(CNEW,NPEAKS)
c     This subroutine is called to display the results of fitting
c     lineshape data only.
      DIMENSION CNEW(100)
      REAL*4 LORE,GAUS,VOIGT,INHOMO
      COMMON/NAME/FUNCT(3,12),INHOMO
      COMMON/USRMSG/TITLE(20),FITTST(20)
      DATA LORE,GAUS,VOIGT/'LORE','GAUS','VOIG'/
      WRITE(6,100)
100   FORMAT(26(5H*****))
      WRITE(6,125)
125   FORMAT(' ')
      WRITE(6,150) (FITTST(I),I=1,20)
150   FORMAT(' THIS IS A ',20A4)
      WRITE(6,175) (TITLE(I), I=1,20)
175   FORMAT(' ',20A4)
      IF(FUNCT(1,1).NE.VOIGT) GO TO 185
      WRITE(6,180) INHOMO
180   FORMAT(' THE INHOMOGENOUS FWHM FOR THE VOIGT FCN IS FIXED TO ='
     ,,F7.3)
185   WRITE(6,125)
      WRITE(6,200)
200   FORMAT(5HOPEAK,T9,'FUNCTION',T24,'INITIAL',T40,'FINAL',T56,'INITIA
     ,L',T73,'FINAL',T88,'INITIAL',T104,'FINAL',T120,'FINAL')
      WRITE(6,300)
300   FORMAT(1H ,T24,'POSITION',T40,'POSITION',T56,'AMPLITUDE',T72,
     ,'AMPLITUDE',T89,'FWHM',T104,'FWHM',T120,'AREA')
      DO 500 I=1,NPEAKS
```

```
      IDX=6*(I-1)
      IF(FUNCT(1,I).NE.GAUS) GO TO 400
c     To calculate the area beneath a Gaussian, 1.064*FWHM*HEIGHT
      AREA=1.06447*CNEW(IDX+4)*CNEW(IDX+6)
      GO TO 500
c     To calculate the area beneath a Lorentzian, 1.57*FWHM*HEIGHT
400   AREA=1.57*CNEW(IDX+4)*CNEW(IDX+6)
      IF(FUNCT(1,I).EQ.VOIGT) AREA=0.0
500   WRITE(6,600) (I,(FUNCT(K,I),K=1,3),(CNEW(IDX+J),J=1,6),AREA)
600   FORMAT(1H ,I3,2X,3A4,7F15.3)
      WRITE(6,125)
      WRITE(6,700)
700   FORMAT(1H0,19HBASELINE PARAMETERS)
      WRITE(6,800)
800   FORMAT(1H ,T16,7HINITIAL,T32,5HFINAL,T48,7HINITIAL,T64,5HFINAL)
      WRITE(6,900)
900   FORMAT(1H ,T16,6HOFFSET,T32,6HOFFSET,T48,5HSLOPE,T64,5HSLOPE)
      WRITE(6,1000) CNEW(6*NPEAKS+1),CNEW(6*NPEAKS+2),CNEW(6*NPEAKS+3),
     1CNEW(6*NPEAKS+4)
1000  FORMAT(12X,E12.5,4X,E12.5,4X,E12.5,4X,E12.5)
      WRITE(6,125)
      WRITE(6,100)
      RETURN
      END
//LKED.SYSLMOD DD DSN=DDS.NONLIN(OUTPUT),
// DISP=OLD,VOL=SER=CITSL5
// EXEC FORTXCL,PARM.FORT='OPT=2',PARM.LKED='LIST,NCAL,LET'
//FORT.SYSIN DD *
c
c     subroutine read-------------------------------------------------------
c
      SUBROUTINE READ(X,Y,N)
      DIMENSION X(500,1),Y(500)
      READ(5,100) N
100   FORMAT(I4)
      WRITE(6,150) N
150   FORMAT(1H0,'NEW DATA SET USED,',I4,' DATA POINTS')
      READ(5,200)(X(I,1),Y(I),I=1,N)
200   FORMAT(E16.9,E16.9)
      RETURN
      END
//LKED.SYSLMOD  DD  UNIT=SYSDA,DSN=DDS.NONLIN(READ),
// DISP=OLD,VOL=SER=CITSL5
// EXEC FORTXCL,PARM.FORT='OPT=2',PARM.LKED='LIST,NCAL,LET'
//FORT.SYSIN DD *
c
c     subroutine plotpk-----------------------------------------------------
c
      SUBROUTINE PLOTPK(X,Y,N,B,M2)
c     This routine does the plotting.  Currently plots on the versatec.
      REAL*4 ORIENT(3),LINE
      INTEGER HORSIZ,VERSIZ
      DIMENSION X(500,1),Y(500),B(50),DOC(3)
```

```
      DIMENSION C(100),PEAKX(151),PEAK(151),SUM(151)
      COMMON/USRMSG/TITLE(20),FITTST(20)
      COMMON/AXSLBL/ HORIZ(16),VERT(16),HORSIZ,VERSIZ,ORIENT
      COMMON/YLIM/IFP,YMIN,YMAX
      COMMON/XLIM/XMIN,XMAX
      COMMON/COMPXY/ITEST,XLNGTH,YLNGTH
      DATA DOC/0.,0.,1./
      DATA LINE/'LINE'/
      DATA VERTST/'VERT'/
c     Draw the axes.
      ITEST=1
      XLNGTH=8.0
      YLNGTH=5.25
      IF(ORIENT(1).NE.VERTST) GO TO 50
      XLNGTH=5.25
      YLNGTH=8.0
50    CONTINUE
      YMAX=YMAX*1.15
      YMIN=0.0
      CALL NEWPEN(2)
      CALL VLABEL(0.0,0.0,XMIN,XMAX,XLNGTH,4,HORIZ,HORSIZ,0,'(F8.1)',8)
      CALL VLABEL(0.0,YLNGTH,XMIN,XMAX,XLNGTH,-4,' ',-1,0,'(F0.0)',0)
      CALL VLABEL(0.0,0.0,YMIN,YMAX,YLNGTH,4,VERT,VERSIZ,1,'(F8.1)',8)
      CALL VLABEL(XLNGTH,0.0,YMIN,YMAX,YLNGTH,4,' ',-1,1,'(F0.0)',0)
c     Write the title at the top of the sheet.
      CALL NEWPEN(5)
      YLONG=YLNGTH+0.1
      CALL SYSSYM(0.0,YLONG,.15,TITLE,80,0.)
      CALL NEWPEN(1)
c     Reduce the number of data points to less than 257.
      DO 200 I=1,5
      NPLOT=N/I
      IF(NPLOT.GT.257) GO TO 200
      ISP=I
      GO TO 204
200   CONTINUE
c     Plot the raw data points.
204   CALL PLOTXY(N,X,Y,XMIN,XMAX,YMIN,YMAX,0,0,3,ISP,DOC)
      XINC=(XMAX-XMIN)/150.
      IF(FITTST(1).NE.LINE) GO TO 600
      XINC1=XINC*10.
c     Draw the baseline.
      DO 205 I=1,16
      XVAL=XMIN+(I-1)*XINC1
      PEAKX(I)=XVAL
205   PEAK(I)=B(M2+1)+B(M2+2)*XVAL
      CALL PLOTXY(16,PEAKX,PEAK,XMIN,XMAX,YMIN,YMAX,0,1,0,1,DOC)
c     Draw each peak, then draw their sum.
      DO 300 I=1,151
      XVAL=XMIN+(I-1)*XINC
300   SUM(I)=B(M2+1)+B(M2+2)*XVAL
      DO 500 IDX=1,M2,3
      DO 400 I=1,151
```

```
      XVAL=XMIN+(I-1)*XINC
      PEAKX(I)=XVAL
      PEAK(I)=PEAKVA(XVAL,B,IDX)
400   SUM(I)=PEAK(I)+SUM(I)
500   CALL PLOTXY(151,PEAKX,PEAK,XMIN,XMAX,YMIN,YMAX,0,1,0,1,DOC)
      CALL PLOTXY(151,PEAKX,SUM,XMIN,XMAX,YMIN,YMAX,1,1,0,1,DOC)
      RETURN
600   DO 700 I=1,151
      XVAL=XMIN+(I-1)*XINC
      PEAKX(I)=XVAL
      PEAK(I)=YMODEL(XVAL,B)
700   CONTINUE
      CALL PLOTXY(151,PEAKX,PEAK,XMIN,XMAX,YMIN,YMAX,1,1,0,1,DOC)
      RETURN
      END
//LKED.SYSLMOD DD DSN=DDS.NONLIN(PLOTPK),
// DISP=OLD,VOL=SER=CITSL5
```

```
// EXEC FORTXCL,PARM.FORT='OPT=2',PARM.LKED='LIST,NCAL,LET'
//FORT.SYSIN DD *
c
c       subroutine lsqenp----------------------------------------------------
c
        SUBROUTINE LSQENP(N,K,M,Y,X,B,IP,IB,IDVT,ICON,IQUIT,IPRNT)
C LSQENP AND CONLIM REVISED FEB., 1975
C REVISED 9-18-73
C  REVISED 11-20-72 TO ADD OPTION FOR NOT PRINTING OBSERVED AND CALCULAT
C       VALUES AFTER CONVERSION.  SET IPRNT LESS THAN 0.
C      REVISED 6-12-70 TO CALCULATE SUM(( F -Y(I))**2) IN DBLE PRECISION
C         NONLINEAR LEAST SQUARES
       DIMENSION BS(50),DB(50),BA(50),G(50),SA(50),P(50),A(50,51)
       DIMENSION X(500,1 ),Y(1),B(1),IB(1)
       COMMON/LSQPLT/IFP,YMIN,YMAX
        COMMON /PARAM/FF,T,E,TAU,AL,GAMCR,DEL,ZETA
       COMMON/WEITS/WTS(500)
        COMMON /AFCLSQ/ SE,PHI,PHIZ,WS,XL,IFSS2,IFSS3,IWS6,I,J,JJ,IBK2,
      ,IBKA,IBKM,IPLOT,BS,SA,A
       REAL*8 PHD,XLL,DTG,GTG
       DATA JBCH,JOCH,JPCH,JXCH,JYCH/1H ,1HO,1HP,1HX,1HY/
       IWS4=IQUIT
       IWS6=ICON
       IPLOT=IFP
       IF (IFP .EQ. 1) SPRD=YMAX-YMIN
C      ---------------------------------------------------------------------
C      MAX NO OF PARAMETERS IS K=50
C      MAX NO OF OBSERVATIONS IS N=500
C                     IWHER = 1 MEANS GET P S AND F
C                     IWHER GREATER THAN 1 MEANS GET F ONLY
   23  IWHER = 0
       GO TO 43
   31  CONTINUE
       CALL FCODE(Y,X,B,F,I)
       IF (IWHER.NE.1)GO TO 39
   34  IF (IFSS2.NE.0)GO TO 39
   35  CONTINUE
       CALL PCODE(P,X,B,F,I)
   39  CONTINUE
       IF (IWHER.EQ.0)GO TO 43
C              1  2   3   4
   42  GO TO(106,363,114,125), IWHER
   43  ITCT=0
       IF (IPLOT .LE. 0) GO TO 55
   49  CONTINUE
       IBCH=JBCH
       IOCH=JOCH
       IPCH=JPCH
       IXCH=JXCH
       IYCH=JYCH
   55  IF(IP.LE.0)GOTO 62
       DO 61 I=1,IP
       IF (IB(I).GT.0)GO TO 61
```

```
   58 WRITE (6,402)
      STOP
   61 CONTINUE
   62 CONTINUE
      XKDB = 1.
C     ..................................................................
C                    START THE CALCULATION OF THE PTP MATRIX
      IBKA=1
      IF(IPRNT .LE. 0) GO TO 82
      WRITE (6,383)N,K,IP,M,IFP,GAMCR,DEL,FF,T,E,TAU,AL,ZETA
   82 CONTINUE
      DO 86 I=1,K
      G (I) =0.
      DO 86 J=1,K
   86 A (I,J)=0.
      GO TO(88,91,91),IBKA
   88 IFSS3=IPRNT
      IFSS2=IDVT
      GO TO 92
   91  IFSS3=1
   92 IF(IFSS3 .GT. 0) WRITE(6,384)(B(J),J=1,K)
C  92 WRITE(6,384)(B(J),J=1,K)
       IF (IFSS3 .LE. 0 .OR. IPRNT.LT. 0) GO TO 99
      IF (IPLOT .LE. 0) GO TO 98
      WS =YMIN+SPRD
      WRITE(6,382)YMIN,WS
      GO TO 99
   98 WRITE (6,386)
   99 I=1
      PHD=0.
      IF (IFSS2.EQ.0)GO TO 104
      GO TO 111
  103 IF (IFSS2.EQ.1)GO TO 112
  104 IWHER=1
C                    GET P S AND F
      GO TO 31
  106 IF (IP.LE.0)GO TO 132
  107 DO 109 II=1,IP
      IWS=IB(II)
  109 P(IWS)=0.
      GO TO 132
C     ..................................................................
C                    THIS IS THE ESTIMATED P S ROUTINE
  111 CONTINUE
  112 IWHER=3
      GO TO 31
  114 FWS=F
      J=1
  116 IF (IP.LE.0)GO TO 120
  117 DO 119 II=1,IP
      IF ((J-IB(II)).EQ.0)GO TO 128
  119 CONTINUE
  120 DBW=B(J)*DEL
```

```
       IF (B(J) .EQ. 0.) DBW = DEL
      TWS=B(J)
      B(J)=B(J)+DBW
      IWHER=4
      GO TO 31
  125 B(J)=TWS
      P(J)=(F-FWS)/DBW
      GO TO 129
  128 P(J)=0.
  129 J=J+1
      IF ((J-K).LE.0)GO TO 116
  131 F=FWS
C                   END OF ESTIMATED P S ROUTINE
C     ..................................................................
C                   NOW, USE THE P S TO MAKE PARTIALS MATRIX
  132 DO 136 JJ=1,K
      G(JJ)=G(JJ)+(Y(I)-F)*P(JJ)
      DO 136 II = JJ,K
      A(II,JJ)=A(II,JJ)+P(II)*P(JJ)
  136 A(JJ,II)=A(II,JJ)
      IF (IPLOT .LE. 0) GO TO 184
  138 IF (IFSS3.LE.0)GO TO 188
C                   PLOTTING Y(I),F
  139 IO = (Y(I)-YMIN)*100./SPRD
      IPP = (F-YMIN)*100./SPRD
      IF (IO.EQ.IPP)GO TO 148
      IF (IO.GT. IPP)GO TO 153
C                   Y(I) OUT FIRST
  143 IP1=IOCH
      IP2=IPCH
      I1=IO
      I2=IPP
      GO TO 157
C                   ONLY ONE CHARACTER
  148 IP1=IYCH
      IP2=IBCH
      I1=IO
      I2=IPP
      GO TO 157
C                   F OUT FIRST
  153 IP1=IPCH
      IP2=IOCH
      I1=IPP
      I2=IO
C                   ZERO PLOTS IN THE LEFT HAND COLUMN, SO I1 IS ITS
C                   OWN BLANK COUNTER
C                   OVERFLOWS PLOT X IN COLUMN 102
C                   UNDERFLOWS ALSO PLOT X IN COLUMN ZERO
  157 IF (I2.LE.101)GO TO 165
  158 I2=101
      IP2=IXCH
      IF (I1.LT.101)GO TO 165
  161 I1=101
```

```
      IP1=IXCH
      IP2=IBCH
      GO TO 171
  165 IF (I1.GE.0)GO TO 171
  166 I1=0
      IP1=IXCH
      IF (I2.GT.0)GO TO 171
  169 I2=1
      IP2=IBCH
  171 I1M1=I1
      I1M2=I2-I1-1
      IF (I1M1.GT.0)GO TO 179
  174 IF (I1M2.GT.0)GO TO 177
  175 WRITE (6,404)IP1,IP2
      GO TO 188
  177 WRITE (6,404)IP1,(IBCH,II=1,I1M2),IP2
      GO TO 188
  179 IF (I1M2.GT.0)GO TO 182
  180 WRITE (6,404)(IBCH,II=1,I1M1),IP1,IP2
      GO TO 188
  182 WRITE (6,404)(IBCH,II=1,I1M1),IP1,(IBCH,II=1,I1M2),IP2
      GO TO 188
  184 WS=Y(I)-F
       IF (IFSS3 .LE. 0 .OR. IPRNT.LT. 0) GO TO 188
  187  WRITE (6,401)X(I,1),Y(I),F,WS
  188 WS=WTS(I)*(Y(I)-F)
      PHD=PHD+WS*WS*1.0D0
      I=I+1
      IF (I.LE.N)GO TO 103
      PHI=PHD
      IF (IP.LE.0)GO TO 199
  193 DO 198 JJ=1,IP
      IWS=IB(JJ)
      DO 197 II=1,K
      A(IWS,II)=0.
  197 A(II,IWS)=0.
  198 A(IWS,IWS)=1.
C     INSERT 1
  199 IF(IBKA .EQ. 1)GO TO 204
      IBKS=1
      CALL        CONLIM(N,K,M,Y,X,B,IP,IB,IBKS,IBD)
      GO TO(82,314,38,359,38),IBD
C                   SAVE SQUARE ROOTS OF DIAGONAL ELEMENTS
  204 CONTINUE
      DO 206 I=1,K
  206 SA(I)=SQRT (A(I,I))
      DO 219 I=1,K
      DO 214 J=1,K
      WS = SA(I)*SA(J)
      IF(WS.GT.0.)GOTO 213
      A(I,J) =0.
      GO TO 214
  213 A(I,J)=A(I,J)/WS
```

```
  214 CONTINUE
      IF(SA(I).GT.0.)GOTO 218
      G(I)=0.
      GO TO 219
  218 G(I)=G(I)/SA(I)
  219 CONTINUE
      DO 221 I=1,K
  221 A(I,I)=1.
      PHIZ=PHI
C                   WE NOW HAVE PHI ZERO
C     ..............................................................
      IF (ITCT.GT.0)GO TO 230
C                   FIRST ITERATION
  225 XL=AL
      ITCT=1
      DO 229 J=1,K
  229 BS(J)=B(J)
C                   BS(J) CORRESPONDS TO PHIZ
  230 IBK1=1
      WS=N-K+IP
      SE=SQRT(PHIZ/WS)
      IF (IFSS3.GT.0)GO TO 239
      IF(IPRNT .LE. 0) GO TO 310
  234 IF (IFSS2.EQ.0)GO TO 237
  235 WRITE (6,387)PHIZ,SE,XLL,GAMMA,XL
      GO TO 310
  237 WRITE (6,388)PHIZ,SE,XLL,GAMMA,XL
      GO TO 310
  239 IF (IFSS2.EQ.0)GO TO 242
  240 WRITE (6,379)PHIZ,SE,XL
      GO TO 310
  242 WRITE (6,385)PHIZ,SE,XL
      GO TO 310
  244 PHIL=PHI
C                   WE NOW HAVE PHI LAMBDA
      DO 247 J=1,K
      IF (ABS(DB(J)/(ABS(B(J)) + TAU)).GE.E)GOTO 251
  247 CONTINUE
      WRITE (6,399)
      IBS=4
      GO TO 371
  251 IF (IWS4.EQ.0)GO TO 257
      IF (IWS4.EQ.1)GO TO 255
      IWS4=IWS4-1
      GO TO 257
  255 WRITE (6,400)
      GO TO 371
  257 XKDB = 1.
      IF (PHIL.GT.PHIZ)GO TO 281
  259 XLS=XL
      DO 262 J=1,K
      BA(J)=B(J)
  262 B(J)=BS(J)
```

```
      IF (XL.GT..00000001)GO TO 268
  264 DO 266 J=1,K
      B(J)=BA(J)
  266 BS(J)=B(J)
      GO TO 82
  268 XL=XL/10.
      IBK1=2
      GO TO 310
  271 PHL4=PHI
C                    WE NOW HAVE PHI(LAMBDA/10)
      IF(PHL4.GT.PHIZ)GOTO 276
  273 DO 274 J=1,K
  274 BS(J)=B(J)
      GO TO 82
  276 XL=XLS
      DO 279 J=1,K
      BS(J)=BA(J)
  279 B(J)=BA(J)
      GO TO 82
  281 IBK1=4
      XLS=XL
      XL=XL/10.
      DO 285 J=1,K
  285 B(J)=BS(J)
      GO TO 310
  287 IF (PHI.LE.PHIZ)GO TO 296
  288 XL=XLS
      IBK1=3
  290 XL=XL*10.
  291 DO 292 J=1,K
  292 B(J)=BS(J)
      GO TO 310
  294 PHIT4=PHI
C                    WE NOW HAVE PHI(10*LAMBDA)
      IF (PHIT4.GT.PHIZ)GO TO 299
  296 DO 297 J=1,K
  297 BS(J)=B(J)
      GO TO 82
  299 IF (GAMMA.GE.GAMCR)GO TO 290
  300 XKDB = XKDB/2.
      DO 303 J=1,K
      IF (ABS(DB(J)/(ABS(B(J))+TAU)).GE.E)GO TO 291
  303 CONTINUE
      DO 305 J=1,K
  305 B(J)=BS(J)
      WRITE (6,410)
      IBS=4
      GO TO 371
C
C     ..................................................................
C                    SET UP FOR MATRIX INVERSION
  310 CONTINUE
      DO 312 I=1,K
```

```
  312 A(I,I)=A(I,I)+XL
C                   GET INVERSE OF A AND SOLVE FOR DB (J)S
      IBKM=1
C     ..............................................................
C                   THIS IS THE MATRIX INVERSION ROUTINE
C                   K IS THE SIZE OF THE MATRIX
  314 CALL GJR(A,K,ZETA,MSING)
      GO TO(316,38),MSING
C     INSERT 2
  316 IF (IBKM .EQ. 1)GO TO 321
      IBKS=2
      CALL       CONLIM(N,K,M,Y,X,B,IP,IB,IBKS,IBD)
      GO TO(82,314,38,359,38),IBD
C                   END OF MATRIX INVERSION, SOLVE FOR DB(J)
  321 DO 325 I=1,K
      DB(I)=0.
      DO 324 J=1,K
  324 DB(I)=A(I,J)*G(J)+DB(I)
  325 DB(I)=XKDB*DB(I)
      XLL=0.0
      DTG = 0.
      GTG = 0.
      DO 334 J=1,K
      XLL=XLL+DB(J)*DB(J)
      DTG = DTG + DB(J)*G(J)
      GTG = GTG + G(J)**2
      IF (SA(J) .GT. 0.0) GO TO 333
C     WRITE (6,332) J,SA(J)
      GO TO 335
  333 CONTINUE
      DB(J)=DB(J)/SA(J)
  335 CONTINUE
      B(J)=B(J)+DB(J)
  334 CONTINUE
      KIP=K-IP
      IF (KIP.EQ.1)GO TO 350
      CGAM=DTG/DSQRT(XLL*GTG)
      JGAM = 1
      IF(CGAM.GT..0)GOTO 342
  340 CGAM = ABS(CGAM)
      JGAM = 2
  342 IF(CGAM .GT. 1.0)CGAM=1.0
      GAMMA = 57.2957795*(1.5707288+CGAM*(-0.2121144+CGAM*(0.074261
     1-CGAM*.0187293)))*SQRT(1.-CGAM)
      GO TO(351,344), JGAM
  344 GAMMA = 180.-GAMMA
      IF (XL.LT.1.0)GO TO 351
  346 WRITE(6,398)XL,GAMMA
      IBS=4
      GO TO 371
  350 GAMMA=0.
  351 XLL=DSQRT(XLL)
      IBK2=1
```

```
      GO TO 359
  354 IF (IFSS3.LE.0)GO TO 358
  355 WRITE (6,380)(DB(J),J=1,K)
      WRITE (6,381)PHI,XL,GAMMA,XLL
  358 GO TO(244,271,294,287),IBK1
C
C     ..................................................................
C                    CALCULATE PHI
  359 I=1
      PHD=0.
      IWHER=2
      GO TO 31
  363 CONTINUE
      PHD=PHD+((Y(I)-F)*1.0D0*WTS(I))**2
      I=I+1
      IF (I.LE.N)GO TO 31
      PHI=PHD
C     INSERT 3
      IF (IBK2 .EQ. 1)GO TO 354
      IBKS=3
      CALL       CONLIM(N,K,M,Y,X,B,IP,IB,IBKS,IBD)
      GO TO(82,314,38,359,38),IBD
  371 CONTINUE
      IBKS=4
      CALL       CONLIM(N,K,M,Y,X,B,IP,IB,IBKS,IBD)
      GO TO(82,314,38,359,38),IBD
C     ..................................................................
   38 RETURN
  332 FORMAT(5X'J=',I5,5X'SA(J) = ',E15.6)
  376 FORMAT (25I3)
  377 FORMAT (7F10.0)
  378 FORMAT(12A6 )
  379 FORMAT (/13X,4H PHI 14X,4H S E             9X,7H LAMBDA   6X,
     1 25H ESTIMATED PARTIALS USED  / 5X,2E18.8,  E13.3 )
  380 FORMAT(/12H INCREMENTS 5E18.8/(12X,5E18.8) )
  381 FORMAT (13X,4H PHI 10X,7H LAMBDA 6X,7H GAMMA  6X, 7H LENGTH  /
     1 5X, E18.8, 3E13.3)
  382 FORMAT(1X,1E9.2,86X,1E9.2 /1X,1H+ 99X,1H+ )
  383 FORMAT( 5H1N = I3,5X,5H K = I3,5X,5HIP = I3,5X,5H M = I3,5X,
     1 7H IFP = I3,5X,13HGAMMA CRIT = E10.3,5X,6HDEL = E10.3/6H FF =
     2E10.3,5X,5H T = E10.3,5X,5H E = E10.3,5X,7H TAU = E10.3,5X,6H XL =
     3  E10.3 , 4X, 7HZETA = E10.3 /)
  384 FORMAT(/12H PARAMETERS 5E18.8/(12X,5E18.8) )
  385 FORMAT (/13X,4H PHI 14X,4H S E             9X,7H LAMBDA 6X,
     1 25H ANALYTIC PARTIALS USED   /5X, 2E18.8,  E13.3)
 386   FORMAT(//T12,'X(I,1)',T31,'Y OBS.',T49,'Y PRED.',T68,'DIFF'/)
  387 FORMAT (/13X,4H PHI 14X,4H S E 11X,7H LENGTH 6X, 7H GAMMA 6X,
     1 7H LAMBDA 6X, 25HESTIMATED PARTIALS USED  /5X, 2E18.8, 3E13.3)
  388 FORMAT (/13X,4H PHI 14X,4H S E 11X,7H LENGTH 6X, 7H GAMMA 6X,
     1 7H LAMBDA 6X, 24HANALYTIC PARTIALS USED  /5X, 2E18.8, 3E13.3)
  389 FORMAT(2X,I3,20H PARAMETER NOT USED   )
  390 FORMAT(2X,I3,12H NONE FOUND   )
  391 FORMAT(2X,I3,36X,2E18.8  )
```

```
  392 FORMAT(1H /13H PTP INVERSE )
  393 FORMAT(1H /30H PARAMETER CORRELATION MATRIX  )
  394 FORMAT( 2X,I3,5E18.8)
  395 FORMAT( 1H /1H / 13X,4H STD 17X, 16H ONE - PARAMETER 21X,
     1 14H SUPPORT PLANE / 3X, 2H B 7X,6H ERROR 12X, 6H LOWER 12X,
     2 6H UPPER 12X, 6H LOWER 12X, 6H UPPER   )
  396 FORMAT( 1H /1H /30H  NONLINEAR CONFIDENCE LIMITS  / /
     1 16H PHI CRITICAL = E15.8     )
  397 FORMAT(1H / 6H  PARA 6X,8H LOWER B 8X,10H LOWER PHI 10X,8H UPPER B
     1 8X,10H UPPER PHI  )
  398 FORMAT(18H GAMMA LAMBDA TEST,5X,2E13.3)
  399 FORMAT(14H EPSILON TEST  )
  400 FORMAT(11H FORCE OFF  )
  401 FORMAT (5X,6E18.8/59X,2E18.8)
  402 FORMAT ( 40H BAD DATA, SUBSCRIPTS FOR UNUSED BS = 0   / / / )
  403 FORMAT(2X,I3,5E18.8 )
  404 FORMAT(1H , 110A1  )
  405 FORMAT(10A1)
  406 FORMAT (7F10.0)
  407 FORMAT (8F10.0)
  408 FORMAT(1H1)
  409 FORMAT( 5H1N = I3,5X,5H K = I3,5X,5HIP = I3,5X,5H M = I3,5X,
     1                              /   6H FF = E10.3,5X,5H T = E10.3,
     2 5X,5H E = E10.3,5X,7H TAU = E10.3   /    )
  410 FORMAT (19H GAMMA EPSILON TEST    )
  411 FORMAT (3X,I5,2X,10F10.4)
  412 FORMAT (27H0 NEGATIVE DIAGONAL ELEMENT   )
      END
      BLOCK DATA
      COMMON/LSQPLT/IFP,PLOT(2)
      COMMON /PARAM/ PARAM(8)
      COMMON/WEITS/WTS(500)
      DATA IFP,PLOT/0,2*0.0/
      DATA PARAM/4.,2.,.00005,.001,.01,45.,.00001,.1E-70/
      DATA WTS/500*1.0/
      END
      SUBROUTINE CONLIM(N,K,M,Y,X,B,IP,IB,IBKS,IBD)
C     ..................................................................
C                  THIS IS THE CONFIDENCE LIMIT CALCULATION
      DIMENSION BS(50),SA(50),A(50,51)
      DIMENSION X(500,1),Y(1),B(1),IB(1)
       COMMON /PARAM/FF,T,E,TAU,AL,GAMCR,DEL,ZETA
       COMMON /AFCLSQ/ SE,PHI,PHIZ,WS,XL,IFSS2,IFSS3,IWS6,I,J,JJ,IBK2,
     ,IBKA,IBKM,IPLOT,BS,SA,A
C     TO INITIATE CONLIM
      IF (IBKS .EQ. 4)GO TO 21
      GO TO(15,17,18),IBKS
   15 IBKA1=IBKA-1
      GO TO(27,32),IBKA1
   17 GO TO 43
   18 IBK21=IBK2-1
      J=INDEX
      GO TO(158,27,125,134,144),IBK21
```

```
   21 DO 22 J=1,K
   22 B(J)=BS(J)
      WRITE (6,201)N,K,IP,M,FF,T,E,TAU
      IBKA=2
C                    THIS WILL PRINT THE Y,YHAT,DELTA Y
      IBD=1
      GO TO 204
   27 IF (IPLOT .LE. 0) GO TO 32
   28 IBKA=3
      IPLOT=0
      IBD=1
      GO TO 204
   32 WS=N-K+IP
      SE=SQRT(PHI/WS)
      PHIZ=PHI
      IF (IFSS2.EQ.0)GO TO 38
   36 WRITE (6,189)PHIZ,SE,XL
      GO TO 39
   38 WRITE(6,190) PHIZ,SE,XL
C                    NOW WE HAVE MATRIX A
   39 CONTINUE
      IBKM=2
      IBD=2
      GO TO 204
C
C                    NOW WE HAVE C = A INVERSE
   43 DO 45 J=1,K
      IF(A(J,J).LT..0)GO TO 47
   45 SA(J)=SQRT(A(J,J))
      IBOUT=0
      GO TO 48
   47 IBOUT=1
   48 KST=-4
      WRITE (6,194)
   50 KST=KST+5
      KEND=KST+4
      IF (KEND.LT.K)GO TO 54
      KEND=K
   54 DO 55 I=1,K
   55 WRITE (6,196)I,(A(I,J),J=KST,KEND)
      IF (KEND.LT.K)GO TO 50
      IF (IBOUT.EQ.0)GO TO 61
      WRITE (6,203)
      IBD=3
      GO TO 204
   61 DO 68 I=1,K
      DO 68 J=1,K
      WS=SA(I)*SA(J)
      IF(WS.GT. 0.)GOTO 67
   65 A(I,J)=0.
      GO TO 68
   67 A(I,J)=A(I,J)/WS
   68 CONTINUE
```

```
      DO 70 J=1,K
   70 A(J,J)=1.
      WRITE (6,195)
      KST=-9
   73 KST=KST+10
      KEND=KST+9
      IF (KEND.LT.K)GO TO 77
      KEND=K
   77 DO 78 I=1,K
   78 WRITE (6,202)I,(A(I,J),J=KST,KEND)
      IF (KEND.LT.K)GO TO 73
C                    GET T*SE*SQRT(C(I,I))
      DO 81 J=1,K
   81 SA(J)=  SE*SA(J)
   82 WRITE (6,197)
      WS=K-IP
      DO 98 J=1,K
      IF (IP.LE.0)GO TO 89
   86 DO 88 I=1,IP
      IF (J.EQ.IB(I))GO TO 97
   88 CONTINUE
   89 HJTD=SQRT(WS*FF)*SA(J)
      STE=SA(J)
      OPL=BS(J)-SA(J)*T
      OPU=BS(J)+SA(J)*T
      SPL=BS(J)-HJTD
      SPU=BS(J)+HJTD
      WRITE ( 6,200)J,STE,OPL,OPU,SPL,SPU
      GO TO 98
   97 WRITE (6,191)J
   98 CONTINUE
C                  NONLINEAR CONFIDENCE LIMIT
      IF (IWS6.EQ.1) IBD=3
      IF (IWS6.EQ.1)GO TO 204
      WS=K-IP
      WS1=N-K+IP
      PKN=WS/WS1
      PC=PHIZ*(1.+FF*PKN)
      WRITE (6,198)PC
      WRITE (6,199)
      IFSS3=1
      J=1
  109 IBKP=1
      DO 112 JJ=1,K
  112 B(JJ)=BS(JJ)
      IF (IP.LE.0)GO TO 117
  114 DO 116 JJ=1,IP
      IF (J.EQ.IB(JJ))GO TO 173
  116 CONTINUE
  117 DD=-1.
      IBKN=1
  119 D=DD
      B(J)=BS(J)+D*SA(J)
```

```
      IBK2=4
      IBD=4
      INDEX=J
      GO TO 204
  125 PHI1=PHI
      IF (PHI1.GE.PC)GO TO 137
  127 D=D+DD
      IF (D/DD.GE.5.)GO TO 177
  129 B(J)=BS(J)+D*SA(J)
      IBK2=5
      IBD=4
      INDEX=J
      GO TO 204
  134 PHID=PHI
      IF (PHID.LT.PC)GO TO 127
      GO TO 146
  137 D=D/2.
      IF (D/DD.LE..001)GO TO 177
  139 B(J)=BS(J)+D*SA(J)
      IBK2=6
      IBD=4
      INDEX=J
      GO TO 204
  144 PHID=PHI
      IF (PHID.GT.PC)GO TO 137
  146 XK1=PHIZ/D+PHI1/(1.-D)+PHID/(D*(D-1.))
      XK2=-(PHIZ*(1.+D)/D+D/(1.-D)*PHI1+PHID/(D*(D-1.)))
      XK3=PHIZ-PC
      BC = (SQRT(XK2*XK2-4.*XK1*XK3)-XK2)/(2.*XK1)
      GO TO(151,153),IBKN
  151 B(J)=BS(J)-SA(J)*BC
      GO TO 154
  153 B(J)=BS(J)+SA(J)*BC
  154 IBK2=2
      IBD=4
      INDEX=J
      GO TO 204
  158 GO TO(159,164),IBKN
  159 IBKN=2
      DD=1.
      BL=B(J)
      PL=PHI
      GO TO 119
  164 BU=B(J)
      PU=PHI
      GO TO(167,169,171,175),IBKP
  167 WRITE (6,196) J, BL, PL, BU, PU
      GO TO 185
  169 WRITE (6,193) J, BU, PU
      GO TO 185
  171 WRITE (6,196)J,BL, PL
      GO TO 185
  173 WRITE (6,191)J
```

```
      GO TO 185
  175 WRITE (6,192)J
      GO TO 185
  177 GO TO(178,180),IBKN
C                   DELETE LOWER PRINT
  178 IBKP=2
      GO TO 158
  180 GO TO(181,183),IBKP
C                   DELETE UPPER PRINT
  181 IBKP=3
      GO TO 158
C                   LOWER IS ALREADY DELETED, SO DELETE BOTH
  183 IBKP=4
      GO TO 158
  185 J=J+1
      J1=J-1
      IF (J1 .NE. K)GO TO 109
      DO 184 JJ=1,K
  184 B(JJ)=BS(JJ)
      IBD=5
  189 FORMAT (/13X,4H PHI 14X,4H S E              9X,7H LAMBDA   6X,
     1 25H ESTIMATED PARTIALS USED  / 5X,2E18.8,  E13.3 )
  190 FORMAT (/13X,4H PHI 14X,4H S E              9X,7H LAMBDA 6X,
     1 25H ANALYTIC PARTIALS USED   /5X, 2E18.8,  E13.3)
  191 FORMAT(2X,I3,20H PARAMETER NOT USED    )
  192 FORMAT(2X,I3,12H NONE FOUND    )
  193 FORMAT(2X,I3,36X,2E18.8  )
  194 FORMAT(1H /13H PTP INVERSE )
  195 FORMAT(1H /30H PARAMETER CORRELATION MATRIX  )
  196 FORMAT( 2X,I3,5E18.8)
  197 FORMAT( 1H /1H / 13X,4H STD 17X, 16H ONE - PARAMETER 21X,
     1 14H SUPPORT PLANE / 3X, 2H B 7X,6H ERROR 12X, 6H LOWER 12X,
     2 6H UPPER 12X, 6H LOWER 12X, 6H UPPER    )
  198 FORMAT( 1H /1H /30H  NONLINEAR CONFIDENCE LIMITS  / /
     1 16H PHI CRITICAL = E15.8      )
  199 FORMAT(1H / 6H  PARA 6X,8H LOWER B 8X,10H LOWER PHI 10X,8H UPPER B
     1 8X,10H UPPER PHI  )
  200 FORMAT(2X,I3,5E18.8 )
  201 FORMAT( 5H1N = I3,5X,5H K = I3,5X,5HIP = I3,5X,5H M = I3,5X,
     1                              /   6H FF = E10.3,5X,5H T = E10.3,
     2 5X,5H E = E10.3,5X,7H TAU = E10.3   /    )
  202 FORMAT (3X,I5,2X,10F10.4)
  203 FORMAT (27H0 NEGATIVE DIAGONAL ELEMENT   )
  204 RETURN
      END
      SUBROUTINE GJR(A,N,EPS,MSING)
C GJR   OBJECT DECK DATE 9-18-73
C     GAUSS-JORDAN-RUTISHAUSER MATRIX INVERSION WITH DOUBLE PIVOTING.
      DIMENSION A(50,50),B(50),C(50),P(50),Q(50)
      INTEGER P,Q
      MSING=1
      DO 39 K=1,N
C     DETERMINATION OF THE PIVOT ELEMENT
```

```
      PIVOT=0.
      DO 13 I=K,N
      DO 13 J=K,N
      IF(ABS(A(I,J))-ABS(PIVOT))13,13,10
   10 PIVOT=A(I,J)
      P(K)=I
      Q(K)=J
   13 CONTINUE
      IF(ABS(PIVOT)-EPS)56,56,15
C     EXCHANGE OF THE PIVOTAL ROW WITH THE KTH ROW
   15 IF(P(K)-K)16,21,16
   16 DO 20 J=1,N
      L=P(K)
      Z=A(L,J)
      A(L,J)=A(K,J)
   20 A(K,J)=Z
C     EXCHANGE OF THE PIVOTAL COLUMN WITH THE KTH COLUMN
   21 IF(Q(K)-K)22,27,22
   22 DO 26 I=1,N
      L=Q(K)
      Z=A(I,L)
      A(I,L)=A(I,K)
   26 A(I,K)=Z
   27 CONTINUE
C     JORDAN STEP
      DO 36 J=1,N
      IF(J-K)33,30,33
   30 B(J)=1./PIVOT
      C(J)=1.
      GO TO 35
   33 B(J)=-A(K,J)/PIVOT
      C(J)=A(J,K)
   35 A(K,J)=0.
   36 A(J,K)=0.
      DO 39 I=1,N
      DO 39 J=1,N
   39 A(I,J)=A(I,J)+C(I)*B(J)
C     REORDERING THE MATRIX
      DO 54 M=1,N
      K=N-M+1
      IF(P(K)-K)43,48,43
   43 DO 47 I=1,N
      L=P(K)
      Z=A(I,L)
      A(I,L)=A(I,K)
   47 A(I,K)=Z
   48 IF(Q(K)-K)49,54,49
   49 DO 53 J=1,N
      L=Q(K)
      Z=A(L,J)
      A(L,J)=A(K,J)
   53 A(K,J)=Z
   54 CONTINUE
```

```
   55 RETURN
   56 WRITE (6,57) P(K),Q(K),PIVOT
   57 FORMAT(16HOSINGULAR MATRIX3H I=I3,3H J=I3,7H PIVOT=E16.8/)
      MSING=1
      GO TO 55
      END
//LKED.SYSLMOD DD DSN=DDS.NONLIN(LSQENP),
// DISP=OLD,VOL=SER=CITSL5
//
```

APPENDIX V.

SOLUTIONS TO DIFFERENTIAL EQUATIONS MODELING TRAP-TO-TRAP ENERGY TRANSFER

APPENDIX V.

This appendix summarizes the solutions for the differential equations used to model energy transfer between the monomers (m) and dimers (d) in DBN. Three cases are considered: (1) the m-to-d and d-to-m transfer rates are time independent, (2) both transfer rates depend on time as $t^{-1/2}$ and (3) the m-to-d rate goes as $t^{-1/2}$ and the d-to-m rate is a constant. The rate equation models are approximate and do not conserve state occupation probabilities.

CASE 1.

Define $n_m(t)$ as the population of the monomer, β_m as the intrinsic monomer decay rate, ω_{md} as the m-to-d transfer rate. Similarly, define a set of rates for the dimer by replacing subscripts "d" with "m" and "m" with "d" where appropriate. A phenomenological set of coupled equations are used:

$$\dot{n}_m = -(\beta_m + \omega_{md})n_m + \omega_{dm}n_d$$

$$\dot{n}_d = -(\beta_d + \omega_{dm})n_d + \omega_{md}n_m.$$

A more exact treatment would solve explicitly for the ground state and excited state probabilities, e.g. P_m for the excited monomer and $1-P_m$ for the ground state monomer occupation probabilities. Laplace transform the two equations:

$$s\bar{n}_m - n_m(0) = -\beta'\bar{n}_m + \omega_{dm}\bar{n}_d$$

$$s\bar{n}_d - n_d(0) = \omega_{md}\bar{n}_m - \alpha\bar{n}_d$$

where $\beta' = (\beta_m + \omega_{md})$ and $\alpha = (\beta_d + \omega_{dm})$, $\bar{n}_m$, $\bar{n}_d$ are the transforms of n_m and n_d. Algebraically manipulating the transformed equations:

$$\bar{n}_m(s + \beta') = n_m(0) + \omega_{dm}\bar{n}_d$$

$$\bar{n}_d = \frac{n_d(0) + \omega_{md}\bar{n}_m}{(s + \alpha)}$$

Substitute the expression for $\bar{n}_d$ into the expression for $\bar{n}_m$ to find

(1) $$\bar{n}_m = \frac{n_m(0)(s + \alpha) + \omega_{dm}n_d(0)}{(s + \alpha)(s + \beta') - \omega_{dm}\omega_{md}}$$

Find the expressions for $\bar{n}_m$ in terms of s and constants

$$\bar{n}_m = \frac{n_m(0) + \omega_{dm}\bar{n}_d}{(s + \beta')}$$

substitute into the expression for $\bar{n}_d$:

$$\bar{n}_d(s + \alpha) = n_d(0) + \frac{\omega_{md}(n_m(0) + \omega_{dm}\bar{n}_d)}{(s + \beta')}$$

(2) $$\bar{n}_d = \frac{n_d(0)(s + \beta') + \omega_{md}n_m(0)}{(s + \alpha)(s + \beta') - \omega_{md}\omega_{dm}}$$

Now we want to do the inverse Laplace transform so we must find the zeros of the denominators for the expressions for $\bar{n}_d$ and $\bar{n}_m$ (thus we will find the residues for the inverse Laplace transform and we can do a partial fraction decomposition). Equations (1) and (2) can be recast as (we'll find the same poles this way)

$$\bar{n}_m = \frac{n_m(0)(s + \alpha) + \omega_{dm}n_d(0)}{(s - s_1)(s - s_2)}$$

$$\bar{n}_d = \frac{n_d(0)(s + \beta') + \omega_{dm} n_d(0)}{(s - s_1)(s - s_2)}$$

where s_1 and s_2 are the zeros of $(s + \alpha)(s + \beta') - \omega_{md}\omega_{dm}$ and are given by

$$s_{1,2} = \frac{-(\alpha + \beta')}{2} \pm \frac{[(\alpha + \beta')^2 + 4(\omega_{dm}\omega_{md} - \alpha\beta')]^{1/2}}{2}$$

Substitute in the expressions for α and β' and let $\beta_m = \beta_d = \beta'$.

$$s_{1,2} = 1/2[(2\beta + \omega_{dm} + \omega_{md}) \pm (\omega_{dm} + \omega_{md})]$$

$$s_1 = \beta \ , \quad s_2 = \beta + \omega_{md} + \omega_{dm}$$

Now, do a partial fraction decomposition on the expression for $\bar{n}_m$;

$$\frac{n_m(0)(s + \alpha) + n_d(0)\omega_{dm}}{(s - s_1)(s - s_2)} = \frac{A}{(s - s_1)} + \frac{B}{(s - s_2)}$$

One finds the coefficients A andB to be (easily check by substitution)

$$\frac{[n_m(0) + n_d(0)]\omega_{dm}}{\omega_{dm}\omega_{md}} = A$$

$$\frac{[n_m(0)\omega_{md} - n_d(0)\omega_{dm}]}{\omega_{md} + \omega_{dm}} = B$$

Therefore, collecting all the previous results:

$$\bar{n}_m(t) = \frac{n_m(0)(s + \alpha) + n_d(0)\omega_{dm}}{(s - s_1)(s - s_2)}$$

$$= \frac{[n_m(0) + n_d(0)]\omega_{dm}}{(\omega_{md} + \omega_{dm})(s - s_1)} + \frac{[n_m(0)\omega_{md} - n_d(0)\omega_{dm}]}{(\omega_{md} + \omega_{dm})(s - s_2)}$$

Thus, the inverse Laplace transform is (substituting back in the expressions for s_1 and s_2)

$$n_m(t) = \left[\frac{(n_m(0)+n_d(0))\omega_{dm}}{\omega_{md} + \omega_{dm}}\right] e^{-\beta t} + \left[\frac{n_m(0)\omega_{md} - n_d(0)\omega_{dm}}{\omega_{md} + \omega_{dm}}\right] e^{-(\beta + \omega_{md}+\omega_{dm})t}$$

Similarly, one finds

$$n_d(t) = \left[\frac{(n_m(0)+n_d(0))\omega_{md}}{\omega_{dm} + \omega_{md}}\right] e^{-\beta t} + \left[\frac{n_m(0)\omega_{md}-n_d(0)\omega_{dm}}{\omega_{dm} + \omega_{md}}\right] e^{-(\beta+\omega_{md}+\omega_{dm})t}$$

which can be tested by differentiation.

CASE 2.

ω_{md} and ω_{dm} depend on time as $t^{-1/2}$. One cannot do a Laplace transform on the system of equations since the transform of terms like $n_m(t)\omega_{md}t^{-1/2}$ and $n_d(t)\omega_{dm}t^{-1/2}$ cannot be explicitly evaluated for arbitrary $n_m(t)$, $n_d(t)$. In other words, we have

$$\dot{n}_m = P_m - (\beta_m + \omega_{md}t^{-1/2})n_m + \omega_{dm}t^{-1/2}n_d$$

$$\dot{n}_d = P_d - (\beta_d + \omega_{dm}t^{-1/2})n_d + \omega_{md}t^{-1/2}n_m .$$

Therefore, one guesses ata a solution by naively replacing ω_{md} by $\omega_{md}t^{-1/2}$ and ω_{dm} by $\omega_{dm}t^{-1/2}$ in just the exponential arguments. Fortunately, the resulting solution is exact as tested by substitution.

$$n_m(t) = \left[\frac{\omega_{dm}(n_m(0)+n_d(0))}{\omega_{md} + \omega_{dm}}\right] e^{-\beta t} + \left[\frac{\omega_{md}n_m(0)-\omega_{dm}n_d(0)}{\omega_{md} + \omega_{dm}}\right] e^{-(\beta t+2\omega_{md}t^{1/2}+2\omega_{dm}t^{1/2})}$$

$$n_d(t) = \left[\frac{\omega_{md}(n_m(0)+n_d(0))}{\omega_{md} + \omega_{dm}}\right] e^{-\beta t} + \left[\frac{\omega_{dm}n_d(0)-\omega_{md}n_m(0)}{\omega_{md} + \omega_{dm}}\right] e^{-(\beta t+2\omega_{md}t^{1/2}+2\omega_{dm}t^{1/2})}$$

CASE 3

ω_{md} goes as $t^{-1/2}$ and ω_{dm} is a constant. Again, the Laplace transform cannot be performed due to terms containing $t^{-1/2}$ and a solution must be guessed at. I have arrived at a variety of approximate solutions with error terms having different time dependences, but the the solution used in fitting the data was:

$$n_m(t)= \frac{\omega_{dm}(n_m(0)+n_d(0))e^{-\beta t}}{\omega_{md}t^{-1/2}+\omega_{dm}} + \left[\frac{\omega_{md}t^{-1/2}n_m(0)-\omega_{dm}n_d(0)}{\omega_{md}t^{-1/2}+\omega_{dm}}\right] e^{(-\beta t-2\omega_{md}t^{1/2}-\omega_{dm}t)}$$

$$n_d(t)=\frac{\omega_{md}t^{-1/2}(n_m(0)+n_d(0))e^{-\beta t}}{\omega_{md}t^{-1/2}+\omega_{dm}} + \left[\frac{\omega_{dm}n_d(0)-\omega_{md}t^{-1/2}n_m(0)}{\omega_{md}t^{-1/2}+\omega_{dm}}\right] e^{(-\beta t-2\omega_{md}t^{1/2}-\omega_{dm}t)}$$

Differentiating the solutions, one finds

$$\dot{n}_m=-\beta n_m-\omega_{md}t^{-1/2}n_m+\omega_{dm}n_d + \frac{0.5t^{-3/2}\omega_{md}\omega_{dm}(n_m(0)+n_d(0))e^{-\beta t}(1-e^{[-2\omega_{md}t^{1/2}-\omega_{dm}t]})}{(\omega_{md}t^{-1/2}+\omega_{dm})^2}$$

$$\dot{n}_d = -\beta n_d + \omega_{md}t^{-1/2}n_m - \omega_{dm}n_d$$

$$- \frac{0.5\omega_{md}t^{-3/2}\omega_{dm}(n_m(0)+n_d(0))e^{-\beta t}(1-e^{[-2\omega_{md}t^{1/2}-\omega_{dm}t]})}{(\omega_{md}t^{-1/2}+\omega_{dm})^2}$$

For the trial solutions to be correct, the last term in the last two equations must be negligible. Since the prefactors are small (for typical fitting parameters) and the exponential factors range from 0 to 1, the approximation should be good enough.